

**UNIVERSITE DU QUÉBEC**

THÈSE PRÉSENTÉE À  
L'UNIVERSITÉ DU QUÉBEC À CHICOUTIMI  
COMME EXIGENCE PARTIELLE  
AU DOCTORAT EN INGÉNIERIE

PAR  
**MAJID KERMANI KOOSHEH**

ICE SHEDDING FROM CABLES AND CONDUCTORS –  
A CRACKING MODEL OF ATMOSPHERIC ICE

DELESTAGE DE GLACE DES CABLES ET DES CONDUCTEURS-  
UN MODELE DE RUPTURE FRAGILE DE LA GLACE  
ATMOSPHERIQUE

**DECEMBER 2007**



### Mise en garde/Advice

Afin de rendre accessible au plus grand nombre le résultat des travaux de recherche menés par ses étudiants gradués et dans l'esprit des règles qui régissent le dépôt et la diffusion des mémoires et thèses produits dans cette Institution, **l'Université du Québec à Chicoutimi (UQAC)** est fière de rendre accessible une version complète et gratuite de cette œuvre.

Motivated by a desire to make the results of its graduate students' research accessible to all, and in accordance with the rules governing the acceptance and diffusion of dissertations and theses in this Institution, the **Université du Québec à Chicoutimi (UQAC)** is proud to make a complete version of this work available at no cost to the reader.

L'auteur conserve néanmoins la propriété du droit d'auteur qui protège ce mémoire ou cette thèse. Ni le mémoire ou la thèse ni des extraits substantiels de ceux-ci ne peuvent être imprimés ou autrement reproduits sans son autorisation.

The author retains ownership of the copyright of this dissertation or thesis. Neither the dissertation or thesis, nor substantial extracts from it, may be printed or otherwise reproduced without the author's permission.

To my wife, Rozita

for her encouragement and unsparing support

and my son, Siavash

for his patience and understanding during this study.

## RÉSUMÉ

Le givrage atmosphérique est à la source de sérieux problèmes d'origine électrique et mécanique sur les réseaux de transport et de distribution de l'énergie électrique. Le délestage naturel de glace de câbles et conducteurs, une conséquence du givrage atmosphérique, est à la source de nombreux problèmes, d'où la nécessité de l'étude de la rupture fragile de la glace atmosphérique. Des pannes majeures sur les réseaux électriques pendant les tempêtes de verglas seraient évitables par l'amélioration des méthodes de déglacage et de prévention du givrage. Pour ce faire, il est nécessaire d'approfondir nos connaissances sur les propriétés mécaniques de la glace atmosphérique.

Les objectifs de cette recherche, dans le cadre de la problématique générale du délestage de glace, sont l'étude et l'estimation des contraintes s'appliquant à la glace atmosphérique accumulée sur un câble, la mesure de ses propriétés mécaniques et le développement d'un modèle de rupture fragile de la glace atmosphérique.

Les forces exercées par le vent et la charge de glace sont les facteurs les plus importants dans le délestage. La force du vent crée trois types d'oscillation sur les lignes de transport d'énergie : galop (haute amplitude, basse fréquence), vibration éolienne (basse amplitude, haute fréquence) et oscillation de sillage (wake-induced oscillation). Le changement des caractéristiques aérodynamiques du câble cause des oscillations de grande amplitude (galop). Au cours de la vibration éolienne, l'alternance de vortex causés par le vent sur le câble est la cause de cette vibration. L'oscillation de sillage se produit dans les joncteurs empaquetés et à une amplitude moyenne. La charge de la glace peut causer sa fissuration ou accélérer sa rupture en augmentant l'inertie de masse. Quelques facteurs indirects fournissent des conditions appropriées pour la rupture de la glace par réduction de force ou élimination de l'adhérence au câble.

Afin d'estimer les contraintes développées dans la glace accumulée sur un câble pendant le galop ou la vibration éolienne, deux modèles d'éléments finis ont été développés. La vibration éolienne et celle du galop sur un câble recouvert de glace ont été simulées pour déterminer les données de déplacement et de charge, qui servent d'intrants pour ces modèles. Les équations de mouvement du câble ont été appliquées à un câble recouvert de glace et résolues avec MATLAB pour obtenir des séries temporelles des mouvements du câble, des forces aérodynamiques, de la tension horizontale additionnelle agissant sur le câble pendant la vibration et le moment causé par le retour élastique. Le modèle ABAQUS a indiqué que, au cours du galop, les contraintes les plus élevées dans le sens du diamètre vertical de la glace sont atteintes lorsque le point médian du câble se situe aux positions les plus élevées et les plus basses de sa trajectoire.

Pour étudier la morphologie des grains et des bulles d'air de la glace atmosphérique, la glace a été accumulée sur un cylindre rotatif dans la soufflerie réfrigérée du CIGELE. Pour

l'accumulation de la glace atmosphérique, on a utilisé une teneur en eau liquide de  $2,5 \text{ g/m}^3$ , une vitesse du vent de  $10 \text{ m/s}$ , de même que trois températures d'accumulation de  $-6 \text{ }^\circ\text{C}$ ,  $-10 \text{ }^\circ\text{C}$  et  $-20 \text{ }^\circ\text{C}$ . L'étude de minces sections de glace atmosphérique a indiqué que la taille des grains de glace diminue avec la température d'accumulation de la glace. La taille moyenne des grains de glace atmosphérique est approximativement de  $1.5 \text{ mm}$ ,  $0.5 \text{ mm}$  et de  $0.4 \text{ mm}$  pour la glace accumulée à  $-6 \text{ }^\circ\text{C}$ ,  $-10 \text{ }^\circ\text{C}$  et  $-20 \text{ }^\circ\text{C}$ , respectivement. Pour des épaisseurs de glace plus grandes que  $2 \text{ mm}$ , les grains sont allongés et perpendiculaires à l'axe du cylindre, pour la glace accumulée à  $-10 \text{ }^\circ\text{C}$  et  $-6 \text{ }^\circ\text{C}$ . Les expériences sur les effets du champ électrique à haute tension sur la glace atmosphérique confirment que la présence d'un champ électrique à haute tension affecte la structure, la densité et la quantité de la glace accumulée sur les conducteurs.

La résistance à la compression de la glace atmosphérique augmente avec la diminution de la température d'essai. En outre, on a constaté que la résistance de la glace augmente avec l'augmentation du taux de déformation jusqu'à une valeur de  $10^{-3} \text{ s}^{-1}$ , et puis diminue à des taux plus élevés de contrainte. La résistance à la compression de la glace atmosphérique augmente également avec la décroissance de la température d'accumulation. À des taux plus élevés de contrainte, cependant, dû à l'activation des fissures, la résistance à la compression de la glace accumulée à  $-20 \text{ }^\circ\text{C}$  est moindre que celle accumulée à  $-10 \text{ }^\circ\text{C}$ . Les résultats de la résistance à la flexion de la glace atmosphérique indiquent qu'aux taux inférieurs de contrainte, la résistance à la flexion de la glace augmente avec le décroissement de la température, mais qu'aucun effet de la température n'est observé aux taux plus élevés de contrainte. Dépendamment de la température, augmenter le taux de contrainte peut augmenter ou diminuer la résistance à la flexion de la glace atmosphérique. La résistance à la flexion de la glace atmosphérique accumulée à  $-10 \text{ }^\circ\text{C}$  s'est avérée plus élevée que celle des deux autres types de glace atmosphérique à cause de sa structure plus forte, de la plus petite taille de ses grains et de son manque relatif de cavités. Le module effectif de la glace atmosphérique s'est avéré augmenter avec l'augmentation des taux de déformation. Les résultats des essais de résistance à la rupture de la glace atmosphérique prouvent qu'elle diminue au fur et à mesure que la température de l'accumulation de glace décroît.

Pour l'étude du comportement de rupture fragile de la glace atmosphérique, un modèle ABAQUS a été développé pour analyser la progression d'une fissure quasi statique d'une poutre bidimensionnelle à trois-points. Des surfaces potentielles de fissuration ont été modélées en tant que surfaces de contact maîtresses et assujetties. On a assumé que les surfaces prédéterminées de fissuration sont partiellement collées au départ de sorte que les extrémités des cassures puissent être identifiées explicitement par ABAQUS/Standard.

Pour la modélisation du comportement de fissuration de la glace atmosphérique, le taux de contrainte a été décomposé en deux parties : taux de contrainte élastique et de fissuration. La contrainte élastique récupérable est associée à la déformation de treillis et liée à l'effort appliqué correspondant selon la loi de Hooke. La relation entre les contraintes locales et les contraintes de fissuration aux interfaces de fissures a été définie par une

matrice de fissurations diagonale qui dépend de l'état des fissures existantes. Un critère de Rankine a été utilisé pour détecter le déclenchement des fissures. Les composantes de la matrice de fissurations diagonale ont été déterminées expérimentalement en tenant compte des propriétés mécaniques du matériel.

Un modèle tridimensionnel a été développé en utilisant ABAQUS pour étudier le comportement fragile et la fissuration de la glace atmosphérique. La force calculée par le modèle d'ABAQUS pour la rupture de la poutre est en écart de 2% par rapport à la valeur moyenne de la force de rupture observée en laboratoire. Toutefois, la déflexion de la poutre à la rupture montre l'erreur de 19% par rapport à la glace testée. L'erreur est attribuée à l'inexactitude de la mesure du débattement du faisceau, aux différences entre les dimensions du faisceau et le module de Young des échantillons de glace et les valeurs correspondantes dans le modèle d'ABAQUS, et au manque d'analyse de plasticité dans le modèle.

Un autre modèle basé sur ABAQUS a été développé pour simuler la fissuration fragile de la glace atmosphérique sur un câble. Les résultats montrent une erreur de 14% et de 47% dans la prévision de la force de rupture et de la déflexion à la rupture, respectivement. A part les causes des erreurs mentionnées pour le modèle de trois-points, la différence entre la rigidité flexural du câble et le cylindre, la différence entre la forme de glace dans le modèle et les essais expérimentaux, et l'inégalité de la surface de la glace sont quelques sources des erreurs.

La rupture des poutres de glace lors des essais à trois-points a été étudiée en utilisant une caméra vidéo à haute vitesse. L'initiation, la propagation des fissures et la rupture mécanique de la glace atmosphérique ont été étudiées avec trois vitesses différentes de formation d'images (20000 IPS, 75000 IPS et 150000 IPS). Les vitesses maximales pour ces essais étaient de 360, 750 et 1275 m/s et les vitesses moyennes de fissuration était de 253, 427 et 563 m/s.

## ABSTRACT

Atmospheric icing is a source of serious electrical and mechanical problems in power transmission and distribution networks. Natural ice shedding from cables and conductors, a consequence of atmospheric icing, create many problems wherefrom the necessity of studying brittle cracking of atmospheric ice arises. Major breakdowns in the power network during severe ice storms are avoidable by improving anti-icing and de-icing techniques. To do this, it is indispensable to increase our knowledge on the mechanical properties of atmospheric ice.

The objectives of this research, as a part of the general ice shedding problem, are to estimate the stresses in atmospheric ice on cables, measure the mechanical properties of atmospheric ice and develop a model for the cracking activity of atmospheric ice in the brittle region.

Wind force and ice load are the most important factors in ice shedding. Wind force creates three types of oscillation in power transmission lines: galloping (high amplitude low frequency), aeolian vibration (low amplitude high frequency), and wake induced oscillation. Altered aerodynamic characteristics of cable cause oscillation with high amplitude (galloping). In aeolian vibration, alternate shedding of wind-induced vortices from the top and bottom side of the cable causes conductor vibration. Wake induced oscillation occurs in bundled contactors and has a medium amplitude. The ice load may break the ice or accelerate its breaking by increasing the mass inertia. Some indirect factors provide suitable conditions for ice breaking by reducing the ice strength or eliminating its adhesion to the cable.

To estimate the stresses developed in the ice accreted on an overhead cable during galloping and aeolian vibration, two finite element models were developed. The galloping and aeolian vibrations of an iced cable were simulated to determine the displacement and load data, which serve as input for these models. The equations of cable motion were applied to an iced cable, and solved by a MATLAB code to obtain time histories of cable motion, aerodynamic forces, additional horizontal tension acting in the cable during vibration and torque due to spring back. The ABAQUS model revealed that during galloping, the highest stresses developed along the vertical diameter of the ice when the mid-point of the cable reached the highest and lowest positions in its trajectory.

To study the grain structure and air bubbles of atmospheric ice, the atmospheric ice was accumulated on a rotating cylinder in the wind tunnel of CIGELE. For the accumulation of atmospheric ice, the liquid water content of  $2.5 \text{ g/m}^3$ , wind speed of  $10 \text{ m/s}$  and three accumulation temperatures  $-6^\circ\text{C}$ ,  $-10^\circ\text{C}$  and  $-20^\circ\text{C}$  were set. Thin section studies revealed that the grain size of atmospheric ice decreases with decreasing accumulation temperature. The average grain size of atmospheric ice is approximately  $1.5 \text{ mm}$ ,  $0.5 \text{ mm}$  and  $0.4 \text{ mm}$  for the ice accumulated at  $-6^\circ\text{C}$ ,  $-10^\circ\text{C}$  and  $-20^\circ\text{C}$ , respectively. At thicknesses greater than

about 2 mm in the ice accumulated at  $-10^{\circ}\text{C}$  and  $-6^{\circ}\text{C}$ , the grains are elongated perpendicular to the cylinder axis. Investigations on the effects of a high-voltage electric field on the atmospheric ice confirm that the presence of an electric field affects the structure, density and amount of ice accreted on conductors.

The compressive strength of atmospheric ice increases with a decreasing test temperature. It was also found that ice strength increases with increasing strain rate up to  $10^{-3}\text{s}^{-1}$ , and then decreases at higher strain rates. The compressive strength of atmospheric ice also increases with decreasing accumulation temperatures. At higher strain rates, however, owing to activation of cracks, the compressive strength of ice accumulated at  $-2^{\circ}\text{C}$  is less than the one accumulated at  $-10^{\circ}\text{C}$ . The results of experiments on the bending strength of atmospheric ice show that at lower strain rates the bending strength of the ice increases with decreasing temperature, but no temperature effect is seen at higher strain rates. Depending on the temperature, increasing the strain rate can increase or decrease the bending strength of atmospheric ice. The bending strength of atmospheric ice accumulated at  $-10^{\circ}\text{C}$  has been found to be higher than that of the two other types of atmospheric ice due to its stronger structure owing to its smaller grain size and its relative lack of cavities. The effective modulus of atmospheric ice has been found to increase with increasing strain rates. The results of fracture toughness tests on the atmospheric ice show that fracture toughness decreases with decreasing accumulation temperature.

To study the cracking behaviour of atmospheric ice, an ABAQUS model was developed that analyzes the quasi-static crack growth in a two dimensional three-point beam. Potential crack surfaces were modeled as slave and master contact surfaces. The predetermined crack surfaces were assumed to be initially partially bonded, so that the crack tips can be identified explicitly by ABAQUS/Standard.

To model the cracking activity of atmospheric ice, the strain rate was decomposed into two parts: elastic and cracking strain rate. The recoverable elastic strain is associated with the lattice deformation and related to the corresponding applied stress by Hooke's law. The relation between local stresses and cracking strains at the crack interfaces was defined by a diagonal cracking matrix that depends on the state of the existing cracks. A Rankine criterion was used to detect crack initiation. The components of the diagonal cracking matrix were obtained by experimental work and by the mechanical properties of the material.

A three dimensional model was developed using ABAQUS to study the brittle cracking of atmospheric ice. The calculated force for beam fracture by the ABAQUS model showed 2% error with respect to the average value of failure force in experimental work. However, the calculated beam deflection at failure showed 19% error in comparison with the ice tests. The error is attributed to the inaccuracy of the measurement of the beam deflection, to differences between the beam dimensions and the Young's modulus of the ice samples and the corresponding values in the ABAQUS model, and to the lack of a plasticity analysis in the model.

Another ABAQUS model that simulates the brittle cracking of atmospheric ice on the cable was developed and its results showed 14% and 47% error in the prediction of failure force and deflection at failure, respectively. Besides the causes of error mentioned for the three points beam model, the difference between the flexural rigidity of the cable and the cylinder, the difference between the ice shape in the model and the experimental tests, and the unevenness of the surface of the ice are some sources of the errors.

The fracture of ice beams in three-point bending tests was studied using high-speed video cameras. The initiation, propagation and fracture of atmospheric ice beams were investigated with three different imaging speeds (20000 FPS, 75000 FPS and 150000 FPS). The peak crack speeds in these tests were 360, 750 and 1275 m/s and the average crack speeds were 253.3, 427 and 562.6 m/s.

## ACKNOWLEDGEMENTS

I would like to express my deepest gratitude to my supervisor Prof. Masoud Farzaneh, who is the Chairholder of the NSERC/Hydro-Quebec Industrial Chair on Atmospheric Icing of Power Network Equipment (CIGELE) and the Canada Research Chair on Atmospheric Icing Engineering of Power Network (INGIVRE) at the Université du Québec à Chicoutimi. It was a terrific honour for me to work with him and profit from his knowledge, support, and encouragement during my Ph.D. study.

I would like to express my particular appreciation to Dr. Robert Gagnon, the co-director of this research work for his valuable guidance that helped me immensely. It was a great pleasure and honour to work with him over several years.

I want also to convey my great appreciation to Dr. László E. Kollár for his very useful guidance and suggestions in this study.

I am grateful to the reviewers of my thesis, Prof. Anand Goel and Prof. Augustin Gakwaya for their comments and for accepting to be members of my thesis committee.

I am also grateful to the researchers, professionals and technicians at CIGELE, Pierre Camirand, Marc André Perron, Xavier Bouchard and Denis Masson. Thanks also to Yvette Boulay for her work in editing this thesis.

Last, but not least, I would like especially to thank my wife Rozita and my little son Siavash for the patience they have shown during my absence due to my work and for their unconditional support and encouragement. I will never forget the moments that my son asked me to stay at home on holidays and my wife explained to him the necessity of my overtime work.

## TABLE OF CONTENTS

RÉSUMÉ.....	iii
ABSTRACT.....	vi
ACKNOWLEDGMENTS.....	ix
TABLE OF CONTENTS.....	x
LIST OF FIGURES.....	xv
LIST OF TABLES.....	xxiii
GLOSSARY OF NOTATIONS.....	xxiv
CHAPTER 1            INTRODUCTION .....	1
1.1 General.....	1
1.2 The ice shedding problem.....	2
1.3 General objectives.....	6
1.4 General Methodology.....	9
1.5 Statement of original contribution.....	11
1.6 Structure of the thesis.....	12
1.7 Conclusion.....	14
CHAPTER 2            INFLUENCING FACTORS ON ICE SHEDDING .....	16
2.1 Introduction.....	16
2.2 Natural loads.....	16
2.1.1 Wind effects.....	16
Conductors Galloping.....	18
Aeolian vibration.....	20
Wake- induced oscillation.....	23
2.1.2 Ice load.....	28
2.1.3 Other loads .....	29
2.2 Ice constitutive behavior.....	29
2.2.1 Ice structure.....	29

2.3 Other influencing factors.....	34
2.3.1 Torsional stiffness and tension of cable.....	34
2.3.2 Ice shape.....	35
2.4 Study of ice shedding due to thermal shock.....	36
2.4.1 Test procedure and results.....	38
2.5 Conclusion.....	39
CHAPTER 3 ESTIMATION OF STRESSES IN ATMOSPHERIC ICE.....	40
3.1 Introduction.....	40
3.2 Estimation of loads in Galloping. ....	41
3.2.1 Equation of cable motion.....	42
3.2.2 Loads and stresses in atmospheric ice.....	47
• Stresses due to cable bending.....	47
• Aerodynamic forces.....	48
• Torsional loads .....	48
• Additional tension in the cable and the ice.....	49
• Load due to ice mass inertia.....	50
3.2.3 Calculation of forces and displacements .....	50
3.2.4 Modeling stress variation during galloping with ABAQUS .....	51
3.2.5 Results and discussion.....	52
• Galloping simulation.....	54
• Stress analysis.....	55
3.3 Estimation of loads in Aeolian vibration .....	60
3.3.1 Equation of motion in Aeolian vibration.....	61
3.3.2 Other forces in Aeolian Vibration.....	65
3.3.3 Calculation of forces and displacements in Aeolian Vibration.....	65
3.3.4 Modeling of stress variation during Aeolian vibration with ABAQUS .....	66
3.3.5 Results and discussion.....	67

3.4 Conclusion .....	71
<b>CHAPTER 4 ICE ACCUMULATION CONDITIONS AND GRAIN SIZE</b>	
<b>OBSERVATION.....</b>	<b>74</b>
4.1 Introduction.....	74
4.2 Ice accumulation conditions.....	74
4.2.1 Ice accumulation equipment.....	74
4.2.2 Air speed.....	77
4.2.3 Air temperature.....	77
4.2.4 Air pressure and air humidity.....	77
4.2.5 Liquid Water Content (LWC) .....	78
4.3 Grain structure and air bubble inclusions.....	79
4.4 Effect of electric field on atmospheric ice.....	87
4.5 Conclusion.....	90
<b>CHAPTER 5 MECHANICAL PROPERTIES OF ATMOSPHERIC ICE.....</b>	<b>92</b>
5.1 Introduction.....	92
5.2 Compressive strength of atmospheric ice.....	93
5.2.1 Test results and discussion.....	94
5.3 Bending strength and effective modulus of atmospheric ice.....	101
5.3.1 Test conditions.....	103
5.3.2 Results of bending tests.....	106
5.3.3 Discussion.....	117
5.4 Fracture toughness of atmospheric ice.....	121
5.4.1 Experimental techniques for Fracture toughness tests.....	122
5.4.2 Test results and discussion.....	123
5.5 Young's Modulus.....	128
5.5.1 Measurement of Young's modulus of atmospheric ice.....	129
5.5 Conclusion.....	132
<b>CHAPTER 6 CRACK PROPAGATION IN ICE.....</b>	<b>135</b>

6.1 Introduction.....	135
6.2 Crack nucleation in ice.....	135
6.3 Crack propagation .....	138
6.4 Prediction of the direction of crack propagation.....	143
6.4.1 Maximum tangential stress criterion.....	143
6.4.2 Maximum energy release rate criterion.....	144
6.4.2 $K_{II} = 0$ criterion.....	145
6.5 Modeling the Crack propagation in Atmospheric ice.....	145
6.5.1 Model characteristics .....	146
6.5.2 Results and discussion.....	149
6.6 Conclusion.....	152
<b>CHAPTER 7 THE ELASTIC-CRACKING MODEL .....</b>	<b>153</b>
7.1 Introduction.....	153
7.2 The Elastic strain.....	158
7.3 The cracking strain.....	159
7.3.1 Crack detection and post-cracking condition .....	160
7.4 Constitutive equations.....	163
7.5 Tension softening model.....	164
7.6 Cracked shear model.....	166
7.7 Conclusion.....	169
<b>CHAPTER 8 CRACKING MODEL OF ATMOSPHERIC ICE .....</b>	<b>171</b>
8.1 Introduction.....	171
8.2 The cracking model of a three-point beam .....	171
8.2.1 General specification of the model.....	171
8.2.2 Mechanical properties of atmospheric ice .....	173
8.2.3 Results and discussion.....	175
8.3 The cracking model of atmospheric ice on the cable .....	183
8.3.1 General specification of the model.....	183

8.3.2. Mechanical properties of materials in the model .....	184
8.3.3 Results and discussion.....	192
8.4 Conclusion.....	193
CHAPTER 9 HIGH SPEED VIDEO OBSERVATION OF ICE FRACTURE.....	195
9.1 Introduction.....	195
9.2 Ice samples.....	196
9.3 Results and discussion.....	202
9.4 Conclusion.....	202
CHAPTER 10 GENERAL CONCLUSIONS AND RECOMMENDATIONS .....	204
10.1. General conclusions.....	204
10.2 Recommendations for future works.....	208
10.2.1 The scope of the ice shedding problem.....	208
10.2.2 Estimation of stresses in atmospheric ice on the cable.....	208
10.2.3 Measurements of mechanical properties of atmospheric ice.....	209
10.2.4 The brittle cracking model of atmospheric ice .....	209
REFERENCES.....	210
APPENDIX A.....	221
APPENDIX B.....	223

## LIST OF FIGURES

<b>Figure 1.1.</b> The ice mass reduction phenomenon, (a) Heat exchange between a piece of accreted ice on electrical line, the electrical conductor, and the environment, (b) Mechanical force components ( Eskandarian 2005).....	4
<b>Figure 1.2.</b> Elements of the general problem of ice shedding by mechanical breaking.....	5
<b>Figure 2.1.</b> Drag, lift and moment on cable.....	17
<b>Figure 2.2.</b> Lissajous figures for displacement at center of span (Ohkuma <i>et al.</i> ,1998).....	20
<b>Figure 2.3.</b> Regimes of fluid flow across smooth circular cylinders (Blevins, 1990).....	23
<b>Figure 2.4.</b> Wake induced oscillation in power transmission lines (Van Dyke and Havard, 2005).....	24
<b>Figure 2.5.</b> Classification of wake-induced motions (Doocy, 1979).....	25
<b>Figure 2.6.</b> Atomic arrangement in ice crystal.....	30
<b>Figure 2.7.</b> Major axes and planes of hexagonal ice $I_h$ .....	30
<b>Figure 2.8.</b> Polycrystalline ice (Eskandarian,2005).....	31
<b>Figure 2.9.</b> Effect of air temperature on strength of atmospheric ice. ( $w = 0.4 \text{ g/m}^3$ , $d = 20 \text{ } \mu\text{m}$ , $\dot{\epsilon} = 0.76 \text{ mm/min}$ ) (Druez <i>et al.</i> , 1986 ).....	32
<b>Figure 2.10.</b> Effect of wind speed on strength of atmospheric ice. ( $w = 0.8 \text{ g/m}^3$ , $d = 40 \text{ } \mu\text{m}$ , $\dot{\epsilon} = 0.76 \text{ mm/min}$ ) (Druez <i>et al.</i> , 1986 ).....	32
<b>Figure 2.11.</b> Deformation mode map for polycrystalline ice: $T = - 10^\circ\text{C}$ , $d = 5 \text{ mm}$ ( Wu and Niu, 1995).....	33
<b>Figure 2.12.</b> Ice shape for rigid and soft cable (Fu ,2005).....	35
<b>Figure 2.13.</b> The characteristic forms of the glaze ice and sleet accretion on the structure round elements (Kazakevitch and Grafsky.,1998).....	36
<b>Figure 3.1.</b> Cable displacement in horizontal, $D_x$ , vertical, $D_y$ , and transverse, $D_z$ , directions.....	43

<b>Figure 3.2.</b> Loads and movement of a piece of cable on corresponding curves.....	49
<b>Figure 3.3.</b> Steps to estimate the stresses developing in atmospheric ice during galloping.....	53
<b>Figure 3.4.</b> Cable displacement at mid-span during galloping.....	54
<b>Figure 3.5.</b> The trajectory of mid-point of cable during galloping.....	54
<b>Figure 3.6.</b> Variations of distributed wind force in transverse and vertical directions.....	55
<b>Figure 3.7.</b> Variations of stresses due to additional tension in cable.....	55
<b>Figure 3.8.</b> Stresses in 4 elements in the external layer of atmospheric ice.....	56
<b>Figure 3.9.</b> Stresses in 4 elements in the internal layer of atmospheric ice.....	56
<b>Figure 3.10.</b> Position of elements which are the objects of Figs. 8, 9, 12 and 13.....	56
<b>Figure 3.11.</b> Stress distribution in cable and atmospheric ice.....	58
<b>Figure 3.12.</b> Normal stresses in 4 elements in the external layer of atmospheric ice.....	58
<b>Figure 3.13.</b> Normal stresses in 4 elements in the internal layer of atmospheric ice.....	59
<b>Figure 3.14.</b> Stress distribution along horizontal diameter of cable-ice composition.....	59
<b>Figure 3.15.</b> Stress distribution along vertical diameter of cable-ice composition .....	60
<b>Figure 3.16.</b> Variations of distributed wind force in vertical directions.....	68
<b>Figure 3.17.</b> Variations of stresses due to additional tension in cable.....	68
<b>Figure 3.18.</b> Stresses in 4 elements in the external layer of atmospheric ice during Aeolian vibration.....	69
<b>Figure 3.19.</b> Stresses in 4 elements in the internal layer of atmospheric ice during Aeolian vibration.....	69
<b>Figure 3.20.</b> Position of elements which are the objects of Figs. 3.18, 3.19, 3.21 and 3.22.....	70
<b>Figure 3.21.</b> Normal stresses in 4 elements in the external layer of atmospheric ice.....	70
<b>Figure 3.22.</b> Normal stresses in 4 elements in the internal layer of atmospheric ice.....	71
<b>Figure 3.23.</b> Stress distribution along horizontal diameter of cable-ice composition at 0.15 s in Aeolian vibration.....	71
<b>Figure 3.24.</b> Stress distribution along vertical diameter of cable-ice composition at 0.15 s in Aeolian vibration.....	72
<b>Figure 3.25.</b> Stress distribution in cable and atmospheric ice at 0.15 s in Aeolian vibration.....	72

<b>Figure 4.1.</b> Schematic illustrating specimen position in accumulated atmospheric ice and loading direction during test.....	76
<b>Figure 4.2.</b> Ice accumulation on aluminum cylinder.....	78
<b>Figure 4.3.</b> Wind tunnel at CIGELE.....	79
<b>Figure 4.4.</b> Three types of atmospheric ice. Left to right: accumulation temperature of -3 °C, -10°C and -20°C.....	80
<b>Figure 4.5.</b> Thin section of ice accumulated at -6 °C. The section is the same orientation as the top surface of the specimen shown in Figure 4.1 where the loading direction is vertical in the image.....	81
<b>Figure 4.6.</b> Thick section showing air bubbles in ice accumulated at -6°C. The orientation is the same as in Figure 4.5.....	82
<b>Figure 4.7.</b> Thin section of atmospheric ice accumulated at -10°C. The orientation is the same as in Figure 4.5.....	82
<b>Figure 4.8.</b> Thick section showing air bubbles in ice accumulated at -10°C. The orientation is the same as in Figure 4.5.....	83
<b>Figure 4.9.</b> Thin section showing cavities and possibly small cracks in ice accumulated at -20°C. The orientation is the same as in Figure 4.5.....	83
<b>Figure 4.10.</b> Thin section showing cavities and many small bubbles in ice accumulated at -20°C. This section corresponds to ice that is closer to the aluminum cylinder than the ice in Figure 4.9. ....	84
<b>Figure 4.11.</b> Thin section showing grain structure in ice accumulated at -20°C. The orientation is the same as in Figure 4.5.....	85
<b>Figure 4.12.</b> Thin section showing grain structure in ice accumulated at -20°C closer to the aluminum cylinder than the thin section in Figure 4.11. The orientation is the same as in Figure 4.5.....	85
<b>Figure 4.13.</b> Thin section showing grains near the cylinder surface (bottom) in atmospheric ice accumulated at -10°C. The orientation of the thin section corresponds to the orientation of the end face of the specimen shown in Figure 4.1. ....	86

<b>Figure 4.14.</b> Thin section showing grains near the cylinder surface (bottom) in atmospheric ice accumulated at $-6^{\circ}\text{C}$ . The orientation of the thin section corresponds to the orientation of the end face of the specimen shown in Figure 4.1. ....	86
<b>Figure 4.15.</b> Thin section showing grains near the cylinder surface (bottom) in atmospheric ice accumulated at $-20^{\circ}\text{C}$ . The orientation of the thin section corresponds to the orientation of the end face of the specimen shown in Figure 4.1.....	87
<b>Figure 4.16 .</b> Appearance of ice accretions on an aluminum cylinder with different electric field (Farzaneh, 2000).....	88
<b>Figure 4.17.</b> Weight of ice deposited per meter of conductor under energized conditions (Farzaneh, 2000).....	89
<b>Figure 4.18.</b> Mean density of ice deposits under energized conditions (Farzaneh, 2000). 89	
<b>Figure 5.1.</b> Test configuration for measuring the compressive strength of atmospheric ice.....	94
<b>Figure 5.2.</b> Compressive strength of atmospheric ice accumulated at $-10^{\circ}\text{C}$ and tested at $-3^{\circ}\text{C}$ . The error bars in this figure, and the ones that follow, correspond to the standard error in the results for the tests conducted at each set of parameters....	96
<b>Figure 5.3.</b> Compressive strength of atmospheric ice accumulated at $-10^{\circ}\text{C}$ and tested at $-10^{\circ}\text{C}$ .....	96
<b>Figure 5.4.</b> Compressive strength of atmospheric ice accumulated at $-10^{\circ}\text{C}$ and tested at $-20^{\circ}\text{C}$ .....	97
<b>Figure 5.5.</b> Compressive strength of atmospheric ice accumulated at $-10^{\circ}\text{C}$ and tested at various temperatures.....	97
<b>Figure 5.6.</b> Compressive strength of atmospheric ice accumulated at $-6^{\circ}\text{C}$ and tested at $-6^{\circ}\text{C}$ . ....	99
<b>Figure 5.7.</b> Compressive strength of atmospheric ice accumulated at $-20^{\circ}\text{C}$ and tested at $-20^{\circ}\text{C}$ .....	99
<b>Figure 5.8.</b> Compressive strength of atmospheric ice accumulated at various temperatures and tested at their accumulation temperature.....	100

<b>Figure 5.9.</b> Comparison of strength data from the present study with results from other studies.....	101
<b>Figure 5.10.</b> Specimen Dimensions in bending tests.....	104
<b>Figure 5.11.</b> Test configuration for measuring the bending strength of atmospheric ice..	105
<b>Figure 5.12.</b> Bending strength of atmospheric ice accumulated at $-10^{\circ}\text{C}$ and tested at $-3^{\circ}\text{C}$ . The error bars in this figure, and the ones that follow, correspond to the standard error in the results for the tests conducted at each set of parameters.....	107
<b>Figure 5. 13.</b> Bending strength of atmospheric ice accumulated at $-10^{\circ}\text{C}$ and tested at $-10^{\circ}\text{C}$ .....	108
<b>Figure 5. 14.</b> Bending strength of atmospheric ice accumulated at $-10^{\circ}\text{C}$ and tested at $-20^{\circ}\text{C}$ .....	109
<b>Figure 5.15.</b> Effective modulus of atmospheric ice accumulated at $-10^{\circ}\text{C}$ and tested at $-3^{\circ}\text{C}$ .....	109
<b>Figure 5.16.</b> Effective modulus of atmospheric ice accumulated at $-10^{\circ}\text{C}$ and tested at $-10^{\circ}\text{C}$ .....	109
<b>Figure 5. 17.</b> Effective modulus of atmospheric ice accumulated at $-10^{\circ}\text{C}$ and tested at $-20^{\circ}\text{C}$ .....	110
<b>Figure 5.18.</b> Plot of flexural stress versus time for beam bending tests at $-10^{\circ}\text{C}$ and various strain rates (unit of strain rate $\text{s}^{-1}$ ).....	110
<b>Figure 5.19.</b> Bending strength of atmospheric ice accumulated at $-10^{\circ}\text{C}$ and tested at various temperatures.....	110
<b>Figure 5.20.</b> Effective modulus of atmospheric ice accumulated at $-10^{\circ}\text{C}$ and tested at various temperatures.....	111
<b>Figure 5.21.</b> Comparison of bending strength of atmospheric ice with values of other researchers for fresh water ice and glacier ice. (T.I.T= Top In Tension; B.I.T= Bottom In Tension).....	113
<b>Figure 5.22.</b> Comparison of effective modulus of atmospheric ice with values of other researchers for fresh water ice. (T.I.T= Top In Tension; B.I.T= Bottom In Tension).....	114

<b>Figure 5.23.</b> Bending strength of atmospheric ice accumulated at $-6^{\circ}\text{C}$ and tested at $-6^{\circ}\text{C}$ .....	116
<b>Figure 5.24.</b> Bending strength of atmospheric ice accumulated at $-20^{\circ}\text{C}$ and tested at $-20^{\circ}\text{C}$ .....	116
<b>Figure 5.25.</b> Effective modulus of atmospheric ice accumulated at $-6^{\circ}\text{C}$ and tested at $-6^{\circ}\text{C}$ . .....	117
<b>Figure 5.26.</b> Effective modulus of atmospheric ice accumulated at $-20^{\circ}\text{C}$ and tested at $-20^{\circ}\text{C}$ . .....	117
<b>Figure 5.27.</b> Bending strength of atmospheric ice accumulated and tested at various temperatures.....	118
<b>Figure 5.28.</b> Effective modulus of atmospheric ice accumulated and tested at various temperatures.....	118
<b>Figure 5.29.</b> Fracture toughness test of atmospheric ice.....	123
<b>Figure 5.30.</b> The specimen dimensions in the fracture toughness tests.....	124
<b>Figure 5.31.</b> Force versus notch opening displacement in the fracture toughness tests.....	124
<b>Figure 5.32.</b> Fracture toughness of various types of atmospheric ice. The error bars in this figure correspond to the standard error in the results for the tests conducted at each set of parameters.....	126
<b>Figure 5.33.</b> Comparison of fracture toughness of ice with the results of other investigators for freshwater ice.....	127
<b>Figure 5.34.</b> Young's modulus of atmospheric ice accumulated at $-10^{\circ}\text{C}$ and tested at various temperatures.....	131
<b>Figure 5.35.</b> Young's modulus of atmospheric ice accumulated and tested at various temperatures. ....	131
<b>Figure 5.36.</b> Stress-strain curve for various strain rates on atmospheric ice.....	132
<b>Figure 6.1.</b> Describing the stresses in the vicinity of crack.....	142
<b>Figure 6.2.</b> Contour for evaluation of the $J$ -integral.....	145
<b>Figure 6.3.</b> The three-point beam subjected to Mode I loading.....	147
<b>Figure 6.4.</b> Finite element mesh for the three-point bend specimen.....	147

<b>Figure 6.5.</b> Comparison between the values of force required for crack propagation in the model and five ice tests.....	150
<b>Figure 6.6.</b> The variation of normal stress in several nodes before and after crack propagation.....	151
<b>Figure 6.7.</b> Contours of normal stress during crack propagation.....	151
<b>Figure 7.1.</b> A typical strain history for ice in uniaxial loading (Eskandarian, 2005).....	154
<b>Figure 7.2.</b> The modes of cap-model: (1) Pure tension yield, (2) Tension-shear yields,(3) Pure shear yield, (4) shear –cap yield,(5) pure cap yield, and (6) Pure viscoelastic deformation.....	157
<b>Figure 7.3.</b> Rankine criterion in the deviatoric plane.....	161
<b>Figure 7.4.</b> Cracking conditions for Mode I cracking.....	162
<b>Figure 7.5.</b> Cracking conditions for Mode II cracking (crack opening dependent model).....	163
<b>Figure 7.6.</b> Post-failure stress-fracture energy curve [1].....	165
<b>Figure 7.7.</b> Shear retention factor dependence on crack opening [1].....	167
<b>Figure 7.8.</b> Piecewise linear form of the shear retention model [1].....	169
<b>Figure 8.1.</b> The three-point beam configuration in the tests and ABAQUS model.....	172
<b>Figure 8.2.</b> The finite element model geometry.....	173
<b>Figure 8.3.</b> Comparison between the graph of force versus time in the model and five ice tests.....	176
<b>Figure 8.4.</b> a) Variation of normal stress versus time for four elements in Figure 8.4-b. b) The position of four elements at the middle of the beam.....	177
<b>Figure 8.5.</b> Variation of normal stress in the element B in Figure 8.4-b.....	177
<b>Figure 8.6.</b> The contour of stress in four different steps of fracture of the three-point beam.....	178
<b>Figure 8.7.</b> Comparison between the graph of force versus displacement in the model and five ice tests.....	178
<b>Figure 8.8.</b> Comparison between the model result with different Youngs' Modulus and the average value of the ice tests.....	180

<b>Figure 8.9.</b> Comparison between the graph of force versus displacement in the model (Young's modulus of 8 GPa) and five ice tests.....	180
<b>Figure 8.10.</b> The variation of normal stress along the path A-A in Figure 8.10.....	181
<b>Figure 8.11.</b> The path of crack propagation.....	182
<b>Figure 8.12.</b> The model of cracking activity in atmospheric ice on the cable.....	184
<b>Figure 8.13.</b> The Bersimis cable with 7 steel and 45 aluminum strings.....	185
<b>Figure 8.14.</b> Schematic of the cable fixture for bending tests.....	185
<b>Figure 8.15.</b> Variation of flexural rigidity versus cable deflection.....	186
<b>Figure 8.16.</b> Variation of force versus time in the ABAQUS model and five tests with cable and accreted ice.....	188
<b>Figure 8.17.</b> An ice sample around the Bersimis cable.....	189
<b>Figure 8.18.</b> a) Variation of normal stress versus time for four elements in Figure 8.17-b b) The position of four elements at the middle of the ice-cable beam.....	190
<b>Figure 8.19.</b> Contour of normal stress at the cross-section of the ice-cable beam.....	191
<b>Figure 8.20.</b> Variation of force versus displacement in the ABAQUS model and five tests with cable and accreted ice.....	192
<b>Figure 8.21.</b> Variation of force versus beam deflection in the ABAQUS model ( E= 8 GPa) and five tests.....	192
<b>Figure 9.1.</b> a) Three-point beam without notch , b) Three-point beam with notch.....	197
<b>Figure 9.2.</b> The variation of crack propagation speed versus time.....	200
<b>Figure 9.3.</b> The crack propagation distance from the crack tip versus time.....	200
<b>Figure 9.4.</b> Thin section of a reconstituted beam.....	201
<b>Figure 9.5.</b> Thin sections showing the propagation of crack through the grains.....	202
<b>Figure 9.6.</b> The three steps of crack propagation in atmospheric ice.....	202
<b>Figure A. 1.</b> A schematic of elements used in the definition of the interaction integral. (a) Crack tip contour $\Gamma$ on the plane locally perpendicular to the crack front where $s$ represents the location of the crack tip. (b) Line-load applied in the direction of crack advance along the crack front. (c) Volume $V$ which encloses the crack front segment $s - \varepsilon \leq s \leq s + \varepsilon$ (Zhao <i>et al.</i> , 2007).....	224

## LIST OF TABLES

<b>Table 2.1.</b> Comparison of three types of conductor motion.....	28
<b>Table 2.2.</b> Characteristics of the cable and the atmospheric ice.....	37
<b>Table 3.1.</b> Characteristics of the span, cable and ice.....	53
<b>Table 5.1.</b> Results of compression tests of atmospheric ice accumulated at -10 °C and tested at various temperatures.....	95
<b>Table 5.2.</b> Results of compression tests of atmospheric ice accumulated at various temperatures and tested at the same temperature.....	98
<b>Table 5.3.</b> Results of bending tests on ice accumulated at -10°C and tested at -3°C. ....	106
<b>Table 5.4.</b> Results of bending tests on ice accumulated at -10°C and tested at -10°C.....	107
<b>Table 5.5.</b> Results of bending tests on ice accumulated at -10°C and tested at -20°C. ...	108
<b>Table 5.6.</b> Results of bending tests on ice accumulated at -6°C and tested at -6°C.....	115
<b>Table 5.7.</b> Results of bending tests on ice accumulated at -20°C and tested at -20°C.....	115
<b>Table 5.8.</b> Results of fracture toughness tests of atmospheric ice. T <sub>a</sub> = Accumulation temperature, T <sub>t</sub> = Test temperature.....	125
<b>Table 5.9.</b> Young's modulus of atmospheric ice. T <sub>a</sub> = Accumulation temperature, T <sub>t</sub> = Test temperature.....	130
<b>Table 8.1.</b> Results of the ABAQUS model for various values of Young's modulus.....	179
<b>Table 8.2.</b> The force and the beam deflection at failure.....	187
<b>Table 9.1.</b> Data of 7 ice fracture tests with ice beams without notch.....	198
<b>Table 9.2.</b> Results of high speed video observations in three tests.....	199

## GLOSSARY OF NOTATIONS

$\theta$	Temperature in °C
$\theta_m$	Cable rotation at mid-span around its centerline
$\delta_{ij}$	The Kronecker delta
$\delta$	Cross head speed
$\varepsilon^c$	The crack strain
$\varepsilon^e$	The elastic strain
$\varepsilon^{ie}$	The inelastic strain
$\varepsilon^p$	The plastic strain
$\hat{\varepsilon}_{ij}$	Tensorial components of strain tensor in monocystal principal coordinate
$\varepsilon_{ij}^{ck}$	Total crack strain in the global Cartesian coordinate system
$\varepsilon^{ve}$	The viscoelastic strain
$\omega_1$	Natural frequency in the transverse direction
$\omega_2$	Natural frequency in the vertical direction
$\omega_s$	Frequency of Aeolian vibration
$\xi_1$	Damping ratio in transverse direction
$\xi_2$	Damping ratio in vertical direction
$\Phi$	Porosity
$\varphi_1(s)$	Mode shape in the transverse direction
$\varphi_2(s)$	Mode shape in the vertical direction
$\sigma_f$	Flexural strength
$\sigma_{ij}$	Stress tensor
$\rho$	Shear retention factor,
$\rho_a$	Air density
$\kappa_\alpha^x$	Internal-state variables for each yield system.

$\gamma$	Grain boundary surface energy
$\hat{\gamma}_{ij}$	Engineering component of shear strain in monocystal coordinate system.
$\lambda_x^p$	Plastic consistency parameter of the yield surface
$A_c$	Cross-section area of the cable
$A_i$	Cross-section area of the atmospheric ice
$a$	Notch length
$a_T$	Temperature dependent parameter
$b$	Material constant
$c$	Damping coefficient per unit length
$C_1$	Material constant
$C_{ijkl}$	The components of elastic stiffness tensor
$C_{ijkl}^{ve}$	The viscoelastic tangent material stiffness tensor
$C_L$	Lift coefficient
$d$	Sag of the cable
$d_c$	Cylinder diameter
$d_g$	Grain size
$ds'$	Deformed cable segment
$D_i$	Diameter of atmospheric ice
$D_x(s, t)$	Cable displacement in the horizontal direction
$D_y(s, t)$	Cable displacement in the vertical direction
$D_z(s, t)$	Cable displacement in the transverse direction
$D^{ck}$	Diagonal cracking matrix
$E_c$	Young's modulus of the cable
$E_f$	Effective modulus
$E_i$	Young's modulus of the atmospheric ice
$F$	Failure load
$f$	Fracture criterion
$F_1(s, t)$	External loading per unit length in the vertical direction

$F_2(s, t)$	External loading per unit length in the transverse direction
$f_v$	Vortex shedding frequency
$f_{ij}(\theta)$	Angular functions
$G$	Shear modulus of the uncracked material
$G_f$	Fracture energy $G$
$GJ$	Torsional rigidity of the cable
$g_x$	Potential function
$H$	Horizontal component of the cable tension
$h$	Beam height
$h_t$	Heat transfer
$h_\alpha^x$	Hardening functions for $x^{\text{th}}$ plastic system
$H_\alpha^x$	Hardening parameters for $x^{\text{th}}$ plastic system
$\nu_{air}$	Kinematics viscosity of air.
$I$	Moment of inertia with respect to horizontal axis of the beam cross-section.
$K$	Stress intensity factor
$k_0$	Constant in equation (9)
$k_0$	Constant
$K_I$	Stress intensity factor (mode I)
$K_{II}$	Stress intensity factors (modes II)
$K_{III}$	Stress intensity factors (modes III)
$K_I^k$	Stress intensity factors at the tip of the putative crack (mode I)
$K_{II}^k$	Stress intensity factors at the tip of the putative crack (mode II)
$K_a$	Thermal conductivity of air
$K_i$	Thermal conductivity of ice
$K_s$	Skin effect factor
$L$	Cable length
$L$	Beam length
$L_1$	Length of a piece of cable in the middle of the span

$L_b$	Beam length
$m$	Mass per unit length of the cable including the ice mass
$O(r^{1/2})$	Auxiliary displacement field
$R$	Electrical resistance of cable
$r_c$	Radius of cable
$r_i$	Radius of ice around the cable
$s$	Spatial coordinate along the curved length of the cable
$S_{ijkl}^m$	Elastic compliance tensor
$\hat{S}_{ij}$	Principal elastic compliance components of material
$t$	Time
$T$	Nonsingular elastic T-stress
$T$	Transformation matrix
$T_0$	Static tension of the cable
$T_a$	Additional dynamic tension in the cable
$T_A$	Torque at the suspension points of the cable
$T_{am}$	Ambient temperature
$T_c$	Torque due to spring back of the cable
$T_{ca}$	Cable temperature
$U$	Velocity of wind or flow
$w$	Beam width
$x$	Coordinate along the cable span
$y$	Amplitude of the vibration
$y(s)$	Static profile of the cable

# CHAPTER 1

## INTRODUCTION

### 1.1 General

The accumulation of atmospheric ice on power transmission lines is a source of tremendous damage to power networks. It is common knowledge that in cold regions significant ice layers may accumulate on cables and conductors. This accumulation can produce major problems such as overloading the conductors and towers, galloping of cables in high wind conditions, ice shedding, short-circuits due to wire sag, etc. The ice storm on January 1998 that hit Québec, the Eastern part of Ontario and neighbouring US states was one of the most terrible catastrophic ice storms in the world. The structural damage to Hydro-Québec's grid alone was more than 600 collapsed steel towers and another 100 damaged. In total, more than 1,300 km of power lines were affected because of the failure of more than 16000 line components. Damage to the power distribution system alone cost several hundreds of millions of dollars after this ice storm, [Ref. 97]. Such ice storms also hit Asian and European countries and even some southern US states such as Arkansas and Texas (December 2000). In these ice storms many transmission lines collapsed under vertical loads that were near the theoretical design loads. Some towers collapsed due to premature failure and cascade collapse, while the wind at that time was classified as moderate at most.

Impulse loads due to sudden ice shedding are another source of trouble in power networks. Ice shedding is the name given to the physical phenomenon that occurs when the accreted ice suddenly drops off of the cables, either naturally or as a result of some form of intervention. The dynamic effect of ice shedding on transmission lines creates two major categories of concern: electrical and mechanical. A lack of clearance between adjacent cables, cables and towers, and cables and the ground are the main electrical concerns. Mechanical concerns include the impact of suspension strings on towers, which may result in broken insulators. Ice shedding may also cause mechanical problems with excessive tensions generated in the cables and, eventually, large unbalanced loads on towers.

Anti-icing and de-icing methods should be investigated to reduce these damages and to improve the mechanical characteristics of line components. Obviously, studying ice shedding as one of the most important problems in power transmission lines can shed light on the ambiguous angles of this path.

## **1.2 The ice shedding problem**

The ice-shedding phenomenon can be classified as a type of ice mass reduction. Ice mass reduction can be caused by three physical mechanisms: ice melting, ice sublimation and mechanical ice breaking.

In ice mass reduction by melting, the principal characteristic is the air temperature, which obviously has to be equal to or above  $0^{\circ}\text{C}$ . Other parameters such as current intensity and conductor electrical resistance (that influences the Joule effect), as well as convective heat transfer (wind speed), solar radiation, ice thickness, shape and surface roughness of ice

are influencing factors on ice melting. This process has two phases. The first phase corresponds to ice melting characterized by a relative low mass reduction rate. The second phase corresponds to the falling of ice chunks, under the effect of wind and gravity forces, when melting occurs at the cable ice interface. The first phase does not normally last for a long time if the temperature remains above 0°C because it is replaced by the second phase. The ice mass reduction rate by melting has been reported about 0.3 kg/m.h for periods of a few hours in the case of falling ice chunks (phase II) and much lower in the case of water running off (phase I) (Bernardein, 1989).

In ice mass reduction by sublimation, the most important affecting atmospheric factors are relative humidity, temperature and wind velocity. The sublimation rate increases as temperature and wind velocity increase, and when relative humidity decreases. According to measurements conducted by Bernardein (1989), the ice mass reduction rate by sublimation is low, ranging between 3 to 20 g/m.h. This phenomenon occurs at the ice-air interface and consequently the sublimation rate should increase with the ice accretion external surface and therefore with the ice load and the ice porosity.

Ice mass reduction by mechanical breaking is produced by adhesive or cohesive failure of the ice due to stress/strain conditions beyond ice rheological limits. Initiation and propagation of such failures are complex and can be induced by static loads (torsion, bending, tension) or dynamic loads related to wind effects (vibration, galloping, impulse load, etc.). Bernardein (1989) reported a value of 0.658 Kg/m.h for the rate of ice shedding by mechanical ice breaking. It is the highest rate in that study.

The ice-shedding phenomenon (sudden drop off of atmospheric ice from the cables) normally occurs by mechanical breaking of ice or by a combined mechanism created by the interaction of two or three of the above-mentioned processes. Obviously, the combination of melting and mechanical ice breaking is more frequent than other mechanisms and it can occur when adhesion between ice and cable is eliminated by the Joule effect and other factors ( e.g. wind force) causing ice shedding.

Each ice-shedding mechanism (melting, sublimation and mechanical breaking) can be characterized separately by environmental parameters, mechanical and electrical characteristics of the line, accretion regime, ice load variations, etc. A schematic of the ice mass reduction phenomenon and the mechanical forces applied to the system of power lines and towers is shown in Figure 1.1.

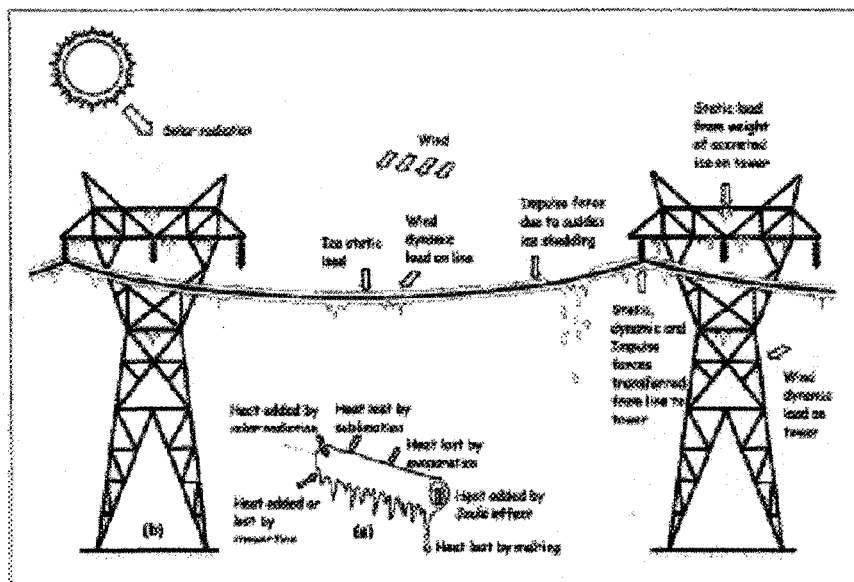


**Figure 1.1:** The ice mass reduction phenomenon, (a) Heat exchange between a piece of accreted ice on the electrical line, the electrical conductor, and the environment, (b) Mechanical force components (Eskandarian 2005).

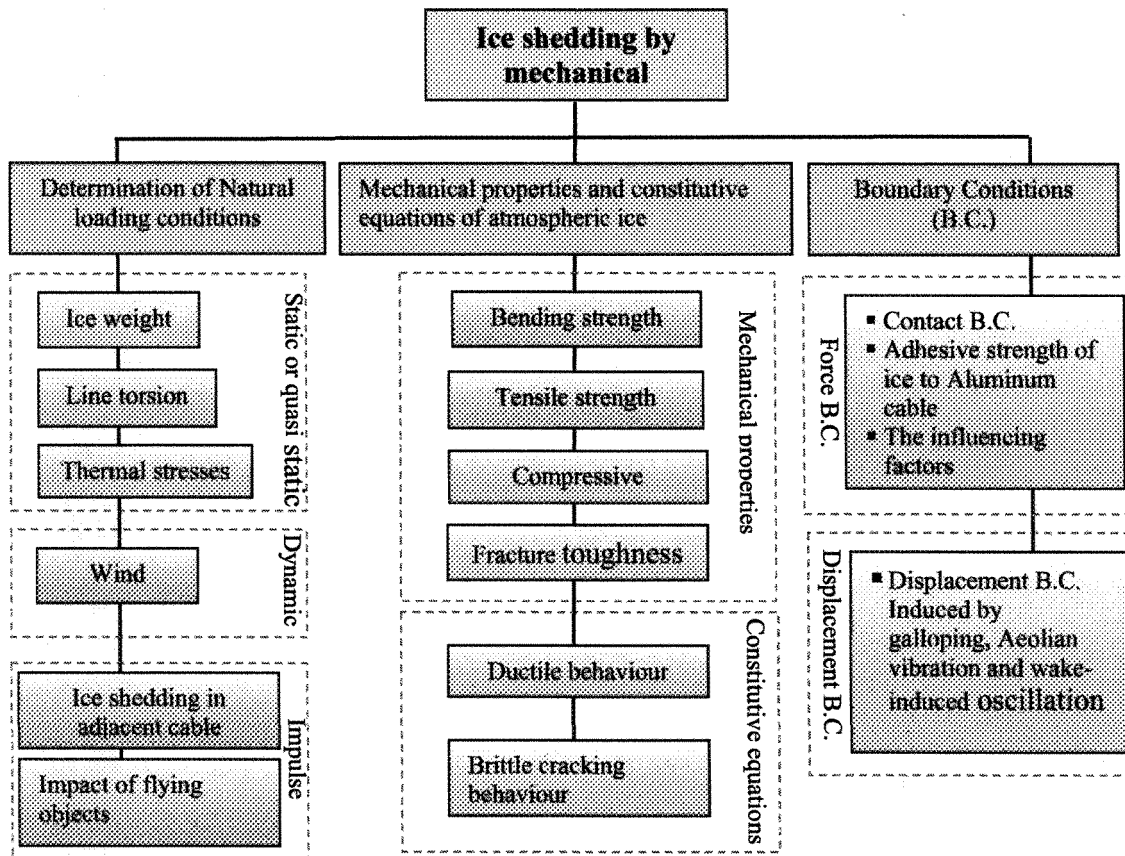


**Figure 1.2:** Elements of the general problem of ice shedding by mechanical breaking.

The four elements that should be precisely described in the general problem of ice shedding by mechanical breaking are loading scenarios, mechanical properties, constitutive equations and boundary conditions (Figure 1.2). The natural forces exerted on a piece of ice deposit can be divided into: (a) static loads (ice weight, torsional loads from cable twist, thermal stresses resulting from temperature gradients in ice deposit resulting from the Joule effect and temperature changes); (b) dynamic wind loads causing galloping, aeolian vibration and wake-induced oscillation, and (c) impulse loads created by ice shedding in adjacent cable and impact of flying objects. The mechanical properties of material,

bending, compressive and tensile strengths of atmospheric ice are important in this problem. On the other hand, the fracture toughness of atmospheric ice is a determining factor in studying its brittle behaviour. As governing equation, here, the balance equation, is enough for the isothermal process of this study.

As a contact boundary condition, the adhesive strength at the ice-aluminium interface is to be studied, where the influencing factors should also be determined. Conductor displacements originate from the wind forces in an ice accretion process. This can be assumed to be a displacement boundary condition after taking out the rigid body motion from the conductor displacements. Finally, the ice constitutive equations should be described to relate the stress field within the material to the induced strain field.

### **1.3 General objectives**

The main objective of this research, as a part of the general ice shedding problem, is to present a model for cracking activity of atmospheric ice in the brittle region. The term "brittle" refers to the capability of the model to predict the mechanical behaviour of atmospheric ice at higher strain rates. Another objective of this research work is the estimation of stresses in the atmospheric ice on the cable. The results of this part of the study shed light on the level of stress and its variation during ice shedding and can be useful for a better understanding of the ice shedding phenomenon and its prediction. To achieve the above-mentioned objectives, a good knowledge in mechanical properties of atmospheric ice is indispensable and a lack of information and data in this field leads us to do some experimental work to obtain the mechanical characteristics of atmospheric ice.

Within the general framework of the present research, the following steps were taken in order to achieve the predefined objectives:

- 1) Study the ice shedding phenomenon and its influencing factors: This part of the study was important for a better recognition of load balance. Based on the results, realistic material modeling can be formulated for ice.
- 2) Study galloping, aeolian vibration and wake-induced oscillation to find the cable displacements during these vibrations: The results of this part of the study were input data for a finite element model. Having a solid background in cable dynamics was essential for developing a model for the estimation of stresses induced in atmospheric ice.
- 3) Modeling atmospheric ice on the cable to estimate the stresses induced by galloping, aeolian vibration: These are two models developed by using the commercial finite element software ABAQUS. The input data in these models are wind force, cable displacement, spring back torque of the cable, , the ice density, Young's modulus of the ice, additional tension in the cable and atmospheric ice. The results or output of these models are the variation of stresses at various points in the atmospheric ice with time. The physical properties of ice were obtained from other studies.
- 4) Review of previous research work on the mechanical properties of atmospheric ice and other types of polycrystalline ice: Although the nature of atmospheric ice is different from other types of ice, the reported results of other investigations were useful for comparing with the results of atmospheric ice. Furthermore, the review of

previous works helps us to know the standards and common methods (or at least comments and recommendations) for ice accumulation, sample preparation, cold room conditions, test conditions, etc.

- 5) Experimental test to obtain mechanical properties of atmospheric ice: All models need some material parameters for constitutive equations. For atmospheric ice we had to obtain these parameters by experimental tests in the laboratory. These parameters are compressive strength, bending strength, fracture toughness and Young's modulus of atmospheric ice. To determine these properties, many tests need to be conducted to study the effects of temperature, load rate and ice accumulation conditions on each mechanical property.
- 6) Observation of texture and grain size (morphology) in laboratory: The texture and crystallographic orientation strongly influence the mechanical behaviour of atmospheric ice. The grain structure, air bubble content and ice structure of various types of atmospheric ice were studied in thin section. The study of atmospheric ice grain observations from previous research was very useful for comparing with our results and for helping us study the effects of ice accumulation condition on grain size, grain structure and air bubbles in atmospheric ice.
- 7) Study brittle cracking theories and review previous research on crack nucleation and propagation in ice: Since no investigation on crack nucleation and propagation in atmospheric ice has been published yet, studies on other types of polycrystalline ice were reviewed.

- 8) Review of previous research work on the modeling of mechanical behaviour of atmospheric ice: A non-cracking model for viscoelastic behaviour of atmospheric ice has been developed by Eskandarian (2005). In his model, three macroscopic strain components, the instantaneous elastic strain ( $\varepsilon^e$ ), the delay viscoelastic deformation ( $\varepsilon^{ve}$ ), and the permanent viscoplastic flow ( $\varepsilon^p$ ), characterize the non-cracking viscoplastic behaviour of atmospheric ice in a ductile regime. A short review of this model was useful for the present research.
- 9) Develop a brittle cracking model using the commercial finite element software ABAQUS: In this model, the theories of brittle cracking govern various aspects of the problem, including the crack initiation and post-cracking behaviour of atmospheric ice. To validate the results of this model, some experimental tests were conducted in the laboratory of CIGELE.

#### **1.4 General Methodology**

To investigate ice shedding and achieve the above-mentioned objectives, the following steps ought to be taken:

##### **1-Estimation of stress on atmospheric ice on the cable:**

The applied stress and strain on atmospheric ice on a cable in various conditions must be clearly understood. The data must include the range of stresses and strains, and their variation during a galloping or aeolian vibration cycle. Obviously, some parameters such as wind velocity, angle of attack, conductor characteristics, diameter of the atmospheric ice,

span characteristics, etc. are influencing factors on the amplitude of galloping and aeolian vibration, and their displacement curve.

To estimate the stresses in atmospheric ice in galloping and aeolian vibration, the equation of motion of the cable in these phenomena was required. Substituting the intervening parameters of our problem into the equation of motion of the cable, the position of each point of the cable in a given instant was obtained. The ABAQUS software was used and the position of each point of the cable was assumed as the boundary condition whereupon the stresses in the atmospheric ice were calculated. For a more accurate estimation, the effect of other loads, such as aerodynamic forces, ice weight and torsional spring back of the cable, were taken into account in the analysis.

## 2- Model of cracking activity of atmospheric ice:

For modeling the brittle cracking of atmospheric ice, the effects of precursors and microcracks were taken into account. According to the experiments on the ice, the deformation behaviour of ice in the ductile-brittle transition and brittle region is dominated by the nucleation and propagation of microcracks. Therefore, the mechanical properties of various types of atmospheric ice and their grain structure, microcracks and bubble contents must be known. To obtain the mechanical properties, some experimental work was conducted and the most important material parameters (compressive strength, bending strength, fracture toughness, etc.) were obtained. To study the grain structure, thin sections from various parts of atmospheric ice were prepared and by using a microscope with polarized filters, the grains were photographed.

To model the cracking activity of atmospheric ice, the strain rate is decomposed into two parts: elastic and cracking strain rate. The recoverable elastic strain is associated with the lattice deformation and represents the uncracked material. Hooke's law relates the elastic strain field to the corresponding applied stress. The constitutive properties are characterized by the effective Young's and shear moduli as well as the effective Poisson ratio.

To obtain the stress-strain relation in the presence of a crack, a local Cartesian system is defined, which is aligned with the crack directions. Thus the strains in the local Cartesian system and the transformation between global and local strains are obtained; the transformation between stresses in the global and the local cracking systems can be noted. A Rankine criterion is used to detect the crack initiation. By assuming that the relationship between the local stresses and the cracking strains at the crack interfaces is defined by a diagonal cracking matrix that depends on the state of the existing cracks, the crack strain is obtained. The components of the diagonal cracking matrix can be obtained by experimental work and from the mechanical properties of the material. Finally, by using the strain rate decomposition and the elasticity, the stress-strain relationship is obtained. After describing the behaviour of atmospheric ice using the theories of fracture mechanics, the results of this model must be validated by the actual behaviour of the atmospheric ice. To do this, some bending tests are needed.

### **1.5 Statement of original contribution**

The original contributions of the present study are outlined in this section, while the explanations, the corresponding theoretical formulations, experimental results and the numerical models are detailed in Chapters 2 to 9:

- 1) Study of ice shedding and its influencing factors.
- 2) Study of cable displacements during galloping and aeolian vibration, and formulation of the cable movements during these phenomena.
- 3) Development of a MATLAB code for the calculation of the cable displacements, aerodynamic forces, additional tension in the cable, additional tension in the atmospheric ice and torque due to spring back of the cable.
- 4) Development of two ABAQUS models for simulation and estimation of stresses induced in atmospheric ice during galloping and Aeolian vibration.
- 5) Laboratory texture and grain size observation in order to relate the mechanical properties of several types of atmospheric ice to their structure.
- 6) Measurement of compressive strength, bending strength, effective modulus, fracture toughness and Young's modulus of various types of atmospheric ice and comparing the tests results with the results of other investigators with other types of ice.
- 6) Development of a two dimensional model for the purpose of simulating crack propagation in atmospheric ice and comparing its results with experimental tests.
- 7) Development of a three dimensional model for the purpose of simulating the brittle cracking of atmospheric ice and comparing its results with experimental tests.
- 8) Expansion of the brittle cracking model of atmospheric ice to the ice accreted on an aluminum cable as a Fixed-Fixed beam and comparing its results with experimental tests.
- 9) Measurement of crack propagation speed in atmospheric ice accumulated at  $-10^{\circ}\text{C}$  and comparing the test results with the results of other investigators with other types of ice.

## 1.6 Structure of the thesis

This thesis is composed of 10 chapters. In the previous sections, a short history of the typical problems created by the atmospheric icing of power lines was given and the statement of the problem, the necessity of the research, the general objectives and the methodology were outlined. In each chapter of this thesis, a literature review relevant to the subject of that chapter is given. When the results of the experiment are discussed, they are compared with the results of other investigators. A brief conclusion is given at the end of each chapter, while the general conclusions and recommendations are presented in the last chapter, followed by a reference list and a few appendices. The steps below are followed within the general framework of this research:

- 1) The ice shedding phenomenon and its influencing factors will be discussed in Chapter 2, along with the effect of each factor and the extent of the problem. Some factors such as wind load (which acts as galloping, aeolian vibration and wake-induced oscillation) and ice constitutive behaviour (effect of temperature, ice accumulation condition, etc.) are explained.
- 2) The cable displacements during galloping and aeolian vibrations and variation of other loads (cable tension, aerodynamic forces, etc.) are calculated in Chapter 3. The models of atmospheric ice on the cable during galloping and aeolian vibration are presented and their results are discussed. These models were developed using ABAQUS.
- 3) The condition and set up for ice accumulation, the sample preparation procedure, ice tests conditions, the apparatus, etc. are given in Chapter 4, along with the results

of laboratory texture and grain size observations (the grain structure, air bubble content and ice structure).

- 4) The results of experimental tests for measuring the mechanical properties of atmospheric ice, including compressive strength, bending strength, effective modulus, fracture toughness and Young's modulus will be presented in Chapter 5.
- 5) A brief explanation about crack nucleation and propagation in ice, followed by a two dimensional model for crack propagation of atmospheric ice, will be given in Chapter 6 and the model results will be compared with the values of other investigators and with experimental work from the CIGELE lab.
- 6) A short review of the sole model of ductile behaviour of atmospheric ice developed by Eskandarian (2005) and the theoretical aspects of the brittle cracking model of atmospheric ice will be presented in Chapter 7. Also, the theoretical aspects of an elastic-cracking model, which governs the analysis of brittle cracking behaviour in ABAQUS, will be explained in this chapter.
- 7) A model of brittle cracking of atmospheric ice developed using ABAQUS is explained in Chapter 8, as well as the expansion of this model to ice on cable. The results of these models are compared with the experimental work.
- 8) The results of experimental work to measure crack propagation speed and its behaviour in a three-point beam are given in Chapter 9.
- 9) General conclusion and recommendations for future studies are presented in Chapter 10.

## 1.7 Conclusion

Uncontrolled ice shedding creates many serious problems in the power transmission line industry. The general objective of this research, as a part of the general ice shedding problem, are the estimation of stresses in atmospheric ice on cables, measurement of the mechanical properties of atmospheric ice and modeling the brittle behaviour of atmospheric ice.

To achieve these objectives, the applied stress and strain on atmospheric ice on a cable in various conditions must be clearly understood. To estimate the stresses in atmospheric ice in galloping and aeolian vibration, the equation of motion of the cable in these phenomena is required. The commercial finite element software ABAQUS is used to simulate the loads and boundary conditions during galloping and aeolian vibration. The effect of other forces such as aerodynamic forces, ice weight and torsional spring back of the cable must be taken into account in stresses and strains applied to atmospheric ice.

For modeling the brittle cracking of atmospheric ice, the effects of precursors and microcracks are taken into account. To do this, the mechanical properties of various types of atmospheric ice, their grain structure and microcrack as well as air bubble content should be known. To model the cracking activity of atmospheric ice, the strain rate is decomposed into two parts: elastic and cracking strain rate. Hooke's law relates the elastic strain field to the corresponding applied stress. To obtain the stress-strain relation in the presence of a crack, the Rankine criterion is used to detect crack initiation and a diagonal cracking matrix relates the stresses to the corresponding strains. The results of this model must be validated by the actual behaviour of atmospheric ice using the results of some bending tests.



## **CHAPTER 2**

### **INFLUENCING FACTORS ON ICE SHEDDING**

#### **2.1 Introduction**

Ice shedding is classified as a type of ice mass reduction. The ice mass reduction can be caused by three physical mechanisms: ice melting, ice sublimation and mechanical ice breaking. Ice shedding, or the sudden dropping off of atmospheric ice, is created by mechanical breaking or its combination with the two other mechanisms. In this chapter, the ice shedding phenomenon and factors influencing it will be discussed in more detail.

Ice shedding is influenced by many factors. Some factors have direct influence and act as a source of energy for ice breaking, and they can be called natural loading in the ice shedding problem. On the other hand, several factors have indirect influence and provide suitable conditions for ice breaking by reducing the ice strength or eliminating its adhesion to the cable. These factors are divided into two categories: ice constitutive behaviours and miscellaneous factors. These factors will be explained in the following paragraphs.

#### **2.2 Natural loads**

##### **2.1.1 Wind effects**

The interaction of natural wind with the surface roughness of the earth produces a wind character that is gusty or turbulent as opposed to being smooth and uniform. Turbulence or gusts produce velocity fluctuations that are spatial and temporal in character. Therefore, the

wind force acting on a cable will vary in direction as well as magnitude vertically and horizontally at any point in time. Static wind loads are derived from an assumption of a steady, uniform wind and are the lift, drag and moment forces as shown in Figure 2.1. The magnitude of these forces will vary with changes in the angle of attack and with cross-sectional shape.

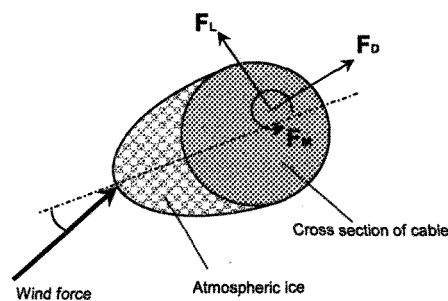


**Figure 2.1.** Drag, lift and moment on cable.

When ice or wet snow accretion builds up on conductors of overhead power lines, and a wind force acts across the result in profile, the conductors can rotate, move and vibrate in low amplitude high frequency (aeolian vibration) or in high amplitude low frequency (galloping) mode. In this study, all these wind induced motions in the cable are called cable dynamics.

Energy absorbed by a cable and its atmospheric ice, may be dissipated by internal friction at the molecular level; by inter-strand friction; by transference to clamps; dampers, spacers and suspension assemblies; by crack nucleation, crack propagation and consequently fracture of atmospheric ice; by transference to adjoining wires (in the case of bundled conductors); or by the return of the energy to the wind.

The relative magnitudes of these dissipations, and their phase positions within each motion cycle, determine whether the conductor motion will be suppressed, sustained, or accelerated. In fact, cable dynamic applies intensive stress to the atmospheric ice accreted on the cable. Impact and cyclic load due to cable dynamic can play a key role in the fracture of atmospheric ice.

The intensive wind loads have two effects on ice breaking. Firstly, they can break the ice by inducing a load beyond the ultimate strength of atmospheric ice. Secondly, they have a tremendous effect on the fatigue life of ice because of their influence on the damage created by smaller wind loads and vibration. The wind loads with small amplitudes can break the ice by favouring the propagation of the cracks initially created by loads in a higher amplitude range.

The most important types of cable dynamic that can cause the ice shedding will be discussed in the following paragraphs.

#### ➤ **Conductor Galloping**

Galloping of ice-coated conductors is a low frequency, high amplitude, wind induced vibration associated with the effect of atmospheric ice deposits on the conductors. Galloping of ice-accreted conductors is associated with their altered aerodynamic characteristics, relative to those of normally cylindrical bar conductors. This phenomenon occurs when the aerodynamic lift on the conductor can be modulated by the periodic motion of the conductor in such a way that the variations in lift act to augment or at least sustain that periodic motion. Galloping usually requires moderate to strong winds at an angle greater than about  $45^\circ$  to the line, a deposit of atmospheric ice upon the conductor

lending it suitable aerodynamic characteristics, and positioning of the ice deposit (angle of attack) so as to favour aerodynamic instability. Galloping is favoured if the ice shape is uniform and the angle of attack along the span is constant. In long single-conductor spans, the eccentric weight of the deposit may be great enough to significantly twist the conductor. Since the conductor span is fixed against rotation at the ends, this eccentric ice load will twist the conductor most at mid-span and the angle of twist will become progressively smaller going from that point toward the supports. The angle of attack will thus vary along the span.

Ice shape also varies along the span. Near the span extremities, ice deposited on the top windward surface will progressively thicken with the continued impingement of freezing droplets. Ice deposited on that quadrant remains in that quadrant. Near mid-span, however, continued deposition of ice causes a progressive rotation of the conductor, so that the ice coating is “wrapped on”. Because of this rotation, the first film of ice, which is initially in the upper windward quadrant, may ultimately face directly windward, or down, or even directly leeward, depending upon the torsional stiffness of the span and the duration of icing conditions. The shape of this “wrapped on” ice is different from the ice deposited near the span ends, where little rotation takes place.

This rotation of the conductor may have the effect of changing its ability to gallop as the ice storm progresses. The twisting may change the angle of attack remote from the towers, to values where the reverse is true.

Torsional stiffness is thought to influence the number of loops that occur in natural galloping. A span with low torsional stiffness, due to a large span length or small conductor

diameter, tends to experience large rotation at mid-span resulting in an ice shape having aerodynamic characteristics poorly suited to galloping

The curve of mid-span motion varies with the wind velocity and angle of attack. Figure 2.2 shows some different curves of motion for a triangular shape of atmospheric ice (Ohkuma *et al.*, 1998). The effect of galloping on ice shedding will be discussed in detail in the next chapters.

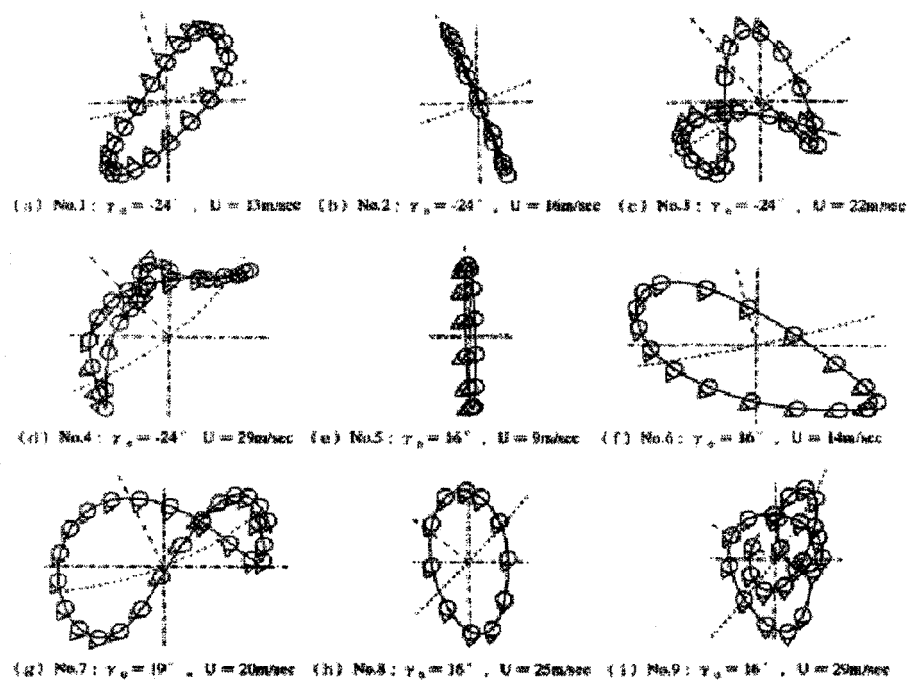


Figure 2.2. Lissajous figures for displacement at center of span (Ohkuma *et al.*, 1998).

### ➤ Aeolian Vibration

The primary cause of conductor vibration is the alternate shedding of wind-induced vortices from the top and bottom side of the conductor. The action creates an alternating

pressure unbalance, inducing the conductor to move up and down at right angles to the direction of airflow.

The three primary variables involved in vortex shedding from a circular cylinder are the cylinder diameter, the fluid velocity, and the kinematic viscosity of the particular fluid. Results obtained in various fluids and with different cylinder diameters can be correlated if velocities are expressed in terms of the Reynolds number, a dimensionless velocity term:

$$R = \frac{U d_c}{\nu_{air}} \quad (2.1)$$

where U is velocity,  $d_c$  cylinder diameter and  $\nu_{air}$  kinematic viscosity of the air.

The major Reynolds number regimes of vortex shedding from a smooth circular cylinder are given in Figure 2.3 (Blevins, 1990).

A dimensionless number that relates free stream velocity, cylinder diameter, and vortex frequency is the Strouhal number:

$$S_s = \frac{f_v d_c}{U} \quad (2.2)$$

where  $f_v$  is the vortex shedding frequency in units of Hertz (cycles per second), and  $d_c$  is the cylinder diameter and U is the free stream flow velocity approaching the cylinder. The Strouhal number shows a moderate variation for Reynolds numbers between 500 and 20,000. For a cylinder having a shape similar to the overhead transmission line conductor, the Strouhal number of 0.185 has been reported. The wind power (p) transferred from the wind to a vibrating conductor may be expressed in the following general form:

$$p = d_c^4 f_v^3 fnc \left( \frac{y}{d_c} \right) \quad (2.3)$$

where  $y$  is the vibration amplitude (Blevins, 1990).

The vibration amplitude is determined by a power balance between what is provided by the wind and what is dissipated by the cable self-damping and by any dampers. Ice and/or snow precipitations will affect aeolian vibrations through different mechanisms. A snow cover may smooth terrain obstacles that would normally contribute to wind velocity fluctuations. A more constant wind velocity and azimuth will give results that are more propitious to severe aeolian vibrations (Van Dyke and Havard, 2005).

When ice is present, other factors will also contribute to increasing the severity of aeolian vibrations. For example, an iced conductor may lock the cable strands together so that cable internal damping through strand slippage decreases. Moreover, it is well known that internal cable damping depends heavily on the cable's mechanical tension. The ice weight will increase cable tension, which will also reduce conductor self-damping.

Equ. 2.3 shows that when ice accretion increases, assuming the cable diameter and frequency remains constant, aeolian power increases to about the fourth power of the diameter (Doocy, 1979).

It is important to distinguish the conductor motion and lift variation here from those involved in galloping discussed in the previous pages. The frequencies involved in galloping are less than one tenth and usually less than one hundredth of those for aeolian vibration for the same wind velocity. Conductor amplitudes in galloping often exceed a meter, whereas they rarely exceed a few centimetres in aeolian vibration. The two phenomena are not directly related.

The effect of aeolian vibration on ice shedding will be discussed in detail in the next chapters.

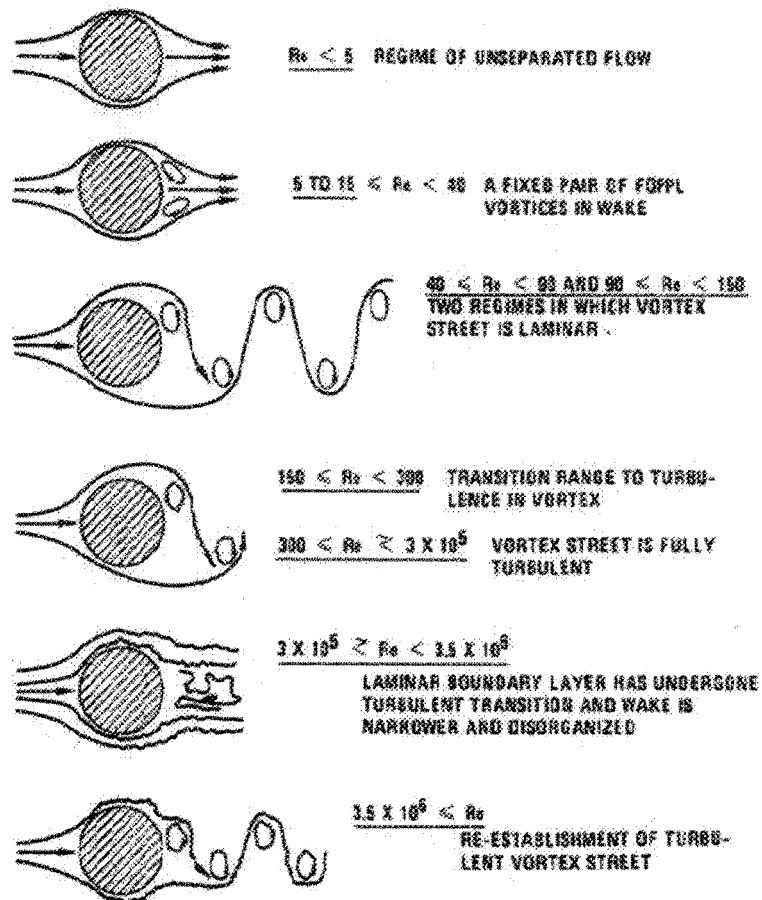


Figure 2.3. Regimes of fluid flow across smooth circular cylinders (Blevins, 1990).

### ➤ Wake-induced oscillation

Wake-induced oscillation is the third major wind induced motion recognized as a significant problem in transmission lines. It is particular to bundled conductors and encompasses several types of motion observed in conductor bundles that are caused by the aerodynamic shielding of leeward-lying conductors by windward ones. The leeward

conductors that lie in the wake of windward conductors are subjected to forces not experienced by a single conductor. These forces permit wind induced motion to occur that is particular to bundles (Figure 2.4).

The motions occur in moderate to strong winds, usually in the range of 7 to 8 m/s. Also they may occur with ice on the conductors or when there is rain. The rotations are most often observed when the conductors are bare and dry.

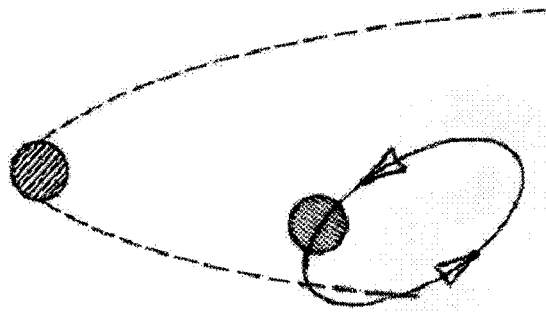


**Figure 2.4.** Wake induced oscillation in power transmission lines  
(Van Dyke and Havard, 2005).

The four principal types of wake-induced motion are illustrated in Figure 2.5.

Three of these types, those shown in B, C and D of the figure are termed “rigid-body modes”, since little distortion of the cross-section of the bundle occurs. They are similar to the fluttering motions of a ribbon.

The rigid-body modes may occur with one or several loops in the span, the two-loop forms being the most common for vertical and horizontal galloping. The rolling mode has been observed with as many as eight loops in the span. The one loop form is uncommon. When more than one loop occurs, the node points between the loops do not appear to be associated with spacer locations.

The vertical galloping mode is occasionally observed in the form of a traveling wave rather than a standing loop. The wave has a length in the order of 50 or 100 meters and travels back and forth along the span, being reflected at the towers. Peak to peak amplitudes greater than a meter have been observed. Traveling waves in the rolling and horizontal galloping modes have not been reported.

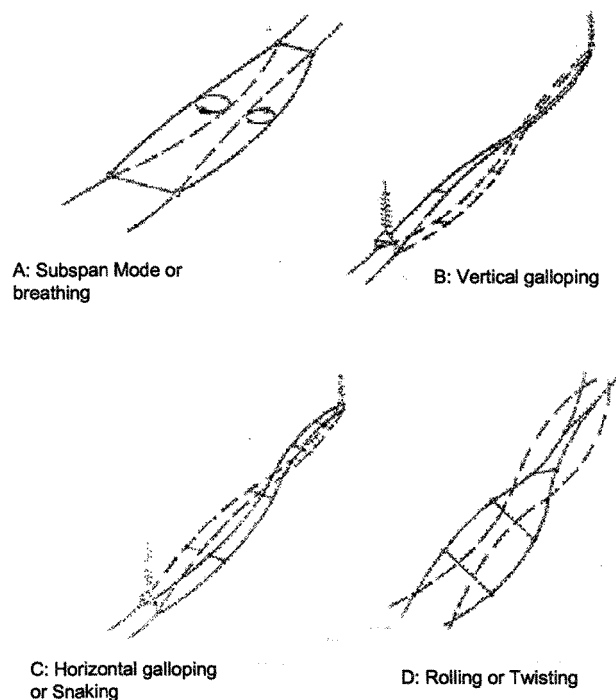


**Figure 2.5.** Classification of wake-induced motions (Doocy, 1979).

The subspan mode is the most frequently reported. Since the elliptical orbit traced by the conductors usually have their major axes horizontal, the motions are easily seen from the ground. However, large amplitudes in the rolling also give an appearance similar to the subspan mode if the observer is not directly under the bundle.

In the subspan mode, both sub-conductors in a windward-leeward pair usually participate in the motion, the leeward having the higher amplitude. Not all pairs in a bundle necessarily participate to the same degree. For example, in a four conductor square bundle, the upper or lower pair may have a considerably greater amplitude than the others.

In a bundle with a large number of sub-conductors, their association into windward – leeward pairs is apparently not meaningful, since some sub-conductors are upwind of one sub-conductor and downwind of another. In such bundles, all conductors in the top or bottom quadrant may oscillate as a group, but in a complex pattern.

When spans are susceptible to oscillation, there is a minimum, or threshold, wind velocity required to initiate motion. When the threshold is exceeded by winds of about normal direction to the line and from the proper side, oscillation starts and quickly becomes more severe as the wind increases beyond the threshold. The threshold wind velocity is a convenient parameter for classifying the susceptibility of individual spans to wake-induced oscillation.

Aside from location or terrain, several other variables influence susceptibility. The major ones are:

a) Number and arrangement of sub-conductors

The four-conductor bundle is the most susceptible and the three-bundle is the least susceptible to wake-induced oscillations.

b) Separation between windward –leeward pairs of sub-conductors

The separation between cables is commonly expressed in terms of the ratio  $a/d$ . Increasing  $a/d$  tends to make bundles less susceptible to oscillation and sufficiently large values appear to stabilize bundles for all winds.

c) Angle of attack or tilt of the bundle

The tilt range in which instability is most likely to occur is approximately  $5^\circ$  to  $15^\circ$ . However, the specific ranges for particular spans show some differences. The direction of tilt, toward or away from the wind that results in instability appears to depend upon the type of bundle. Tilt is considered positive if the leeward conductor is in the upper wake of the windward one, and negative if it is in the lower wake. The subspan mode is observed in square four-bundles only for negative tilts, while most observations of the subspan mode in two-bundles are of positive tilts. Vertical galloping is usually associated with large positive tilts and horizontal galloping and rolling with small tilts of either sign.

d) Type and positioning of spacing devices

The use of most spacers results in shorter average subspan length and increases in the threshold wind velocity.

Table 2.1 shows a comparison of the three types of conductor motions (Doocy, 1979). The numerical ranges shown for frequency, amplitude, wind velocity and time required to cause damage are intended to provide a comparison among the three types of vibration. They do not show either extreme limits or normal operating conditions for any one particular span or line. The relative importance of individual factors may vary widely from line to line.

	Aeolian Vibration	Galloping	Wake-induced oscillation
Type of overhead line affected	All	All	Bundled conductors
Approx. Frequency Range (Hz)	3 to 150	0.08 to 3	0.15 to 10
Approx. Range of vibration (expressed in conductor diameters)	0.01 to 1	5 to 300	0.5 to 80
Wind velocity	1 to 7 m/s	7 to 18 m/s	4 to 18 m/s
Damage (approx. time required for severe damage to develop)	3 months to 20 years	1 to 48 hours	1 month to 8 years
Direct cases of damage	Metal fatigue due to cyclic bending	High dynamic loads	Conductor clashing, accelerated wear in hardware

**Table 2.1.** Comparison of three types of conductor motion (Doocy, 1979).

In this work, we are going to study ice-shedding from a single conductor. Since wake-induced oscillation occurs only in bundled conductors, it is beyond the scope of this study.

### 2.1.2 Ice load

The other important influencing factor in ice shedding is the mass of ice accreted on the cable. The ice load may break ice or accelerate its breaking by several mechanisms:

- If the adhesive force between ice and cable is eliminated by the Joule effect or the ambient temperature, the ice will drop due to its weight.
- The ice load during ice accretion (especially at a higher icing rate) can prevail over the adhesive force between ice and cable and cause ice shedding.
- The ice load can propagate cracks in atmospheric ice.
- Ice mass inertia can break the ice during cable motion and vibration (which is a very important issue in this study).

- During ice accretion, the ice load can rotate and bend the cable and create tension and bending stress in already accreted ice.
- It is well known that internal cable damping depends heavily on the cable's mechanical tension. The ice load increases cable tension, which also reduces conductor self-damping. Thus, a heavier ice load causes more cable tension and ice shedding.

### **2.1.3 Other loads**

Other events can influence ice shedding when a load or impact is suddenly applied to transmission lines, such as the rupture of an adjacent cable, ice shedding in an adjacent cable, flashover and the impact of flying objects. These events are not controllable. Their prediction and investigation are beyond the scope of this study.

## **2.2 Ice constitutive behaviour**

The occurrence of atmospheric ice shedding from power transmission lines is closely related to the adhesive and cohesive strength of the atmospheric ice. Before proceeding, it is worth noting the structure and molecular lattice of ice.

### **2.2.1 Ice structure**

Ice possesses more than 12 different crystal structures. At ordinary pressures, the stable phase of ice is called ice I. This phase can be classified into two closely related variants: hexagonal ice  $I_h$ , whose crystal symmetry is reflected in the shape of snowflakes, and cubic ice  $I_c$ , with a crystal structure similar to a diamond that can be formed by depositing vapour at very low temperatures, below  $-130^\circ\text{C}$ .

On a macro-scale, ice is a polycrystalline material. Its texture depends on the growth process and its thermo-mechanical history. In an ideal lattice of ice  $I_h$ , four oxygen atoms surround each oxygen atom in a tetrahedral arrangement inside the lattice with an angle of  $109^{\circ}28'$ . A pair of hydrogen atoms surrounds one oxygen atom with an angle of  $104^{\circ}31'$ . Between each pair of oxygen atoms, there is only one hydrogen atom (Figure 2.6).

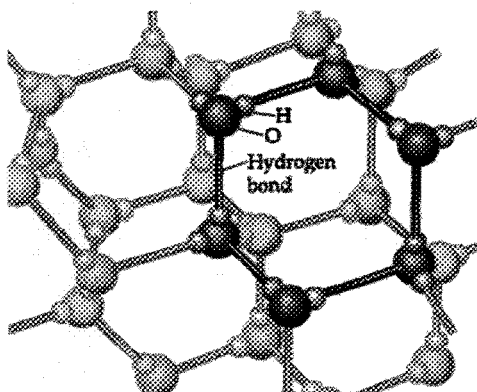


**Figure 2.6.** Arrangement of atoms in ice crystals.

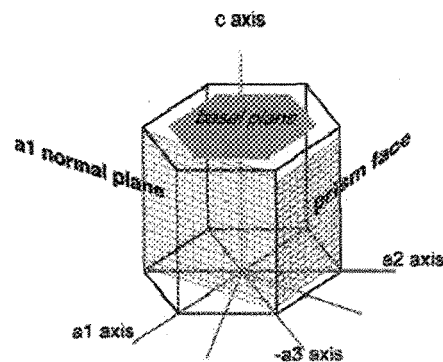


**Figure 2.7.** Major axes and planes of hexagonal ice  $I_h$ .

The hexagonal structure is the only one found in nature as sea, river or atmospheric ice. The hexagonal prism includes two hexagonal “basal” faces and six rectangular “prism” faces (Figure 2.7). Depending on the length of the c-axis compared to the a-axis, the hexagonal prism can be “plate-like” or “column-like”. External factors, such as super cooling, temperature, water flow and impurities, affect the growth of ice grains and their shape. Orientation and grain size strongly influence the elasticity of ice (Moller, 1982).

The individual grains in polycrystalline ice may be granular, columnar or a less common form (Figure 2.8). The mechanical behaviour of granular ice (for example rime) can be considered isotropic.

There are different types of columnar ice in nature. Types S1 and S2 are transversely isotropic. S3 is transversely orthotropic. In S1 ice, the crystallographic c-axis (normal to the basal planes) is parallel to the long axis of the columnar-shaped grains. In the case of S2 ice, the c-axis is random within a plane whose orientation is more or less perpendicular to the long axis of the columnar-shaped grains. In S3 ice, the c-axis is strongly aligned within that plane.

Glaze deposits on electrical cables can be considered as S1 or S2 ice (Eskandarian, 2005)

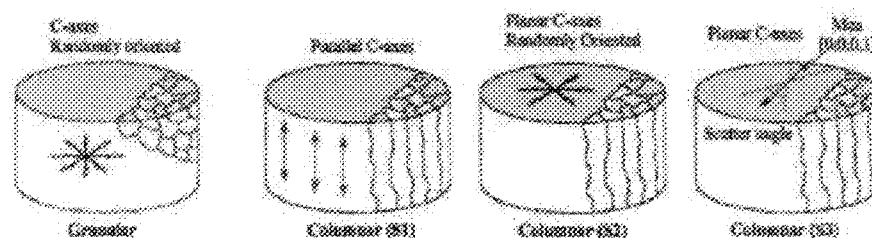
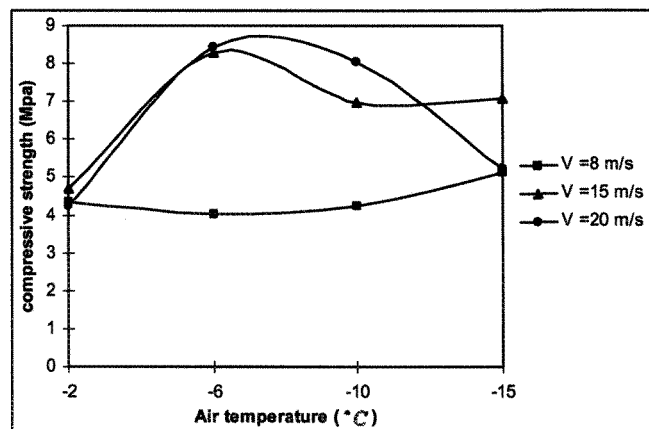


Figure 2.8. Polycrystalline ice (Eskandarian,2005).

Some studies of the mechanical properties of atmospheric ice have shown that compressive and tensile strengths are greatly dependent on temperature, wind velocity, load rate, liquid water content of air and the mass mean diameter of super-cooled droplets during accretion. The mechanical properties of atmospheric ice vary considerably according to the type of ice, which in turn depends mainly on the meteorological conditions prevailing during ice formation. For example, a decrease of a few degrees in temperature, all other conditions being the same, is sufficient to change the type of ice produced from glaze to hard rime, or from hard rime to soft rime, each having very different mechanical properties. Druetz *et al.* (1986) concluded that the compressive, tensile and adhesive strengths of atmospheric ice increase or go through a maximum as a function of decreasing air

temperature. In our compression tests on various types of atmospheric ice (Chapter 5), the same result was obtained. Figure 2.9 shows the dependence of the compressive ice strength on air temperature. In the following figures,  $w$  is the liquid water content of air,  $d$  the mean volume droplet diameter,  $\dot{\epsilon}$  strain rate and  $V$  wind speed.



**Figure 2.9.** Effect of air temperature on the strength of atmospheric ice. ( $w = 0.4 \text{ g/m}^3$ ,  $d = 20 \text{ } \mu\text{m}$ ,  $\dot{\epsilon} = 0.76 \text{ mm/min}$ ) (Druez *et al.*, 1986).

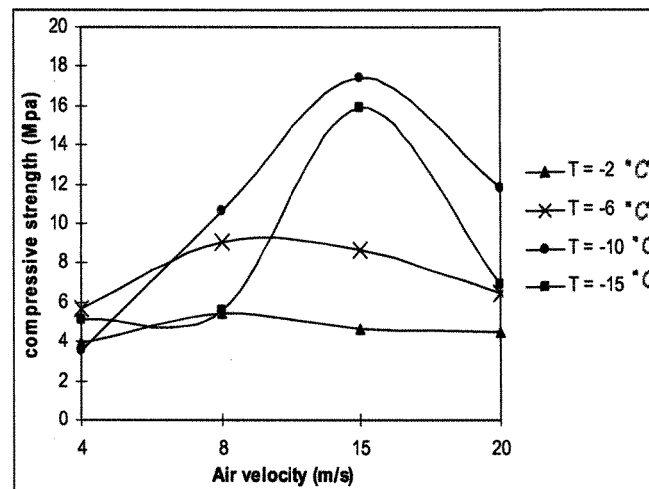


**Figure 2.10.** Effect of wind speed on the strength of atmospheric ice. ( $w = 0.8 \text{ g/m}^3$ ,  $d = 40 \text{ } \mu\text{m}$ ,  $\dot{\epsilon} = 0.76 \text{ mm/min}$ ) (Druez *et al.*, 1986).

Druez *et al* (1986) also found that the compressive and tensile strengths of atmospheric ice increase or go through a maximum as a function of increasing air velocity during ice accretion (Figure 2.10). In addition, Druez *et al.* (1986) found that the mechanical properties of atmospheric ice are affected by the liquid water content and droplet diameter. According to their tests, the compressive, tensile and adhesive strengths of atmospheric ice increase with increasing values of liquid water content of air and mean volume droplet diameter during ice accretion.

Previous investigations (Hawkes and Mellor, 1972; Schulson and Canon, 1984; Schwarz *et al.*, 1981; Wu and Niu, 1994) have shown an appreciable dependence of ice strength on the strain rate. Generally, three domains of deformation can be identified in stress-strain rate graphs. These domains for ice tested at  $-10^{\circ}\text{C}$  are distinguished as follows (Figure 2.11).

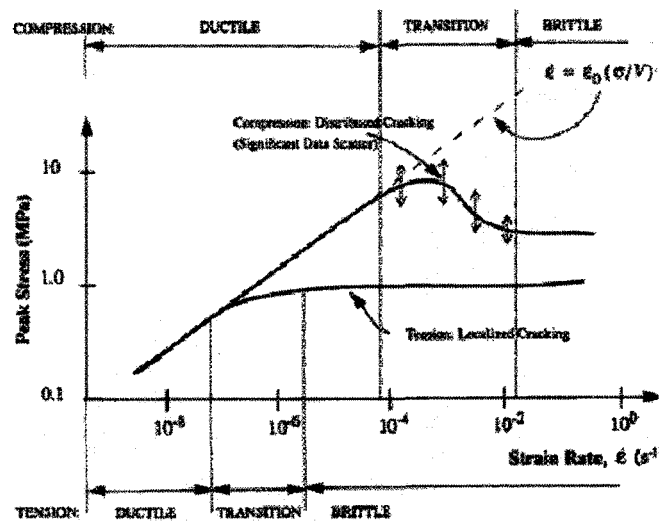


Figure 2.11. Deformation mode map for polycrystalline ice:  $T = -10^{\circ}\text{C}$ ,  $d = 5$  mm (Wu and Niu, 1995).

For compression at strain rates lower than  $10^{-4}\text{s}^{-1}$ , ice shows ductile behaviour that is non-linear and generally viscoelastic up to very large viscous strains with no sign of material damage or microcrack formation, while the ductile regime in tension is associated with strain rates less than  $10^{-7}\text{s}^{-1}$ .

The transition in compression occurs within a narrow range of strain rates (between  $10^{-4}$  and  $10^{-2}\text{s}^{-1}$ ) and the maximum stresses occur in this regime. This regime in tension occurs within a lower strain rate range (between  $10^{-7}$  and  $10^{-6}\text{s}^{-1}$ ).

Beyond the transitional domain but within the quasi-static domain of high strain rates (less than  $1\text{s}^{-1}$ ), the brittle behaviour dominates and strength is essentially independent of the strain rate. In this domain, the mechanical behaviour of ice is linear (Wu and Niu, 1994).

With these considerations in mind, one can conclude that each factor that causes a reduction in strength and adhesion of ice to the cable can pave the way for ice shedding.

Another aspect of constitutive behaviour of atmospheric ice is the dependence of its mechanical properties on the test temperature. The compressive, tensile and adhesive strengths of atmospheric ice increase with decreasing test temperatures. This behaviour was observed in fresh water ice by many researchers (e.g. Schulson, 1990).

## **2.3 Other influencing factors**

### **2.3.1 Torsional stiffness and tension of cable**

Cable torsional stiffness influences ice accretion and ice shedding. In the case of two similar cables with different torsional stiffness, the ice accretion on the soft cable exhibits a

perceivably circular shape while ice on the rigid cable is asymmetrically distributed underneath. Intuitively, ice on a rigid cable tends to shed from the cable due to aerodynamic or gravitational forces (Figure 2.12) (Fu, 2004).

The internal cable damping depends heavily on the cable's mechanical tension. Therefore, vibration and motion in a cable with more tension can shed more ice. The ice weight will increase cable tension, which will also reduce conductor self-damping. Thus more ice causes more cable tension and more ice shedding.

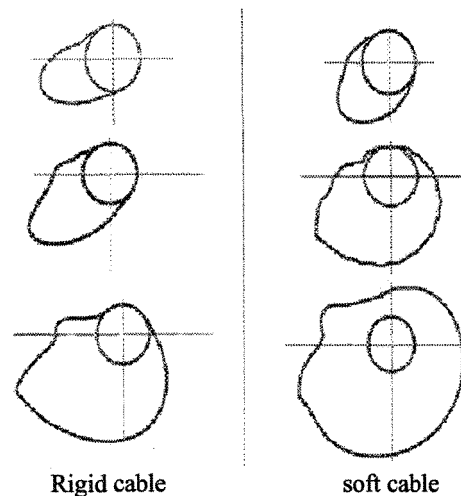
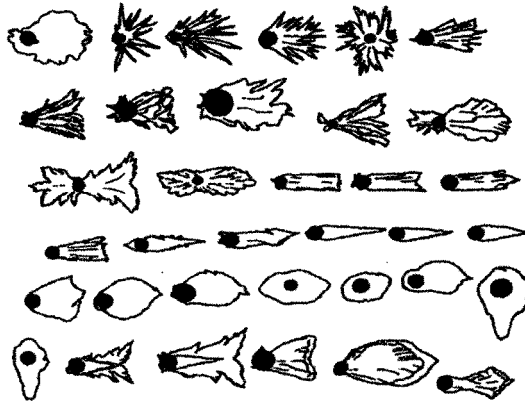


Figure 2.12. Ice shape for rigid and soft cable (Fu, 2004).

### 2.3.2 Ice shape

Another factor that influences ice shedding is ice shape. It has two different effects on ice shedding. Firstly, its form can change the aerodynamic forces on itself as well as on the cable and therefore change oscillation amplitudes. Secondly, its shape determines the resistance of ice against shedding. The shapes that surround the cable and have less air drag show more resistance to ice shedding. The most characteristic forms of the glaze ice and sleet accretion are presented in Figure 2.13 (Kazakevitch and Grafsky, 1998).



**Figure 2.13.** The characteristic forms of glaze ice and sleet accretion on round structure elements (Kazakevitch and Grafsky, 1998).

#### 2.4 Study of ice shedding due to thermal shock

One of the several factors thought to influence ice shedding is ice fracturing due to thermal shock created by variations in ambient temperature or Joule effect in the cable. To study the effect of air temperature variation and the Joule effect in ice fracture, two tests were conducted.

To investigate the Joule effect, a minimum electrical current is applied in the cable. The value of the current intensity is calculated from (Zsolts, 2006).

$$I = \sqrt{\frac{T_{ca} - T_{am}}{R \cdot K_s} \left( \frac{1}{\frac{1}{2 \cdot K_i \cdot \pi} \ln\left(\frac{r_i}{r_c}\right) + \frac{1}{2r_i \cdot \pi \cdot h_t}} \right)} \quad (2.4)$$

where  $R$  is the electrical resistance of the cable,  $K_s$  is the skin effect factor,  $K_i$  is the thermal conductivity of ice,  $r_i$  is the radius of the ice around the cable (ice thickness plus cable radius),  $r_c$  is the radius of cable,  $T_{ca}$  is cable temperature,  $T_{am}$  is ambient temperature and  $h_t$  is the heat transfer coefficient, which can be calculated as follows:

$$h = k_a \sqrt{\frac{U}{2\nu_{air} \cdot r_i}} \quad (2.5)$$

where  $U$  is air velocity,  $K_a$  is the thermal conductivity of air,  $\nu_{air}$  is the kinematic viscosity of air.

To obtain the value of  $h$  and  $I$ , the characteristics of the cable and the atmospheric ice were selected as the data presented in Table 2.2.

Parameter	Value	Unit
Skin effect factor	1.07	---
Electrical resistance of cable	$4.22 \times 10^{-5}$	$\Omega/m$
Thermal conductivity of ice	2.2	W/m.K
Radius of ice around the cable	37.55	mm
Cable radius	17.55	mm
Cable temperature	-2	$^{\circ}C$
Ambient temperature	-25	$^{\circ}C$
Kinematic viscosity of air	$1.368 \times 10^{-5}$	$m^2/s$
Thermal conductivity of air	0.025	W/m.K
Air velocity	10	m/s

**Table 2.2.** Cable and atmospheric ice characteristics.

The heat transfer coefficient  $h_t$  and the required current intensity to increase the cable temperature to  $-2^{\circ}C$  are obtained  $79.1 \text{ w/m}^2\text{C}$  and  $2165.6 \text{ A}$ , respectively.

#### 2.4.1 Test procedure and results

A one meter long BERSIMIS cable was prepared for this test. The liquid water content of atmospheric ice was set at  $2.5 \text{ g/m}^3$ ; air velocity during accumulation was  $10 \text{ m/s}$ ; and the ice accumulation temperature was  $-10^{\circ}C$ . After the ice was allowed to accumulate in a

wind tunnel, the temperature of the ice was reset to  $-25^{\circ}\text{C}$ . The ice remained at this temperature for 1 hour. Then a current intensity of 2150 A was applied to the cable. After 45 minutes the cable temperature reached  $-2^{\circ}\text{C}$  and the atmospheric ice was carefully scanned. No sign of cracking due to thermal shock was observed.

The current was then disconnected and the atmospheric ice was allowed to cool down to  $-25^{\circ}\text{C}$  where it was kept for 1 hour. Finally, it was removed from the wind tunnel and exposed to a  $20^{\circ}\text{C}$  air flow at a velocity of 5 m/s. Of course, these conditions never happen in nature, but the worst condition was chosen to investigate the effect of temperature variation on atmospheric ice. After 10 minutes, the ice was scanned and again no cracks were observed.

These tests show that in real conditions, ice shedding from power transmission lines never occurs owing to a thermal gradient between ice and cable. Neither is the thermal shock due to temperature variation created by meteorological conditions an influencing factor of ice shedding.

## **2.5 Conclusion**

Ice shedding is influenced by some direct and some indirect factors. The direct influencing factors act as a source of energy for ice breaking and ice shedding. Wind force and ice load are the most important ones. Wind force creates three types of oscillations in power transmission lines, which are galloping (high amplitude low frequency), aeolian vibration (low amplitude, high frequency) and wake-induced oscillation. In galloping vibration, altered aerodynamic characteristics of the cable cause oscillation. In aeolian

vibration, alternate shedding of wind-induced vortices from the top and bottom of the cable cause conductor vibration. The action creates an alternating pressure imbalance, inducing the conductor to move up and down at right angles in the direction of airflow. The ice load may break the ice or accelerate its fracturing by several mechanisms: the ice may be dropped by its weight, ice mass inertia can break it during cable motion and vibration, etc. The indirect factors provide suitable conditions for ice breaking by reducing the ice strength or eliminating its adhesion to the cable. These factors can be divided into two categories: ice constitutive behaviours and miscellaneous factors. The compressive, tensile and adhesive strengths of atmospheric ice are greatly dependent on temperature, wind velocity, liquid water content of air and mean diameter of supercooled droplets during ice accretion. The strength of atmospheric ice also depends on the load rate and temperature during ice shedding. The three miscellaneous influencing factors in ice shedding are cable torsional stiffness and tension of the cable and ice shape. Under certain circumstances, all of the above-mentioned factors can work together and cause ice shedding.

Two tests showed that the thermal gradient between the external surface of the ice and the surface of the cable does not cause ice shedding from power transmission lines, neither due to the Joule effect nor to thermal shock caused by temperature variation by meteorological conditions.

## **CHAPTER 3**

### **ESTIMATION OF STRESSES IN ATMOSPHERIC ICE**

#### **3.1 Introduction**

Three types of vibrations created by wind on power transmission lines were explained in the previous chapter and are classified as galloping, aeolian vibration and wake-induced oscillation. These vibrations are associated with bending and additional tension in the cable, which can lead to damage to the power network. If ice accumulates on the cable, then stresses also develop in the ice, which may lead to ice shedding. In this chapter, an attempt was made to estimate these stresses and their variations with respect to load variations during galloping and aeolian vibration.

Owing to the complexity of this problem, it is necessary to simplify some sophisticated aspects of the natural conditions, as follows:

- a) Normally, ice shapes on power transmission lines are not exactly cylindrical and uniform; it is more symmetrical in the middle of the span than in other parts. We assume cylindrical and uniform ice shape all along the cable. However, in the calculation of wind loads on the cable, the functions of wind force obtained from wind tunnel tests for asymmetrically (D shape) iced cables are used.
- b) Movements and vibrations of towers during galloping and aeolian vibration are negligible.

- c) Wind velocity does not change during galloping and aeolian vibration, and it is uniform all along the cable.
- d) The ice is fully attached to the cable and there is no slide or separation between them.

### **3.2 Estimation of loads in Galloping**

Galloping of suspended cables has been studied by many researchers (e.g Abdel-Rohman and Spencer, 2004; Yu *et al.*, 1993; Luongo and Piccardo, 1998; Ohkuma *et al.*, 1998). Irvine and Caughey (1974) developed a linear theory for free vibration of a uniform suspended cable in which both in-plane and out-of-plane motions were considered. The results of this theory have been used by many researchers to model galloping behavior. Yu *et al.* (1993) developed a three-degree-of-freedom model to describe and predict different galloping behaviors of a single iced electrical transmission line. Ohkuma *et al.* (1998) focused on the effects of wind turbulence on galloping, and tried to explore the galloping behavior of a four-bundle overhead transmission line in gusty winds. Luongo and Piccardo (1998) derived a two-degree-of-freedom model to examine the aeroelastic behavior of a flexible elastic suspended cable driven by the mean wind speed blowing perpendicularly to the plane of the cable. Abdel-Rohman and Spencer (2004) used the results of Luongo and Piccardo (1998) to study the motions called along-wind and across-wind responses of a suspended cable. They also investigated the effect of a vertical viscous damper at a certain location of the cable.

Only a few of the vast number of publications concerning galloping are mentioned in the above paragraph. To the best of this author's knowledge, however, none of them discusses in detail the stresses that develop in the ice accretion during the vibration. In this section,

we tried to estimate these stresses and their variations during galloping. We applied the calculation of cable galloping motion, which was developed by Abdel-Rohman and Spencer (2004) and Luongo and Piccardo (1998), for a cable covered with atmospheric ice. The results of this calculation are the displacements of each point along the cable in vertical and transverse directions, as well as aerodynamic forces and other loads on the ice. These results are used in a new model constructed using the ABAQUS finite element software. This model provides an estimate of the stress level in different parts of the atmospheric ice on the cable and its variation through a galloping cycle.

### 3.2.1 Equation of cable motion

Galloping of power transmission lines is one of the most important phenomena during which stresses develop on atmospheric ice. The significant deformation of the iced cable during this high-amplitude vibration induces stresses in the atmospheric ice. This deformation can be estimated by modeling the cable motion in galloping and obtaining the position of each point along the cable. Therefore, the equation of motion describing cable galloping will be considered. For a more accurate estimate, the following forces and stresses should be applied on atmospheric ice: aerodynamic forces, additional tension in the cable due to vibration, ice mass inertia and torque due to cable spring back. The basic equations of motion of a suspended cable are the following (Abdel-Rohman and Spencer, 2004; Luongo and Piccardo, 1998)

$$\frac{\partial}{\partial s}[(T_0 + T_a) \frac{\partial(x + D_x)}{\partial s}] = m \frac{\partial^2 D_x}{\partial t^2} \quad (3.1)$$

$$\frac{\partial}{\partial s} [(T_0 + T_a) \frac{\partial (y + D_y)}{\partial s}] = -mg + m \frac{\partial^2 D_y}{\partial t^2} + c \frac{\partial D_y}{\partial t} + F_1(s, t) \quad (3.2)$$

$$\frac{\partial}{\partial s} [(T_0 + T_a) \frac{\partial D_z}{\partial s}] = m \frac{\partial^2 D_z}{\partial t^2} + c \frac{\partial D_z}{\partial t} + F_2(s, t) \quad (3.3)$$

in which  $s$  is the spatial coordinate along the curved length of the cable;  $t$  is the time;  $x$  is the coordinate along the cable span;  $y(s)$  is the cable static profile;  $D_x(s, t)$ ,  $D_y(s, t)$  and  $D_z(s, t)$  are, respectively, the displacement in the horizontal, vertical and transverse directions (Figure 3.1),  $m$  is the cable mass per unit length, including ice mass,  $c$  is the damping coefficient per unit length,  $T_0$  is the static tension;  $T_a$  is the additional dynamic tension in the cable;  $F_1(s, t)$ , and  $F_2(s, t)$  are, respectively, the external loading per unit length in the vertical and transverse directions. When additional dynamic tension is applied to the cable with accreted ice, this tension is divided between the cable and ice according to the following relations:

$$T_{ac} = \frac{T_a A_c E_c}{A_c E_c + A_i E_i} \quad (3.4)$$

$$T_{ai} = \frac{T_a A_i E_i}{A_c E_c + A_i E_i} \quad (3.5)$$

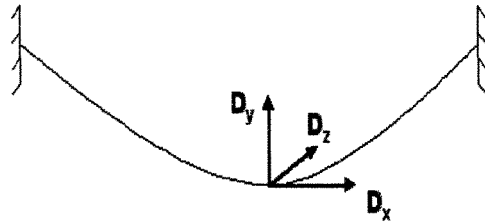


**Figure 3.1.** Cable displacement in horizontal,  $D_x$ , vertical,  $D_y$ , and transverse,  $D_z$ , directions. where  $E_i$  and  $E_c$  are Young's modulus of atmospheric ice and cable, and  $A_i$  and  $A_c$  are cross-section areas of the ice and cable, respectively.

Since the ratio of sag to span in power transmission lines is less than 1:8 and horizontal loads are negligible in this model, we can consider the horizontal displacement  $D_x$  to be equal to zero (Abdel-Rohman and Spencer, 2004; Irvine and Caughey, 1974). The solution,  $D_y$  and  $D_z$ , of the equations of motion can be obtained by a separation of variables:

$$D_z(s, t) = \varphi_1(s)W(t) \quad (3.6)$$

$$D_y(s, t) = \varphi_2(s)V(t) \quad (3.7)$$

where  $\varphi_1(s)$  and  $\varphi_2(s)$  are the mode shapes in the transverse and vertical directions respectively, and can be determined as (Abdel-Rohman and Spencer, 2004):

$$\varphi_1(s) = A_n \sin\left(\frac{n\pi s}{l}\right) \quad n=1, 2, 3, \dots \quad (3.8)$$

$$\varphi_2(s) = k_0 \left[ 1 - \tan\left(\frac{1}{2}\omega\pi\right) \sin\left(\frac{\pi\omega s}{l}\right) - \cos\left(\frac{\pi\omega s}{l}\right) \right] \quad (3.9)$$

where  $k_0$  is a constant chosen to make  $\varphi_2(l/2) = 1$ ,  $l$  is cable length and  $\omega = \omega_2 / \omega_1$ .  $\omega_1$  and  $\omega_2$ , the natural frequencies in the transverse and vertical directions, can be obtained as follows:

$$\omega_1 = \frac{n\pi}{L} \sqrt{\frac{H}{m}} \quad n=1, 2, 3, \dots \quad (3.10)$$

$$\omega_2 = q \sqrt{\frac{H}{m}} \quad (3.11)$$

with  $L$  is span length and  $H$  denoting the horizontal component of cable tension which can be obtained by solving equation (3.12) numerically:

$$d = \frac{H}{mg} \left[ \cosh\left(\frac{mgl}{2H}\right) - 1 \right] \quad (3.12)$$

where  $d$  is the sag of the cable and  $q$  can be calculated from the following equation ( Irvine and Caughey, 1974):

$$\tan\left(\frac{1}{2}qL\right) = \left(\frac{1}{2}qL\right) - \left(\frac{4}{\lambda^2}\right)\left(\frac{1}{2}qL\right)^3 \quad (3.13)$$

The parameter  $\lambda^2$  takes the form:

$$\lambda^2 = \left(\frac{8d}{L}\right)^2 \frac{L}{(HL_e/E_c A_c)} \quad (3.14)$$

$$L_e = \int_0^L \left(\frac{ds}{dx}\right)^3 dx \approx L \left(1 + 8\frac{d^2}{L^2}\right) \quad (3.15)$$

In order to decrease the number of equations of motion and the complexity of analysis, this problem is solved for first mode shape only ( $n=1$ ). After simplifying equations (3.2) and (3.3), substituting equations (3.6) - (3.15) into them, and applying Galerkin's method, one obtains the equation of motion of the cable as follows (Abdel-Rohman and Spencer, 2004):

$$\ddot{W} + 2\xi_1\omega_1\dot{W} + \omega_1^2W + n_5WV^2 + n_6WV^2 + n_7WV^3 = F_1(t) \quad (3.16)$$

$$\ddot{V} + 2\xi_2\omega_2\dot{V} + \omega_2^2V + n_1V^2 + n_2W^2 + n_3V^3 + n_4VW^2 + F_2(t) = 0 \quad (3.17)$$

where  $\xi_1$  and  $\xi_2$  are damping ratios in transverse and vertical directions, whereas  $F_1(t)$  and  $F_2(t)$  are determined as below.

The aerodynamic forces are determined referring to a spring mounted damped rigid cylinder of infinite length with two translational d.o.f, subjected to a bidirectional turbulent

flow of velocity  $U_0(s, t)$ . These forces can be estimated from (Abdel-Rohman and Spencer, 2004 )

$$F_1(s, t) = \frac{1}{2} \rho D U_r^2 (C_d G_s \gamma - C_l \sin \gamma) \quad (3.18)$$

$$F_2(s, t) = \frac{1}{2} \rho D U_r^2 (C_d \sin \gamma + C_l \cos \gamma) \quad (3.19)$$

where  $\rho$  is the air density,  $D$  is the cable diameter,  $C_d$  is the drag coefficient,  $C_l$  is the lift coefficient,  $\gamma$  is the angle of attack and  $U_r$  is the relative wind speed with respect to the cable motion that can be obtained by

$$U_r^2 = [U_0(s, t) - \dot{D}_z(s, t)]^2 + \dot{D}_y^2(s, t) \quad (3.20)$$

in which  $U_0(s, t)$  is the mean wind speed,  $\dot{D}_y(s, t)$  is the velocity response of the cable in  $Y$ -direction and  $\dot{D}_z(s, t)$  is the velocity response of the cable in  $Z$ -direction.

It is easily shown that:

$$U_0(s, t) - \dot{D}_z(s, t) = U_r(s, t) \cos \gamma \quad (3.21)$$

$$\dot{D}_y(s, t) = U_r(s, t) \sin \gamma \quad (3.22)$$

$$\tan \gamma = \frac{\dot{D}_y(s, t)}{U_0(s, t) - \dot{D}_z(s, t)} \quad (3.23)$$

Substituting equations (3.27), (3.28) and (3.29) into (3.24) and (3.25) one obtains:

$$F_1(s, t) = \frac{1}{2} \rho D [U_0(s, t) - \dot{D}_z(s, t)]^2 C_1(\gamma) \quad (3.24)$$

$$F_2(s, t) = \frac{1}{2} \rho D [U_0(s, t) - \dot{D}_z(s, t)]^2 C_2(\gamma) \quad (3.25)$$

Where  $C_1(\gamma)$  and  $C_2(\gamma)$  are force functions and can be written as polynomials in  $\tan(\gamma)$  as follows:

$$C_1(\gamma) = \sec^2 \gamma (C_d \cos \gamma - C_l \sin \gamma) = \sum_{i=0}^N a_i \tan^i \gamma \quad (3.26)$$

$$C_2(\gamma) = \sec^2 \gamma (C_d \sin \gamma + C_l \cos \gamma) = \sum_{i=0}^N b_i \tan^i \gamma \quad (3.27)$$

Where  $N$  is the degree of the polynomial, and  $a_i$  and  $b_i$  are constants that can be determined from wind tunnel test data.

Using equations (3.23)-(3.27) in the equations of  $F_1(t)$  and  $F_2(t)$  in appendix A one can obtain:

$$F_1(t) = d_0 + d_1 \dot{W} + d_2 \dot{W}^2 + d_3 \dot{V} + d_4 \dot{W}\dot{V} + d_5 \dot{V}^2 + \sum_{k=3}^N d_{(2k)} \dot{V}^k + \sum_{k=3}^N d_{(2k+1)} \dot{V}^k \dot{W}^{(k-2)} \quad (3.28)$$

$$F_2(t) = e_0 + e_1 \dot{W} + e_2 \dot{W}^2 + e_3 \dot{V} + e_4 \dot{W}\dot{V} + e_5 \dot{V}^2 + \sum_{k=3}^N e_{(2k)} \dot{V}^k + \sum_{k=3}^N e_{(2k+1)} \dot{V}^k \dot{W}^{(k-2)} \quad (3.29)$$

The coefficients  $n_i$ ,  $d_i$  and  $e_i$  are defined in Appendix A.

Finally, the equations of motion of a galloping cable can be written by combining equations (3.16) and (3.17) with equations (3.28) and (3.29). We obtain:

$$\begin{aligned} & \ddot{W} + 2\xi_1 \omega_1 \dot{W} + \omega_1^2 W + n_5 W V^2 + n_6 W V^2 + n_7 W V^3 \\ & = d_0 + d_1 \dot{W} + d_2 \dot{W}^2 + d_3 \dot{V} + d_4 \dot{W}\dot{V} + d_5 \dot{V}^2 + \sum_{k=3}^N d_{(2k)} \dot{V}^k + \sum_{k=3}^N d_{(2k+1)} \dot{V}^k \dot{W}^{(k-2)} \end{aligned} \quad (3.30)$$

$$\begin{aligned} & \ddot{V} + 2\xi_2 \omega_2 \dot{V} + \omega_2^2 V + n_1 V^2 + n_2 W^2 + n_3 V^3 + n_4 V W^2 + \\ & e_0 + e_1 \dot{W} + e_2 \dot{W}^2 + e_3 \dot{V} + e_4 \dot{W}\dot{V} + e_5 \dot{V}^2 + \sum_{k=3}^N e_{(2k)} \dot{V}^k + \sum_{k=3}^N e_{(2k+1)} \dot{V}^k \dot{W}^{(k-2)} = 0 \end{aligned} \quad (3.31)$$

### 3.2.2 Loads and stresses in atmospheric ice

- Stresses due to cable bending

The most important stress that causes ice shedding from power transmission lines during galloping is bending stress. When galloping causes the cable to bend, the atmospheric ice on the cable resists this deformation. However, if the force overcomes the resistance of the atmospheric ice, the ice breaks and may shed. The position of each point along the cable during galloping (results of the calculation presented in Section 3.2.1) will be used in the ABAQUS model to determine the stresses developing in the atmospheric ice.

- **Aerodynamic forces**

As mentioned above, aerodynamic forces cause cable galloping and this movement can produce bending moment and additional tension in the cable. However, these forces also apply some loads directly to the atmospheric ice. Equations (3.30) and (3.31) express the loads of aerodynamic force per unit length in transverse and vertical directions, respectively. To take into account the effect of these forces on a piece of atmospheric ice in the middle of a span, it is sufficient to apply them in the ABAQUS model as a distributed force on the ice (see Figure 3.2).

- **Torsional loads**

Power transmission cables are very flexible and tend to rotate when ice builds up asymmetrically on their surface. Due to such a rotation, the ice mass tends to be evenly distributed on the surface of the cables. This can explain why the ice shape observed on transmission lines is predominantly circular. During ice accretion, when the ice on the cable is not symmetric, two factors can apply torsional load on the cable, ice weight and aerodynamic force due to wind speed. However, when ice accumulates on the cable and

takes a cylindrical shape, the torsional load due to wind becomes negligible. The rotational angle of the iced cable depends upon the torsional rigidity of the cable and the amount of ice accreted on it.

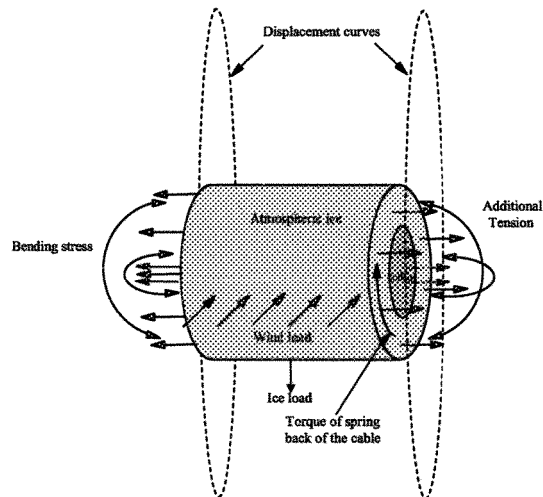


Figure 3.2. Loads and movement of a piece of cable on corresponding curves.

The relationship between the rotation of the cable at mid-span around its centerline,  $\theta_m$ , and the torque at the suspension points,  $T_A$ , due to cable spring back can be written as follows :

$$\frac{T_A \frac{l}{2}}{GJ} = \theta_m \quad (3.32)$$

where  $GJ$  is torsional rigidity of cable,  $l$  is cable length, and constant ice thickness is assumed along the entire span. Once  $\theta_m$  is known, the torque of spring back,  $T_c$ , which is applied by the cable to the end point of a piece of ice located in the middle of the span, can be determined as follows:

$$T_c = \frac{2\theta_m L_1 GJ}{l^2} \quad (3.33)$$

where  $L_1$  is the length of piece of cable (torque in Figure 3.2). Since a short piece of the cable-ice composition in the middle of the span is analyzed, i.e.  $L_1 \ll l$ , the torque,  $T_C$ , is significantly smaller than the other loads discussed above.

- **Additional tension in the cable and the ice**

As mentioned above, cable motion during galloping induces additional tension in the cable and the atmospheric ice. The stresses due to these additional tensions are calculated using the following formulae:

$$\sigma_c = E_c \frac{ds' - ds}{ds} \quad (3.34)$$

$$\sigma_i = E_i \frac{ds' - ds}{ds} \quad (3.35)$$

where  $ds'$  is the deformed cable segment. These terms were considered in the model constructed in ABAQUS (additional tensions in Figure 3.2).

- **Load due to ice mass inertia**

The ice load is induced by acceleration due to cable motion or gravity force. In this model the effect of this load is calculated using the ABAQUS software.

### 3.2.3 Calculation of forces and displacements

In order to obtain the displacement of each point of the cable during galloping (as mentioned in Section 3.2.1), the constants  $n_i$ ,  $d_i$ , and  $e_i$  in equations (3.30) and (3.31) should first be determined. These constants together with the initial cable tension,  $T_0$ , and the natural frequencies in transverse and vertical directions,  $\omega_1$  and  $\omega_2$ , are calculated by a

code written in MAPLE. The output data of this code are the scalars corresponding to  $T_0$ ,  $\omega_1$  and  $\omega_2$ , as well as three matrices providing the constants  $n_i$  ( $1 \times 7$ ),  $d_i$  ( $1 \times 15$ ) and  $e_i$  ( $1 \times 15$ ).

The cable motion during galloping is simulated by a program developed in MATLAB. All the results provided by the MAPLE code, the cable and ice characteristics, the wind velocity,  $U_0$ , and the damping ratios in vertical and transverse directions,  $\xi_1$  and  $\xi_2$ , are defined as input data for the MATLAB implementation. This program solves equations (3.30) and (3.31) numerically (using the Runge Kutta method) and determines the displacements of two ends of a piece of cable with ice in the middle of the span. Furthermore, it computes the aerodynamic forces on the ice, the torque applied to the ice due to cable spring back, and the additional tension in the cable and the ice. All of these values are tabulated as time functions, and then are used as loads and displacements in the ABAQUS model described in the next section.

#### **3.2.4 Modeling stress variation during galloping with ABAQUS**

The simulation of cable motion and the load calculation provide all the parameters needed to determine the stress in the ice and its variation during galloping. A model of a piece of cable with uniform cylindrical ice accretion is constructed in ABAQUS, which computes the stress developing in the ice through one or more cycles of galloping. The curves representing cable motion at each end of the modeled piece, as sketched in Figure 3.2, are obtained as output data of the MATLAB program. The additional cable tension and aerodynamic forces are also added as input data, while the effects of ice load and inertia are

determined in the ABAQUS calculation. Figure 3.2 shows schematically the movement of a piece of cable, as well as the forces and the torque applied on the atmospheric ice.

The analysis was carried out in the Dynamic Explicit condition with ABAQUS, which uses a consistent, large-deformation theory and the model can undergo large rotations and large deformation. The element type for the cable and the ice is C3D8R. This is a three-dimensional element with 8 nodes and suitable for continuum stress/displacement analysis with reduced integration. The variations of transverse and vertical displacements, aerodynamic forces, and additional tension in the cable and the ice were tabulated in 8 tables. Each table has two columns, the first one containing the time data, while the second one lists the above-mentioned parameters at each instance. The total time of analysis is 3.33s. In order to have a more accurate estimate, both ends of the cable-ice piece at the beginning of the analysis were set in the positions that represent the initial shape of the ice and cable before any deformation. The ice was assumed to adhere strongly to the cable surface without sliding and separation.

The flowchart in Figure 3.3 shows the steps that were taken to estimate the stresses developing in the atmospheric ice.

### **3.2.5 Results and discussion**

The preliminary calculations with MAPLE, the galloping simulation with MATLAB and the stress analysis in ABAQUS were applied for a typical example. Table 3.1 shows the characteristics of the span, cable and ice considered in this example.

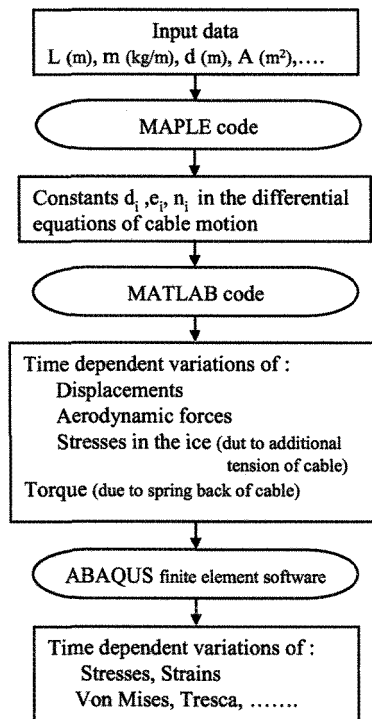
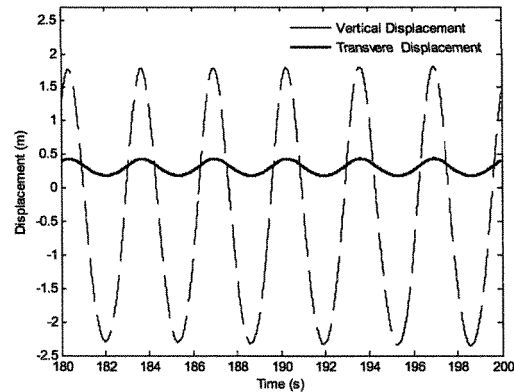


Figure 3.3. Steps to estimate the stresses developing in atmospheric ice during galloping.

Parameter	Value	Unit
Cable type	BERSIMIS ACSR 42/7	---
Cable diameter	35.1	mm
Young's modulus of cable	62	GPa
Mass per unit length of cable	2.185	kg/m
Cable torsional rigidity	351	N.m/Rad
Cable cross-section area	725.2	mm <sup>2</sup>
Span length	300	m
Cable sag	8.04	m
Ice type	Hard rime and glaze	---
Ice thickness on cable	25	mm
Density of ice	900	Kg/m <sup>3</sup>
Young's modulus of ice	9.31	GPa
Wind velocity	6	m/s
Rotation angle due to ice accretion at span centre	405°	Degree

Table 3.1. Characteristics of span, cable and ice.



**Figure 3.4.** Cable displacement at mid-span during galloping.

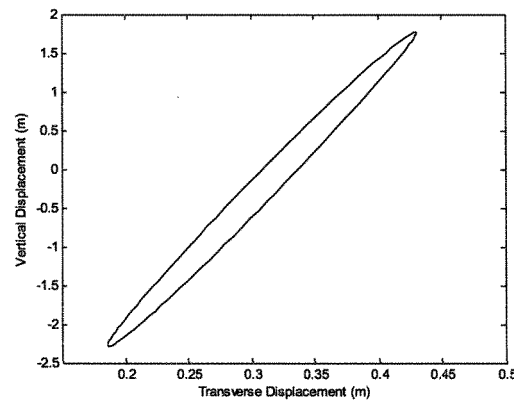


**Figure 3.5.** The trajectory of the mid-point of the cable during galloping.

- **Galloping simulation**

Preliminary calculations were first carried out with the data presented in Table 3.1, and then the galloping of the cable-ice composition was simulated. The cable displacement in the middle of the span in transverse and vertical directions is shown in Figure 3.4. A full cycle of galloping lasts 3.33s, and it is also clear that the amplitude of vertical motion is significantly greater than that in the transverse direction. The trajectory of the mid-point of the cable is demonstrated in Figure 3.5. The results of wind load and stress calculations are presented in Figures 3.6 and 3.7. Figure 3.6 shows the variations of distributed wind forces

in vertical and transverse directions during a full cycle of vibration, whereas Figure 3.7 shows the stresses due to additional tension in the cable and the atmospheric ice.

- **Stress analysis**

The data presented in Table 3.1 and the results of calculations discussed in Section 3.2.1 and 3.2.2 were applied as inputs for the stress analysis on a piece of cable-ice composition in the middle of the span. The length of this piece was set at 10 cm.

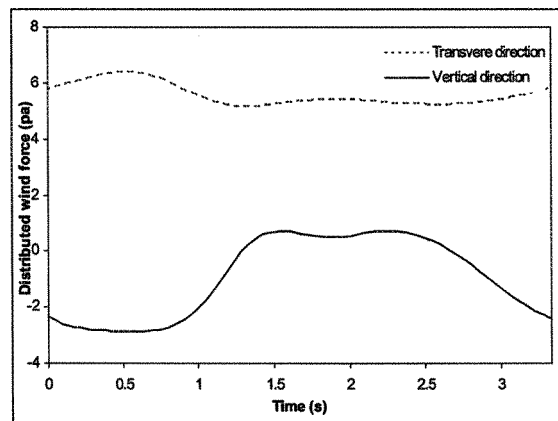


**Figure 3.6.** Variations of distributed wind force in transverse and vertical directions.

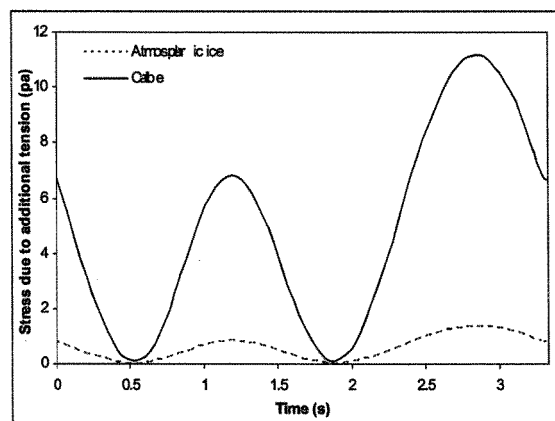


**Figure 3.7.** Variations of stresses due to additional tension in cable.

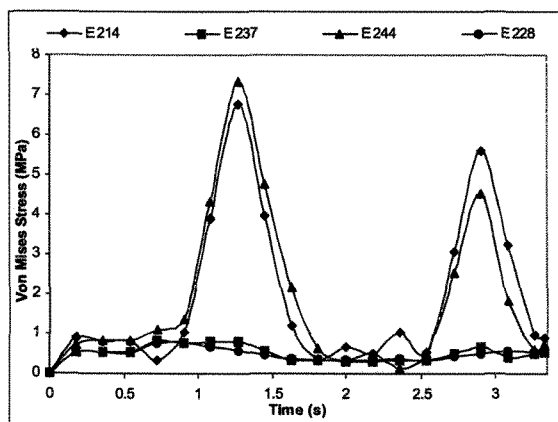


Figure 3.8. Stresses in 4 elements in the external layer of atmospheric ice.

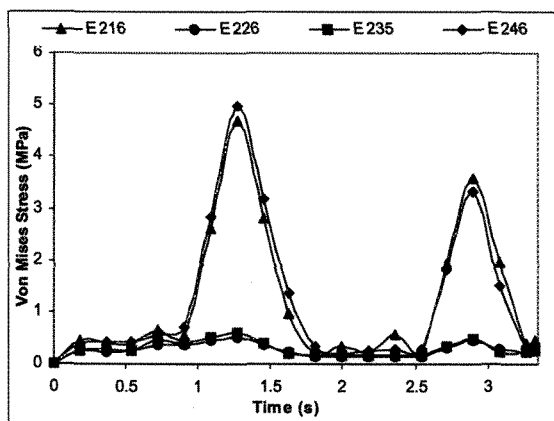


Figure 3.9. Stresses in 4 elements in the internal layer of atmospheric ice.

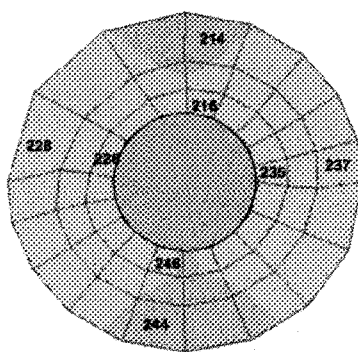


Figure 3.10. Position of the elements that are the objects of Figures 8, 9, 12 and 13.

Stresses in several elements were calculated during one cycle of galloping and the results for the elements in various positions are shown in Figures 3.8 and 3.9. Figure 3.10

illustrates the positions of these elements in the middle of the 10 cm piece of ice cover. As shown in Figures 3.8 and 3.9, the Von Mises stresses reach their maximum values at instances 1.27s and 2.9s, when the mid-point of the cable is at the highest and lowest positions of its trajectory. Numerically, these maximum values are 7.33 MPa and 5.61 MPa for the elements in the external layer, and 4.99 MPa and 3.59 MPa for the element(s) in the internal layer. According to Figure 3.5, the vertical displacement of the cable reaches its limits twice in one cycle: first at 1.27s when the mid-point of the cable is at the highest position of its trajectory, and then at 2.9s when this point reaches the lowest position. The stress is greater in the first case, because the transverse position of the mid-point of the cable is the farthest from its location in static equilibrium at 1.27s, while it is nearest at 2.9s.

The mechanical properties of atmospheric ice were measured in this study and will be discussed in the following chapters. According to the results of the ice tests (Chapter 5), the bending strength of atmospheric ice at  $-10^{\circ}\text{C}$  varies with the strain rate, but it may be taken to be approximately 2.73 MPa. Although the Von Mises stress is not equivalent to the bending stress, it mainly arises from the bending load in this case. Thus, since the Von Mises stress is significantly greater in some ice elements than the bending strength of ice, this model predicts ice fracture from the part of the cable under examination.

Ice failure will initiate at the top and bottom sides of the atmospheric ice, because stresses are highest in these locations, while the stress level does not exceed the bending strength in the elements on the left and right sides of the cable. A section of iced cable with stress distribution is illustrated in Figure 3.11.

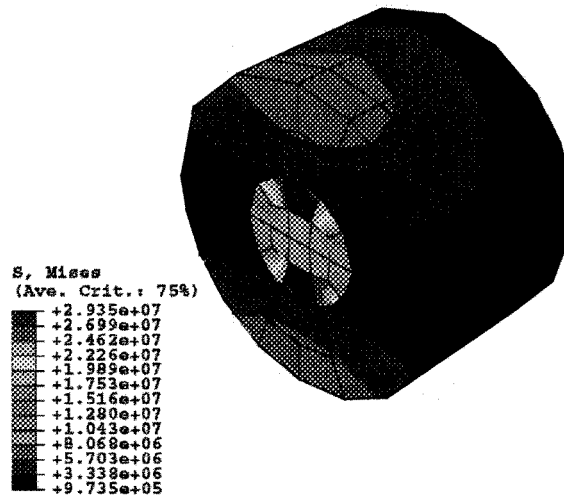


Figure 3.11. Stress distribution in cable and atmospheric ice.

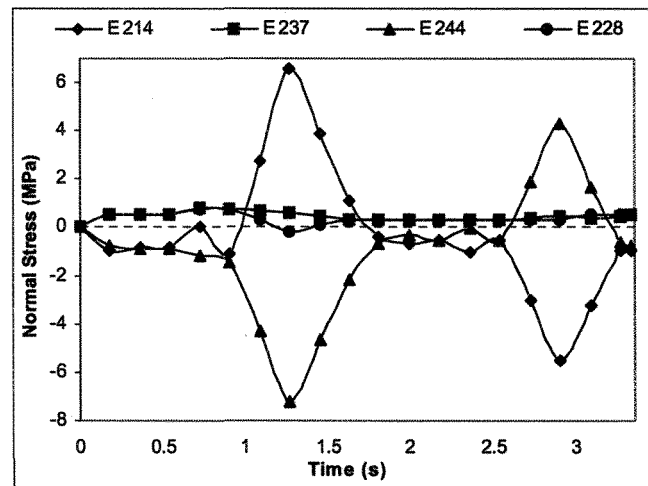


Figure 3.12. Normal stresses in 4 elements in the external layer of atmospheric ice.

Figures 3.12 and 3.13 show normal stresses parallel to the cable axis in the same elements as in Figures 3.8 and 3.9, respectively. When the cable approaches its highest position, the elements on the top of the cable (elements No. 214 and 216) will be under tension, whereas the bottom elements (No. 244 and 246) will be under compression.

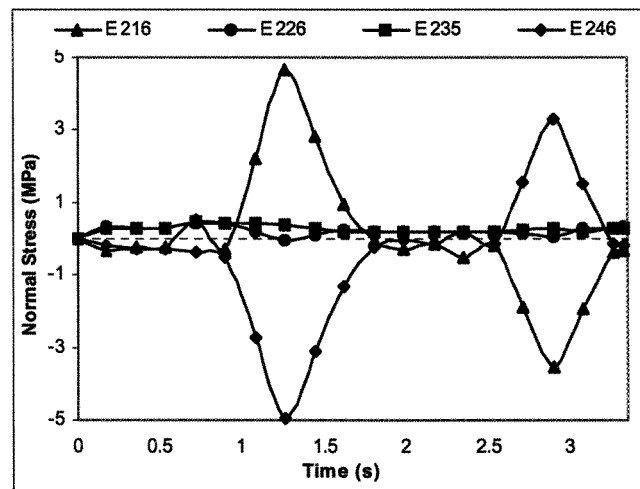


Figure 3.13. Normal stresses in 4 elements in the internal layer of atmospheric ice.

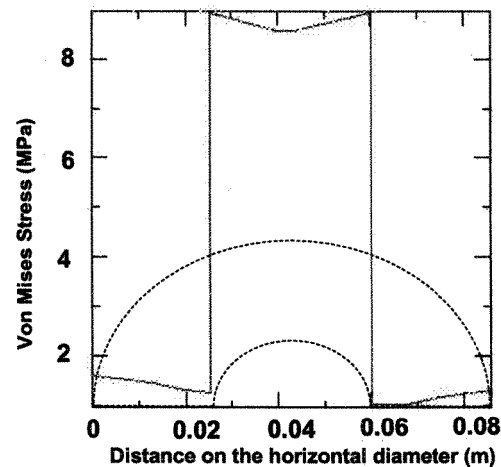


Figure 3.14. Stress distribution along horizontal diameter of cable-ice composition.

The direction of stresses changes when the cable approaches its lowest position. The elements on the neutral axis (elements No. 228, 226, 235 and 237) endure the minimum normal stress arising from additional horizontal tension caused by the cable motion. Figures 3.14 and 3.15 show the distribution of Von Mises stress along the horizontal and vertical diameters of the iced cable in the middle of the 10 cm piece. As expected, the stresses in the internal layers of the ice (and cable) are less than in the external layers.

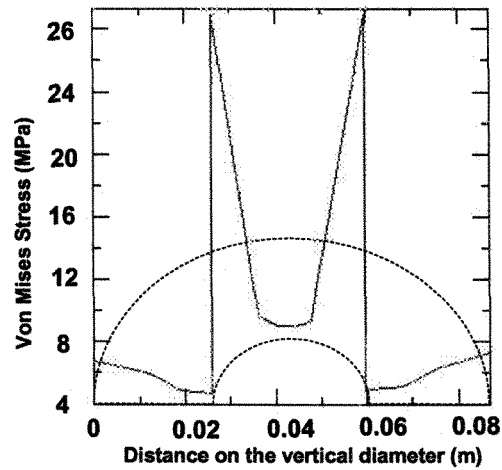


Figure 3.15. Stress distribution along vertical diameter of cable-ice composition.

### 3.3 Estimation of loads in aeolian vibration

Aeolian vibration is a high frequency low amplitude type of oscillation in power transmission lines. The primary cause of conductor vibration is the alternate shedding of wind-induced vortices from the top and bottom sides of the conductor. The action creates an alternating pressure unbalance, inducing the conductor to move up and down at right angles to the direction of the air flow.

Aeolian vibration has been studied by other researchers (e.g. CIGRE Working Group 01, 1978, CIGRE Working Group 11, 1998). To the author's knowledge, however, a comprehensive analysis for determining the displacement of each point of the cable in aeolian vibration that covers the damping effect and wind force has not previously been published.

To estimate the stresses in this type of vibration (as with galloping), we have to study the behavior of the conductor.

### 3.3.1 Equation of motion in aeolian vibration

We can rewrite equation (3.2) for aeolian vibration as below:

$$HV_{(x,t)}'' + h_{(t)}\left(\frac{-8d}{L^2}\right) = m\ddot{V} + c\dot{V} + F_0 \sin \omega_s t \quad (3.36)$$

where

$$F_0 = \frac{1}{2} \rho_a C_L D_i U \quad (3.37)$$

$$\omega_s = 2\pi \frac{S_s U}{D_i} \quad (3.38)$$

and  $\rho_a$  is air density,  $C_L$  is the lift coefficient,  $D_i$  is the diameter of atmospheric ice,  $U$  is air velocity,  $S_s$  is Strouhal number.

To solve equation (3.36) we assume

$$V_{(x,t)} = \sum_i k_0 \varphi_i(x) T_i(t) \quad (3.39)$$

$$\text{and} \quad h_{(t)} = \sum_i \tilde{h} T_i(t) \quad (3.40)$$

where  $\varphi_i(x)$  is

$$\varphi_i(s) = 1 - \tan\left(\frac{1}{2}\beta L\right) \sin(\beta x) - \cos(\beta x) \quad (3.41)$$

$$\text{and} \quad k_0 = \frac{8d\tilde{h}}{H(\beta L)^2}, \quad \beta = \omega_2 \sqrt{\frac{m}{H}} \quad (3.42)$$

The constant  $k_0$  and natural frequency  $\omega_2$  were defined in equations (3.9) and (3.11), respectively. Substituting these functions into equation (3.36) gives

$$\sum_i H k_0 \varphi_i'' T_i - \sum_i \frac{8d\tilde{h}}{L^2} T_i = \sum_i m k_0 \varphi_i \ddot{T}_i + \sum_i c k_0 \varphi_i \dot{T}_i + F_0 \sin \omega_s t \quad (3.43)$$

Multiplying each term by  $\varphi(x)$  and integrating gives

$$\begin{aligned} \sum_i Hk_0 T_i \int_0^L \varphi_i'' \varphi_n dx - \sum_i \frac{8d\tilde{h}}{L^2} T_i \int_0^L \varphi_n dx = \\ \sum_i mk_0 \ddot{T}_i \int_0^L \varphi_i \varphi_n(x) + \sum_i ck_0 \dot{T}_i \int_0^L \varphi_i \varphi_n dx + F_0 \sin \omega_s t \int_0^L \varphi_n dx \end{aligned} \quad (3.44)$$

by assumption :

$$\int_0^L \varphi_m \varphi_n'' dx = 0 \quad \text{if } m \neq n \quad (3.45)$$

$$\int_0^L \varphi_m (H\varphi_n'' - \frac{8d\tilde{h}}{L^2}) dx = 0 \quad (3.46)$$

we obtain

$$T_n k_0 H \int_0^L \varphi_i'' \varphi_n dx - T_n \frac{8d\tilde{h}}{L^2} \int_0^L \varphi_n dx = mk_0 \ddot{T}_n \int_0^L \varphi_n^2 dx + ck_0 \dot{T}_n \int_0^L \varphi_n^2 dx + F_0 \sin \omega_s t \int_0^L \varphi_n dx \quad (3.47)$$

we assume

$$A = \int_0^L \varphi_n(x) \varphi_n''(x) dx, \quad B = \int_0^L \varphi_n^2(x) dx, \quad G = \int_0^L \varphi_n(x) dx,$$

$$D = H A k_0 - \frac{8d\tilde{h}}{L^2} \cdot G = \frac{8d}{L^2} \left( \frac{A}{\beta^2} - G \right) \tilde{h} \quad (3.48)$$

we have

$$-mk_0 B \ddot{T}(t) - ck_0 B \dot{T}_n(t) + D T_n(t) = G F_0 \sin \omega_s t \quad (3.49)$$

Substituting  $k_0$  in this equation gives

$$-m \frac{8d\tilde{h}}{H(\beta L)^2} B \ddot{T}(t) - c \frac{8d\tilde{h}}{H(\beta L)^2} B \dot{T}_n(t) + \frac{8d}{L^2} \left( \frac{A}{\beta^2} - G \right) \tilde{h} T_n(t) = G F_0 \sin \omega_s t \quad (3.50)$$

or

$$a_2 \ddot{T}(t) - a_1 \dot{T}_n(t) + a_0 T_n(t) = \frac{G F_0}{\tilde{h}} \sin \omega_s t \quad (3.51)$$

where

$$a_0 = \frac{8d}{L^2} \left( \frac{A}{\beta^2} - G \right), \quad a_1 = -c \frac{8d}{H(\beta L)^2} B \quad \text{and} \quad a_2 = -m \frac{8d}{H(\beta L)^2} B \quad (3.52)$$

The equation (3.51) depends only on time and has a general and a particular solution.

$$T = T_g + T_p \quad (3.53)$$

The general solution of this differential equation is

$$a_2 \ddot{T}(t) - a_1 \dot{T}_n(t) + a_0 T_n(t) = 0 \Rightarrow \lambda_{1,2} = \frac{a_1 \pm \sqrt{a_1^2 - 4a_0 a_2}}{2a_2} = \alpha_1 \mp i\beta_1 \quad (3.54)$$

Therefore, the general solution is

$$T_g = e^{\alpha_1 t} (A_1 \cos \beta_1 t + B_1 \sin \beta_1 t) \quad (3.55)$$

The particular solution of this equation is obtained by the assumption

$$T_p = P \cos \omega_s t + q \sin \omega_s t \quad (3.56)$$

Therefore, we can substitute  $T_p$  in equation (3.51):

$$\dot{T}_p = -P\omega_s \sin \omega_s t + q\omega_s \cos \omega_s t, \quad \ddot{T}_p = -p\omega_s^2 \cos \omega_s t - q\omega_s^2 \sin \omega_s t \quad (3.57)$$

We have:

$$\begin{aligned} & -a_2 P \omega_s^2 \cos \omega_s t - a_2 q \omega_s^2 \sin \omega_s t - a_1 P \omega_s \sin \omega_s t + a_1 q \omega_s \cos \omega_s t + \\ & a_0 p \cos \omega_s t + a_0 q \sin \omega_s t = \frac{GF_0}{h} \sin \omega_s t \end{aligned} \quad (3.58)$$

We can rewrite this equation as below.

$$(-a_2 q \omega_s^2 - a_1 P \omega_s + a_0 q) \sin \omega_s t + (-a_2 p \omega_s^2 + a_1 q \omega_s + a_0 p) \cos \omega_s t = \frac{GF_0}{h} \sin \omega_s t \quad (3.59)$$

So we have

$$-a_2 q \omega_s^2 - a_1 P \omega_s + a_0 q = \frac{GF_0}{h} \quad (3.60)$$

$$-a_2 p \omega_s^2 + a_1 q \omega_s + a_0 p = 0 \quad (3.61)$$

Substituting  $q$  from equation (3.61) in (3.60) gives

$$q = \frac{a_2 p \omega_s^2 - a_0 p}{a_1 \omega_s} \quad (3.62)$$

$$P = \frac{GF_0 a_1 \omega_s}{h(2a_0 a_2 \omega_s^2 - a_2^2 \omega_s^4 - a_1^2 \omega_s^2 - a_0^2)} \quad (3.63)$$

Then the solution of equation (3.51) will be

$$T = e^{\alpha t} (A_1 \cos \beta_1 t + B_1 \sin \beta_1 t) + P \cos \omega_s t + q \sin \omega_s t \quad (3.64)$$

$A_1$  and  $B_1$  can be determined from the initial conditions

$$T(0) = 0 \quad \text{and} \quad \dot{T}(0) = 0 \quad (3.65)$$

We get:

$$A_1 = -P, \quad B_1 = -\frac{q \omega_s + \alpha_1 A_1}{\beta_1} \quad (3.66)$$

Therefore the  $T(t)$  will be obtained

$$T = e^{\alpha t} \left( -P \cos \beta_1 t - \frac{q \omega_s - P \alpha_1}{\beta_1} \sin \beta_1 t \right) + P \cos \omega_s t + q \sin \omega_s t \quad (3.67)$$

In equation (3.54), if  $\beta_1 = 0$ , we obtain

$$A_1 = -P - B_1, \quad B_1 = \frac{\lambda_1 p - q \omega_s}{\lambda_2 - \lambda_1} \quad (3.68)$$

Therefore, the  $T(t)$  will be

$$T = A_1 e^{\lambda_1 t} + B_1 e^{\lambda_2 t} + P \cos \omega_s t + q \sin \omega_s t \quad (3.69)$$

### 3.3.2 Other forces in aeolian Vibration

To have a more accurate estimate of stresses in atmospheric ice in aeolian vibration, other forces should be added to the model.

Some of these forces, as with galloping, are aerodynamic forces, which are

$$F_v = F_0 \sin \omega_s t \quad (3.70)$$

$$F_w = \frac{1}{2} \rho C_d D_i U \quad (3.71)$$

where  $C_d$  is the drag coefficient.

Furthermore, there are two other sources of stress in aeolian vibration, which are the additional tension in the cable and atmospheric ice that can be obtained by the same method as explained in section 3.2.2.

Again, the stresses due to ice load and ice mass inertia will be taken into account in the ABAQUS model.

### 3.3.3 Calculation of forces and displacements in aeolian vibration

The cable motion during aeolian vibration was simulated by a program developed in MATLAB. All the constants (e.g. the cable and ice characteristics, the wind velocity,  $U_0$ , and the damping ratio in vertical direction) are defined as input data for the MATLAB implementation. This program determines the displacements of two ends of a piece of cable with ice in the middle of the span as well as the aerodynamic forces on the ice, the torque applied to the ice due to cable spring back, and the additional tension in the cable and the ice. All of these values are tabulated as time functions.

According to the results of the MATLAB code, the amplitude of aeolian vibration for the BERSIMIS cable with a thickness of 2.5 cm accreted ice in a wind with 4 m/s velocity is 0.08 mm. So far, to the best of the author's knowledge, there is no published field measurement on the level of amplitude of aeolian vibration in a similar condition to this study. It is hard to find agreement or disagreement with the results of this model. Doocy (1979) reported a general value for the amplitude of aeolian vibration without citing any specific condition (Table 2.1). As was explained in Chapter 2, the numbers in Table 2.1 do not represent extreme limits or normal operating conditions and the characteristics of the vibrations (amplitude, frequency, etc) may vary widely from line to line. In comparison with the values reported by Doocy (1979), the result of the MATLAB code is lower than the expected value, which is between 0.85 mm and 85 mm. It is obvious that the stress level in this amplitude is very low and insufficient for ice shedding. The level of stress in atmospheric ice during low amplitude vibration (0.85 mm) is also very low. Therefore, we assume that the aeolian vibration of the cable has the maximum possible value of amplitude (i.e. 85 mm) and a frequency of 54.6 Hz. Vibration with this great amplitude and frequency never happens in transmission lines, but the worst conditions were selected here to study the stress variation in atmospheric ice.

#### **3.3.4 Modeling of stress variation during aeolian vibration with ABAQUS**

As explained in the section on galloping, a model of a piece of cable with uniform cylindrical ice accretion is constructed in ABAQUS, which computes the stress developing in the ice through one or more cycles of aeolian vibration.

The displacement of the cable was applied to each end of the modeled piece. The additional cable tension and aerodynamic forces are also added as input data, while again the effects of ice load and inertia are determined in the ABAQUS calculation.

As explained in section 3.2, the analysis was carried out in the Dynamic Explicit condition with ABAQUS. The element type for cable and ice is C3D8R. The variations of vertical displacements, aerodynamic forces, additional tension in the cable and the ice were tabulated in 6 tables. Each table has two columns, the first one containing the time data, while the second one lists the above-mentioned parameters at each instance. The total time of analysis is 0.3s. The ice was assumed to adhere strongly to the cable surface without sliding and separation.

### **3.3.5 Results and discussion**

The aeolian vibration simulation with MATLAB and the stress analysis in ABAQUS were applied for a typical example with characteristics mentioned in the galloping simulation (Table 3.1). A full cycle of vibration lasts 0.12s. The results of wind load and stress calculations are presented in Figures 3.16 and 3.17. Figure 3.16 shows the variations of distributed wind forces in vertical directions during three full cycles of vibration, whereas Figure 3.17 shows the stresses due to additional tension in the cable and the atmospheric ice.

The data presented in Table 3.1 and the results of the calculations discussed in Sections 3.3.3 and 3.3.4 were applied as inputs for the stress analysis on a 10 cm piece of the cable-ice composition in the middle of the span. The results of the calculated stresses in several elements during three cycles of aeolian vibration in various positions are shown in Figures

3.18 and 3.19. The positions of these elements in the middle of the 10 cm piece of the ice cover are illustrated in Figure 3.20. Figures 3.18 and 3.19 show that the Von Mises stresses reach their maximum values when the mid-point of the cable is at the highest and lowest positions of its trajectory. Numerically, these maximum values are 7700 Pa for the elements in the external layer, and 5800 Pa for the elements in the internal layer.

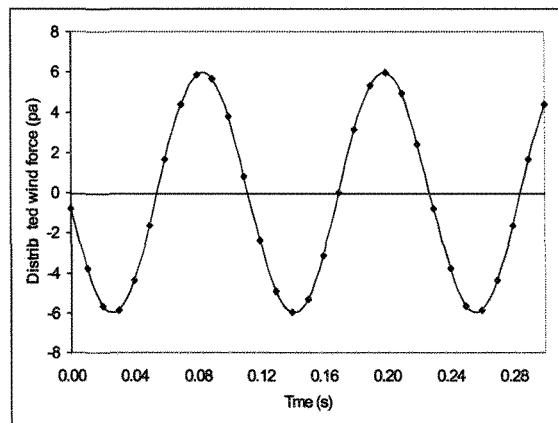


Figure 3.16. Variations of distributed wind force in vertical directions.

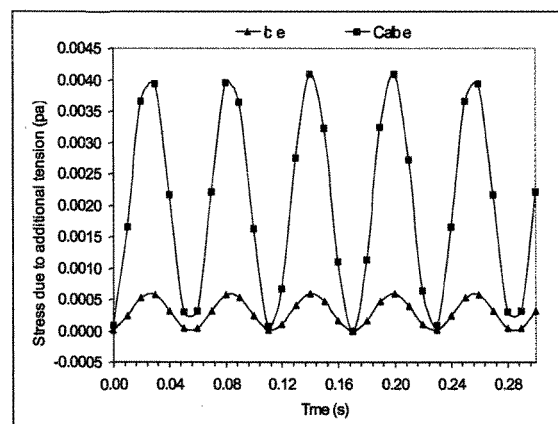
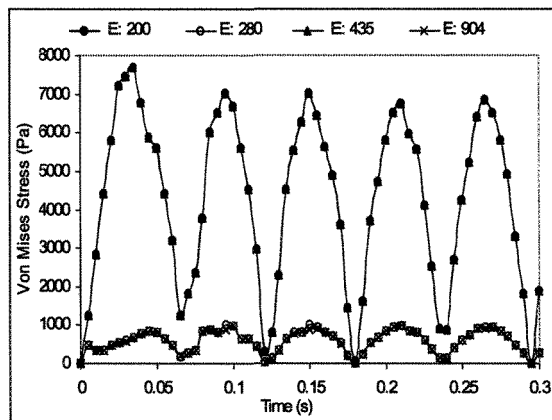
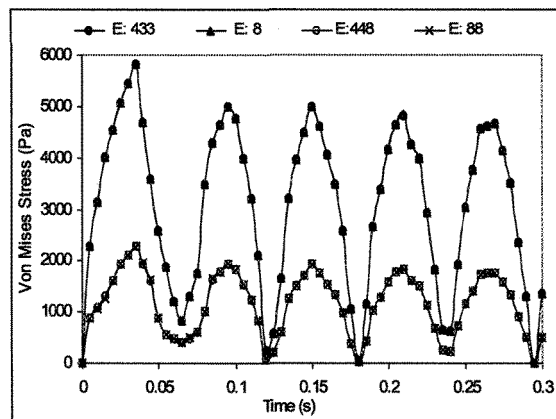


Figure 3.17. Variations of stresses due to additional tension in cable.



**Figure 3.18.** Stresses in 4 elements in the external layer of atmospheric ice during an aeolian vibration.



**Figure 3.19.** Stresses in 4 elements in the internal layer of atmospheric ice during an aeolian vibration.

Since the Von Mises stress in all elements is significantly less than the bending strength of atmospheric ice ( 2.73 MPa), according to this model no ice shedding happens under these conditions.

Figures 3.21 and 3.22 show normal stresses in vertical direction (perpendicular to the cable axis) in the same elements as in Figures 3.18 and 3.19, respectively. When the cable approaches its highest position, the elements on the top of the cable (elements No. 435 and 433) will be under tension, whereas the bottom elements (No. 8 and 200) will be under compression. The direction of stresses changes when the cable approaches its lowest

position. The elements close to the neutral axis (elements No. 904, 280, 88 and 448) endure less stress because the strains are smaller in this area.

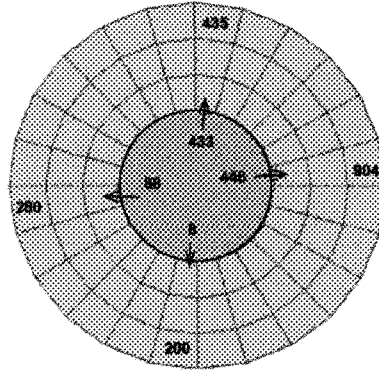


**Figure 3.20.** Position of the elements that are the objects of Figures 3.18, 3.19, 3.21 and 3.22.

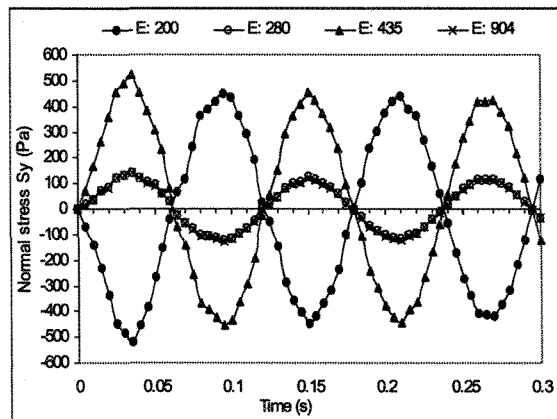


**Figure 3.21.** Normal stresses in 4 elements in the external layer of atmospheric ice.

Figures 3.23 and 3.24 show the distribution of Von Mises stress along the horizontal and vertical diameters of the iced cable in the middle of the 10 cm piece at 0.15s. As expected and seen in galloping, the stresses in the internal layers of the ice (and cable) are less than in the external layers.

A section of iced cable with stress distribution at 0.15s during an aeolian vibration is illustrated in Figure 3.25.

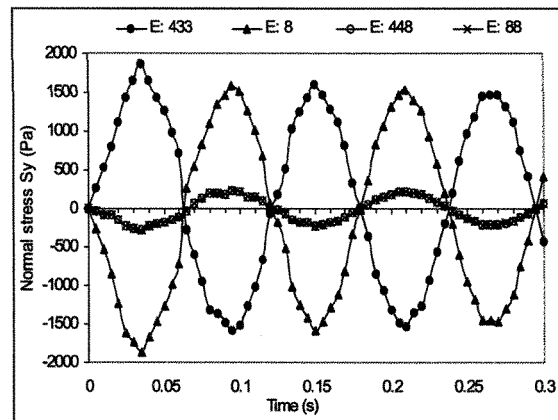


Figure 3.22. Normal stresses in 4 elements in the internal layer of atmospheric ice.

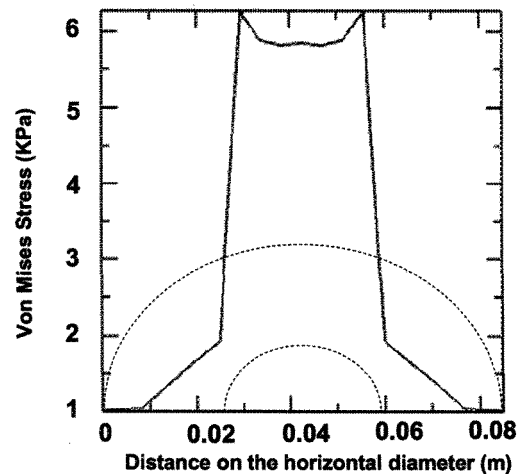


Figure 3.23. Stress distribution along the horizontal diameter of cable-ice composition at 0.15s in an aeolian vibration.

### 3.4 Conclusion

Two finite element models were developed to estimate the stresses developed in the ice accreted on an overhead cable during galloping and aeolian vibration. In order to determine all displacement and load data that serve as input for these models, galloping and aeolian vibration of an iced cable were simulated.

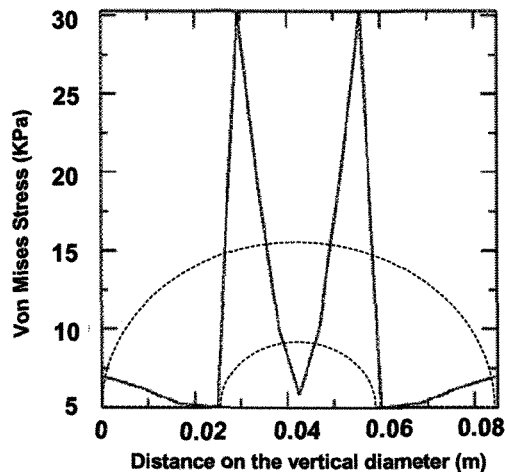


Figure 3.24. Stress distribution along the vertical diameter of cable-ice composition at 0.15s in an aeolian vibration.

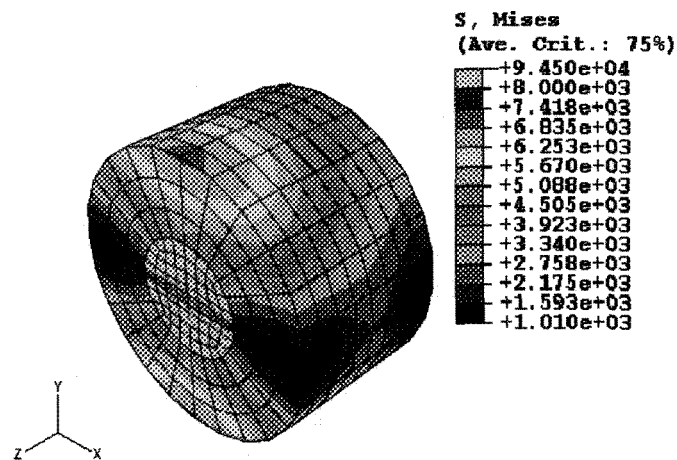


Figure 3.25. Stress distribution in cable and atmospheric ice at 0.15s in an aeolian vibration.

To model the galloping, the equations of cable motion as derived for galloping in former publications were applied for an iced cable, and solved by a MATLAB code to obtain time histories of cable motion, aerodynamic forces, additional horizontal tension acting in the cable during vibration and torque due to spring back. In the example considered in this study, a 10 cm long piece of iced cable in the middle of the span was under examination.

Thus, the input data were determined at the two end points of this piece. The finite element model was constructed using the ABAQUS commercial software and it computed the stresses in the atmospheric ice accreted on the cable. The model revealed that the highest stresses developed along the vertical diameter of the ice when the mid-point of the cable reached the highest and lowest positions in its trajectory. These stresses exceeded the bending strength of ice in the particular case of this study, thus, the model predicted ice failure. Using the method and the model developed in this research work, the level of stresses in atmospheric ice may be estimated for any other loading condition.

The other ABAQUS model was developed to simulate the stress distribution in atmospheric ice during aeolian vibration. In the example of this analysis, again a 10 cm long piece of iced cable in the middle of the span was studied and the input data were determined at the two end points of this piece. Under the conditions given for aeolian vibration, the maximum Von Mises stresses are 7700 Pa for the elements in the external layer, and 5800 Pa for the elements in the internal layer. These values are significantly less than the bending strength of atmospheric ice. According to this model, no ice shedding occurs under the selected conditions of the atmospheric ice and the cable.

## **CHAPTER 4**

### **ICE ACCUMULATION CONDITIONS AND GRAIN SIZE**

#### **OBSERVATION**

##### **4.1 Introduction**

The mechanical properties of atmospheric ice are dependent on temperature, load rate, type and structure of atmospheric ice. Ice type and structure can be influenced by the meteorological conditions prevalent during its formation, such as wind velocity, liquid water content of air, mean volume droplet diameter and temperature. Therefore, one of the most important aspects in this investigation is selecting the experimental conditions for the ice accumulation and ice tests.

The criteria for selecting the ice accumulation and experimental conditions for measuring the mechanical properties of atmospheric ice as well as the results of grain size observation will be given in this chapter.

##### **4.2 Ice accumulation conditions**

The ice accumulation conditions for this study were created in the CIGELE (Industrial Chair on Atmospheric Icing of Power Network Equipment at Université du Québec à Chicoutimi) atmospheric icing research wind tunnel. The characteristics of this tunnel and the ice accumulation conditions are described below.

###### **4.2.1 Ice accumulation equipment**

The CIGELE atmospheric icing research wind tunnel is a closed-loop (air-recirculated) low-speed icing wind tunnel. Icing conditions identical to those encountered during various icing processes in nature, can be simulated in this tunnel.

The experimental modeling of the icing conditions was carried out using the three main systems inside the wind tunnel: the fan; the refrigeration unit, and the nozzle spray-bar systems.

Using dedicated software, it was possible to set air speed from 0 to 29 m/s. The desired ambient temperature in the icing wind tunnel could be set by a remote control system with  $\pm 0.5^{\circ}\text{C}$  accuracy.

The technique used in this wind tunnel to simulate atmospheric icing processes is to inject warm water into a cold air stream through nozzles located at the trailing edge of the horizontal spray bar, designed in the shape of a NACA0012 airfoil. Water and air are supplied to the three nozzles on the spray-bar through the three independent water and air supply lines. Atmospheric ice was accumulated on an aluminum cylinder. The distance between the spray nozzles and the cylinder was long enough for thermodynamic equilibrium to be reached between the air flow at its highest velocity and the largest droplets. The water supply was linked to a reservoir of regular domestic tap water, while the air supply was provided by a compressor using ambient air. The droplet size distribution of the aerosol cloud depends on the combination of air and water pressures and, within a certain temperature range, on the flow rate of water in the supply line. T-type copper / constantan thermocouples were installed in the two covers in the ceiling of the test section, at the entrance, midpoint and exit points, providing data on variations in air

temperature at these three locations throughout each experiment. The absolute and relative humidity were measured using a humidity probe placed inside a plastic/aluminum fairing specially designed to resist freezing. The aluminum cylinder (diameter 78 mm and length 590 mm) for the ice accumulation was placed in the middle of the test section of the wind tunnel and rotated at a constant speed of 2 rev/min. Before ice accumulation, the cylinder was cleaned with alcohol and set in place for two hours while the system was cooling down. After ice accumulation was finished, the cylinder was removed from the test section and the accumulated ice was cut with a warm aluminum blade to avoid any mechanical stress that might cause cracks. The resulting ice slices were then carefully prepared using a microtome to avoid crack formation. In preparation of ice samples and thin sections, the microtome was adjusted carefully to prevent any crack formation. Any sample with broken edges was discarded. The average interval between ice accumulation and compression tests was 5 hours. Figure 4.1 shows the position of specimens extracted from the accumulated ice on the cylinder and load direction in mechanical tests.

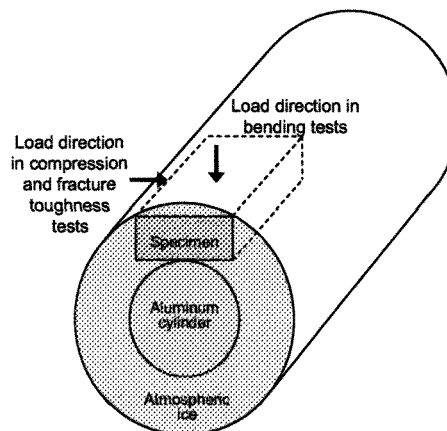


**Figure 4.1.** Schematic illustrating specimen position in accumulated atmospheric ice and loading direction during test.

Specimen dimensions, as mentioned in ASTM E111-97, were determined by averaging three measurements of the three axes of the samples.

In preparing the specimens, the guidelines recommended by the IAHR working group on test methods (Schwarz *et al.*, 1981) were used.

#### **4.2.2 Air speed**

Air speeds that typically lead to natural glaze ice formation range from ultra low to medium speeds. Therefore, the following three values of air speed were considered: 2 m/s, 5 m/s and 10 m/s (Mousavi, 2003). However, at air speeds lower than 5 m/s, the influence of gravity on the spatial distribution of liquid water content (LWC) and droplet size fields can affect the ice accretion process. Thus, in order to make the experimental work more manageable and to obtain a more uniform ice layer, the air velocity value of 10 m/s was chosen.

#### **4.2.3 Air temperature**

The following three ambient temperature values were selected for the accumulation of atmospheric ice:  $-6^{\circ}\text{C}$ ,  $-10^{\circ}\text{C}$  and  $-20^{\circ}\text{C}$  as representative of warm, medium and cold icing conditions.

As mentioned before, the usual air temperature during winter is  $-10^{\circ}\text{C}$  and most of the tests for measurement of mechanical properties of atmospheric ice (chapter 5) were carried out at this temperature. In this text, when we mention a 'type' of atmospheric ice, we are referring to the ice that was obtained at one of the accumulation temperatures.

#### **4.2.4 Air pressure and air humidity**

The air pressure during ice accumulation was 1 NACA standard atmosphere at sea level ( $P_{st} = 101325$  Pa) and the relative humidity ranged from 0.81% to 0.92%.

#### 4.2.5 Liquid Water Content (LWC)

The liquid water content (LWC) denotes the mass of water per unit volume of air and is a function of the difference between the air and water line pressures, air speed and, within a certain range of the temperature, the flow rate of water in the supply line. The LWC for the wind tunnel of CIGELE as a function of these parameters was calibrated by Karev *et al.* (in press). The LWC for icing conditions in nature varies between 0.5 and 10  $g/m^3$  and the CIGELE wind tunnel can cover this range. During the calibration, the LWC at the test section of the wind tunnel was measured using the accepted standard technique known as the rotating icing cylinder method (Stallabrass, 1978). In the first stage, we tried to obtain atmospheric ice using a LWC of about 1  $gr/m^3$ , but the resulting ice was not solid and was characterized by a lot of holes and cavities. Preparing samples and measuring mechanical properties of ice in this condition would be a challenge and was not done.

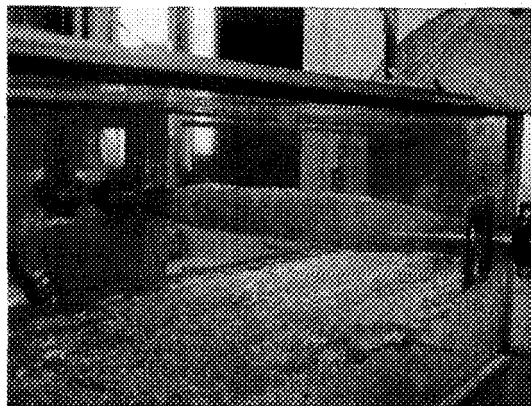


Figure 4.2. Ice accumulation on aluminum

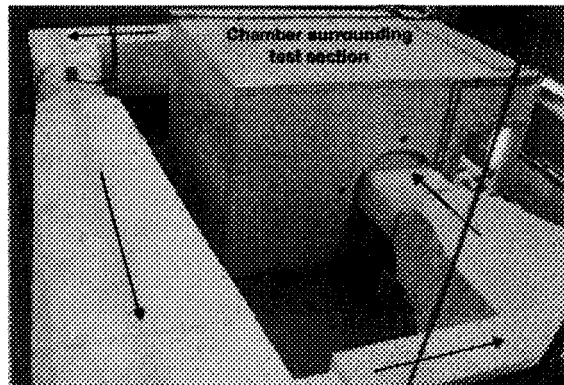


Figure 4.3. Wind tunnel at CIGELE.

Therefore it was necessary to increase LWC to at least  $2.5 \text{ gr/m}^3$  in order to obtain solid and uniform atmospheric ice without large cavities. The corresponding air pressure and water pressure were 15 psi (103.42 kPa) and 55 psi (379.21 kPa), respectively. This adjustment gives a mean droplet diameter of  $80 \mu\text{m}$  approximately. Figure 4.2 illustrates the ice accumulation on an aluminum cylinder in the test section of the wind tunnel. Figure 4.3 shows the CIGELE wind tunnel.

The three types of atmospheric ice obtained from the above-mentioned conditions have distinctive differences in appearance (Figure 4.4). The ice accumulated at temperatures closer to  $0^\circ\text{C}$  is transparent and changes to opaque when the accumulation temperature decreases. This is in agreement with the observation reported by Laforte *et al.* (1983) and Eskandarian (2005).

#### 4.3 Grain structure and air bubble inclusions

Detailed microstructure and air bubble observations for atmospheric ice accumulated at temperatures ranging from  $-2^\circ\text{C}$  to  $-15^\circ\text{C}$ , air velocity from 4 m/s to 20 m/s, and LWC from  $0.4 \text{ gr/m}^3$  to  $0.8 \text{ gr/m}^3$  were reported by Laforte and Phan (1983). Also, Eskandarian (2005)

studied the grain structure of atmospheric ice accumulated at air speeds ranging from 5 m/s to 10 m/s, air temperature from  $-10^{\circ}\text{C}$  to  $-20^{\circ}\text{C}$  and LWC from  $0.5 \text{ gr/m}^3$  to  $1 \text{ gr/m}^3$ . The atmospheric ice studied in the present research is somewhat different from the ice of the two above-mentioned works. This is due to differences in the meteorological conditions during ice accumulation.

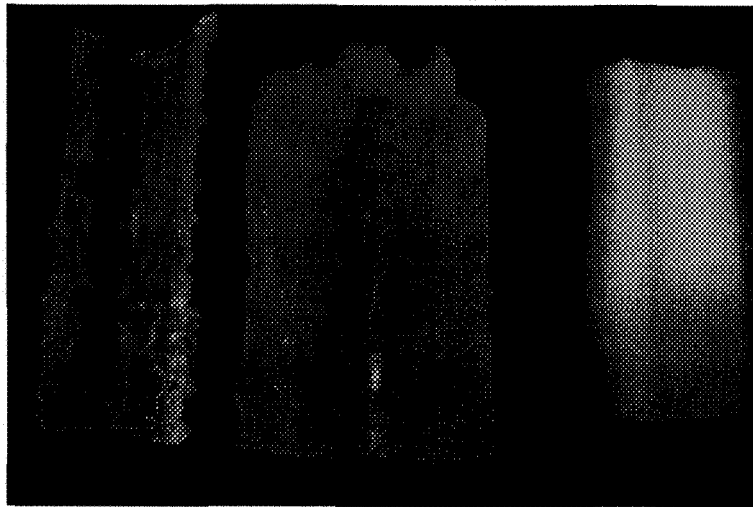


**Figure 4.4.** Three types of atmospheric ice.  
Left to right: accumulation temperature of  $-3^{\circ}\text{C}$ ,  $-10^{\circ}\text{C}$  and  $-20^{\circ}\text{C}$ .

As mentioned above, three types of atmospheric ice were grown and studied, distinguished by their accumulation temperature. For each type, thin sections were prepared and grain size, grain shape and air bubble content were investigated. A brief explanation of these observations is given below.

For thin sections of atmospheric ice accumulated at  $-6^{\circ}\text{C}$  (parallel to cylinder axis), the average grain size is approximately 1.5 mm, and varies from 0.5 to 3 mm ( Figure 4.5).

At temperatures above  $-10^{\circ}\text{C}$  air bubbles nucleate when the concentration of dissolved air in the liquid reaches a critical value at the growth front. Therefore, the air bubble

content of atmospheric ice depends on the growth conditions, including air temperature, droplet size, liquid water content and ice deposit temperature. The formation of voids at colder temperatures will be explained in the following paragraphs. Other researchers have observed that air bubble density in atmospheric ice decreases with ice deposit temperature (Laforte and Phan, 1983; Eskandarian, 2005). Figures 4.6 and 4.8 show similar behavior. It was observed that the average diameter of the bubbles in the ice accumulated at  $-6^{\circ}\text{C}$  is roughly 0.07 mm, with considerable variation in size. The porosity of ice is defined as the ratio of voids or bubble volume to the total volume of the ice sample. Ice porosity was approximately 2.9% at the accumulation temperature of  $-6^{\circ}\text{C}$ , based on the measured volume and mass of samples.

For atmospheric ice accumulated at  $-10^{\circ}\text{C}$ , the grain size is considerably smaller than that accumulated at  $-6^{\circ}\text{C}$ .



**Figure 4.5.** Thin section of ice accumulated at  $-6^{\circ}\text{C}$ . The section is the same orientation as the top surface of the specimen shown in Figure 4.1 where the loading direction is vertical in the image.

As apparent in Figure 4.7, the average grain size for ice obtained in  $-10^{\circ}\text{C}$  is less than 0.5 mm. From this fact, one may conclude that the grain size of atmospheric ice decreases with decreasing deposit temperature, which is in agreement with the observations of

Laforte and Phan (1983). As will be explained in the following sections, this grain size has an important effect on the mechanical properties of this type of atmospheric ice.

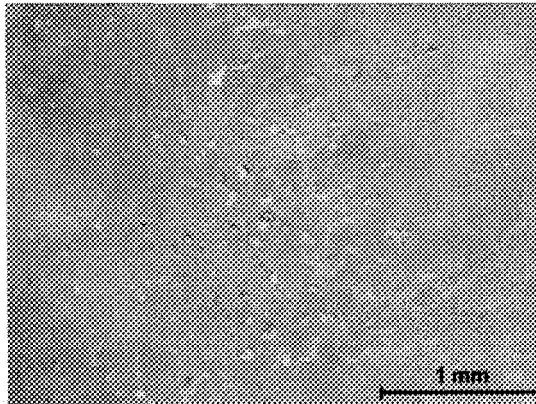


**Figure 4.6.** Thick section showing air bubbles in ice accumulated at  $-6^{\circ}\text{C}$ . The orientation is the same as in Figure 4.5.

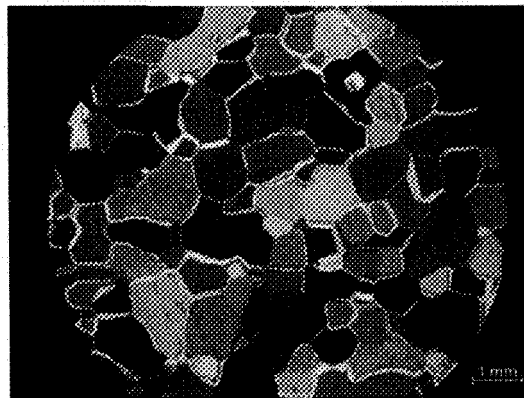


**Figure 4.7.** Thin section of atmospheric ice accumulated at  $-10^{\circ}\text{C}$ . The orientation is the same as in Figure 4.5.

The density of air bubbles for this type of ice is greater than that for ice accumulated at  $-6^{\circ}\text{C}$  (Figure 4.8). The average diameter of bubbles for this type of ice is roughly 0.1 mm, with considerable variation in size. According to the measurements of sample mass and volume, the porosity of the ice accumulated at  $-10^{\circ}\text{C}$  was approximately the same as the ice accumulated at  $-6^{\circ}\text{C}$ . The more cloudy appearance of the ice accumulated at  $-10^{\circ}\text{C}$ , however, indicated a greater number of bubbles per unit volume, which implies the average

diameter of the air bubbles in this type of atmospheric ice is less than that of ice accumulated at  $-6, ^\circ\text{C}$ .

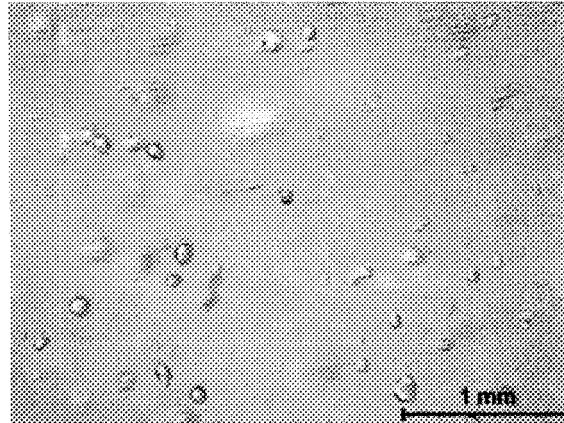


**Figure 4.8.** Thick section showing air bubbles in ice accumulated at  $-10^\circ\text{C}$ . The orientation is the same as in Figure 4.5.

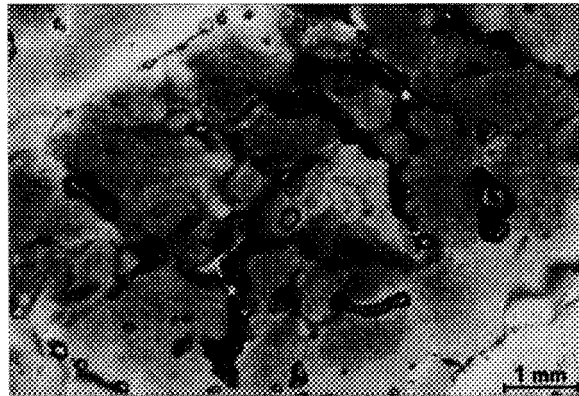


**Figure 4.9.** Thin section showing cavities and possibly small cracks in ice accumulated at  $-20^\circ\text{C}$ . The orientation is the same as in Figure 4.5.

The structure of the atmospheric ice accumulated at  $-20^\circ\text{C}$  is different from the other two types. In this case, a significant number of cavities and possibly cracks are visible. The presence of these cavities is ascribed to the high freezing rate of droplets, which eliminates the opportunity of filling the cavities.

In thin sections from this type of ice, the structure of the grains is more complex and the grain boundaries are more angular than the ice accumulated at  $-10^{\circ}\text{C}$  and the cavities are distinctive (Figures 4.9, 4.10, 4.11 and 4.12).

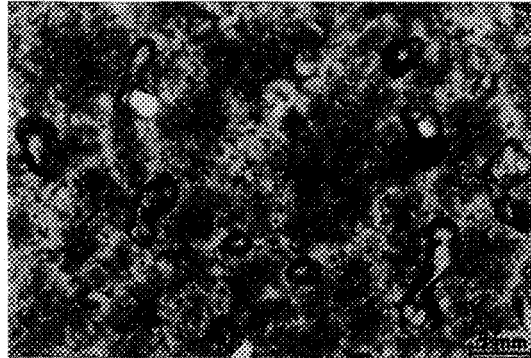


**Figure 4.10.** Thin section showing cavities and many small bubbles in ice accumulated at  $-20^{\circ}\text{C}$ . This section corresponds to ice that is closer to the aluminum cylinder than the ice in Figure 4.9.

The thin sections in Figures 4.10 and 4.12 correspond to ice that is closer to the aluminum cylinder than the ice in Figure 4.9 and 4.11, and therefore has more small grains and air bubbles giving some areas a dark cloudy appearance (Figure 4.10). The thin section in Figure 4.11 has an average grain size less than 0.4 mm. The polarized filters were oriented to highlight the grain structure in Figures 4.11 and 4.12 more so than Figures 4.9 and 4.10, where the intention was to highlight cavities. The thin section of this type of atmospheric ice that is parallel to the cylinder axis shows that the grains near the aluminum cylinder are very fine, which can be attributed to the rapid heat transfer between the impinging droplets and the aluminum cylinder leading to the formation of the primary layers of the ice (Fig 4.12).

The porosity of this type of atmospheric ice was found to be 8.5%. The higher value of porosity is due to the significant amount of cavities and voids.

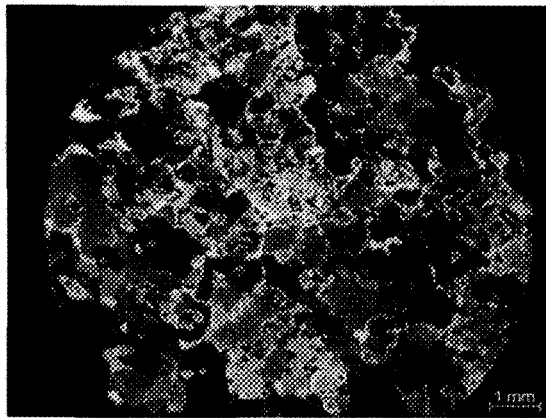


**Figure 4.11.** Thin section showing grain structure in ice accumulated at  $-20^{\circ}\text{C}$ . The orientation is the same as in Figure 4.5.

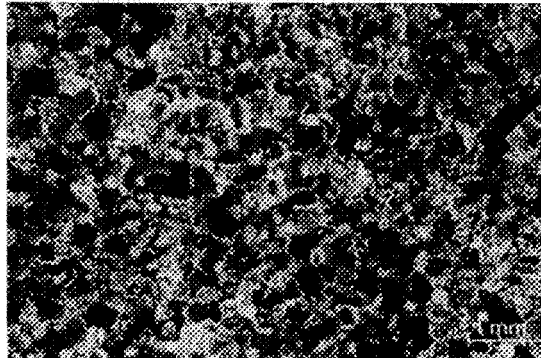


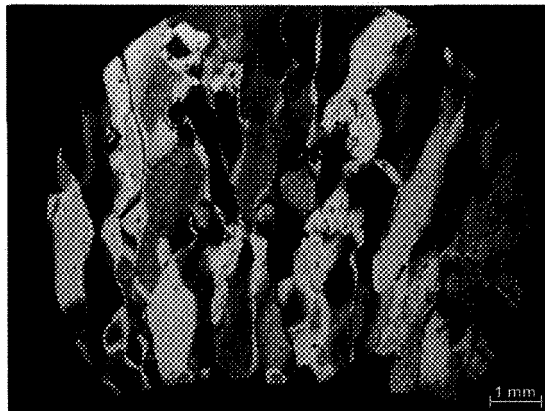
**Figure 4.12.** Thin section showing grain structure in ice accumulated at  $-20^{\circ}\text{C}$  closer to the aluminum cylinder than the thin section in Figure 4.11. The orientation is the same as in Figure 4.5.

At thicknesses greater than about 2 mm in the ice accumulated at  $-10^{\circ}\text{C}$ , the grains are elongated perpendicular to the cylinder axis. Figure 4.13 shows the grains near the cylinder surface. This finding is in agreement with Eskandarian (2005).

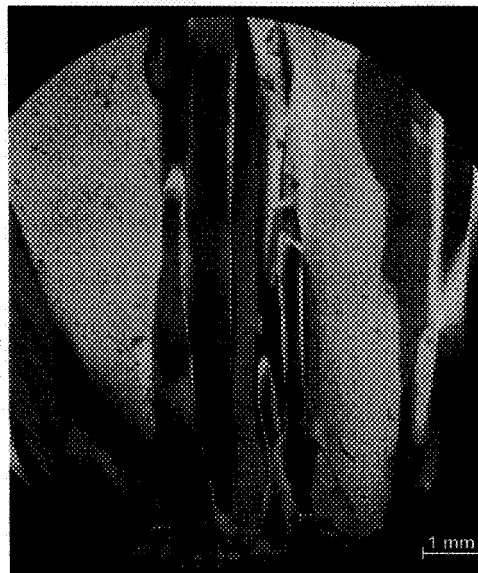
Thin sections perpendicular to the cylinder axis from the ice accumulated at  $-6^{\circ}\text{C}$  (Figure 4.14) show similar grain structure, but in this case the ice grows more slowly, whereby the columnar grains are somewhat bigger.

Figure 4.15 shows the thin section perpendicular to cylinder axis prepared from atmospheric ice accumulated at  $-20^{\circ}\text{C}$ . As observed in this figure, the grain structure in this

ice is different from two other types owing to the very high freezing rate. In this thin section, the cavities are again visible and, due to the smallness of grains and the high freezing rate, the columnar structure is not nearly as apparent.



**Figure 4.13.** Thin section showing grains near the cylinder surface (bottom) in atmospheric ice accumulated at  $-10^{\circ}\text{C}$ . The orientation of the thin section corresponds to the orientation of the end face of the specimen shown in Figure 4.1.



**Figure 4.14.** Thin section showing grains near the cylinder surface (bottom) in atmospheric ice accumulated at  $-6^{\circ}\text{C}$ . The orientation of the thin section corresponds to the orientation of the end face of the specimen shown in Figure 4.1.

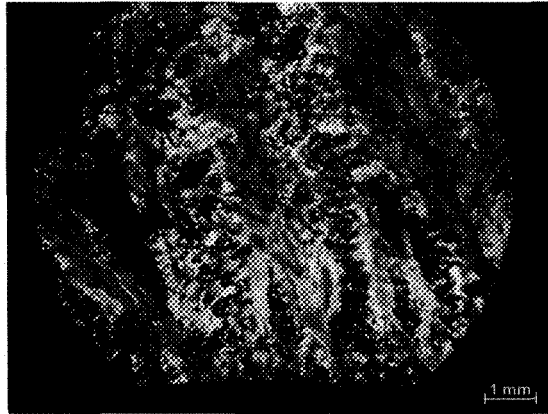


**Figure 4.15.** Thin section showing grains near the cylinder surface (bottom) in atmospheric ice accumulated at  $-20^{\circ}\text{C}$ . The orientation of the thin section corresponds to the orientation of the end face of the specimen shown in Figure 4.1.

#### 4.4 Effect of electric field on atmospheric ice

In addition to the ice accumulation conditions explained in section 4.2, the physical appearance of ice and its characteristics are related to the electric field strength at the surface of the conductors and to the polarity of applied voltage (Farzaneh, 2000; Farzaneh and Laforte, 1994; Teisseyre and Farzaneh, 1990).

Farzaneh and Laforte (1994) used a soft aluminum cylinder, 3.15 cm in diameter, placed along the axis of a cylindrical mesh cage, 1 m in diameter, in a cold room at a temperature of  $-10^{\circ}\text{C}$ , to study the effect of an electric field on accreted ice. The volume-median diameter of supercooled droplets was approximately 40  $\mu\text{m}$ , and the intensity of ice accretion for these experiments approximately  $2.1 \text{ g/m}^2\text{s}$ , with no electric field applied. They found that in the absence of an electric field, the type of ice deposited is hard rime with small protuberances on its surface (Figure 4.16-a). In the presence of an electric field, these protuberances grow like trees with thin lateral feathery branches (Figures 4.16-b-d).

When the electric field is positive (Figure 4.16-c), ice trees and side branches appear to be more numerous and thinner than those grown in an AC field (Figure 4.16-b). When the voltage is negative (Figure 4.16-d), the trunks of the ice feathers are even thinner than those observed under AC and DC+ voltage.

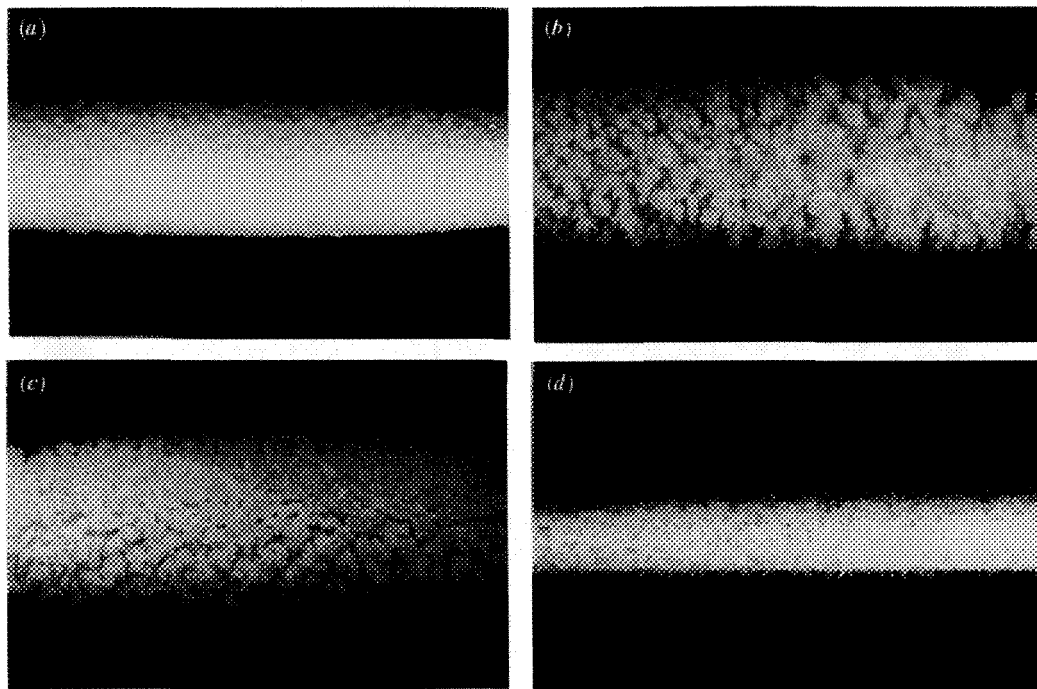


**Figure 4.16 .** Appearance of ice accretions on an aluminum cylinder with different electric fields (Farzaneh, 2000).

Farzaneh and Laforte (1994) also studied the effect of an electric field on the mass accumulated on the aluminum cylinder. They found that the weight of accreted ice first increases with an electric field strength up to  $10 \text{ kV cm}^{-1}$ , then sharply decreases (Figure 4.17). In the case of a negative electric field above  $15 \text{ kV cm}^{-1}$ , the amount of ice accreted is almost negligible. Under AC and DC+, the decrease in the weight of ice accretion with the increase in electric field strength is much smaller than that measured under DC-.

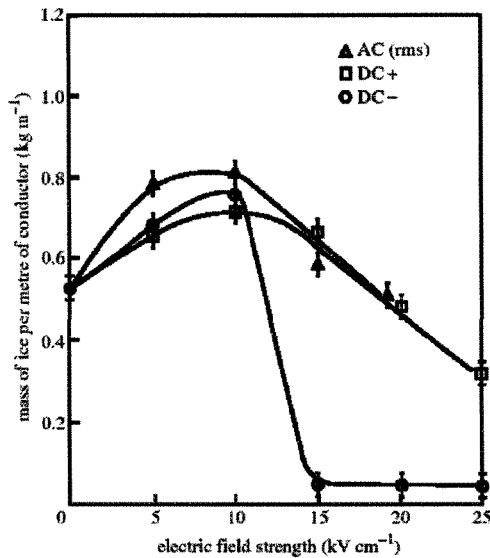


Figure 4.17. Weight of ice deposited per meter of conductor under energized conditions (Farzaneh, 2000).

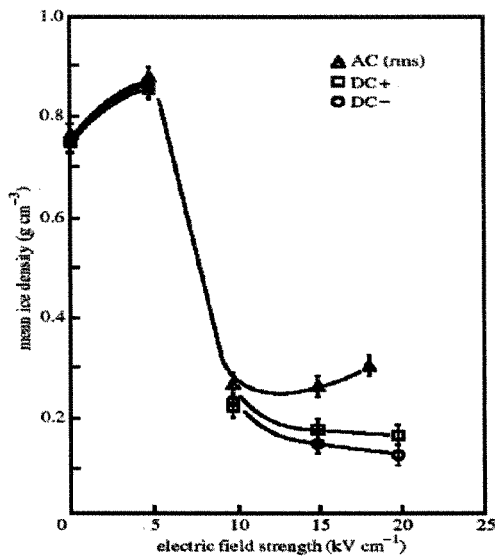


Figure 4.18. Mean density of ice deposits under energized conditions (Farzaneh, 2000).

Variations in the density of ice accumulated on the aluminum cylinder was also investigated by Farzaneh and Laforte (1994). They showed that the ice density first rises

under energized conditions up to  $5 \text{ kV cm}^{-1}$ , then decreases sharply as the electric field strength increases (Figure 4.18).

Farzaneh *et al.* (1996, 1997) studied the effects of an electric field on the structural parameters of ice grown under energized conditions. The results of their experiments revealed that lattice parameters  $a$  and  $c$  show values approximately 0.08% higher for ice grown under an electric field strength of  $-15 \text{ kV cm}$  when compared with the values obtained under non-energized conditions. With an electric field of  $+15 \text{ kV cm}^{-1}$ , parameters  $a$  and  $c$  show a change of the same magnitude, but of the opposite sign. Changes to the relative position of oxygen and deuterium atoms were less significant when the ice was grown under the influence of an electric field.

#### **4.5 Conclusion**

Using a rotating cylinder in the CIGELE atmospheric icing wind tunnel, ice was accumulated at a LWC of  $2.5 \text{ g/m}^3$ , a wind speed of  $10 \text{ m/s}$  and various accumulation temperatures. The atmospheric ice was accumulated at three different temperatures:  $-6^\circ\text{C}$ ,  $-10^\circ\text{C}$  and  $-20^\circ\text{C}$ . Thin sections of these three types of atmospheric ice showed that grain size decreases with decreasing accumulation temperatures. The average grain size of atmospheric ice accumulated at  $-6^\circ\text{C}$  is approximately  $1.5 \text{ mm}$ , and varies from  $0.5$  to  $3 \text{ mm}$ . The average diameter of the bubbles in this ice is roughly  $0.07 \text{ mm}$ , with considerable variation in size, and the ice porosity was approximately  $2.9\%$ . The average grain size for ice obtained in  $-10^\circ\text{C}$  is less than  $0.5 \text{ mm}$ . The average diameter of bubbles for this type of ice is roughly  $0.1 \text{ mm}$ , with considerable variation in size. The porosity of this type of atmospheric ice was found to be approximately the same as the ice accumulated at  $-6^\circ\text{C}$ . In

atmospheric ice accumulated at  $-20^{\circ}\text{C}$ , a significant number of cavities and possibly cracks are visible. The average grain size in this ice is less than 0.4 mm. The porosity of this type of atmospheric ice was found to be 8.5% and this higher value of porosity is due to the significant amount of cavities and voids. At thicknesses greater than about 2 mm in the ice accumulated at  $-10^{\circ}\text{C}$  and  $-6^{\circ}\text{C}$ , the grains are elongated perpendicularly to the cylinder axis.

The investigations on the effects of a high-voltage electric field on the atmospheric ice confirm that the presence of an electric field affects the structure, density and amount of ice accreted on conductors. In general, and under certain conditions, the amount and density of ice deposits decrease with an increase in the electric field at the surface of the high-voltage conductors. This decrease in amount and density is more pronounced under negative voltage than under positive and alternating voltage. The type of ice deposited on an aluminum cylinder in the absence of an electric field is hard rime with small protuberances on its surface. These protuberances grow like trees with thin lateral feathery branches when an electric field is applied on the aluminum cylinder. The effect of a high-voltage electric field on the mechanical properties of atmospheric ice should be investigated in future studies and its results will be useful for developing models of ice behaviour.

## CHAPTER 5

# THE MECHANICAL PROPERTIES OF ATMOSPHERIC ICE

### 5.1 Introduction

Despite the longstanding problem of atmospheric icing on network equipment, the mechanical properties and behavior of this type of ice under various loading conditions are still unclear. In this research work, more than 350 tests were carried out to measure the mechanical properties of atmospheric ice, including compressive strength, bending strength, effective modulus, fracture toughness and Young's modulus. These are some properties of atmospheric ice that are required for modeling ice behaviour. To measure the mechanical properties, the ice was accumulated in the closed-loop wind tunnel of CIGELE at three different temperatures (-6, -10 and -20 °C) and with a liquid water content value of 2.5 gr/ m<sup>3</sup>. Each type of ice was tested at the same temperature at which it had been accumulated. The usual air temperature during winter is -10°C. However, to study the temperature dependence of the mechanical behavior of the ice, some experiments were done at -3°C and -20°C, which is typical of Quebec winter. As mentioned in the previous chapter, thin sections of the three types of atmospheric ice reveal that the average grain size for accumulated ice is 1.5 mm, 0.5mm and 0.4 mm, for accumulation temperatures of -6, -10 and -20°C, respectively.

Unlike the other types of ice (lake, river, sea ice, etc.), very few studies on the mechanical properties of atmospheric ice have been reported. Perhaps the most important

research on the mechanical properties of atmospheric ice is in Druetz *et al.* (1986), where ice was accumulated at various air temperatures and air speeds, and was tested at the same temperature at which it had been accumulated. The liquid water content of the air (LWC) was set at 0.4 and 0.8 g/m<sup>3</sup>. The droplet diameter for these two values of LWC was set at 20 and 40  $\mu\text{m}$ , respectively. Also, two strain rates were used for strength tests and several wind velocities for ice accumulation. Druetz *et al.* (1989) also measured the tensile strength of atmospheric ice accumulated at temperatures ranging from -3°C to -20°C, where the liquid water content was set at 0.8 g/m<sup>3</sup> and 1.2 g/m<sup>3</sup> and the droplet diameter for these two values of LWC was set 40  $\mu\text{m}$ .

For other types of ice, however, particularly fresh water ice, there are a great number of published studies (e.g. Hawkes and Mellor, 1972; Mellor and Cole, 1981; Jones, 1982; Schulson and Canon, 1984; Schulson, 1990). These results were used for comparison with the results of the present study on atmospheric ice. In this work, a wide range of strain rates has been used and a considerable number of experiments has been performed. To yield statistically reliable values for the compressive strength of atmospheric ice, tests at each set of parameters have been repeated at least five times.

## **5.2 Compressive strength of atmospheric ice**

In chapter 2, ice constitutive behavior, the dependency of the ice strength on the strain rate was explained. The three domains of deformation in stress-strain rate graphs (ductile, transitional and brittle regimes) were introduced. For compression, at strain rates less than  $10^{-4}\text{s}^{-1}$ , ice shows ductile behavior, the transition occurs within a narrow range of strain rate

(between  $10^{-4}$  and  $10^{-2}\text{s}^{-1}$ ), and at higher strain rates, the brittle behavior dominates and strength is essentially independent of strain rate. The ductile regime in tension is associated with strain rates less than  $10^{-7}\text{s}^{-1}$  and the transition regime lies within a lower strain rate range (between  $10^{-7}$  and  $10^{-6}\text{s}^{-1}$ ).

The phenomenon of ice shedding usually occurs in the transitional and brittle domains. Furthermore, strain rate in natural ice shedding is not more than  $10^{-2}\text{s}^{-1}$ . Hence, in this study the loads for compression tests were applied at strain rates ranging between  $3 \times 10^{-5}$  and  $3 \times 10^{-2}\text{s}^{-1}$ .

Each sample was uniaxially loaded and the axial strain was measured by an extensometer. The dimensions of the specimens in these tests were 20-mm thick, 45-mm long and 40-mm high. Load was applied onto the specimens in the direction shown in Figure 5.1. The specimens were kept at the test temperature for two hours before the test.

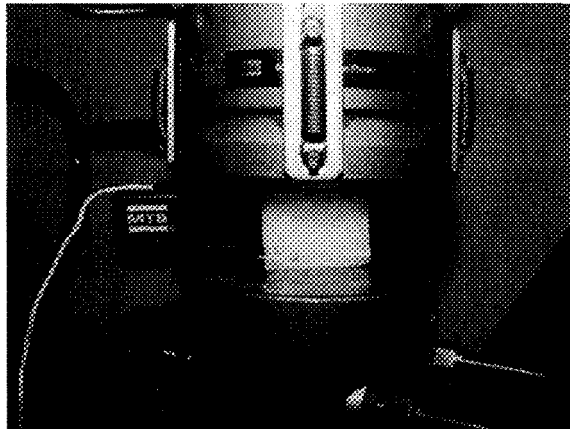


**Figure 5.1.** Test configuration for measuring the compressive strength of atmospheric ice.

### **5.2.1 Test results and discussion**

Table 5.1 shows the results of uniaxial compression tests of the atmospheric ice accumulated at  $-10^{\circ}\text{C}$  and tested at  $-3^{\circ}\text{C}$ ,  $-10^{\circ}\text{C}$  and  $-20^{\circ}\text{C}$ . Figures 4.2, 4.3 and 4.4 show the variation of the compressive strength of atmospheric ice at these three temperatures.

Row	Strain Rate (1/s)	$T_a = -10^{\circ}\text{C}, T_t = -3^{\circ}\text{C}$			$T_a = -10^{\circ}\text{C}, T_t = -10^{\circ}\text{C}$			$T_a = -10^{\circ}\text{C}, T_t = -20^{\circ}\text{C}$		
		Compressive Strength (MPa)	Ave. Of Similar Conditions (MPa)	ST. Dev (MPa)	Compressive Strength (MPa)	Ave. Of Similar Conditions (MPa)	ST. Dev (MPa)	Compressive Strength (MPa)	Ave. Of Similar Conditions (MPa)	ST. Dev (MPa)
1	3.00E-05	2.810	2.408	0.338	2.725	2.687	0.311	5.480	3.721	1.094
2	3.00E-05	2.305			2.681			4.140		
3	3.00E-05	1.958			2.640			2.888		
4	3.00E-05	2.622			2.209			2.978		
5	3.00E-05	2.642			3.083			3.138		
6	1.00E-04	3.513	2.951	0.463	3.940	3.535	0.517	6.223	4.260	1.270
7	1.00E-04	3.315			4.178			4.800		
8	1.00E-04	2.511			3.291			3.788		
9	1.00E-04	2.929			2.901			3.188		
10	1.00E-04	2.408			3.392			3.330		
11	3.00E-04	3.982	3.480	0.383	5.667	4.580	0.849	6.464	5.593	0.782
12	3.00E-04	3.767			5.112			5.516		
13	3.00E-04	3.387			4.519			6.149		
14	3.00E-04	3.146			3.603			4.438		
15	3.00E-04	3.118			3.901			5.399		
16	1.00E-03	5.832	4.558	0.900	7.297	5.478	1.443	3.806	6.396	3.130
17	1.00E-03	4.879			7.210			8.715		
18	1.00E-03	5.273			4.900			7.412		
19	1.00E-03	3.632			3.868			2.432		
20	1.00E-03	3.872			5.145			9.615		
21	1.00E-03	3.863			4.448					
22	3.00E-03	4.172	3.802	1.032	7.423	5.017	1.565	6.920	6.322	2.184
23	3.00E-03	3.092			5.046			4.900		
24	3.00E-03	3.935			5.100			7.320		
25	3.00E-03	2.064			3.112			3.433		
26	3.00E-03	4.726			4.405			9.035		
27	1.00E-02	4.464	3.290	0.880	2.290	3.388	0.935	4.065	4.398	1.511
28	1.00E-02	3.262			4.428			6.284		
29	1.00E-02	2.125			2.627			3.522		
30	1.00E-02	2.872			4.184			2.554		
31	1.00E-02	3.727			3.418			5.545		
32	3.00E-02	2.936	2.935	0.402	3.357	3.116	0.824	5.015	4.250	2.278
33	3.00E-02	2.862			3.524			1.680		
34	3.00E-02	2.307			2.908			3.384		
35	3.00E-02	3.268			1.811			3.441		
36	3.00E-02	3.307			3.879			7.733		

**Table 5.1.** Results of compression tests of atmospheric ice accumulated at  $-10^{\circ}\text{C}$  and tested at various temperatures.

As previously mentioned, at low strain rates, ice behaves as a ductile material. In these figures, considerable scatter is evident in both the ductile and brittle regions. However, the greatest scatter is in the transient region (strain rates between  $10^{-4}$  and  $10^{-2}$ ), where both

types of behavior and associated scatter are occurring. In general, the results of these tests are in strong agreement with the results of other investigators in many aspects.

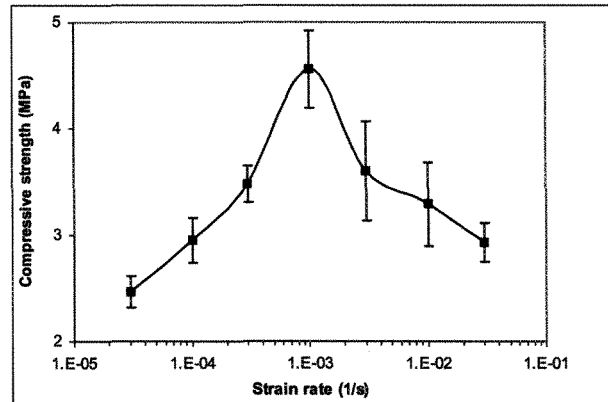


**Figure 5.2.** Compressive strength of atmospheric ice accumulated at  $-10^{\circ}\text{C}$  and tested at  $-3^{\circ}\text{C}$ . The error bars in this figure, and the ones that follow, correspond to the standard error in the results for the tests conducted at each set of parameters.

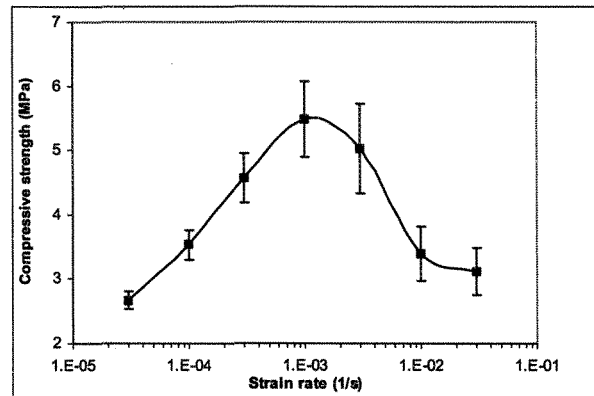


**Figure 5.3.** Compressive strength of atmospheric ice accumulated and tested at  $-10^{\circ}\text{C}$ .

As reported by many researchers (e.g. Schulson, 1990) and made clear in Figure 5.5, the compressive strength of atmospheric ice increases with decreasing test temperature.

As is the case for polycrystalline ice grown in laboratory, the strength of this ice also increases and then decreases with increasing strain rate.

Table 5.2 shows the results of uniaxial compression tests on atmospheric ice accumulated at  $-6^{\circ}\text{C}$  and  $-20^{\circ}\text{C}$  and tested at the same temperature. Figures 5.6 and 5.7 show the values of the compressive strength of atmospheric ice accumulated at  $-6^{\circ}\text{C}$ , and  $-20^{\circ}\text{C}$ .

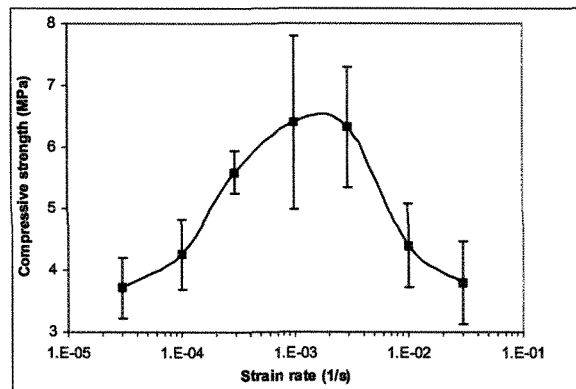


**Figure 5.4.** Compressive strength of atmospheric ice accumulated at  $-10^{\circ}\text{C}$  and tested at  $-20^{\circ}\text{C}$ .

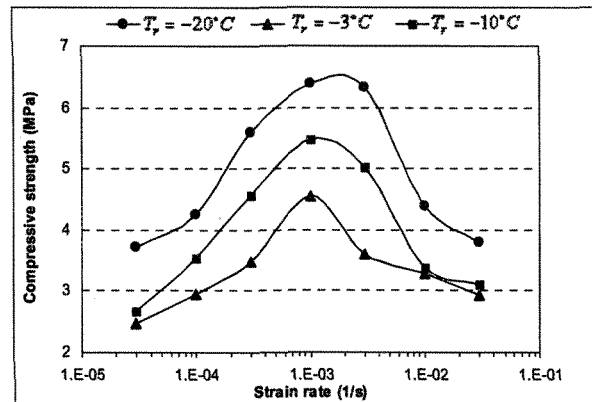


**Figure 5.5.** Compressive strength of atmospheric ice accumulated at  $-10^{\circ}\text{C}$  and tested at various temperatures.

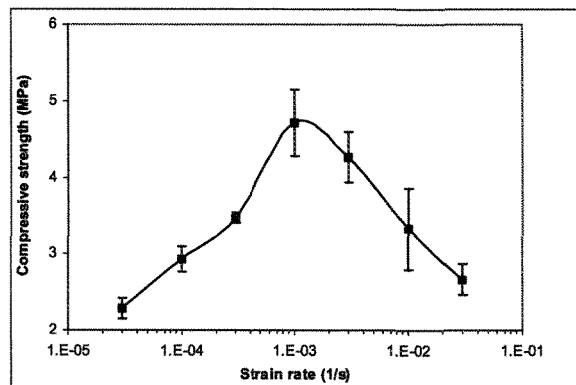
As mentioned by Wu and Niu (1994) and demonstrated by Schulson (1990), the compressive strength of ice increases with decreasing grain size. In these tests, as previously mentioned and shown by Laforte and Phan (1983), grain size decreases as accumulation temperature decreases. In Figure 5.8, it is observed that the compressive

strength of ice increases at strain rates lower than  $10^{-3} \text{ s}^{-1}$  when grain size decreases for the three types of atmospheric ice. At higher strain rates, however, the compressive strength of ice accumulated at  $-20^{\circ}\text{C}$  is less than that for ice accumulated at  $-10^{\circ}\text{C}$ . We conclude from this that the strength of the ice is more sensitive to the presence of cavities and cracks at the higher strain rates than at the lower ones, where the grain size is the dominating factor.

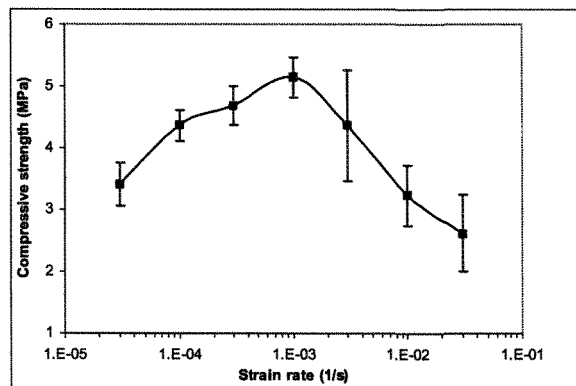
Row	Strain Rate (1/s)	$T_a = -6^{\circ}\text{C}, T_c = -6^{\circ}\text{C}$			$T_a = -20^{\circ}\text{C}, T_c = -20^{\circ}\text{C}$		
		Compressive Strength (MPa)	Ave. Of Similar Conditions (MPa)	ST. Dev. (MPa)	Compressive Strength (MPa)	Ave. Of Similar Conditions (MPa)	ST. Dev. (MPa)
1	3.00E-05	2.644	2.283	0.306	4.236	3.406	0.783
2	3.00E-05	2.559			3.588		
3	3.00E-05	2.180			3.702		
4	3.00E-05	1.925			2.126		
5	3.00E-05	2.104			3.375		
6	1.00E-04	3.419	2.932	0.373	4.972	4.369	0.559
7	1.00E-04	2.936			4.942		
8	1.00E-04	3.029			4.233		
9	1.00E-04	2.375			3.847		
10	1.00E-04	2.901			3.552		
11	3.00E-04	3.544	3.475	0.157	5.065	4.676	0.709
12	3.00E-04	3.272			4.861		
13	3.00E-04	3.664			3.649		
14	3.00E-04	3.360			4.064		
15	3.00E-04	3.536			5.563		
16	1.00E-03	6.330	4.714	0.972	5.112	5.145	0.726
17	1.00E-03	3.911			5.664		
18	1.00E-03	4.205			4.713		
19	1.00E-03	4.894			4.211		
20	1.00E-03	4.229			6.027		
21	3.00E-03	5.357	4.262	0.816	7.271	4.366	2.005
22	3.00E-03	3.470			5.536		
23	3.00E-03	3.832			3.138		
24	3.00E-03	4.327			3.223		
25	3.00E-03	5.234			2.572		
26	3.00E-03	4.347			---		
27	3.00E-03	3.260			---		
28	1.00E-02	2.887	3.529	1.183	3.441	3.236	1.101
29	1.00E-02	2.325			4.627		
30	1.00E-02	2.652			3.856		
31	1.00E-02	3.476			1.982		
32	1.00E-02	5.307			2.277		
33	3.00E-02	3.120	2.553	0.457	2.499	2.615	1.385
34	3.00E-02	3.096			1.178		
35	3.00E-02	2.034			4.250		
36	3.00E-02	2.461			1.360		
37	3.00E-02	2.604			3.768		

Table 5.2. Results of compression tests of atmospheric ice accumulated at various temperatures and tested at the same temperature.

Figure 5.9 shows the comparison between the present values of the compressive strength of atmospheric ice and those of other investigators for freshwater ice. For all freshwater ice tests, the average grain size has been reported as approximately 1 mm and test temperature was  $-10^{\circ}\text{C}$ . These conditions are very close to those of the present study. The results of the only published report on the compressive strength of atmospheric ice, Druetz *et al.* (1986), are included in this figure.



**Figure 5.6.** Compressive strength of atmospheric ice accumulated at  $-6^{\circ}\text{C}$  and tested at  $-6^{\circ}\text{C}$ .



**Figure 5.7.** Compressive strength of atmospheric ice accumulated at  $-20^{\circ}\text{C}$  and tested at  $-20^{\circ}\text{C}$ .

It was shown that air bubbles or voids weaken materials in general (Hosford, 2005). In atmospheric ice, these bubbles can reduce the compressive strength of ice. This is one

reason for the differences between the results of this study and those of other researchers for fresh water ice.

Druez *et al.* (1986) measured the compressive strength of atmospheric ice with various LWC values at different accumulation temperatures. They used two different machines, one for applying a deformation speed of 0.76 mm/min (strain rate of  $10^{-3} \text{ s}^{-1}$ ) and the other for applying a deformation speed of 26 mm/min (strain rate of  $0.04 \text{ s}^{-1}$ ). They accumulated the atmospheric ice on an aluminum cylinder and applied the force to the specimens in the radial direction. In this investigation, the closest results to our own concerned the compressive strength of atmospheric ice accumulated at  $-10^{\circ}\text{C}$  with LWC of  $0.8 \text{ gr/m}^3$  and air velocity of 8 m/s. In spite of the difference between their atmospheric ice and our own, one of their data points (at approximate load rate of  $0.04 \text{ s}^{-1}$ ) is in very good agreement with our results. On the other hand, the data point at load rate  $0.001 \text{ s}^{-1}$  is the highest of any reported data. This difference can be attributed to the differences between liquid water content and air velocity during accumulation and the direction of load in the tests.

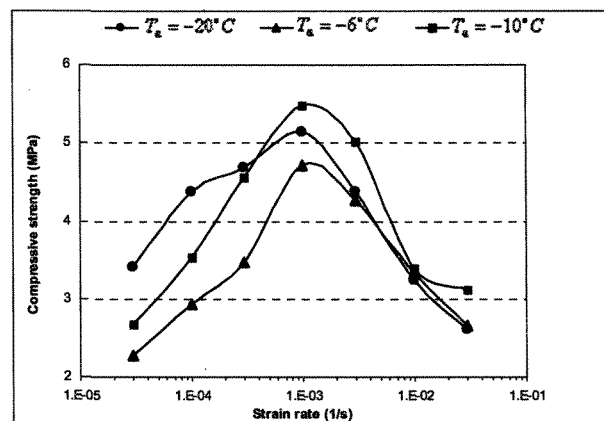


**Figure 5.8.** Compressive strength of atmospheric ice accumulated at various temperatures and tested at their accumulation temperature.

The other contributing causes of the discrepancies between the results of this study and the other investigators' are the size (e.g. Dempsey *et al.*,1999) and geometry of specimens. In this study, as mentioned previously, the specimen dimensions were 20 mm × 45 mm, with a height of 40 mm. The sample dimensions in the tests of Druetz *et al.* (1986) were 10 mm × 10mm × 10 mm, and in the research of Hawkes and Mellor (1972) the specimens were cylindrical with a 35.9-mm diameter and a 77-mm length. In the work of Jones (1982), the specimens were cylindrical with a 20-mm diameter and a 60-mm length.

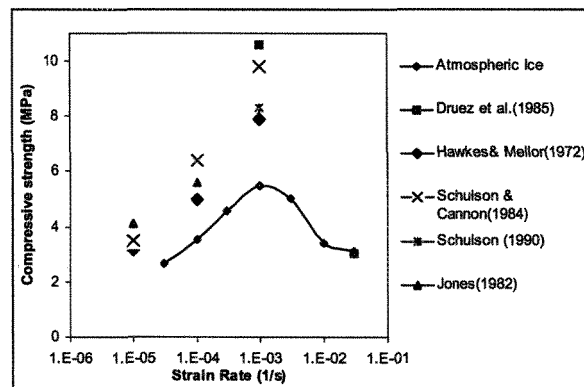


Figure 5.9. Comparison of strength data from the present study with results from other studies.

More experimental work would be required to find out which of the above-mentioned factors has the most influence.

In spite of the differences between the data shown by other researchers and the present data, the trend of increasing strength with a strain rate up to  $10^{-3} \text{ s}^{-1}$  is evident in all the data.

Owing to the complexity of atmospheric ice and the dependency of its structure, grain size, grain shape, air bubbles and cavities on the accumulation conditions and sample position in the accumulated ice, studying the effect of air bubble and grain size separately is not feasible.

### 5.3 Bending strength and effective modulus of atmospheric ice

In contrast to the few studies on atmospheric ice, the flexural strength of other types of ice has been studied by many investigators. For example, Timco and Frederking (1982) performed a series of cantilever beam tests on fresh water ice. They confined themselves to testing only S2 ice at a test temperature of  $-10^{\circ}\text{C}$ . Cantilever beam tests were conducted by those authors in the push-down mode, and the simply supported beams were tested isothermally at  $-10^{\circ}\text{C}$  in both the push-down and pull-up modes. As another example, Frederking and Svec (1985) studied the stress concentration relief at the root of cantilever beams. Their tests were conducted in the top-in-tension mode of fine-grained ice in an outdoor pool at temperatures ranging from  $-5^{\circ}\text{C}$  to  $-20^{\circ}\text{C}$ . Also Dempsey *et al.* (1989) studied the effects of specimen size on the flexural strength and effective modulus of columnar fresh water ice using four-point-bend tests in two sizes. The larger beam thickness and length in one size were almost 1.5 times greater than the corresponding dimensions of the smaller specimen. Considering the differences in the bending results, they concluded that the specimen size can overshadow the results of the flexural strength and effective modulus. Gow and Ueda (1988) performed some bending tests with both cantilever and simply-supported beams of fresh water ice sheets. Their tests within the temperature range from  $-1^{\circ}\text{C}$  to  $-19^{\circ}\text{C}$  revealed that macrocrystalline (S1) and columnar (S2) ice have different flexural characteristics. They ascribed these differences to variations in the size and orientation of the crystals in the ice as well as to the thermal condition of the beams. The results of the above mentioned works were used for comparison with the results of the present study on atmospheric ice.

We could find no report on the bending strength of atmospheric ice in the literature. The lack of comprehensive information about the strength and mechanical properties of atmospheric ice under various loading conditions led to the present study. In this study, the bending strength and effective modulus of atmospheric ice for various accumulation temperatures and strain rates are investigated.

### 5.3.1 Test conditions

Strain rate in a three-point beam test is defined in terms of the strain exerted at the bottom of the beam. According to beam-bending theory for three-point loading, the strain rate is given by

$$\dot{\epsilon} = 6h\delta / L_b^2 \quad (5.1)$$

where  $h$  is the beam height,  $\delta$  is the cross head speed and  $L_b$  is the beam length.

In order to study the effects of strain rate on the flexural strength and effective modulus of atmospheric ice, a wide range of strain rates,  $3 \times 10^{-5} \text{ s}^{-1}$  to  $2 \times 10^{-3} \text{ s}^{-1}$ , was selected and for each set of parameters at least five specimens were tested. According to the guidelines recommended by the IAHR working group on test methods (Schwarz *et al.*, 1981), loading times to failure on the order of 1 second yield satisfactory results. In the present study, this corresponds to the strain rate of  $2 \times 10^{-3} \text{ s}^{-1}$ .

The bending force was applied using a hydraulic actuator to the middle of the beam, normal to the axis, at various cross head speeds. The actuator includes an LVDT, which measures its displacement. The speed and direction of cross head movement is controlled by a servovalve. Another LVDT was positioned on the cross head to measure the deflection

of the top surface at the middle of the beam as force was applied. The variation of force and displacement as functions of time were recorded at 1000 samples per second for strain rates of more than  $3 \times 10^{-5} \text{ s}^{-1}$  and 500 samples per second at  $3 \times 10^{-5} \text{ s}^{-1}$ . The variation of force in the load cell was also monitored continuously and the maximum load during the test was recorded. This maximum load was always within  $\pm 1\%$  of the peak value in the digital record and was used in the calculations. According to Schwarz *et al.* (1981), for beams of fresh water ice (which has the closest structure to atmospheric ice) the ratio of beam width to ice crystal size must be  $\geq 10$  in order to eliminate the grain size effect. Since there were some limitations for specimen size (limit in maximum thickness of ice and maximum size that could be prepared by microtom), the following dimensions were chosen for our specimens: beam width ( $w$ ) 40 mm, beam thickness ( $h$ ) 20 mm and beam length ( $L_b$ ) 70 mm (Figure 5.10).

Tests in which fracture occurred at distances greater than 3 mm from the side of the transverse loading bar (greater than 4.3 % of the beam span in Figure 5.10) were excluded from the averaged values listed in Tables 5.3 to 5.8. Only 8 out of 129 tests had to be discarded for this reason.

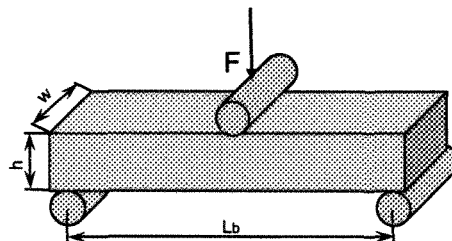
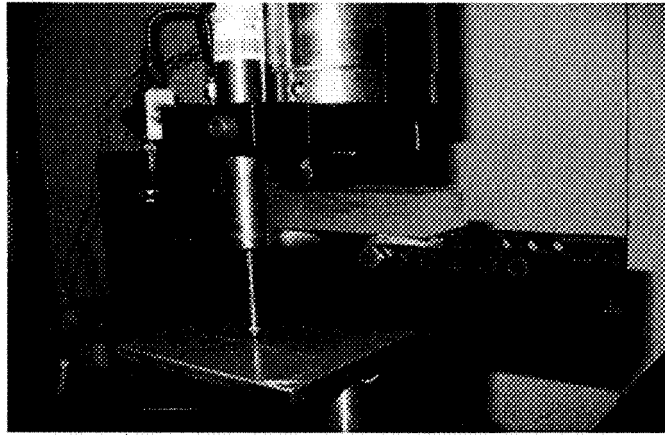


Figure 5.10. Specimen dimensions in bending tests.



**Figure 5.11.** Test configuration for measuring the bending strength of atmospheric ice.

### 5.3.2 Results of bending tests

The individual and averaged values of flexural strength and effective modulus of atmospheric ice accumulated at  $-10^{\circ}\text{C}$  and tested at  $-3^{\circ}\text{C}$ ,  $-10^{\circ}\text{C}$  and  $-20^{\circ}\text{C}$  have been tabulated in Tables 5.3, 5.4 and 5.5, respectively.

The flexural strength  $\sigma_f$  and effective modulus  $E_f$  have been calculated from simple elastic beam theory using the equations:

$$\sigma_f = \frac{3FL_b}{2wh^2} \quad \text{and} \quad E_f = \frac{1}{4w} \left( \frac{L_b}{h} \right)^3 \frac{F}{d} \quad (5.2)$$

where  $F$  is the failure load,  $L_b$  is the length of the beam,  $w$  and  $h$  are width and height of the beam, respectively, measured at the failure plane, and  $d$  is the beam deflection.

The error associated with any particular measurement of bending strength can be determined from the accumulated error associated with all parameters. The uncertainty of  $F$  is 0.25%. The error for  $w$  and  $h$  is associated with the measurement error of the caliper used to measure the dimensions of the beams and scatter in the measurement, which is 0.01mm.

The uncertainty of the measurement of the beam deflection is 0.20%. The uncertainty of L is 4.3%, which refers to the location of the fracture. Therefore, the total uncertainty in any single measurement of the bending strength and the effective modulus is 4.43% and 12.83%, respectively. The inherent scatter in the test results is considerably greater than this. The uncertainty for the failure time is 0.001 second, which corresponds to the time interval of the acquisition rate and the uncertainty of the strain rate measurement is 1.68%.

Figures 5.12 to 5.17 show the variation of bending strength and effective modulus of this type of atmospheric ice at the three test temperatures.

Row	Strain rate (1/s)	Bending strength (MPa)	Ave. Of Bending strength for Similar Conditions (MPa)	Stand. Dev. (MPa)	Time To failure (s)	Effective Modulus (GPa)	Ave. Of effective modulus for Similar Conditions (GPa)	ST. Dev. (GPa)
1	3.E-05	2.78	2.40	0.34	198.43	0.49	0.38	0.10
2	3.E-05	2.22			273.31	0.29		
3	3.E-05	2.33			293.26	0.28		
4	3.E-05	1.95			198.12	0.35		
5	3.E-05	2.89			188.45	0.49		
6	1.E-04	2.24	2.33	0.16	56.56	0.42	0.36	0.10
7	1.E-04	2.23			125.60	0.19		
8	1.E-04	2.51			75.24	0.37		
9	1.E-04	2.16			53.34	0.43		
10	1.E-04	2.48			64.37	0.40		
11	3.E-04	2.95	2.57	0.63	10.97	0.95	0.80	0.33
12	3.E-04	3.55			10.93	1.17		
13	3.E-04	2.92			10.77	0.97		
14	3.E-04	1.75			13.62	0.44		
15	3.E-04	1.66			13.35	0.47		
16	1.E-03	3.44	2.80	0.78	2.63	1.38	1.00	0.27
17	1.E-03	2.53			3.64	0.74		
18	1.E-03	2.92			2.58	1.18		
19	1.E-03	1.35			1.80	0.87		
20	1.E-03	2.25			2.79	0.85		
21	2.E-03	2.63	2.73	0.31	1.24	1.11	1.01	0.18
22	2.E-03	2.52			1.00	1.31		
23	2.E-03	2.67			1.44	0.98		
24	2.E-03	2.77			1.72	0.81		
25	2.E-03	3.32			1.83	0.80		
26	2.E-03	2.45			1.39	0.90		

**Table 5.3.** Results of bending tests on ice accumulated at  $-10^{\circ}\text{C}$  and tested at  $-3^{\circ}\text{C}$ .

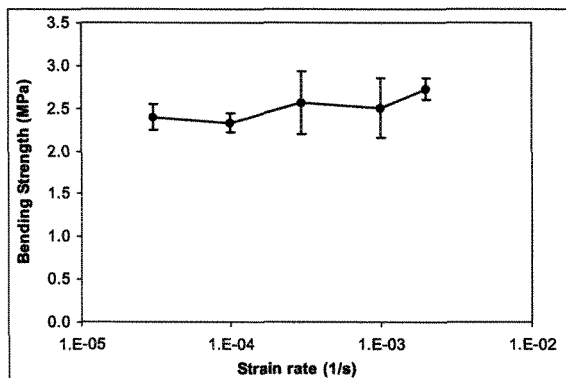


**Figure 5.12.** Bending strength of atmospheric ice accumulated at  $-10^{\circ}\text{C}$  and tested at  $-3^{\circ}\text{C}$ . The error bars in this figure, and the ones that follow, correspond to the standard error in the results for the tests conducted at each set of parameters.

Row	Strain rate (1/s)	Bending strength (MPa)	Ave. Of Bending strength for Similar Conditions (MPa)	ST Dev. (MPa)	Time To failure (s)	Effective Modulus (GPa)	Ave. Of effective modulus for Similar Conditions (GPa)	ST Dev. (GPa)
1	3.E-05	2.50	2.65	0.45	168.94	0.55	0.52	0.12
2	3.E-05	2.92			172.66	0.59		
3	3.E-05	2.64			149.79	0.60		
4	3.E-05	1.94			139.20	0.47		
5	3.E-05	2.45			246.87	0.34		
6	3.E-05	3.18			216.34	0.49		
7	1.E-04	2.46	2.92	0.26	26.58	1.00	0.82	0.19
8	1.E-04	3.02			41.19	1.03		
9	1.E-04	2.97			53.27	0.77		
10	1.E-04	3.11			48.67	0.65		
11	1.E-04	3.04			51.25	0.64		
12	3.E-04	2.88	2.97	0.24	8.84	1.19	1.14	0.24
13	3.E-04	3.26			9.07	1.30		
14	3.E-04	3.18			8.82	1.42		
15	3.E-04	2.65			11.06	0.88		
16	3.E-04	2.68			10.15	0.90		
17	1.E-03	2.86	2.88	0.52	2.78	1.04	0.95	0.23
18	1.E-03	3.28			3.34	1.08		
19	1.E-03	2.00			2.97	0.90		
20	1.E-03	3.19			5.54	0.58		
21	1.E-03	3.10			2.62	1.18		
22	2.E-03	3.41	2.74	0.59	1.52	1.19	1.06	0.17
23	2.E-03	3.02			1.36	1.14		
24	2.E-03	2.13			1.10	1.01		
25	2.E-03	3.02			2.04	0.79		
26	2.E-03	2.10			0.92	1.16		

**Table 5.4.** Results of bending tests on ice accumulated at  $-10^{\circ}\text{C}$  and tested at  $-10^{\circ}\text{C}$ .

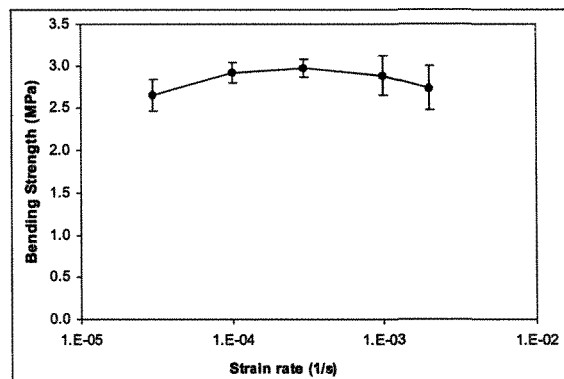
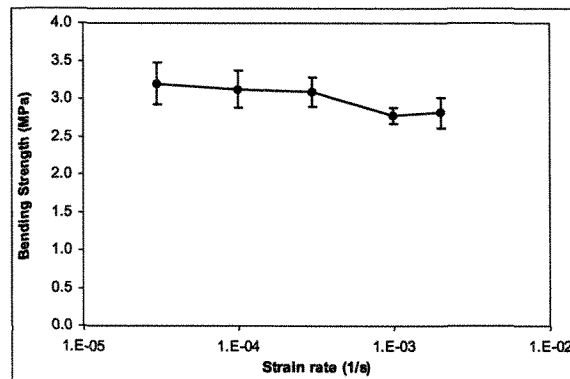


Figure 5.13. Bending strength of atmospheric ice accumulated at  $-10^{\circ}\text{C}$  and tested at  $-10^{\circ}\text{C}$ .

Row	Strain rate (1/s)	Bending strength (MPa)	Ave. Of Bending strength for Similar Conditions (MPa)	ST. Dev. (MPa)	Time To failure (s)	Effective Modulus (GPa)	Ave. Of effective modulus for Similar Conditions (GPa)	ST. Dev. (GPa)
1	3.E-05	3.19	3.20	0.68	168.34	0.66	0.57	0.22
2	3.E-05	3.67			185.93	0.69		
3	3.E-05	4.13			159.61	0.91		
4	3.E-05	3.13			229.24	0.47		
5	3.E-05	2.11	3.12	0.55	203.11	0.36	0.72	0.26
6	3.E-05	2.97			292.49	0.34		
7	1.E-04	2.39			34.36	0.75		
8	1.E-04	3.52			37.68	1.09		
9	1.E-04	3.69	3.08	0.44	64.76	0.59	0.96	0.24
10	1.E-04	2.73			37.72	0.74		
11	1.E-04	3.26			78.39	0.43		
12	3.E-04	3.67			7.99	0.80		
13	3.E-04	2.87	2.78	0.23	7.75	1.29	1.05	0.27
14	3.E-04	2.96			10.97	0.98		
15	3.E-04	2.85			9.00	1.17		
16	3.E-04	2.95			14.84	0.66		
17	3.E-04	2.90	2.62	0.46	11.72	0.66	1.21	0.25
18	1.E-03	2.51			2.67	1.05		
19	1.E-03	2.99			3.12	1.00		
20	1.E-03	2.67			2.06	1.35		
21	1.E-03	2.66	2.62	0.46	4.26	0.62	1.21	0.25
22	1.E-03	3.04			2.49	1.22		
23	2.E-03	2.63			1.07	1.30		
24	2.E-03	2.53			1.58	0.83		
25	2.E-03	2.76	2.62	0.46	1.07	1.33	1.21	0.25
26	2.E-03	3.82			1.25	1.46		
27	2.E-03	2.55			1.15	1.12		

Table 5.5. Results of bending tests on ice accumulated at  $-10^{\circ}\text{C}$  and tested at  $-20^{\circ}\text{C}$ .



**Figure 5.14.** Bending strength of atmospheric ice accumulated at  $-10^{\circ}\text{C}$  and tested at  $-20^{\circ}\text{C}$ .

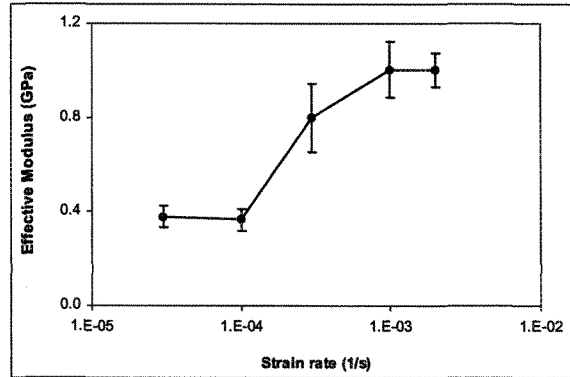


**Figure 5.15.** Effective modulus of atmospheric ice accumulated at  $-10^{\circ}\text{C}$  and tested at  $-3^{\circ}\text{C}$ .

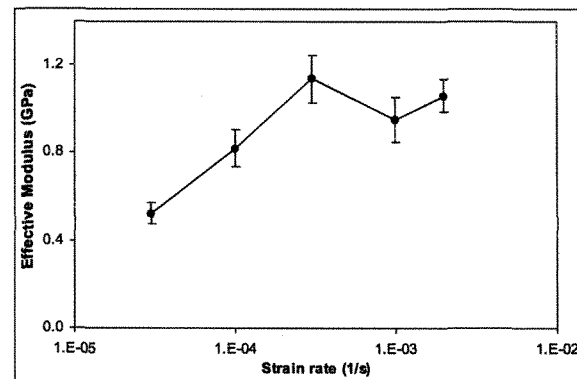


**Figure 5.16.** Effective modulus of atmospheric ice accumulated at  $-10^{\circ}\text{C}$  and tested at  $-10^{\circ}\text{C}$ .

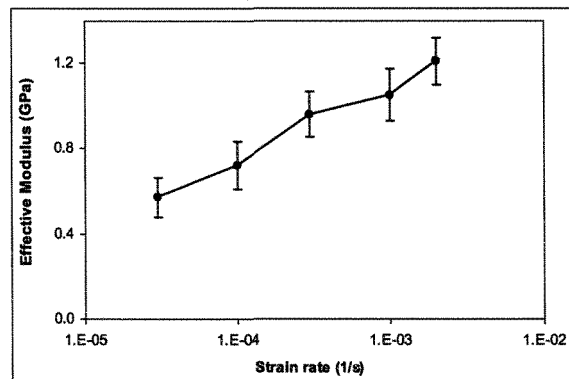


Figure 5.17. Effective modulus of atmospheric ice accumulated at  $-10^{\circ}\text{C}$  and tested at  $-20^{\circ}\text{C}$ .

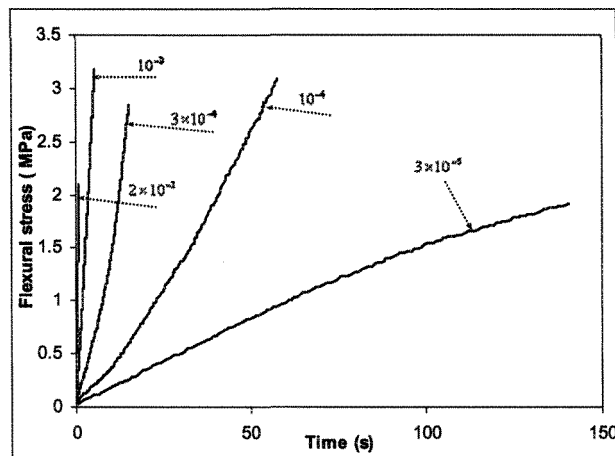


Figure 5.18. Plot of flexural stress versus time for beam bending tests at  $-10^{\circ}\text{C}$  and various strain rates (unit of strain rate  $\text{s}^{-1}$ ).

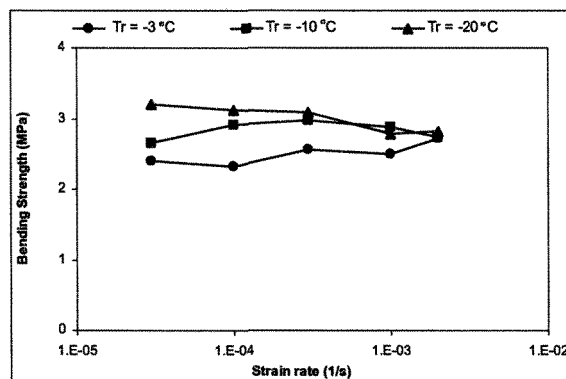
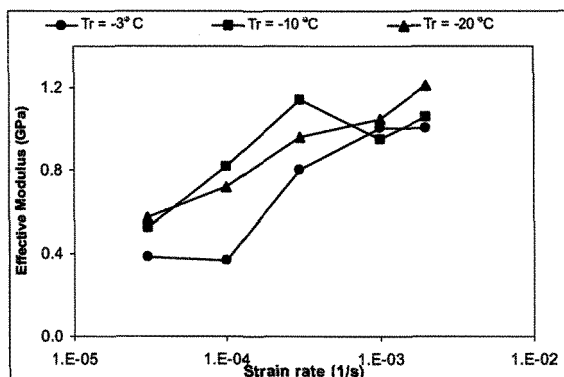


Figure 5.19. Bending strength of atmospheric ice accumulated at  $-10^{\circ}\text{C}$  and tested at various temperatures.



**Figure 5.20.** Effective modulus of atmospheric ice accumulated at  $-10^{\circ}\text{C}$  and tested at various temperatures.

Figure 5.18 shows flexural stress versus time for atmospheric ice accumulated at  $-10^{\circ}\text{C}$ , and tested at the same temperature and at various strain rates. As apparent in this figure, the stress increases in a fairly linear fashion until failure occurs. The maximum flexural stress before failure is defined as the flexural strength of the specimen.

Figures 5.19 and 5.20 show the comparative results of bending strength and effective modulus at different temperatures. Figure 5.19 shows a clear dependency of the bending strength on the test temperature for the three lower strain rates. This trend of increasing strength with decreasing temperature has also been reported by Gagnon and Gammon (1995) for iceberg ice and Gow and Ueda (1988) for fresh water ice.

The average flexural strength of atmospheric ice accumulated at  $-10^{\circ}\text{C}$  and tested at the same temperature at a strain rate of  $10^{-4} \text{ s}^{-1}$  has been calculated to be  $2.92 \pm 0.26 \text{ MPa}$ . So far, to the best of our knowledge, there is no published investigation of the flexural strength of atmospheric ice with which to compare our results. In comparison with fresh water ice, however, Timco and Frederking (1982) reported the bending strength of fresh water ice to be  $2.20 \pm 0.32 \text{ MPa}$  and  $1.77 \pm 0.19 \text{ MPa}$  for three-point beam bending, at approximately

the same strain rate, with top and bottom in tension, respectively. Dempsey *et al.* (1989), in their tests by four-point-bend beams obtained the bending strength of fresh water ice ranging between 1.5 MPa and 1.7 MPa and between 1.2 MPa and 1.7 MPa for smaller and larger beams, respectively.

The average flexural strength of this type of atmospheric ice at the test temperature of  $-10^{\circ}\text{C}$  at a strain rate of  $2 \times 10^{-3} \text{ s}^{-1}$  has been found to be  $2.74 \pm 0.59$  MPa in our study. Gow and Ueda (1988) reported values of  $2.41 \pm 0.29$  MPa and  $1.59 \pm 0.17$  MPa at  $-10^{\circ}\text{C}$  for the three-point beam with top and bottom in tension, respectively.

The average flexural strength of this type of atmospheric ice at  $-3^{\circ}\text{C}$  at a strain rate of  $2 \times 10^{-3} \text{ s}^{-1}$  has been found to be  $2.73 \pm 0.31$  MPa. Lavrov (1971) reported an average bending strength for fresh water ice of approximately 2.01 MPa for S1 ice and 2.16 MPa for S2 ice tested at  $-3^{\circ}\text{C}$  to  $-4^{\circ}\text{C}$ . Gow and Ueda (1988) reported values of  $2.10 \pm 0.39$  MPa and  $1.39 \pm 0.27$  MPa for S1 ice tested at  $-5^{\circ}\text{C}$  with top and bottom in tension, respectively.

At a test temperature of  $-20^{\circ}\text{C}$  for ice accumulated at  $-10^{\circ}\text{C}$ , the average bending strength at the strain rate of  $2 \times 10^{-3} \text{ s}^{-1}$  has been found to be  $2.82 \pm 0.46$  MPa. Gow and Ueda (1988) reported a similar value of  $2.57 \pm 0.29$  MPa and  $1.64 \pm 0.12$  MPa at  $-19^{\circ}\text{C}$  for the three-point-beams with top and bottom in tension, respectively. Figure 5.21 shows the comparison between the present values of the flexural strength of atmospheric ice (at strain rate of  $2 \times 10^{-3} \text{ s}^{-1}$ ) and those of other investigators for fresh water ice and glacier ice. Higher values of flexural strength of atmospheric ice can be attributed to the lower average grain size in comparison with the ice of other studies.

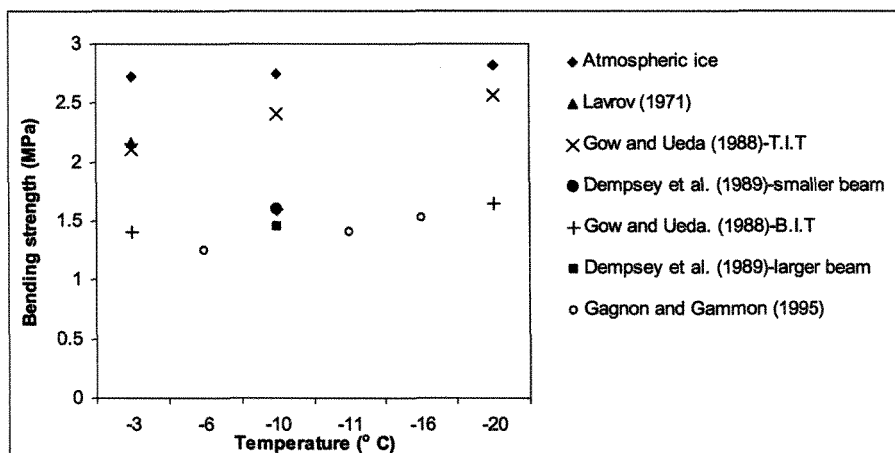


**Figure 5.21.** Comparison of bending strength of atmospheric ice with values of other researchers for fresh water ice and glacier ice. (T.I.T= Top In Tension; B.I.T= Bottom In Tension).

Timco and O'Brien (1994) reviewed the results of many researchers on the flexural strength of fresh water ice and sea ice for both cantilever and simply supported beam tests. According to their research, the flexural strength of fresh water ice lies within a range of 1 MPa to 3 MPa.

At a test temperature of  $-10^{\circ}\text{C}$  and a strain rate of  $2 \times 10^{-3} \text{ s}^{-1}$ , the average effective modulus of atmospheric ice accumulated at  $-10^{\circ}\text{C}$  has been found to be  $1.06 \pm 0.17 \text{ GPa}$ . Timco and Frederking (1982) reported the effective modulus of fresh water ice of cantilever beams to be  $1.6 \pm 0.4 \text{ GPa}$ . Gow and Ueda (1988) reported a similar value of  $6.0 \pm 1.5 \text{ GPa}$  and  $6.4 \pm 1.2 \text{ GPa}$  for three-point-beams of fresh water ice in bottom and top in tension, respectively. Dempsey *et al.* (1989) obtained the effective modulus of fresh water ice ranging between 0.7 GPa and 2 GPa and between 2.5 GPa and 10.5 GPa for smaller and larger beams, respectively, for four-point-bending experiments.

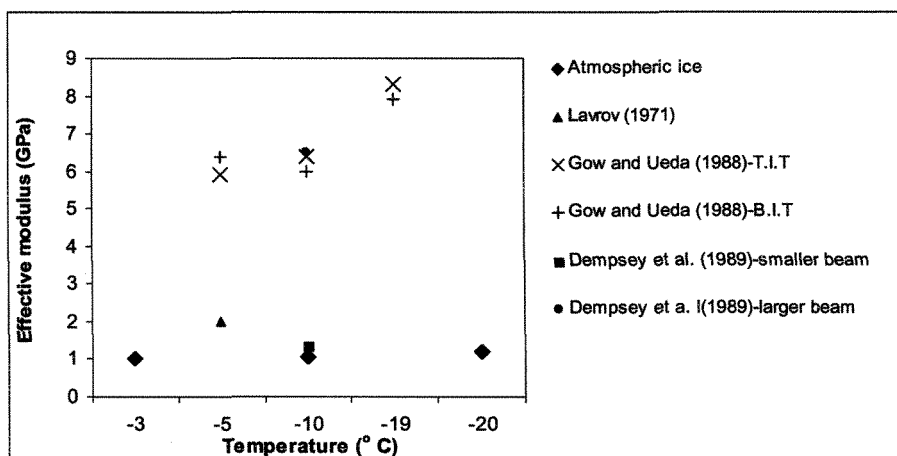


Figure 5.22. Comparison of effective modulus of atmospheric ice with values of other researchers for fresh water ice. (T.I.T= Top In Tension; B.I.T= Bottom In Tension).

The average effective modulus of this type of atmospheric ice at  $-3^{\circ}\text{C}$  at a strain rate of  $2 \times 10^{-3} \text{ s}^{-1}$  is  $1.01 \pm 0.18 \text{ GPa}$ . Gow and Ueda (1988) reported a value of  $5.9 \pm 0.7 \text{ GPa}$  and  $6.4 \pm 1.0 \text{ GPa}$  at a test temperature of  $-5^{\circ}\text{C}$  with top and bottom in tension beam tests, respectively. Lavrov (1971) reported an effective modulus of about  $2 \text{ GPa}$  at a test temperature of  $-5^{\circ}\text{C}$ .

At a test temperature of  $-20^{\circ}\text{C}$  and a strain rate of  $2 \times 10^{-3} \text{ s}^{-1}$  for ice accumulated at  $-10^{\circ}\text{C}$ , the average effective modulus of ice has been found to be  $1.21 \pm 0.26 \text{ GPa}$ . Gow and Ueda (1988) reported values of  $8.3 \pm 2.3 \text{ GPa}$  and  $7.9 \pm 0.9 \text{ GPa}$  at  $-19^{\circ}\text{C}$  for three-point-beam bending tests with top and bottom in tension, respectively. Figure 5.22 shows the comparison between the present values of the effective modulus of atmospheric ice (again accumulated at  $-10^{\circ}\text{C}$  and tested at a strain rate of  $2 \times 10^{-3} \text{ s}^{-1}$ ) and those of other investigators with fresh water ice.

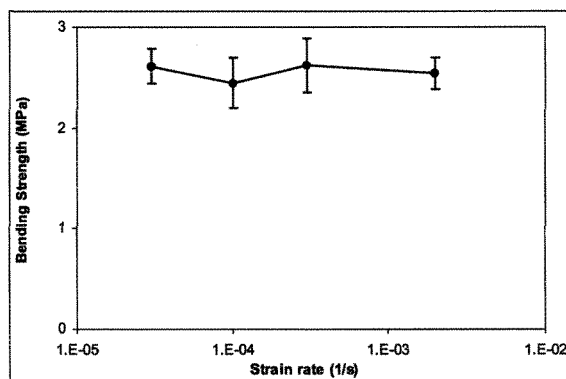
Tables 5.6 and 5.7 show the results of bending tests for two other types of atmospheric ice accumulated at  $-6^{\circ}\text{C}$  and  $-20^{\circ}\text{C}$  and tested at the same temperature as accumulated.

Row	Strain rate (1/s)	Bending strength (MPa)	Ave. Of Bending strength for Similar Conditions (MPa)	ST. Dev. (MPa)	Time To failure (s)	Effective Modulus (GPa)	Ave. Of effective modulus for Similar Conditions (GPa)	ST. Dev. (GPa)
1	3.E-05	2.37	2.61	0.39	123.43	0.69	0.70	0.06
2	3.E-05	2.62			134.82	0.75		
3	3.E-05	3.24			166.77	0.77		
4	3.E-05	2.24			137.61	0.66		
5	3.E-05	2.58			164.24	0.63		
6	1.E-04	2.83	2.45	0.56	35.74	0.65	0.82	0.29
7	1.E-04	3.23			28.21	1.30		
8	1.E-04	2.16			35.21	0.75		
9	1.E-04	1.88			35.73	0.58		
10	1.E-04	2.15			38.52	0.60		
11	3.E-04	2.30	2.62	0.60	9.01	0.91	1.09	0.37
12	3.E-04	2.87			10.21	1.07		
13	3.E-04	3.58			9.35	1.61		
14	3.E-04	2.06			11.94	0.63		
15	3.E-04	2.32			5.84	1.25		
16	2.E-03	2.07	2.54	0.35	0.95	1.24	1.21	0.18
17	2.E-03	2.65			1.13	1.37		
18	2.E-03	3.04			1.24	1.35		
19	2.E-03	2.51			1.16	1.16		
20	2.E-03	2.43			1.59	0.91		

Table 5.6. Results of bending tests on ice accumulated at -6°C and tested at -6°C.

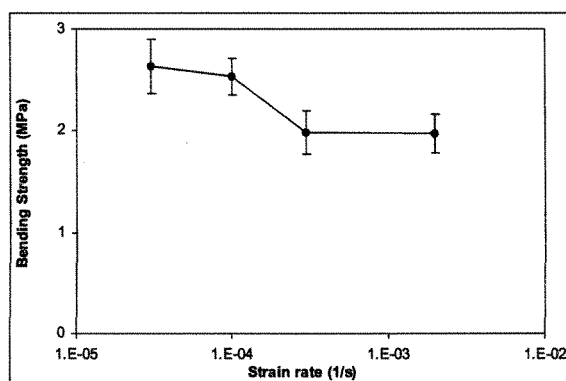
Row	Strain rate (1/s)	Bending strength (MPa)	Ave. Of Bending strength for Similar Conditions (MPa)	ST. Dev. (MPa)	Time To failure (s)	Effective Modulus (GPa)	Ave. Of effective modulus for Similar Conditions (GPa)	ST. Dev. (GPa)
1	3.E-05	2.22	2.63	0.59	104.91	0.73	0.60	0.21
2	3.E-05	3.31			146.19	0.81		
3	3.E-05	3.24			162.13	0.71		
4	3.E-05	2.20			225.46	0.35		
5	3.E-05	2.18			184.25	0.41		
6	1.E-04	2.46	2.53	0.40	21.79	0.71	0.69	0.10
7	1.E-04	2.08			34.14	0.64		
8	1.E-04	2.67			52.41	0.55		
9	1.E-04	3.13			43.14	0.74		
10	1.E-04	2.30			29.26	0.62		
11	3.E-04	2.74	1.96	0.52	7.62	0.74	0.70	0.23
12	3.E-04	2.12			6.92	1.10		
13	3.E-04	1.70			7.57	0.79		
14	3.E-04	1.98			12.07	0.56		
15	3.E-04	2.17			13.71	0.55		
16	2.E-03	1.17			6.71	0.46		
17	2.E-03	2.60	1.97	0.43	1.04	1.30	0.92	0.43
18	2.E-03	2.11			0.80	1.37		
19	2.E-03	1.45			1.17	0.64		
20	2.E-03	1.90			2.66	0.35		
21	3.E-05	1.79			1.00	0.91		
22	3.E-05	1.52			1.53	0.52		

Table 5.7. Results of bending tests on ice accumulated at -20°C and tested at -20°C.



**Figure 5.23.** Bending strength of atmospheric ice accumulated at  $-6^{\circ}\text{C}$  and tested at  $-6^{\circ}\text{C}$ .

Figures 5.23 to 5.26 show the flexural strength and effective modulus of those two types of atmospheric ice. Figures 5.27 and 5.28 demonstrate the comparative values of the bending strength and the effective modulus of all three types of atmospheric ice. In Figures 5.27 and 5.28, it is observed that the bending strength and the effective modulus of atmospheric ice accumulated at  $-20^{\circ}\text{C}$  and tested at the same temperature are lower than the two other types. The reason for these differences will be discussed in the following section.



**Figure 5.24.** Bending strength of atmospheric ice accumulated at  $-20^{\circ}\text{C}$  and tested at  $-20^{\circ}\text{C}$ .

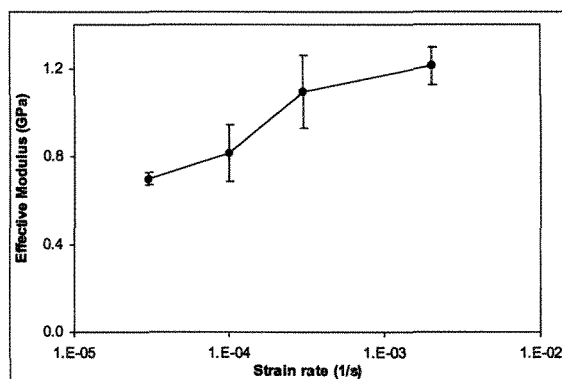


Figure 5.25. Effective modulus of atmospheric ice accumulated at  $-6^{\circ}\text{C}$  and tested at  $-6^{\circ}\text{C}$ .

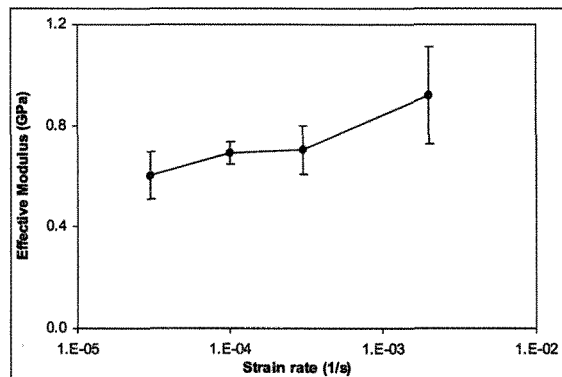


Figure 5.26. Effective modulus of atmospheric ice accumulated at  $-20^{\circ}\text{C}$  and tested at  $-20^{\circ}\text{C}$ .

### 5.3.3 Discussion

In Figure 5.19, it can be observed that at the lower strain rates, the strength of the ice appears to increase with decreasing temperature, as expected. Unfortunately, there are no other data in the literature to compare this trend to for the low strain rates. On the other hand, Figure 5.19 suggests little or no temperature effect at the higher strain rates. Gagnon and Gammon (1995) noticed an increasing trend in the flexural strength with decreasing temperature at a strain rate of  $10^{-3} \text{ s}^{-1}$  for iceberg ice. Gow and Ueda (1988) also observed that increasing trend at a similar strain rate.

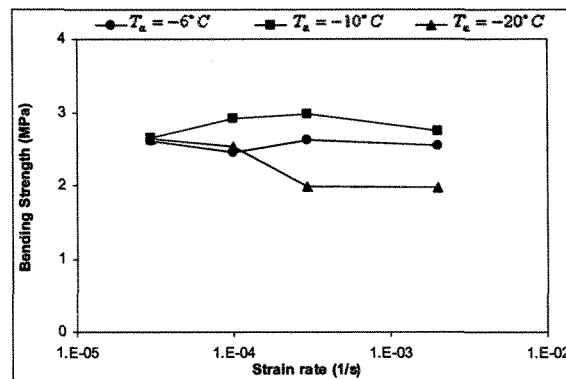


Figure 5.27. Bending strength of atmospheric ice accumulated and tested at various temperatures.

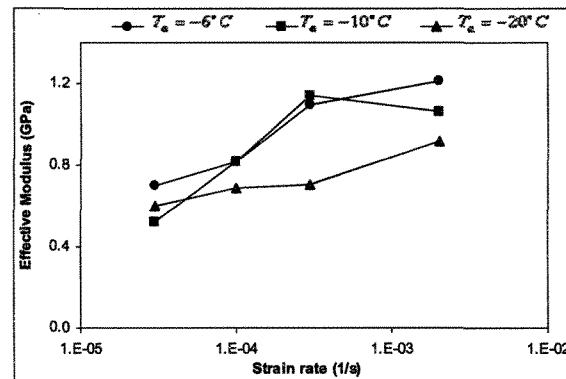


Figure 5.28. Effective modulus of atmospheric ice accumulated and tested at various temperatures.

From the trends observed in Figure 5.19, bearing in mind the inherent scatter in the data (Figures 5.12-5.14), the implication is that strain rate and temperature affect the flexural strength of the ice, in a small but measurable way. Depending on the temperature, the increasing strain rate can either increase or decrease the flexural strength. Again, there is not much in the literature allowing us to make comparisons, but Gagnon and Gammon (1995) also observed that strain rate has an effect on flexural strength, for iceberg ice specimens whose strength increased with strain rate at  $-11^\circ\text{C}$ . While Timco and Frederking (1982) stated that no distinct loading rate effect could be found in their study of the flexural strength of fresh water ice, their data (Figure 3 in their paper) nevertheless show a

statistically significant increase in strength with loading rate for simply supported beams with bottom failure, even over the limited range of the loading rates used for the tests. Furthermore, their cantilever beam tests showed a statistically significant decrease in strength with loading rate over a wider range of loading rates. This discussion shows that the relationship of the flexural strength of ice with respect to temperature and strain rate is not fully understood and warrants further study.

As shown in Figure 5.27, the bending strength of the ice accumulated at  $-10^{\circ}\text{C}$  is higher than that of the two other ice types. The smaller grain size of this ice, as compared to that of ice accumulated at  $-6^{\circ}\text{C}$ , as well as the colder test temperature ( $-10^{\circ}\text{C}$ ) explain its higher bending strength. The similar values obtained for the strength of ice accumulated at  $-10^{\circ}\text{C}$  and tested at  $-3^{\circ}\text{C}$  (Figure 5.12) and that of ice accumulated at  $-6^{\circ}\text{C}$  and tested at  $-6^{\circ}\text{C}$  (Figure 5.23), despite the warmer test temperature of the former, further demonstrates that the bending strength of atmospheric ice accumulated at  $-10^{\circ}\text{C}$  is higher than that at  $-6^{\circ}\text{C}$ .

The lack of cavities and pre-existing cracks in the ice accumulated at  $-10^{\circ}\text{C}$  compared to the ice accumulated at  $-20^{\circ}\text{C}$ , despite the warmer test temperature, results in a stronger structure and higher bending strength for the former. The significant number of cavities, many of which have irregular shapes, contribute to the lower strength observed for ice accumulated at  $-20^{\circ}\text{C}$  because these cavities are susceptible to stress concentration. Comparing Figures 5.14 and 5.24, it can be seen that the average values of bending strength for the ice accumulated at  $-10^{\circ}\text{C}$  and tested at  $-20^{\circ}\text{C}$  are greater than the corresponding values for the ice accumulated at  $-20^{\circ}\text{C}$  and tested at the same temperature.

The difference between the bending strengths of ice accumulated at  $-20^{\circ}\text{C}$  and the other two types is more noticeable at higher strain rates. This is probably due to the stress around the tips of pre-existing cracks in ice accumulated at  $-20^{\circ}\text{C}$  that increases rapidly and causes crack growth before plastic processes dissipate the stress. In Figure 5.27, the bending strength of the ice accumulated at  $-20^{\circ}\text{C}$  and tested at the lowest strain rate ( $3 \times 10^{-5} \text{ s}^{-1}$ ) is almost the same as that of the ice accumulated at the other temperatures.

Figure 5.28 shows that the effective modulus of all three types of atmospheric ice increases as strain rate increases. This implies that the ratio of “load at failure” to “beam deflection at failure” ( $F/d$ ) increases with higher strain rates. This is logical because at a given failure load, beam deflection at low strain rates is higher than at high strain rates. As expected, the effective modulus of ice accumulated at  $-20^{\circ}\text{C}$  at higher strain rates is less than that of the two other types, owing to the presence of cavities and cracks in this ice. The effective modulus of ice accumulated at  $-6^{\circ}\text{C}$  is higher than that of ice accumulated at  $-20^{\circ}\text{C}$ , because the larger grain size and lack of cavities in the ice accumulated at  $-6^{\circ}\text{C}$  make it less deformable (Schulson, 2000).

Furthermore, in spite of the considerable scatter in the data, the effective modulus of the ice accumulated at  $-6^{\circ}\text{C}$  is probably higher than that of the ice accumulated at  $-10^{\circ}\text{C}$ . This is so because the values for the ice accumulated at  $-6^{\circ}\text{C}$  are greater than or equal to those for the ice accumulated at  $-10^{\circ}\text{C}$  throughout the range of strain rates, including the additional data point at  $1 \times 10^{-3} \text{ s}^{-1}$  in Figure 5.16 that is not included in Figure 5.28. This is due to the larger grain size of the ice accumulated at  $-6^{\circ}\text{C}$ , relative to that of the ice accumulated at  $-10^{\circ}\text{C}$ .

The difference between the results of the present study and those of other investigators for bending strength and effective modulus of fresh water ice emanate from two sources. The most important difference is the ice type. There are lots of dissimilarities between atmospheric ice and fresh water ice. The differences in grain size, void ratio, shape and size of bubbles and grain growth direction are some examples.

As mentioned earlier, the average grain size for atmospheric ice accumulated at  $-10^{\circ}\text{C}$  and  $-6^{\circ}\text{C}$  is 0.5 mm and 1.5 mm, respectively. In the tests of Gow and Ueda (1988) and those of Timco and Frederking (1982), however, the average grain size was found to be between 4 mm to 8 mm and 1 mm to 6 mm, respectively.

The other important difference between our tests and those of other researchers is the test sample size, which can affect mechanical properties (Dempsey *et al.*, 1989). The specimen dimensions in our study were 40 mm wide, 20 mm thick and 70 mm long. Timco and Frederking (1982) used sample sizes of 60 mm x 100 mm x 400 mm in their study. The height and width of the samples used by Gow and Ueda (1988) were in a range of 78 mm to 140 mm and the average beam length was between 710 mm and 1020 mm. The large difference in sample size between the present study and the previous ones is likely responsible for some of the differences in the results. The inherent scatter of the test results may also have contributed to the differences (e.g. see effective modulus in Dempsey *et al.*, 1989).

#### **5.4 Fracture toughness of atmospheric ice**

The presence of cracks in the ice can weaken it against the loads. This may occur at stresses below its yield strength, where failure would not normally be expected. To study

the ice behavior in the presence of cracks, a branch of continuum mechanics called Linear Elastic Fracture Mechanics (LEFM) is used. Most of the studies on the behavior of ice by LEFM concentrated on measuring the fracture toughness of the ice. In fracture mechanics, the determination of fracture toughness is a stress analysis problem which involves the applied stress, the loading geometry, dimensions of the sample and the length of the crack which is cut in the ice and sharpened. As noted by Dempsey *et al.* (1989), some investigations of ice fracture toughness were hindered by experimental difficulties, resulting in unreliable data. Laboratory measurements of the fracture toughness of ice made prior to 1989 are often characterized by a wide variation in results (e.g. Liu and Miller, 1979, Goodman and Tabor, 1978). This scatter is thought to reflect the influence of various testing parameters on experimentally determined values of fracture toughness. However, standardization of testing techniques and characterization of experimental variables by Dempsey *et al.* (1989) has resulted in more consistent data.

#### **5.4.1 Experimental techniques for fracture toughness tests**

As explained in section 3.1.3, the atmospheric ice was prepared by a microtome machine. To avoid the effect of grain size, the dimensions of the specimen were chosen according to the guidelines in the ASTM E399-72 and also the recommendations made by Dempsey *et al.* (1989). The notch root was formed by the saw cut and reshaped by razor blades with a curvature radius of 0.1 mm, in order to increase the notch acuity. Figure 5.29 shows the experimental set up for measuring the fracture toughness of atmospheric ice. The critical stress intensity factor ( $K_{IC}$ ) for three-point loading is given by (Dempsey *et al.*, 1989):

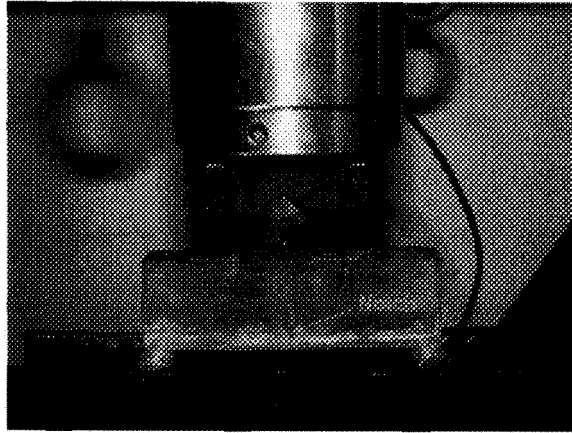


Figure 5.29. Fracture toughness test of atmospheric ice.

$$K_{IC} = 3Ff(a/h)/(4w\sqrt{h}) \quad (5.3)$$

where  $F$  is the load at fracture,  $a$  is the notch length,  $h$  is the specimen height,  $w$  is its width, and the function  $f(a/h)$  is:

$$f(a/h) = -1.186(1 - \frac{a}{h})^2 + 2.474(1 - \frac{a}{h}) - 6.858 + 8.124(1 - \frac{a}{h})^{-1} + 0.045(1 - \frac{a}{h})^{-2} \quad (5.4)$$

Loading was at a rate such that the rate of increase of the fracture toughness was within the range of 70 and 130  $KPa\sqrt{m}/s$  (as mentioned by Dempsey *et al.*, 1989).

According to ASTM E399, the following conditions should be respected for a valid fracture toughness test:

$$a = h - a = w \geq 2.5(K_{IC}/\sigma_y) \quad (5.5)$$

where  $K_{IC}$  is the plain strain fracture toughness and  $\sigma_y$  is the yield stress of the material.

Figure 5.30 shows the specimen dimensions in which  $a$  is 20 mm,  $h$  is 40 mm,  $w$  is 20 mm and the specimen length is 128 mm. The distance between two roller supports is 120 mm and the force  $F$  is applied at the middle of the specimen.

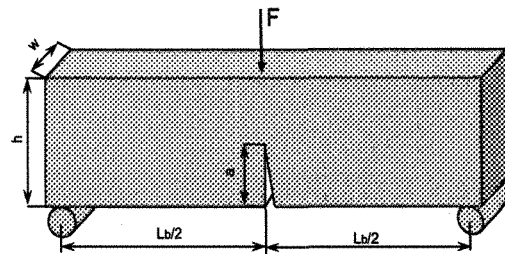


Figure 5.30. The specimen dimensions in the fracture toughness

In order to verify the application of Linear Elastic Fracture Mechanics (LEFM), an extensometer was installed under the beam to measure the notch mouth opening displacement. Figure 5.31 shows a typical force–displacement record. The linear fit to data is good ( $r^2 = 0.993$ ) and it implies that linear elastic fracture mechanics is applicable.

#### 5.4.2 Test results and discussion

Table 5.8 shows the results of fracture toughness of atmospheric ice accumulated at  $-6^\circ\text{C}$ ,  $-10^\circ\text{C}$  and  $-20^\circ\text{C}$ . Again the ice accumulated at  $-10^\circ\text{C}$  was tested at three different temperatures,  $-3^\circ\text{C}$ ,  $-10^\circ\text{C}$  and  $-20^\circ\text{C}$ .

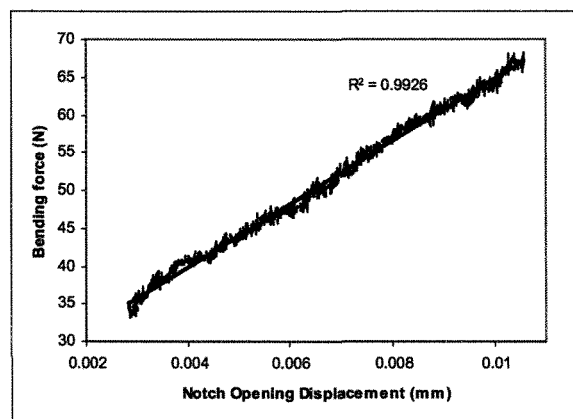


Figure 5.31. Force versus notch opening displacement in the fracture toughness tests.

Row	T <sub>a</sub> (°C)	T <sub>t</sub> (°C)	Fracture Toughness (KPa.m <sup>0.5</sup> )	Average (KPa.m <sup>0.5</sup> )	ST. Dev. (KPa.m <sup>0.5</sup> )
1	-6	-6	130.68	137.75	24.86
2	-6	-6	175.45		
3	-6	-6	123.60		
4	-6	-6	146.96		
5	-6	-6	132.08		
6	-10	-3	162.52	128.60	21.65
7	-10	-3	136.74		
8	-10	-3	108.70		
9	-10	-3	120.32		
10	-10	-3	114.71		
11	-10	-10	114.63	111.17	7.93
12	-10	-10	105.04		
13	-10	-10	121.09		
14	-10	-10	101.33		
15	-10	-10	113.77		
16	-10	-20	117.64	143.28	29.13
17	-10	-20	140.95		
18	-10	-20	114.02		
19	-10	-20	160.94		
20	-10	-20	184.83		
21	-20	-20	84.67	108.04	34.44
22	-20	-20	89.80		
23	-20	-20	148.22		
24	-20	-20	142.39		
25	-20	-20	75.22		

**Table 5.8.** Results of fracture toughness tests of atmospheric ice.  
T<sub>a</sub>= Accumulation temperature, T<sub>t</sub>= Test temperature.

Figure 5.32 shows the results of fracture toughness tests of various types of atmospheric ice. The results of these tests show the fracture toughness of atmospheric ice accumulated at -10°C decreases and then increases with a decreasing test temperature.

The average value of fracture toughness at -3°C is  $128.6 \text{ KPa}\sqrt{m}$ . Liu and Miller (1979) obtained the average value of  $110.5 \text{ KPa}\sqrt{m}$  at -4°C for fracture toughness of fresh water ice. However, the value of fracture toughness of sea ice reported by Urabe *et al.* (1980) is about  $80 \pm 20 \text{ KPa}\sqrt{m}$  and they attributed the difference of their results with those of other investigations for fresh water ice to the differences in the structure of the ice.

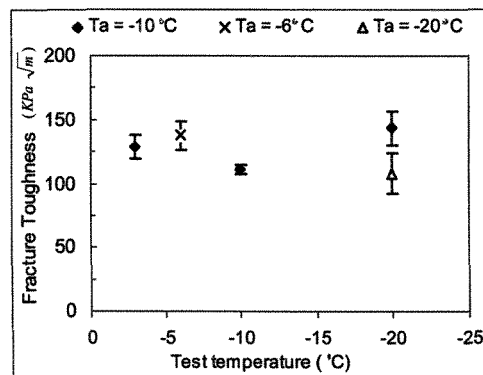


**Figure 5.32.** Fracture toughness of various types of atmospheric ice. The error bars in this figure correspond to the standard error in the results for the tests conducted at each set of parameters.

At a test temperature of  $-10^{\circ}\text{C}$ , the results of our tests show the average value of  $111.17 \text{ KPa}\sqrt{\text{m}}$ . This value agrees well with one reported by Timco and Frederking (1986) for fresh water ice at  $-10^{\circ}\text{C}$ . They found that  $K_{IC} = 188\dot{K}_I^{-0.13}$  for horizontal crack propagation, which is similar to the crack propagation direction in the current study. This equation predicts that for loading rates  $70 < \dot{K}_I < 130 \text{ KPa}\sqrt{\text{m}}/\text{s}$ , the  $K_{IC}$  would range between  $99.8 \text{ KPa}\sqrt{\text{m}}$  and  $108.2 \text{ KPa}\sqrt{\text{m}}$ . Dempsey *et al.* (1989) obtained a value of fracture toughness of fresh water ice in the range of 50 to  $130 \text{ KPa}\sqrt{\text{m}}$  for various grain sizes. Smith *et al.* (1990) in their tests with granular fresh water ice at  $-10^{\circ}\text{C}$  (porosity  $< 4\%$ ) found the fracture toughness between  $83 \text{ KPa}\sqrt{\text{m}}$  and  $112 \text{ KPa}\sqrt{\text{m}}$  within the same load rate of current study. Liu and Loop (1972) reported this value in the range of  $96 \text{ KPa}\sqrt{\text{m}}$  and  $116 \text{ KPa}\sqrt{\text{m}}$  for fresh water ice at test temperature of  $-9^{\circ}\text{C}$ . Liu and Miller (1979) reported the average value of  $116.3 \text{ KPa}\sqrt{\text{m}}$  at  $-9^{\circ}\text{C}$  for fresh water ice.

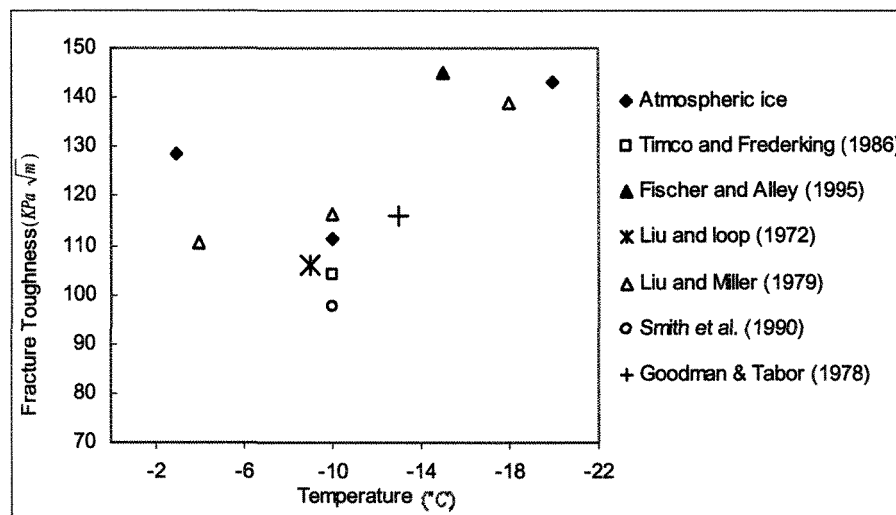


**Figure 5.33.** Comparison of fracture toughness of ice with the results of other investigators for fresh water ice.

Fischer and Alley (1995) used a modified ring (MR) test to determine the fracture toughness of granular fresh water ice at  $-15^{\circ}\text{C}$  and obtained results of  $145 \pm 35 \text{ KPa}\sqrt{m}$ . Liu and Miller (1979) obtained the average value of  $139 \text{ KPa}\sqrt{m}$  at  $-18^{\circ}\text{C}$  for fresh water ice. Goodman and Tabor (1978) obtained the value of  $116 \pm 13 \text{ KPa}\sqrt{m}$  at  $-13^{\circ}\text{C}$  for fresh water ice. Figure 5.33 shows the comparison between the present values of fracture toughness of atmospheric ice and those of other investigators for fresh water ice.

In the Figure 5.32 (and the Table 5.8), it is observed that the average value of fracture toughness of ice accumulated at  $-10^{\circ}\text{C}$  and tested at  $-20^{\circ}\text{C}$  is  $143.28 \text{ KPa}\sqrt{m}$ , while the corresponding value of the ice accumulated at  $-20^{\circ}\text{C}$  and also tested at  $-20^{\circ}\text{C}$  is  $108.04 \text{ KPa}\sqrt{m}$ . Comparing the average value of fracture toughness of the ice accumulated at  $-10^{\circ}\text{C}$  and tested at  $-3^{\circ}\text{C}$  ( $128.60 \text{ KPa}\sqrt{m}$ ) with the corresponding value of the ice accumulated at  $-6^{\circ}\text{C}$  and tested at  $-6^{\circ}\text{C}$  ( $137.75 \text{ KPa}\sqrt{m}$ ), ignoring the small difference in test temperatures and regardless of overlapping the error bars, it seems that the fracture

toughness of atmospheric ice decreases with decreasing accumulation temperature. As mentioned earlier, at test temperatures close to the melting point, the ice shows ductile behavior and it is expected that its resistance against crack propagation increases when the temperature approaches the melting point. The fracture toughness of atmospheric ice accumulated at  $-20^{\circ}\text{C}$  and tested at its accumulation temperature is less than other types because the cavities and possibly pre-existing cracks in this ice lower its resistance against crack propagation. The same factor observed in the compression tests and the bending tests led to the weakness of this ice.

### **5.5 Young's Modulus**

The instantaneous elastic strain has been related to the applied stress by generalized Hook's law. Pure elastic behavior of a single crystal is due primarily to changes in intermolecular distances under an applied stress. However, stress-induced movements of imperfections (e.g. dislocations) can also contribute to the deformation. If the imperfections move to new equilibrium positions, the solid will suffer a permanent deformation in which case its behavior will not be perfectly elastic. However, if the stress is applied and released during a sufficiently short period, the imperfection will have little opportunity to move and the deformation should be elastic. Thus, one can conclude that the elastic constants of ice deduced from high frequency measurements (dynamic loading) are more reliable than the static values obtained by measuring the deformation of ice under static loading. However, several measurements have been made for the elastic modulus and elastic constants of ice in both static and dynamic loading. Measurements of the static elastic moduli of ice made prior to 1940 are reviewed by Dorsey (1940). Dantl (1969) determined the frequency

dependence of the elastic constants of single crystal ice in the range of 5-190 MHz and their temperature dependence from the melting point to  $-140^{\circ}\text{C}$  by a supersonic pulse-echo method and a double-pulse interference technique. Gammon *et al.* (1983) measured elastic constants of natural ice by the Brillouin spectroscopy method. Gagnon (1988) determined the elastic constants of ice  $I_h$  by Brillouin spectroscopy as a function pressure. Many other researchers presented their measurements and formulation for the elastic moduli of granular and columnar ice type as a function of temperature (e.g. Hill, 1952; Sinha, 1978; Sinha, 1989; Michel, 1978). Jacqueline and Menge (1984) determined the Young's modulus of sea ice using uniaxial compression tests at  $-10^{\circ}\text{C}$  and various strain rates.

More recent measurements have been made by different researchers who obtained values of static Young's modulus for polycrystalline ice between 0.3 GPa and 11 GPa.

### **5.5.1 Measurement of Young's modulus of atmospheric ice**

Keeping in mind that the measurement of Young's modulus by static loading has some associated errors (at least for ice), attempts were made to measure this value using an extensometer, which was attached to specimens in compression tests. As predicted, in most of the tests, the first part of the stress-strain curve, which gives the Young's modulus of the ice, was not a straight line and even when it was straight, the line slope in different specimens had a large variation, even in strains less than 0.002. The variation arises from several sources of error. The first and probably the most important factor is the test method. As mentioned before, the static values have less accuracy. The second source of error was using only one extensometer for measuring the strains while, according to ASTM, at least

two extensometers are required. Using more than one extensometer in each specimen was not possible, owing to the small size of the specimen.

Row	T <sub>a</sub> (°C)	T <sub>t</sub> (°C)	Young's modulus (MPa)	Average (MPa)	St. Dev. (MPa)
1	-6	-6	2322	3690.0	1332.0
2	-6	-6	3545		
3	-6	-6	3200		
4	-6	-6	6756		
5	-6	-6	4863		
6	-6	-6	2975		
7	-6	-6	3892		
8	-6	-6	1967		
9	-10	-3	4395	5014.3	881.6
10	-10	-3	4896		
11	-10	-3	4154		
12	-10	-3	4107		
13	-10	-3	6835		
14	-10	-3	5276		
15	-10	-3	5165		
16	-10	-3	5285		
17	-10	-10	1517	4742.2	1899.1
18	-10	-10	2774		
19	-10	-10	7435		
20	-10	-10	6345		
21	-10	-10	5454		
22	-10	-10	4466		
23	-10	-10	5455		
24	-10	-10	4491		
25	-10	-20	5938	4903.3	1349.1
26	-10	-20	3856		
27	-10	-20	6675		
28	-10	-20	7453		
29	-10	-20	5334		
30	-10	-20	3456		
31	-10	-20	4984		
32	-10	-20	4836		
33	-20	-20	7128	5054.2	1777.2
34	-20	-20	2767		
35	-20	-20	3565		
36	-20	-20	4320		
37	-20	-20	6637		
38	-20	-20	7456		
39	-20	-20	4675		
40	-20	-20	3965		

**Table 5.9.** Young's modulus of atmospheric ice.

T<sub>a</sub>= Accumulation temperature, T<sub>t</sub>= Test temperature.

The average value of Young's modulus of various types of atmospheric ice obtained at strain rates close to  $10^{-3}\text{s}^{-1}$  tabulated in Table 5.9. Figure 5.34 shows the results of the measurement of the Young's modulus of atmospheric ice accumulated at  $-10^{\circ}\text{C}$  and tested at various temperatures. According to these tests, the Young's modulus of atmospheric ice accumulated at  $-10^{\circ}\text{C}$  is 5.01GPa, 4.74 GPa and 4.9 GPa at test temperatures  $-3^{\circ}\text{C}$ ,  $-10^{\circ}\text{C}$

and  $-20^{\circ}\text{C}$ , respectively. Although these values are in the range of some other investigators for fresh water ice, they are not in agreement with the values of Young's modulus that Eskandarian (2005) calculated using Hill's averaging technique (Hill, 1952) for atmospheric ice. The value of Young's modulus in his work is obtained by:

$$E_p^{S2} = 9.363(1 - 1.471 \times 10^{-3} \theta)$$

where  $\theta$  denotes the temperature in  $^{\circ}\text{C}$  and "p" stands for "in-plane" of isotropy direction. Therefore, the value of young's modulus for the temperatures between  $-3^{\circ}\text{C}$  and  $-20^{\circ}\text{C}$  is in the range of 9.4 GPa and 9.64GPa.

Figure 5.35 shows the variation of Young's modulus of atmospheric ice accumulated at various temperatures and tested at their accumulation temperature. According to these tests, the average Young's modulus of atmospheric ice accumulated at  $-6^{\circ}\text{C}$  and  $-20^{\circ}\text{C}$  is 3.69 GPa and 5.05 GPa, respectively.

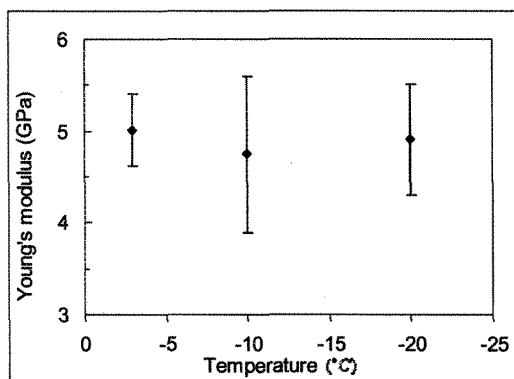


**Figure 5.34.** Young's modulus of atmospheric ice accumulated at  $-10^{\circ}\text{C}$  and tested at various temperatures. The error bars in this figure and Figure 5.35, correspond to the standard error in the results for the tests conducted at each set of parameters.

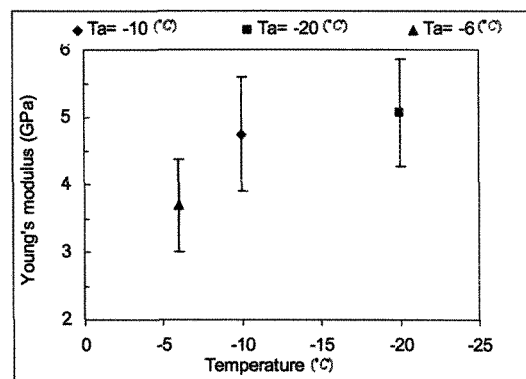


**Figure 5.35.** Young's modulus of atmospheric ice accumulated and tested at various temperatures.

Figure 5.36 shows the stress strain curve of atmospheric ice at strain rate  $10^{-3} \text{ s}^{-1}$ . The straight line in this curve was used for measuring the Young's modulus.

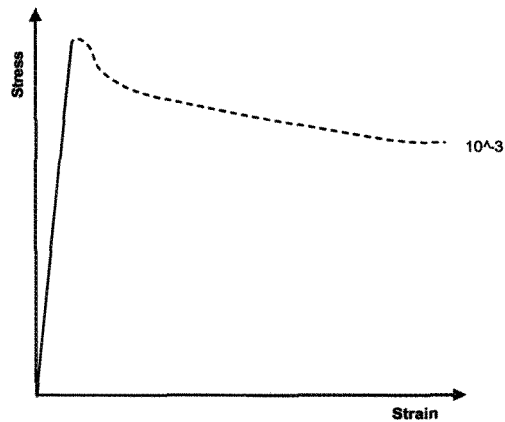


Figure 5.36. Stress-strain curve of atmospheric ice at strain rate  $10^{-3} \text{ s}^{-1}$ .

## 5.6 Conclusion

More than 180 tests have been conducted to measure the compressive strength of atmospheric ice. For the ice accumulated at  $-20^{\circ}\text{C}$ , there are extensive cavities and possibly cracks which can reduce compressive strength. The results of this research show that the compressive strength of atmospheric ice increases with decreasing test temperatures. Also, it was found that ice strength increases with increasing strain rate up to  $10^{-3} \text{ s}^{-1}$ , and then decreases at higher strain rates. Similar observations have been reported in other studies on fresh water ice as well. There is a transition region between strain rates  $10^{-4} \text{ s}^{-1}$  and  $10^{-2} \text{ s}^{-1}$  where the ice may break through cracking when it is brittle, or fail due to viscous strains when it is ductile. Owing to the presence of air bubbles in atmospheric ice and the small size and shape of our specimens, its compressive strength is less than that of fresh water ice reported by other researchers. In comparing the compressive strengths of the three types of

atmospheric ice, it was found that at low strain rates, compressive strength increases with decreasing accumulation temperatures. At higher strain rates, however, owing to the activation of cracks, the compressive strength of ice accumulated at  $-20^{\circ}\text{C}$  is less than the one accumulated at  $-10^{\circ}\text{C}$ .

More than 120 tests were carried out to measure the bending strength and effective modulus of atmospheric ice. The results of these tests show that at lower strain rates, the strength of the ice increases with decreasing temperatures but no temperature effect is seen at the higher strain rates. It is also observed that, depending on the temperature, increasing the strain rate can increase or decrease the ice strength. In view of these observations, the flexural strength behaviour of ice, with respect to temperature and strain rate, needs further investigation.

The bending strength of atmospheric ice accumulated at  $-10^{\circ}\text{C}$  has been found to be higher than that of the two other types of atmospheric ice, due to its stronger structure owing to its smaller grain size and its relative lack of cavities. Also, it has been found that the bending strength of atmospheric ice accumulated at  $-20^{\circ}\text{C}$  decreases with increasing strain rates. The effective modulus of atmospheric ice has been found to increase with increasing strain rates. At higher strain rates for the ice accumulated at  $-20^{\circ}\text{C}$  and tested at the same temperature, the effective modulus is less than the two other ice types. Owing to structural differences between atmospheric ice and fresh water ice, and also to differences in grain size and specimen dimensions in the various previous studies, some differences between our results and those of other researchers on fresh water ice have been observed.

To measure the fracture toughness of various types of atmospheric ice, 25 tests were conducted. The results show that fracture toughness of atmospheric ice decreases with decreasing accumulation temperature. At very cold temperatures (around  $-20^{\circ}\text{C}$ ), the fracture toughness of atmospheric ice increases owing to higher strength. However, the fracture toughness of atmospheric ice accumulated at  $-20^{\circ}\text{C}$  and tested at its accumulation temperature is less than other types because the cavities and possible cracks in this ice lower its resistance against crack propagation.

Despite the fact that the measurement of Young's modulus by static loading has associated errors, attempts were made to measure this value. According to these tests, the average Young's modulus of atmospheric ice accumulated at  $-6^{\circ}\text{C}$ ,  $-10^{\circ}\text{C}$  and  $-20^{\circ}\text{C}$  is 3.69 GPa, 4.74 GPa and 5.05 GPa, respectively.

## CHAPTER 6

### CRACK PROPAGATION IN ICE

#### 6.1 Introduction

In the previous chapters, the dependency of the mechanical properties of atmospheric ice on different factors such as accumulation temperature, accumulation condition (wind velocity, liquid water content of air and mass mean diameter of supercooled droplets during ice accretion), test temperature, ice structure, grain size and loading rate was explained. The ductile, transition and brittle regimes of ice under compressive and tensile stress were also clarified. Experimental observations have confirmed that internal cracking is the physical mechanism responsible for the transition that occurs within a narrower range of lower strain rate in tension than in compression (approximately  $10^{-7}$ - $10^{-6}$  s<sup>-1</sup> in tension and  $10^{-4}$ - $10^{-2}$  s<sup>-1</sup> in compression) [42]. These two modes sometimes are called non-fractural (non-cracking or ductile) and fractural (cracking). This research work only focuses on the brittle behaviour of ice, which is characterized by elastic deformation followed by a sudden fracture. The elastic deformation is caused primarily by changes in intermolecular distances under the applied stresses, and under these circumstances, there is no permanent plastic deformation, which would have been induced by the movement of dislocations. Prior to ice fracture, two steps should take place; crack nucleation and then crack propagation.

#### 6.2 Crack nucleation in ice

True crack nucleation without pre-existing precursors requires that stresses be locally concentrated to levels matching the theoretical cleavage or cohesive strength. There are several candidate mechanisms for this concentration of stress: dislocation pile-up, grain boundary sliding, thermal expansion of extraneous inclusions, elastic anisotropy of the ice crystals and stress concentration at interior flaws (Forest and Colloge, 1995).

At low strain rates (or low stresses), crack initiation was understood in terms of either dislocation pile-up (Gold, 1972) or grain boundary sliding (Sinha, 1984). The behaviour of dislocations at high stresses is poorly known. Gold (1972) has observed the microcrack density during compressive creep of columnar-grained polycrystalline ice and suggested the existence of two crack types on the basis of a statistical analysis. The probability of nucleation for one type of crack increases directly with creep strain. He proposes that stress concentration due to dislocation pile-up is responsible for the first crack type, while the second type is formed by the growth of nuclei due to diffusion or a gradually increasing local stress. The latter type forms mainly at grain boundaries and is characteristic of purely brittle behaviour. Sinha (1984) postulated that grain boundary sliding causes stress concentration at triple points between grains and at jogs at the boundaries, and, consequently, crack nucleation. There is as yet no consensus in the ice literature as to which of the mechanisms is responsible for the nucleation of strain-dependent microcracks. Sunder and Mao (1990) found that elastic anisotropy might govern crack nucleation in tension over a wide range of strain rates. They also reported that the required stress for crack nucleation in compression greatly depends on crystal orientation. Owing to random orientation of crystals in isotropic polycrystalline ice, there can be a distinct beginning and

end to the microcrack nucleation phase when stress is increased and if failure does not occur prematurely.

Elastic anisotropy leads to stress concentrations in an athermal manner and therefore becomes more important at very low temperatures and high strain rates (Gold, 1972). Cole (1989) suggested that stress concentration at grain boundary ledges could result in crack nucleation at high rates of loading.

Kalifa *et al.* (1991), in their experiments using uniaxial compression, found that the critical stress for initial crack nucleation increases strongly with decreasing temperature and exhibits a linear increase with  $d_g^{-1/2}$  (where  $d_g$  is the average grain-size). Schulson (2001) postulated that in tensile tests, cracks nucleate once the inelastic strain, and thus the local tensile stress, reaches a level sufficiently great to overcome intermolecular cohesion.

For solving the problem of an extending precursor in a combined stress field, several solutions, such as the maximum principal stress criterion of Erdogan and Sih (1963) and the minimum strain energy density factor criterion of Sih (1974), can be adopted. In the maximum principal stress approach, critical stress intensity defines the initiation stress, while the direction of extension is postulated to occur in a direction perpendicular to the local maximum tensile stress. In the minimum strain energy density approach, the critical strain energy density factor specifies both the initiation stress and the direction of extension. Sunder and Mao (1990) presented a crack nucleation criterion based on the latter approach for crack nucleation under pure mode I loading in isotropic polycrystalline ice. According to this model, precursors will begin to grow when microscopic fracture toughness reaches a critical value given by:

$$K_{IC} = \left( \frac{2E\gamma}{1-\nu^2} \right)^{\frac{1}{2}} \text{ For plain strain} \quad (6.1)$$

$$K_{IC} = (2E\gamma)^{\frac{1}{2}} \text{ For plain stress} \quad (6.2)$$

where  $\gamma$  is the grain boundary surface energy  $\gamma_{gb}$ , if extension occurs along a boundary facet,  $\gamma$  is the solid vapour surface energy  $\gamma_{sv}$ , if the microcrack extends into the crystal,  $\gamma_{gb}$  is  $0.065 \text{ J.m}^{-2}$  and  $\gamma_{sv}$  is  $0.109 \text{ J.m}^{-2}$  (Sunder and Mao, 1990)

### 6.3 Crack propagation

The presence of cracks and other imperfections (flaws, voids, etc.) in a material may weaken it and cause a premature failure at stresses below the material's yield strength, in cases where failure would not normally occur. Therefore, predicting the behaviour of materials containing cracks requires a special methodology called fracture mechanics. The fundamental principal of fracture mechanics is that a stress field ahead of a sharp crack in a material can be characterized in terms of the stress intensity factor ( $K$ ). Fracture mechanics can be subdivided into two general categories, namely Linear-Elastic and Elastic-Plastic. Linear-Elastic Fracture Mechanics (LEFM) technology is based on an analytical procedure that relates the stress-field magnitude and distribution in the vicinity of a crack tip to the nominal stress applied to the specimen, to the size, shape and orientation of the crack-like discontinuity and to material properties.

Cracks within fine grain materials do not propagate immediately upon nucleation. The applied stress must increase until the mode I stress intensity factor reaches the critical level. During this process, more inelastic deformation occurs and more cracks nucleate. The size

of a crack at a given temperature depends on the applied stress and the microstructural characteristics of the polycrystalline aggregate, such as the orientation, shape and size of the grains. Under certain conditions, these cracks propagate only a short distance before coming to rest within the material. Given sufficiently high stress levels, the cracks can propagate through the material to cause brittle fracture.

Griffith (1921) formulated a fracture criterion based on the hypothesis of a strain energy release rate. He proposed that cracks start propagating when the strain energy release rate reaches or exceeds a critical value, which equals the energy required to form a new surface. Experiments have shown that Griffith's criterion applies well to brittle materials. However, the same experiments have revealed a need for a modified criterion for ductile materials. He based his theory on the hypothesis that brittle materials contain elliptical microcracks of length  $2a$  oriented perpendicular to the maximum principal stress, which present high stress concentrations near their tips. He developed a relationship between crack length ( $a$ ), surface energy connected with traction-free crack surfaces ( $2\gamma$ ), and stress applied to the propagation of a crack in a brittle material:

$$\sigma^2 = 2\gamma E / \pi a \quad (6.3)$$

It was found that the stress field in the area of the crack tip for a simple through thickness crack is completely determined by the quantity  $K$  (stress intensity factor)  $K_I = \sigma \sqrt{\pi a}$ . Subscript  $I$  in the parameter  $K$  refers to mode  $I$  loading, the opening mode. Other modes of deformation at a crack tip are mode  $II$  (sliding mode) and mode  $III$  (tearing mode). The relationship between  $K_I$  and  $\sigma$  depends on crack geometry, body

configuration and loading condition. A crack propagates when the value of stress intensity factor reaches a critical value called critical stress intensity factor  $K_{IC}$ . The fracture energy is the energy necessary to create a unit crack surface and it represents a fracture property with the tensile strength  $f_t$  and the softening law.

Orowan (1950) suggested that the work available for crack propagation in ductile and viscous materials should be equated to the sum of the surface energy and the work associated with plastic and viscous flow. Acoustic and dilatometric studies show that compression cracks start to propagate when the axial compressive stress reaches about one half of the ultimate failure stress, and microscopic observations show that they extend parallel to the compression axis (Ashby and Hallam, 1986). Even if cracks do not propagate under compressive stress, they are responsible for the gradual weakening of the structure as straining proceeds (Kim and Sunder, 1997).

A coordinate system for describing the stresses in the vicinity of a crack is shown in Figure 6.1. For any case of Mode I loading, the stress field in the vicinity of a crack tip is given by:

$$\sigma_x = \frac{K_I}{\sqrt{2\pi r}} \cos \frac{\theta}{2} \left[ 1 - \sin \frac{\theta}{2} \sin \frac{3\theta}{2} \right] + \dots \quad (6.4)$$

$$\sigma_y = \frac{K_I}{\sqrt{2\pi r}} \cos \frac{\theta}{2} \left[ 1 - \sin \frac{\theta}{2} \sin \frac{3\theta}{2} \right] + \dots \quad (6.5)$$

$$\tau_{xy} = \frac{K_I}{\sqrt{2\pi r}} \cos \frac{\theta}{2} \sin \frac{\theta}{2} \cos \frac{3\theta}{2} + \dots \quad (6.6)$$

$$\sigma_z = 0 \quad (\text{plane stress}) \quad (6.7)$$

$$\sigma_z = \nu(\sigma_x + \sigma_y) \quad (\text{plane strain}) \quad (6.8)$$

$$\tau_{zy} = \tau_{zx} = 0 \quad (6.9)$$

where  $K_I$  is the stress intensity factor of the crack and depends on length, geometry and position of the crack. The polar coordinate  $r$  and  $\theta$  lie in the x-y plane, which is normal to the crack. The  $z$  -direction is parallel to the leading edge of the crack (Dowling, 1998). This equation predicts that the stresses rapidly increase near the crack tip. The general equation of the stress field around the crack tip when all three loading modes, I, II and III, are active is given by (Williams, 1957):

$$\sigma_{ij} = \frac{K_I}{\sqrt{2\pi r}} f_{ij}^I(\theta) + \frac{K_{II}}{\sqrt{2\pi r}} f_{ij}^{II}(\theta) + \frac{K_{III}}{\sqrt{2\pi r}} f_{ij}^{III}(\theta) + T\delta_{ij} + (\nu T + E\varepsilon_{33})\delta_{3i}\delta_{3j} + O(r^{1/2}) \quad (6.10)$$

where  $r$  and  $\theta$  are the in-plane polar coordinates centred at the crack tip,  $\sigma_{ij}$  denotes the stress tensor,  $K_I$ ,  $K_{II}$ ,  $K_{III}$  are the modes I, II and III stress intensity factors, respectively,  $T$  is the nonsingular elastic T-stress,  $\varepsilon_{33}$  is the extensional strain along the crack front,  $f_{ij}(\theta)$  are the angular functions and can be found in several references (e.g. Eftis *et al.*, 1977),  $O(r^{1/2})$  is the auxiliary displacement field and  $\delta_{ij}$  is the Kronecker delta. The local axes are defined so that the 1-axis lies in the plane of the crack at the point of interest on the crack front and is perpendicular to the crack front at this point; the 2-axis is normal to the plane of the crack (and thus is perpendicular to the crack front); and the 3-axis lies tangential to the crack front. In plane strain  $\varepsilon_{33} = 0$ ; in plane stress the term  $(\nu T + E\varepsilon_{33})\delta_{3i}\delta_{3j}$  vanishes.

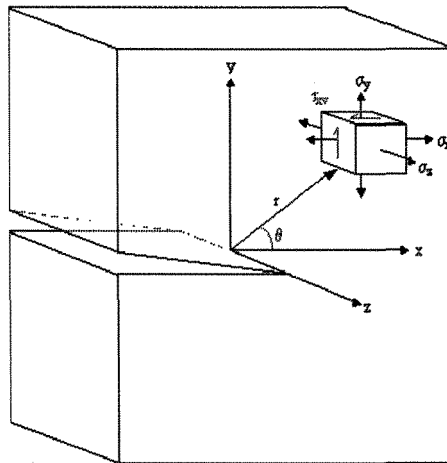


**Figure 6.1.** Describing the stresses in the vicinity of a crack.

The elastic  $T$ -stress is an important parameter that describes stress states near the crack tip and is used as an indicator of the extent to which parameters like the  $J$ -integral are useful characterizations of the deformation field around the crack. The size and shape of the plastic zone of the plane strain crack-tip and the crack tip constraint depend on the sign and magnitude of the  $T$ -stress.  $T$ -stress, in combination with the stress intensity factors (SIFs), ensures a two-parameter characterization of linear elastic crack tip fields. The subject of  $T$ -stress usually arises in the discussions of crack stability and kinking for linear elastic materials. For small amounts of crack growth under Mode I, loading, a straight crack path has been shown to be stable when  $T < 0$ . Otherwise the path will be unstable and will therefore deviate from being straight when  $T > 0$ . A similar trend has been found in three-dimensional crack propagation.  $T$ -stress also has an important effect on brittle fracture under mixed mode I/II loading, such that a combination of singular term (characterized by  $K_I$  and  $K_{II}$ ) and  $T$ -stress controls the crack extension. There are various methods for calculating  $T$ -stress from finite element analysis. Some of these methods were reviewed by

Ayatollahi *et al.* (1998) and Sherry *et al.* (1995) and one of them is explained in Appendix B.

#### 6.4 Prediction of the direction of crack propagation

There are several criteria for the prediction of brittle fracture under mixed mode loading. These criteria can be used for predicting the direction of crack propagation. The maximum tangential stress criterion (Erdogan and Sih, 1963), the maximum principal stress criterion (Maiti and Smith, 1983), the maximum energy release rate criterion (Palaniswamy and Knauss, 1978, and Hussain *et al.* (1974), the minimum strain energy density factor criterion of Sih (1974) and the T-criterion (Theocaris, 1982) are the most important ones. These criteria predict slightly different angles for the initial crack propagation, but they all have the implication that  $K_{II} = 0$  at the crack tip as the crack extends (Cotterell and Rice, 1980). The three most important criteria are explained briefly in the following paragraphs.

##### 6.4.1 Maximum tangential stress criterion

The near-crack-tip stress field for a homogeneous, isotropic linear elastic material is given by

$$\sigma_{\theta\theta} = \frac{1}{\sqrt{2\pi r}} \cos \frac{1}{2}\theta (K_I \cos^2 \frac{1}{2}\theta - \frac{3}{2} K_{II} \sin \theta) \quad (6.11)$$

$$\tau_{r\theta} = \frac{1}{\sqrt{2\pi r}} \cos \frac{1}{2}\theta [K_I \sin \theta + K_{II} (3 \cos \theta - 1)] \quad (6.12)$$

where  $r$  and  $\theta$  are polar coordinates centred at the crack tip in a plane orthogonal to the crack front. The direction of crack propagation can be obtained using either the condition  $\partial\sigma_{\theta\theta}/\partial\theta = 0$  or  $\tau_{r\theta} = 0$ ; i.e.,

$$\hat{\theta} = \cos^{-1} \left( \frac{3K_{II}^2 + \sqrt{K_I^4 + 8K_I^2 K_{II}^2}}{K_I^2 + 9K_{II}^2} \right) \quad (6.13)$$

where the crack propagation angle  $\hat{\theta}$  is measured with respect to the crack plane.  $\hat{\theta} = 0$  represents the crack propagation in the “straight-ahead” direction.  $\hat{\theta} < 0$  if  $K_{II} > 0$ , while  $\hat{\theta} > 0$  if  $K_{II} < 0$ .

#### 6.4.2 Maximum energy release rate criterion

Figure 6.2 shows a crack segment of length  $a$  kinking out of the plane of the crack at an angle  $\hat{\theta}$ . When  $a$  is infinitesimally small compared to all other geometric lengths (including the length of the parent crack), the stress intensity factors  $K_I^k$  and  $K_{II}^k$  at the tip of the crack can be expressed as linear combinations of  $K_I$  and  $K_{II}$ , the stress intensity factors existing prior to kinking for the parent crack:

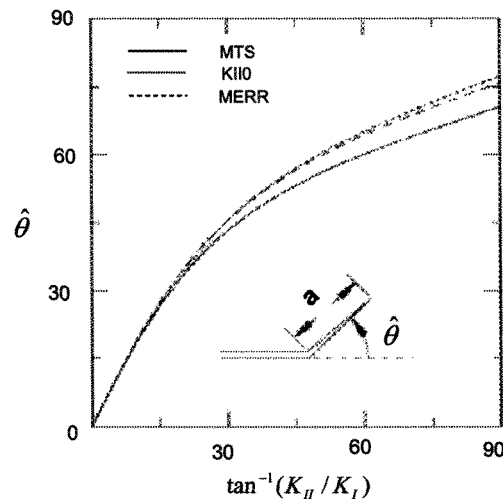


Figure 6.2. Contour for the evaluation of the  $J$ -integral.

$$K_I^k = c_{11}K_I + c_{12}K_{II} \quad (6.14)$$

$$K_{II}^k = c_{21}K_I + c_{22}K_{II} \quad (6.15)$$

The  $\hat{\theta}$ -dependences of the coefficients  $c_{ij}$  are given by Hayashi and Nemat-Nasser (1981) and by He and Hutchinson (1989).

For the crack segment we also have the relation

$$G^k = \frac{1}{E}(K_I^{k2} + K_{II}^{k2}) \quad (6.16)$$

The maximum energy release rate criterion postulates that the parent crack initially propagates in the direction that maximizes  $G^k$ .

#### 6.4.3 $K_{II} = 0$ criterion

This criterion postulates that a crack will initially propagate in the direction that makes  $K_{II}^k = 0$ . It can be seen from Figure 6.2 that the maximum energy release rate criterion and this criterion predict nearly coincident crack propagation angles. By comparison, the maximum tangential stress criterion predicts smaller crack propagation angles.

### 6.5 Modeling the Crack Propagation in Atmospheric Ice

#### 6.5.1 Model characteristics

The crack propagation in atmospheric ice was modeled by analyzing the quasi-static crack growth in a two dimensional three-point beam (planar and axisymmetric). An edge

crack in a three-point bend specimen in plane strain, subjected to Mode I loading, was considered (Figure 6.3). The crack length to specimen width ratio was 0.5. The length of the specimen and its width were 128 mm 40 mm, respectively.

The specimen was subjected to bending loads in such a way that initially a plastic zone developed for the stationary crack. Subsequently, the crack was allowed to grow. To model the specimen geometry, two distinct initially bonded contact surfaces were defined, between which the crack propagates. This model can use three types of fracture criteria, which are critical stress at a certain distance ahead of the crack tip, critical crack opening displacement and crack length versus time. The presented results in this text used the critical stress criterion. This criterion is typically used for crack propagation in brittle materials. The critical stress criterion is defined as

$$f = \sqrt{\left(\frac{\sigma_z}{T}\right)^2 + \left(\frac{\tau_{xz}}{S}\right)^2 + \left(\frac{\tau_{yz}}{S}\right)^2} = 1 \quad \text{for } \sigma_z > 0 \quad (6.17)$$

where  $\sigma_z$  is the normal stress, and  $\tau_{xz}$  and  $\tau_{yz}$  are shear stress components in the interface. T and S are the nominal normal tensile and shear strengths, respectively. In this two-dimensional analysis, the second component of the shear failure stress,  $\tau_{yz}$ , is not applicable.

The distance ahead of the crack tip was measured along the slave surface. The stresses at the specified distance ahead of the crack tip were obtained by interpolating the values at the adjacent nodes. Due to symmetry, only one-half of the specimen is analyzed. The crack tip was modeled as initially blunted so that finite deformation effects near the crack tip can be

taken into account. The mesh was composed of 551 CPS4R elements (Figure 6.4). A reasonably fine mesh, necessary to obtain a smooth load versus crack length relation, was used to model the area in which the plastic zone grows and crack propagation occurs.

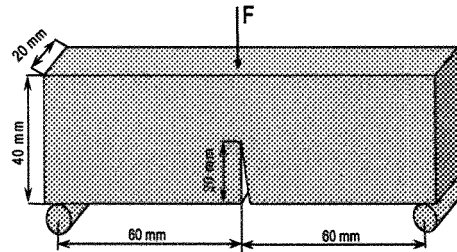


**Figure 6.3.** The three-point beam subjected to Mode I

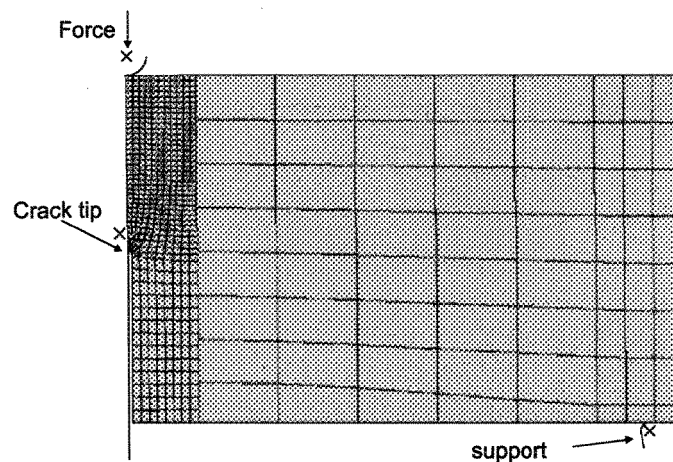


**Figure 6.4.** Finite element mesh for the three-point bend specimen.

Potential crack surfaces were modeled as slave and master contact surfaces. The predetermined crack surfaces were assumed to be initially partially bonded, so that the crack tips can be identified explicitly by ABAQUS/Standard.

An initial condition was defined to identify which part of the crack was initially bonded. The slave surface, the master surface, and a node set that identifies the initially bonded part

of the slave surface were specified. The un-bonded portion of the slave surface behaves as a regular contact surface.

After de-bonding, the traction between the two surfaces is initially carried as equal and opposite forces at the slave node and the corresponding point on the master surface. This force is reduced to zero with time after de-bonding starts at a particular node on the bonded surface. To specify this, a relative amplitude is defined as a function of time after de-bonding starts at a node. Thus, we suppose the force transmitted between the surfaces at slave node  $N$  is  $T^N|_0$  when that node starts to de-bond at time  $t^N|_0$ . Then, for any time  $t > t^N|_0$  the force transmitted between the surfaces at node  $N$  is  $a(t-t^N|_0)T^N|_0$ . The relative amplitude must be 1.0 at the relative time 0.0 and must reduce to 0.0 at the last relative time point given.

Once complete de-bonding has occurred at a point, the bond surfaces act like standard contact surfaces with associated interface characteristics.

Crack propagation analysis is carried out on a nodal basis. The crack-tip node de-bonds when the fracture criterion  $f$  (Equ. 6.17), reaches the value 1.0 within a given tolerance:

$$1 - f_{tol} \leq f \leq 1 + f_{tol} \quad (6.18)$$

The loading point and the support points for the specimen were simulated by analytical rigid surfaces, as shown in Figure 6.4. A concentrated nodal force was applied to the reference node of the rigid surface, which applies the force at the middle of the beam.

In this model, the temperatures can be specified as predefined fields. The specified temperature affects temperature-dependent critical stress.

Regular rectangular mesh CPS4R, which gives good results in crack propagation analyses, was chosen for this model. The Young's modulus of atmospheric ice is  $E=9.31$  GPa and Poisson's ratio of 0.319 (Eskandarian, 2005). The analysis was carried out in two stages. The first stage consisted of pushing the rigid surface 0.001 mm into the specimen. No crack growth was specified during this stage. In the second stage, the crack was allowed to propagate while the nodal force was applied at the middle of the beam. Once a crack-tip node de-bonded, the traction at the tip was initially carried as a reaction force at that node. This force was ramped down to zero according to the pre-defined amplitude curve. The manner in which the forces at the de-bonded nodes were ramped down greatly influenced the convergence of the solution.

### 6.5.2 Results and discussion

Figure 6.5 shows a plot of force versus time before starting the crack propagation. The fracture test of five ice samples with the dimensions as shown in Figure 6.3 shows that the force for crack propagation in this three-point beam test ranges from 51.5 N to 64.5 N. According to the model of crack propagation, this force is 58.5 N, which shows a 97% agreement with the average of ice tests.

Figure 6.6 shows the variation of normal stress in some elements, which break one after another due to crack propagation. As shown in this figure, in the beginning the stress simply increases in each element. When it reaches the failure stress (about 2.73 MPa), the crack propagates and the de-bonded element is eliminated in the analysis, then the stress increases in the next node until failure stress. This process continues until the de-bonding of the last node. The difference between fracture time and the required force for starting the

crack propagation emanates from the difference between specimen dimensions and the crack geometry of ice samples and the model. Furthermore, high sensitivity of the ice to test conditions can play an important role in this difference.

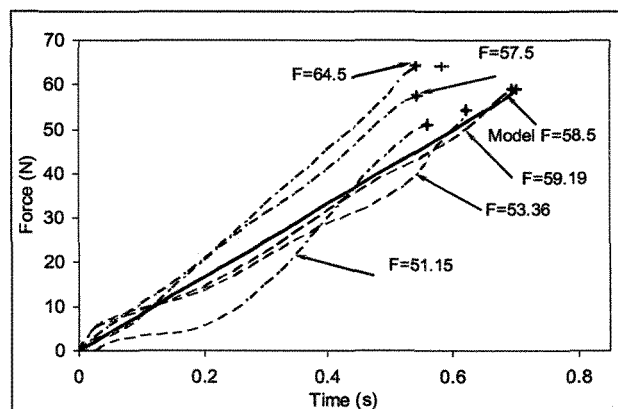


**Figure 6.5.** Comparison between the values of force required for crack propagation in the model and five ice tests.

Contours of the normal stress in the four steps of crack propagation in the model are shown in Figure 6.7.

According to the results of this model, the crack propagation speed in atmospheric ice is 0.093 m/s. This value is considerably less than the value obtained in our high-speed video observation tests (discussed in Chapter 9). This originates from this model's use of the basic theories of crack propagation, which shows the stress variation around the crack tips. It would appear that the calculation of the crack propagation speed in this model is not reliable enough to compare its results with actual tests.

This two dimensional model simulates the crack propagation in atmospheric ice and can be useful for estimating the required force for crack growth and studying the plastic zone

around the crack during its propagation. In more sophisticated loading conditions, where the prediction of the crack path is difficult, such models would be helpful.

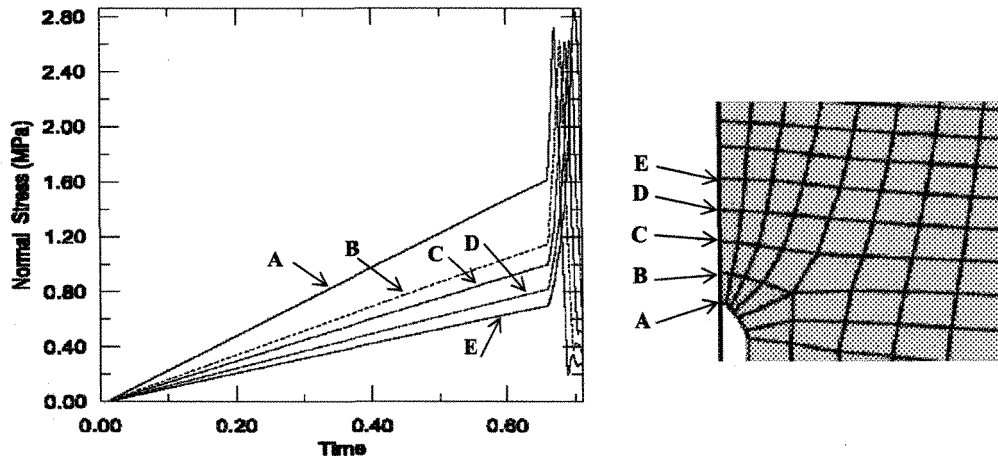


Figure 6.6. The variation of normal stress in several nodes before and after crack propagation.

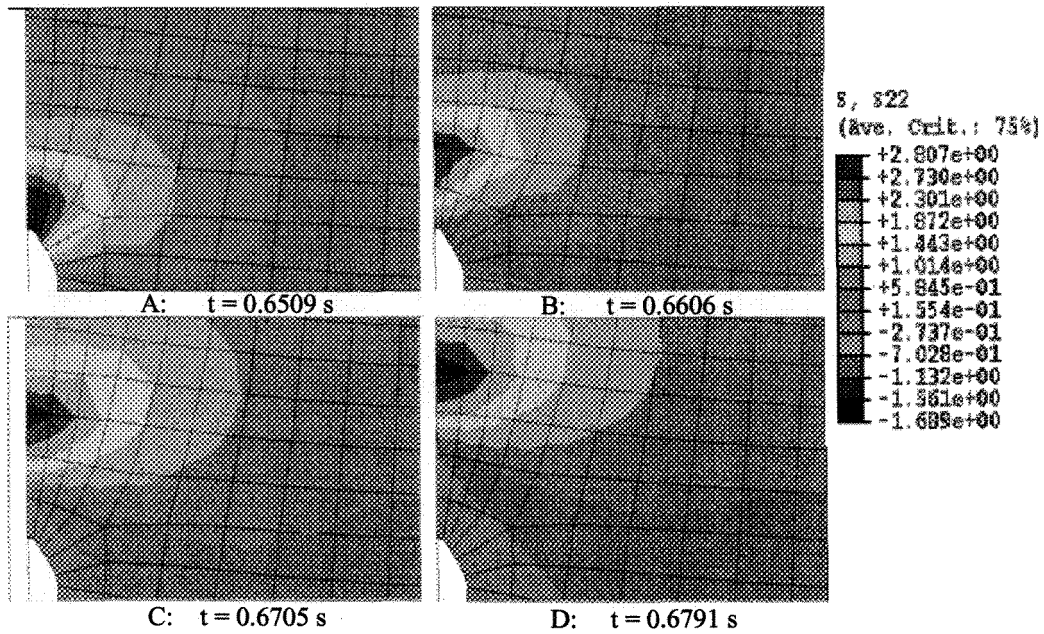


Figure 6.7. Contours of normal stress during crack propagation.

## 6.6 Conclusion

Ice shows ductile and brittle behaviour under loading conditions. For ice to fracture, two steps must take place: crack nucleation and then crack propagation. There are several candidate mechanisms for crack nucleation, but dislocation pile up, grain boundary sliding and elastic anisotropy of the ice crystals are the most important ones. There is as yet no consensus in the ice literature as to which of the mechanisms is responsible for the nucleation of strain-dependent microcracks. Many researchers believe that at low strain rates dislocation pile up or grain boundary sliding is responsible for crack nucleation; at high strain rates, elastic anisotropy or grain boundary sliding is responsible for crack nucleation; and during a thermal excursion, thermal expansion of extraneous inclusions is responsible for crack nucleation.

The crack propagation in atmospheric ice was modeled using ABAQUS finite element software by analyzing the quasi-static crack growth in a two dimensional three-point beam. Potential crack surfaces were modeled as slave and master contact surfaces. The predetermined crack surfaces were assumed to be initially partially bonded so that the crack tips could be identified explicitly by ABAQUS/Standard. The result of the ABAQUS model in prediction of the force required for crack propagation showed good agreement with the experimental tests.

This model is useful for simulating crack growth in more sophisticated loading conditions, where the prediction of the crack path is difficult.

## CHAPTER 7

### THE ELASTIC-CRACKING MODEL

#### 7.1 Introduction

Many mathematical models have been developed to describe the cracking or non-cracking constitution of ice. Conceptually, in the models, efforts are made to describe the ice constitution in a series of explicit rate equations adequate for numerical calculation. However, ice constitutive models may also be derived from a Helmholtz free energy based on some thermodynamic states and internal variables (e.g. Sjolind, 1987; Sunder *et al.*, 1989). Some of the models have been developed particularly for damage formulation and crack propagation (e.g. Sunder and Wu, 1990a; Xiao and Jordaan, 1996; Kim and Sunder, 1997), while the rest are developed in a more general manner for describing the various stages of creep (e.g. Sinha, 1983; Fish, 1991; Zhan *et al.*, 1994; Derradji-Aouat *et al.*, 2000). Some conclusions of these viscoelastic models were reviewed by Eskandarian (2005).

The only model of the behaviour of atmospheric ice was developed by Eskandarian (2005), which is a non-cracking one for viscoelastic behaviour of atmospheric ice. According to Eskandarian's model, the total strain can be divided into the elastic ( $\varepsilon^e$ ) and inelastic ( $\varepsilon^{ie}$ ) parts, provided that the elastic strain is infinitesimal. The elastic part is recoverable and is associated with lattice deformation, while the inelastic part can be

decomposed into a viscoelastic (delay elastic) part ( $\varepsilon^{ve}$ ), a steady-state (plastic) flow ( $\varepsilon^p$ ), and a crack-activity part ( $\varepsilon^c$ ). The viscoelastic part stems from the structural changes associated with the elastic back-stress and drag-stress generated during kinematic and isotropic hardening. The plastic part results from intra-granular mechanism of plastic deformation.

$$\varepsilon = \varepsilon^e + \varepsilon^{ic} = \varepsilon^e + \varepsilon^{ve} + \varepsilon^p + \varepsilon^c \quad (7.1)$$

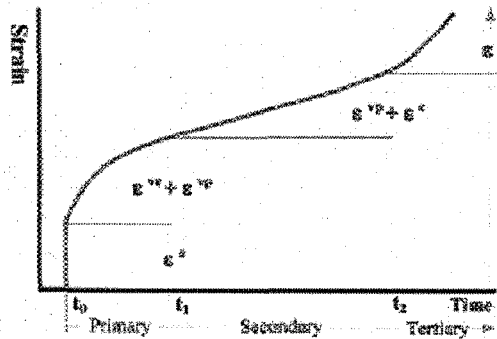


Figure 7.1. A typical strain history for ice in uniaxial loading (Eskandarian, 2005).

According to this model the strain of crack-activity is negligible. Hooke's law of elasticity relates the strain field to the corresponding stress applied to a monocrystal by (Eskandarian, 2005):

$$\{\hat{\varepsilon}^e\} = [\hat{S}]\{\hat{\sigma}\} \quad \text{or} \quad \{\hat{\sigma}\} = [\hat{C}]\{\hat{\varepsilon}^e\} \quad (7.2)$$

where the superscript e refers to elastic deformation, the hat symbol (^) denotes the principal monocrystal values,  $\hat{S}_{ij}$  are the principal elastic compliance components of the material,  $\hat{\varepsilon}_{ij}$  are the tensorial components of the strain tensor in a monocrystal principal coordinate, and  $\hat{\gamma}_{ij}$  are the engineering components of shear strain in a monocrystal coordinate system.

$$\{\hat{\varepsilon}^e\} = \begin{bmatrix} \hat{\varepsilon}_{11}^e \\ \hat{\varepsilon}_{22}^e \\ \hat{\varepsilon}_{33}^e \\ \hat{\gamma}_{23}^e \\ \hat{\gamma}_{13}^e \\ \hat{\gamma}_{12}^e \end{bmatrix} \quad (7.3)$$

$$[\hat{S}] = \begin{bmatrix} \hat{S}_{11} & \hat{S}_{12} & \hat{S}_{13} & 0 & 0 & 0 \\ \hat{S}_{12} & \hat{S}_{11} & \hat{S}_{13} & 0 & 0 & 0 \\ \hat{S}_{13} & \hat{S}_{13} & \hat{S}_{33} & 0 & 0 & 0 \\ 0 & 0 & 0 & \hat{S}_{44} & 0 & 0 \\ 0 & 0 & 0 & 0 & \hat{S}_{44} & 0 \\ 0 & 0 & 0 & 0 & 0 & 2(\hat{S}_{11} - \hat{S}_{12}) \end{bmatrix} \quad (7.4)$$

$$\{\hat{\sigma}\} = \begin{bmatrix} \hat{\sigma}_{11} \\ \hat{\sigma}_{22} \\ \hat{\sigma}_{33} \\ \hat{\sigma}_{23} \\ \hat{\sigma}_{13z} \\ \hat{\sigma}_{12} \end{bmatrix} \quad (7.5)$$

The elastic properties are characterized by the effective Young's and shear moduli, as well as the effective Poisson's ratio for a large number of grains whose c-axes are randomly oriented.

Sinha (1978) proposed an expression for short-term viscoelastic strain under constant stress in freshwater ice. To take into account the effect of air bubbles and porosities, Sinha's formulation was adjusted by replacing the deviatoric elastic strain with the effective poroelastic strain  $\varepsilon_{ij}^e$  that results in:

$$d\varepsilon_{ij}^{ve} = \frac{(1 + d\lambda^{ve})C_1}{d_g} \{1 - \exp[-(a_T \Delta t)^b]\} (\varepsilon_{ij}^e) \quad (7.6)$$

where  $a_T$  is the temperature dependent parameter,  $b$  is the material constant,  $d_g$  is the grain size, and  $C_1$  is the material constant. The stress tensor was related to the elastic tensor as below:

$$d\sigma_{ij} = C_{ijkl}^{ve} (d\varepsilon_{kl}^e + d\varepsilon_{kl}^{ve}) \quad (7.7)$$

where the viscoelastic tangent material stiffness tensor,  $C_{ijkl}^{ve}$  can be calculated using the following equation:

$$C_{ijkl}^{ve} = \frac{C_{ijkl}}{1 + \frac{(1 + d\lambda^{ve})C_1}{d_g} \{1 - \exp[a_T dt]^b\}} \quad (7.8)$$

In Eskandarian's model, three ingredients determine the state of a plastic deformation: a yield function  $f$  that defines the limit of the region of purely elastic response, a flow rule that determines the plastic strain, and a set of hardening laws. The yield function is an equation, which sets a limit on the stress that can be supported by the material when it deforms elastically. The yield behaviour of atmospheric ice (as a porous material) was modeled with several independent plastic yield systems  $f_x$ , which were written in a general form by:

$$f_x(\sigma, T, \kappa_a^x) = 0 \quad (7.9)$$

in which  $T$  denotes the temperature, and  $\kappa_\alpha^x, \alpha=1,2,\dots,n$  denotes a set of internal-state variables for each yield system. The relationship between the plastic strain increment and the applied stress was defined by the flow rule (Eskandarian, 2005):

$$d\varepsilon_{ij}^p = \sum_{x=1}^N d\lambda_x^p \frac{\partial g_x}{\partial \sigma_{ij}} \quad (7.10)$$

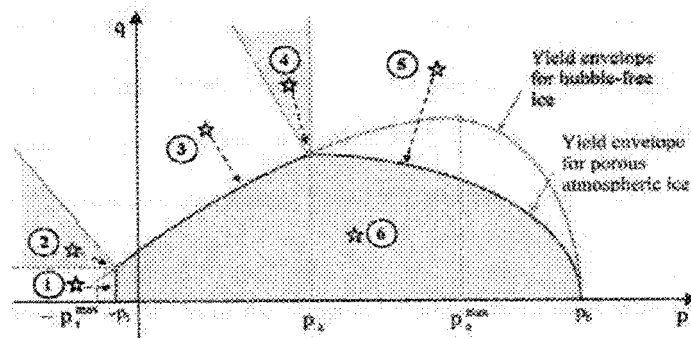


**Figure 7.2.** The modes of cap-model: (1) Pure tension yield, (2) Tension-shear yield, (3) Pure shear yield, (4) Shear cap yield, (5) Pure cap yield, (6) Pure viscoelastic deformation.

where  $g_x$  denotes the potential function,  $\lambda_x^p$ , the plastic consistency parameter of the yield surface  $f_x$ , and  $N$  is the total number of plastic flow systems.

The hardening laws were written in rate form as:

$$dH_\alpha^x = d\lambda_x^p h_\alpha^x(\sigma, T, \kappa_\beta^x) \quad (7.11)$$

where  $H_\alpha^x$  and  $h_\alpha^x$  are the hardening parameters and the hardening functions for  $x^{\text{th}}$  plastic system (related to the yield surface  $f_x$ ), which should be written in rate form.

Figure 7.2 shows the cap-yield envelope of both bubble-free ice and porous atmospheric ice.

The objective of the present study is to develop a model for the cracking activity of atmospheric ice in the brittle regime. To model the cracking activity, one can decompose the strain rate into two parts: elastic and cracking strain rate. The elastic-cracking strain decomposition allows for a separate identification of a cracking strain that represents the state of a crack. The total strain rate can be decomposed as below:

$$d\varepsilon = d\varepsilon^e + d\varepsilon^{ck} \quad (7.12)$$

where  $d\varepsilon$  is the total mechanical strain rate,  $d\varepsilon^e$  is the elastic strain rate and  $d\varepsilon^{ck}$  is the cracking strain rate.

## 7.2 The Elastic Strain

As mentioned above, the recoverable elastic strain is associated with the lattice deformation and is related to the corresponding applied stress by Hooke's law. The principal elastic compliance of a polycrystalline material is determined by taking a spatial average of the elastic constants of all the crystals using a uniform probability density function (Nanthikesan and Sunder, 1994). Eskandarian (2005) obtained the upper and lower boundaries, as well as the average values of polycrystalline elastic constants. He obtained the upper limit of the elastic constants by assuming that all the grains undergo the same uniform strain (Voigt, 1910), and the lower limits of the elastic constants by assuming the uniform stress field for all the grains (Reuss, 1929). He also used Hill's averaging technique (Hill, 1952) and took an algebraic average of the values of the Voigt (1910) and Reuss (1929) assumptions to obtain the elastic constant of polycrystalline ice.

The compliance matrix for polycrystalline materials is:

For Isotropic material:

$$[S] = \begin{bmatrix} \frac{1}{E} & -\frac{\nu}{E} & -\frac{\nu}{E} & 0 & 0 & 0 \\ -\frac{\nu}{E} & \frac{1}{E} & -\frac{\nu}{E} & 0 & 0 & 0 \\ -\frac{\nu}{E} & -\frac{\nu}{E} & \frac{1}{E} & 0 & 0 & 0 \\ 0 & 0 & 0 & \frac{1}{G} & 0 & 0 \\ 0 & 0 & 0 & 0 & \frac{1}{G} & 0 \\ 0 & 0 & 0 & 0 & 0 & \frac{1}{G} \end{bmatrix} \quad (7.13)$$

For transversely isotropic materials:

$$[S] = \begin{bmatrix} \frac{1}{E_p} & -\frac{\nu_p}{E_p} & -\frac{\nu_{pt}}{E_t} & 0 & 0 & 0 \\ -\frac{\nu_p}{E_p} & \frac{1}{E_p} & -\frac{\nu_{pt}}{E_t} & 0 & 0 & 0 \\ -\frac{\nu_{pt}}{E_p} & -\frac{\nu_{pt}}{E_p} & \frac{1}{E_t} & 0 & 0 & 0 \\ 0 & 0 & 0 & \frac{1}{G_p} & 0 & 0 \\ 0 & 0 & 0 & 0 & \frac{1}{G_t} & 0 \\ 0 & 0 & 0 & 0 & 0 & \frac{1}{G_t} \end{bmatrix} \quad (7.14)$$

where all the constants in the above-mentioned matrixes are obtained from Eskandarian (2005).

### 7.3 The cracking strain

To obtain the stress-strain relationship in the presence of a crack, we define a local Cartesian system  $u, v, w$ , which is aligned with the crack directions ( $u$  is normal and  $v$  is

tangential to the crack). The total mechanical strain in the global Cartesian coordinate system in a three-dimensional setting is  $\varepsilon_{ij}^{ck}$ . The strains in the local Cartesian system are:

$$\varepsilon'^{ck} = [\varepsilon'_{uu} \quad \varepsilon'_{vv} \quad \varepsilon'_{ww} \quad \varepsilon'_{uv} \quad \varepsilon'_{uw} \quad \varepsilon'_{vw}] \quad (7.15)$$

The transformation between global and local strains is:

$$\varepsilon_{ij}^{ck} = [T]\varepsilon'^{ck} \quad (7.16)$$

where T is a transformation matrix constructed from the direction cosines of the local cracking coordinate system and is constant in this fixed crack model. Accordingly, the transformation between stresses in global and local cracking systems can be written as:

$$\sigma_{ij}^{ck} = [T]\sigma'^{ck} \quad (7.17)$$

The model neglects any permanent strain associated with cracking. The relationship between the local stresses and the cracking strains at the crack interfaces is:

$$d\sigma'^{ck} = [D^{ck}]d\varepsilon'^{ck} \quad (7.18)$$

where  $[D^{ck}]$  is a diagonal cracking matrix that depends on the state of the existing cracks and  $d\varepsilon'^{ck}$  is the cracking strain rate in the local Cartesian system associated with existing cracks [1]. The definition of the diagonal cracking matrix will be given in the following paragraphs.

### 7.3.1 Crack detection and post-cracking condition

One of the most important aspects in the brittle cracking model is detecting the location where the first crack initiates. A Rankine criterion can be used to detect crack initiation. This criterion, also known as normal stress, Coulomb, or the maximum stress criterion, is

often used to detect crack initiation and to predict the failure of brittle materials. In other words, a crack forms when the maximum (normal) principal tensile stress reaches the uniaxial tension strength. The Rankine crack detection surface is shown in Figure 7.3 in the deviatoric plane.

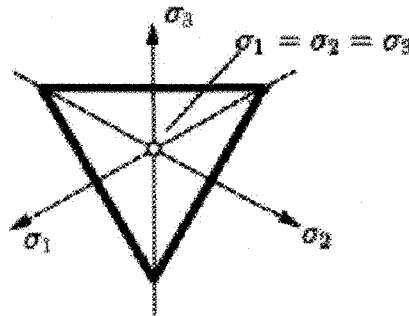


Figure 7.3. Rankine criterion in the deviatoric plane.

The first crack forms when the Rankine criterion for crack formation has been met and the crack surface is taken to be normal to the direction of the maximum tensile principal stress. We assume that cracking is irrecoverable and once a crack has occurred at a point, it remains throughout the rest of the analysis.

After nucleation of the first crack, we assume a consistency condition for cracking written in the crack direction coordinate system in the form of the tensor:

$$C = C(\sigma^{I,ck}, \sigma^{II,ck}) = 0 \quad (7.19)$$

where

$$C = [C_{uu} \ C_{vv} \ C_{ww} \ C_{uv} \ C_{uw} \ C_{vw}]^T \quad (7.20)$$

and  $\sigma^{I,ck}$  represents a tension softening model (Mode I fracture) in the case of the direct components of stress and a shear softening/retention model (Mode II fracture) in the case of

the shear components of stress. The tension softening and the cracked shear model will be explained in sections 7.5 and 7.6. Two cracking states are possible, an actively opening crack state and a closing/reopening crack state. This can be illustrated by writing the cracking conditions for a particular crack normal direction  $u$  explicitly:

$$C_{uu} = C_{uu}(\sigma_{uu}^{tck}, \sigma_t^{lck}) = \sigma_{uu}^{tck} - \sigma_t^{lck}(\varepsilon_{uu}^{tck}) = 0 \quad (7.21)$$

for an actively opening crack, where  $\sigma_t^{lck}(\varepsilon_{uu}^{tck})$  is the tension softening evolution and:

$$C_{uu} = C_{uu}(\sigma_{uu}^{tck}, \sigma_c^{lck}) = \sigma_{uu}^{tck} - \sigma_c^{lck}(\varepsilon_{uu}^{tck}) \Big|_{\varepsilon_{uu}^{topen}} = 0 \quad (7.22)$$

for a closing/reopening crack, where  $\sigma_c^{lck}(\varepsilon_{uu}^{tck}) \Big|_{\varepsilon_{uu}^{topen}}$  is the crack closing/reopening evolution that depends on the maximum crack opening strain.

These conditions represent the tension softening model for the cracking behaviour normal to crack surfaces and are shown graphically in Figure 7.4. We can obtain similar conditions for the other two possible crack normal directions,  $v$  and  $w$ .

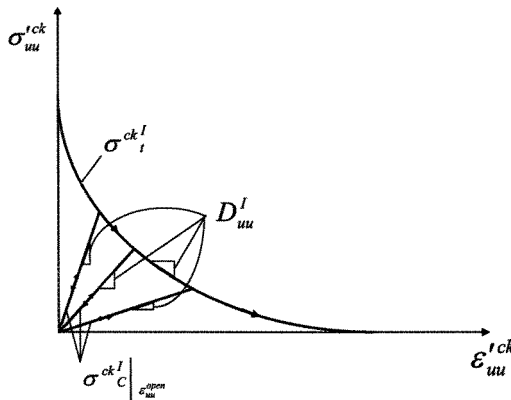


Figure 7.4. Cracking conditions for Mode I cracking.

Although crack initiation is based on Mode I fracture only, post-cracked behaviour includes Mode II as well. The shear cracking conditions can be written for shear component  $uv$  explicitly. It is worth noting that the cracking conditions for the shear components in the crack coordinate system are activated when the associated normal directions are cracked. The crack opening dependent shear model (shear retention model) is written as:

$$C_{uv} = C_{uv}(\sigma_{uv}^{Ick}, \sigma_w^{IIck}) = \sigma_{uv}^{Ick} - \sigma_w^{IIck}(g_{uv}^{ck}, \varepsilon_{uu}^{Ick}, \varepsilon_{vv}^{Ick}) = 0 \quad (7.23)$$

for shear loading or unloading of the crack, where  $\sigma_w^{IIck}(g_{uv}^{ck}, \varepsilon_{uu}^{Ick}, \varepsilon_{vv}^{Ick})$  is the shear evolution that depends linearly on the shear strain and also depends on the crack opening strain. Figure 7.5 illustrates the model.

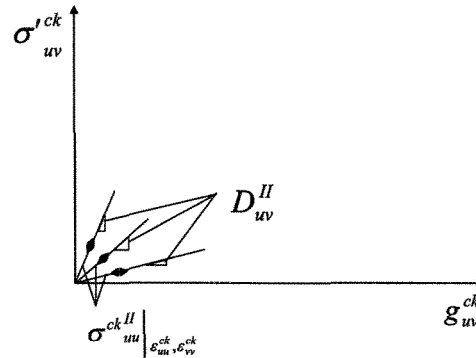


Figure 7.5. Cracking conditions for Mode II cracking (crack opening dependent model).

The definition of the components of the diagonal cracking matrix  $(D_{uu}^I, D_{vv}^I, D_{ww}^I, D_{uu}^{II}, D_{vv}^{II}, D_{ww}^{II})$  is given in Figures 7.4 and 7.5. These components can be obtained by experimental work and from the mechanical properties of the material.

#### 7.4 Constitutive equations

Using the strain rate decomposition Equ. 7.12, the elasticity relation (Equ. 7.2) and the transformation between global and local strains (Equ. 7.16) the rate of stress can be written as:

$$d\sigma = [\hat{C}](d\varepsilon - [T]d\varepsilon^{ck}) \quad (7.24)$$

Multiplying Equ. 7.24 by  $T^T$  and substituting Equ. 7.21 and Equ. 7.18 into the resulting left-hand side yields:

$$d\varepsilon^{ck} = ([D^{ck}] + [T]^T [\hat{C}][T])^{-1} [T][\hat{C}]d\varepsilon \quad (7.25)$$

Finally, substituting Equation 7.25 into Equation 7.24 results in the stress-strain rate equations:

$$d\sigma = \{[\hat{C}] - [\hat{C}][T]([D^{ck}] + [T]^T [\hat{C}][T])^{-1} [T][\hat{C}]\}d\varepsilon \quad (7.26)$$

assuming:

$$[\hat{C}]^{ec} = [\hat{C}] - [\hat{C}][T]([D^{ck}] + [T]^T [\hat{C}][T])^{-1} [T][\hat{C}] \quad (7.27)$$

the stress- strain relationship is determined as:

$$d\sigma = [\hat{C}]^{ec} d\varepsilon \quad (7.28)$$

### 7.5 Tension softening model

As mentioned previously, the Griffith criterion gives good results for pure brittle materials. However, many materials are not perfectly brittle in the Griffith sense and they have some residual load-carrying capacity after reaching the tensile strength. This fact has led to the replacement of purely brittle crack models by tension softening models, in which a descending branch is introduced to model the gradually diminishing tensile strength of the material upon further crack opening. In this study, the brittle fracture concept of Hilleborg

(1976) forms the basis of the post-cracked behaviour in the direction normal to the crack surface. The fracture energy required to form a unit area of the crack surface in Mode I (also known as strain energy release rate,  $G_f$ ) can be obtained from measuring the tensile stress as a function of the crack opening displacement as:

$$G_f = \int \sigma^I da \quad (7.29)$$

It can be shown that fracture energy  $G_f$  and stress intensity factor  $K$  are directly related as:

$$G_f = \frac{K^2}{E} \quad \text{in plane stress} \quad (7.30)$$

$$G_f = \frac{K^2(1-\nu^2)}{E} \quad \text{in plane strain} \quad (7.31)$$

In this model, the post-failure behaviour for direct straining across cracks is specified by applying a fracture energy cracking criterion. In this criterion, we define the failure stress as a tabular function of the associated Mode I fracture energy. This model assumes a linear loss of strength after cracking (Figure 7.6).

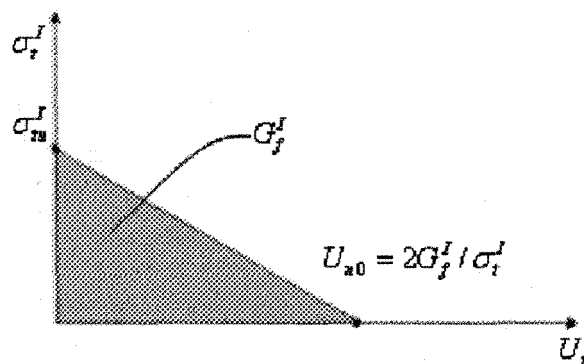


Figure 7.6. Post-failure stress-fracture energy curve [1].

Therefore, the crack normal displacement at which complete loss of strength takes place is:  $U_{n0} = 2G_f^I / \sigma_t^I$ .

The value of fracture energy for atmospheric ice can be obtained from Equation 7.30 by using the values of its fracture toughness and Young's Modulus.

## 7.6 Cracked shear model

The incapability of the numerical models to describe the aggregate interlocking shear resistance mechanism in the crack models was solved with the introduction of a "shear retention factor" to assure a residual friction along the crack directions.

In this study, the post-cracked shear behaviour of a material is based on the common observation that shear behaviour is dependent on the amount of crack opening. In other words, the cracked shear modulus is reduced as the crack opens. Therefore, a shear retention model can be used, in which the post-cracked shear stiffness is defined as a function of the opening strain across the crack. This shear retention model defines the total shear stress as a function of the total shear strain (shear direction  $uv$  is used as an example):

$$\sigma_{uv} = D_{uv}^{II}(\varepsilon_{uu}^{ck}, \varepsilon_{vv}^{ck}) g_{uv}^{ck} \quad (7.32)$$

where  $D_{uv}^{II}(\varepsilon_u^{ck}, \varepsilon_{vv}^{ck})$  is a stiffness that depends on the crack opening, and  $D_{uv}^{II}$  can be expressed as:

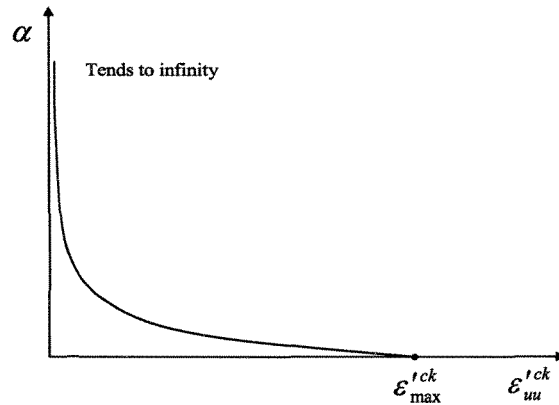


Figure 7.7. Shear retention factor dependence on crack opening [1].

$$D_{uv}^{II} = \alpha(\varepsilon_{uu}^{\prime ck}, \varepsilon_{vv}^{\prime ck}) G \quad (7.33)$$

where  $G$  is the shear modulus of the uncracked material and  $\alpha(\varepsilon_{uu}^{\prime ck}, \varepsilon_{vv}^{\prime ck})$  is a user-defined dependence of the form shown in Figure 7.7.

A mathematical form for this dependence when there is only one crack, related to direction  $u$ , is the power law form [1]:

$$\alpha(\varepsilon_{uu}^{\prime ck}) = \frac{\left(1 - \frac{\varepsilon_{nn}^{\prime ck}}{\varepsilon_{\max}^{\prime ck}}\right)^P}{1 - \left(1 - \frac{\varepsilon_{uu}^{\prime ck}}{\varepsilon_{\max}^{\prime ck}}\right)^P} \quad (7.34)$$

where  $P$  and  $\varepsilon_{\max}^{\prime ck}$  are material parameters. This form satisfies the requirements that  $\alpha \rightarrow \infty$  as  $\varepsilon_{uu}^{\prime ck} \rightarrow 0$  (corresponding to the state before crack initiation) and  $\alpha \rightarrow 0$  as  $\varepsilon_{uu}^{\prime ck} \rightarrow \varepsilon_{\max}^{\prime ck}$  (corresponding to complete loss of aggregate integrity). It should be noted that the bounds of  $\alpha$ , as defined in the model using the elastic-cracking strain

decomposition, are  $\infty$  and zero. This compares with some of the traditional shear retention models where the intact brittle material and cracking strains are not separated. In these models, the shear retention is defined using a shear retention factor  $\rho$ , which can have values between one and zero. The relationship between these two shear retention parameters is:

$$\rho = \frac{\alpha}{(\alpha + 1)} \quad (7.35)$$

The shear retention power law form given in Equation 7.34 can then be written in terms of  $\rho$  as:

$$\rho(\varepsilon'_{uu}{}^{ck}) = \left( 1 - \frac{\varepsilon'_{uu}{}^{ck}}{\varepsilon'_{max}{}^{ck}} \right)^p \quad (7.36)$$

Specifying shear retention factors with values between one and zero is easier and the  $\rho - \varepsilon'_{uu}{}^{ck}$  data are needed. Using the above equations, these data are converted to  $\alpha - \varepsilon'_{uu}{}^{ck}$  data for computation purposes.

Therefore, in shear retention models, the dependence is defined by expressing the post-cracking shear modulus  $G_c$ , as a fraction of the uncracked shear modulus  $G$ :

$$G_c = \rho(\varepsilon'_{uu}{}^{ck})G \quad (7.37)$$

where the shear retention factor  $\rho(\varepsilon'_{uu}{}^{ck})$  depends on the crack opening strain  $\varepsilon'_{uu}{}^{ck}$ . This dependence can be illustrated in piecewise linear form, as shown in Figure 7.8 [1].

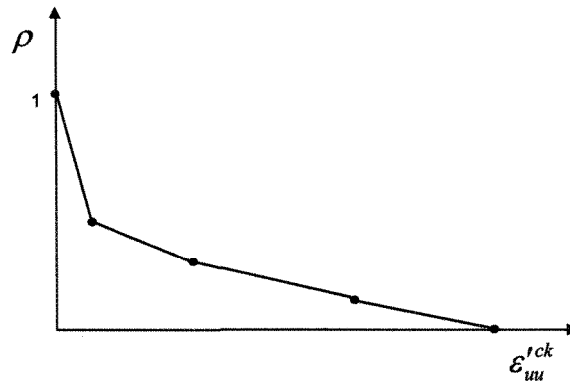


Figure 7.8. Piecewise linear form of the shear retention model [1].

Calibration of the post-cracking shear behaviour (Mode II) requires combined tension and shear experiments, which are difficult to perform. Since such test data are not available, a value for crack opening strain  $\varepsilon'_{uu}{}^{ck}$  is assumed based on previous investigations in the ice literature. It is also assumed that the shear retention factor  $\rho$  goes linearly to zero at this crack opening strain.

## 7.7 Conclusion

To model the cracking activity of atmospheric ice, the strain rate is decomposed into two parts: elastic and cracking strain rate.

The recoverable elastic strain is associated with lattice deformation and related to the corresponding applied stress by Hooke's law. The principal elastic compliance of a polycrystalline material is determined by taking a spatial average of the elastic constants of

all the crystals, using a uniform probability density function. The upper and lower boundaries, as well as the average values of polycrystalline elastic constants, were obtained from other research (Eskandarian, 2005) on modeling the ductile behaviour of atmospheric ice.

To obtain the stress-strain relationship in the presence of a crack, a local Cartesian system is defined, which is aligned with the crack directions. The strains in the local Cartesian system are obtained from a transformation between global and local strains. Then, the transformation between stresses in the global and the local cracking system is written. A Rankine criterion is used to detect crack initiation. The crack strain is obtained by assuming that the relationship between the local stresses and the cracking strains at the crack interfaces is defined by a diagonal cracking matrix that depends on the state of the existing cracks. The components of the diagonal cracking matrix can be obtained by experimental work and from the mechanical properties of the material.

A tension softening model, a descending branch to model the gradually diminishing tensile strength of atmospheric ice upon further crack opening, is adopted. This model uses the post-cracked behaviour of ice in the direction normal to the crack surface.

A shear retention model is defined to model the post-cracked shear stiffness as a function of the opening strain across the crack. This shear retention model defines the total shear stress as a function of the total shear strain.

## **CHAPTER 8**

### **CRACKING MODEL OF ATMOSPHERIC ICE**

#### **8.1 Introduction**

In the previous chapter, the theories of the brittle cracking of materials, including the elastic and crack stress-strain relation, as well as the constitutive equation of the cracking model, the tension softening model and the cracked shear model were explained. Using the above-mentioned theories in ABAQUS, two models for the simulation of the cracking behavior of atmospheric ice were developed. In the first model, a three-point beam of atmospheric ice with a bending force at the middle of the beam was developed and its brittle cracking was studied. In another model, a model of a cylinder of atmospheric ice around a piece of cable with a bending force at the middle of the cable was created and the cracking and fracture of ice was investigated. The specifications of the two models and their results are explained in this section.

#### **8.2 The cracking model of a three-point beam**

##### **8.2.1 General specifications of the model**

In the brittle cracking model of atmospheric ice, it was assumed that the behavior of ice is dominated by tensile cracking and linear elastic in compression. The model of a three-point beam is shown in Figure 8.1. Because of symmetry, only one half of the beam is modeled. Figure 8.2 shows the meshed beam with three-dimensional (C3D8R) elements.

To reduce the analysis time, the region close to the middle of the beam (where the fracture occurs) was meshed with fine elements. The boundary condition on the end surface of the middle of the beam allows the nodes to move vertically, giving the beam deflection. The boundary condition at the end of the beam simulates a simple support, which is pinned at this end. The elements under compressive stress (the elements at the top of the neutral axes of the beam) will not break even if their normal and Mises stresses exceed the predefined limit, because the brittle fracture model is applied on the elements enduring tensile stress.

The bending force is a nodal load distributed along the beam width and it increases linearly from 0 at the first step of the analysis to 420 N at the final step. The crack initiation starts when the normal stress of the elements at the bottom of the beam matches the failure stress, and then the crack propagates to the top of the beam. When the normal stress of an element meets the failure stress, the element breaks, its stress level is reduced to zero according to the tension softening model, and the element is eliminated from the calculations.

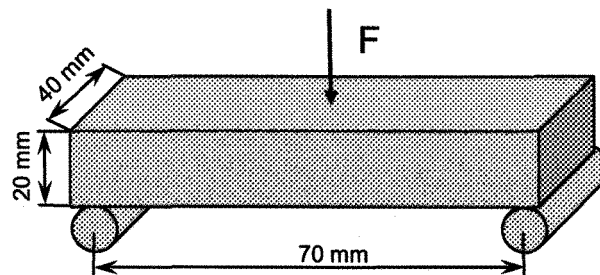


**Figure 8.1.** The three-point beam configuration in the tests and ABAQUS model.

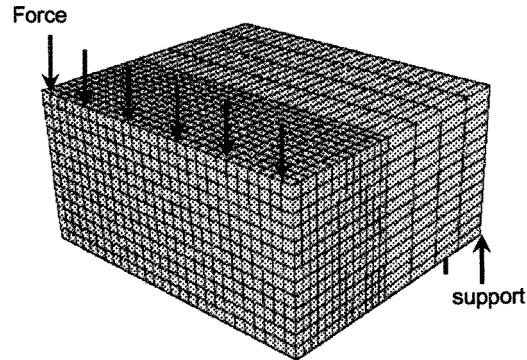


Figure 8.2. The finite element model geometry.

### 8.2.2 Mechanical properties of atmospheric ice

The mechanical properties of atmospheric ice play a key role in obtaining realistic results. The elastic constants of atmospheric ice for this model are obtained from Eskandarian (2005). According to his investigation, the elastic constants of S2 ice can be calculated from the following equations:

$$\begin{aligned}
 E_p^{S2} &= 9.363(1 - 1.471 \times 10^{-3} \theta), & E_t^{S2} &= 9.551(1 - 1.471 \times 10^{-3} \theta) \\
 G_p^{S2} &= 3.528(1 - 1.471 \times 10^{-3} \theta), & G_t^{S2} &= 3.140(1 - 1.471 \times 10^{-3} \theta) \\
 \nu_p^{S2} &= 0.327, & \nu_{tp}^{S2} &= 0.319, & \nu_{pt}^{S2} &= 0.312
 \end{aligned} \tag{8.1}$$

where  $\theta$  denotes the temperature in  $^{\circ}\text{C}$ , and subscripts “t” and “p” stand for “transverse”, or in column direction, and “in-plane” of isotropy, respectively. In this study, the temperature is set at  $-10^{\circ}\text{C}$ , wherefore the elastic constants E and G are:

$$\begin{aligned}
 E_p^{S2} &= 9.5 \text{ GPa}, & E_t^{S2} &= 9.69 \text{ GPa} \\
 G_p^{S2} &= 3.58 \text{ GPa}, & G_t^{S2} &= 3.19 \text{ GPa}
 \end{aligned} \tag{8.2}$$

There is the negligible temperature dependence for Poisson ratios (Eskandarian, 2005).

To take into account the effect of porosity, the following equation can be used (Eskandarian, 2005)

$$\varepsilon_{ij}^e = \frac{1}{1-\Phi} S_{ijkl}^m \sigma_{kl} \quad (8.3)$$

where  $S_{ijkl}^m$  is the elastic compliance tensor and  $\Phi$  is the porosity of atmospheric ice.

Therefore, the elastic constants of atmospheric ice are obtained as below

$$\begin{aligned} E_p^{S2} &= 9.22 \text{ GPa}, E_t^{S2} = 9.4 \text{ GPa} \\ G_p^{S2} &= 3.47 \text{ GPa}, G_t^{S2} = 3.1 \text{ GPa} \\ \nu_p^{S2} &= 0.325, \nu_p^{S2} = 0.319, \nu_{pt}^{S2} = 0.312 \end{aligned} \quad (8.4)$$

Since the ABAQUS finite element software cannot analyze the cracking model of a transversely isotropic material and the difference between “transverse” and “in-plane” values of elastic constants of atmospheric ice is negligible, we use the average value of these parameters and consider the ice as an isotropic material with the following elastic constants.

$$E^{S2} = 9.31 \text{ GPa}, G_p^{S2} = 3.28 \text{ GPa}, \nu_p^{S2} = 0.319 \quad (8.5)$$

Another mechanical property that should be determined for this model is fracture energy  $G_f$ . According to experimental works in the laboratory of the CIGELE, the fracture toughness of atmospheric ice at  $-10^\circ\text{C}$  is  $111.17 \text{ MPa}/\sqrt{\text{m}}$ . Substituting this value in the equation 3.23 and Young’s modulus 9.31 GPa gives  $G_f = 3.77 \times 10^{-4} \text{ N/m}$ .

The cracking failure stress is another mechanical property obtained from experimental works in CIGELE and it has a value of 2.73 MPa.

The beam is loaded by the vertical nodal force that increases linearly from 0 to 420 N at the center of the beam.

### 8.2.3 Results and discussion

Figure 8.3 shows a plot of force versus time in ice beams tested at the CIGELE and the ABAQUS model of atmospheric ice. The fracture test of five ice samples with the dimensions in Figure 8.1 indicates that the maximum force at failure of this three-point beam is in the range between 328.2 N and 482.3 N. According to this brittle cracking model, the force at failure is 414.1 N. The average force at failure in these five tests is 405.04 N. Comparing this value with the value predicted by the ABAQUS model, we obtain an error of 2%, which shows very good agreement with experimental results. As evident in Figure 8.3, the specimens break suddenly when the stress reaches its highest level, and after nucleation of the first crack, this crack propagates through the material very fast. In the model, the graph of force versus time shows similar behavior. This behavior was expected because of the very small value of the fracture energy of atmospheric ice. This means the ice shows a little resistance against crack propagation, as seen in the model and in the results of the experimental work.

Figure 8.4-a shows the variation of normal stress versus time in four elements shown in Figure 8.4-b. Obviously, the first element that fails is element A and since no crack existed prior to the fracture of this element, its failure stress is higher than other elements and is equal to the failure strength of atmospheric ice (2.73 MPa). After the fracture of this element, the crack propagates rapidly to element B. In element B, just an instant after the failure of element A, the stress decreases a little, due to the removal of the stresses in the

preceding elements and then increases again to resist crack propagation (Figure 8.5). This reduction and resistance was also observed in the two dimensional model of crack propagation in the three-point beam. Then, the stress in element B increases for a while but never reaches 2.73 MPa, owing to the low level of fracture energy, which defines the post-failure behavior of material. After the failure of element B, the normal stress in this element decreases to zero and the crack propagates to the next elements.

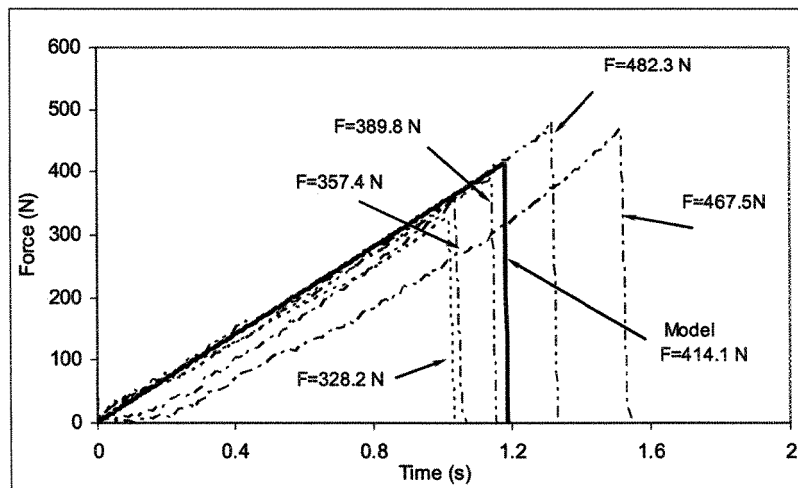


**Figure 8.3.** Comparison between the graph of force versus time in the model and five ice tests.

Therefore, the fracture of elements B, C and D has four steps :

- 1- Stress augmentation before fracture of previous element
- 2- Stress reduction owing to the fracture of the previous element
- 3- Stress augmentation due to the resistance of material against crack propagation
- 4- Failure of the element and reduction of stress to zero

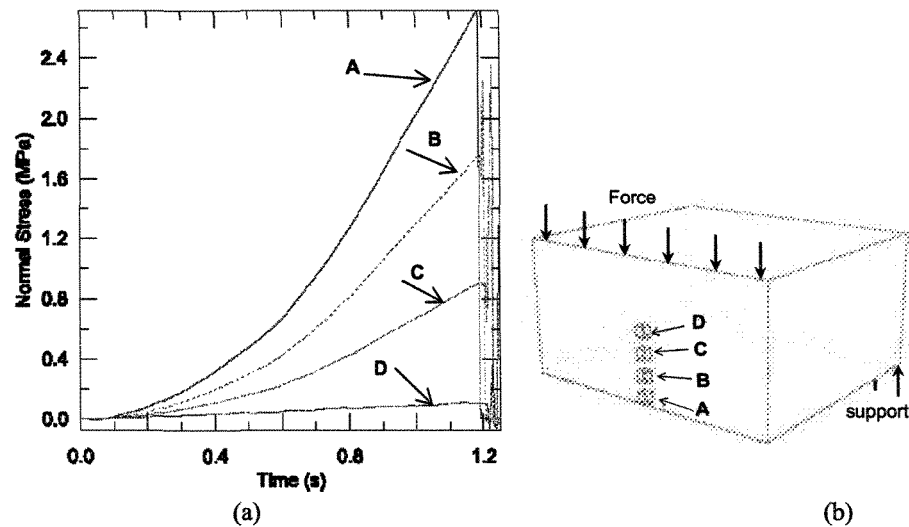


Figure 8.4. a) Variation of normal stress versus time in four elements in Figure 8.4-b. b) The position of four elements at the middle of the beam.

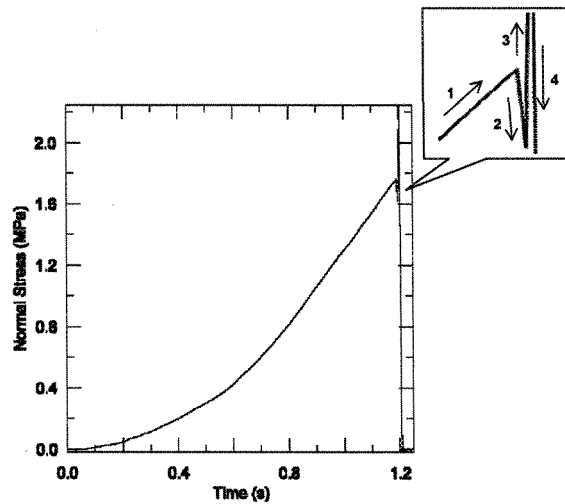
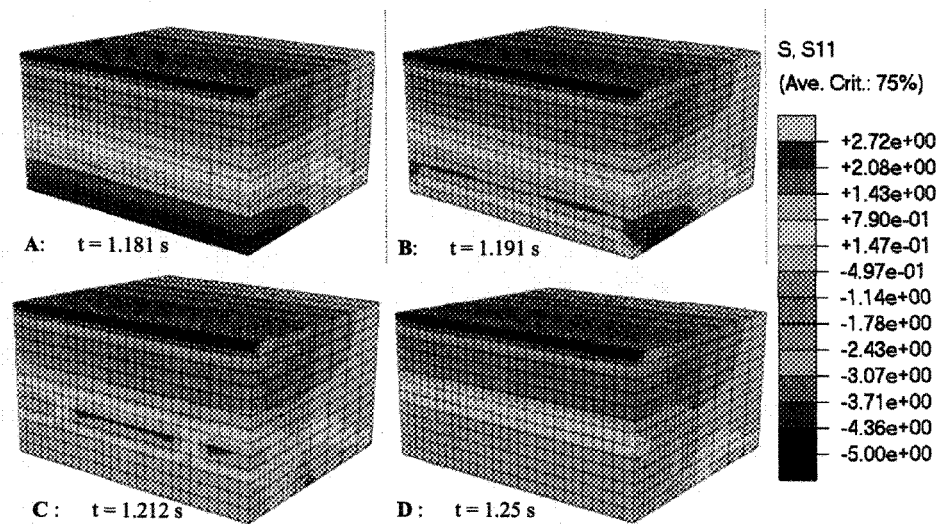


Figure 8.5. Variation of normal stress in the element B in Figure 8.4-b.

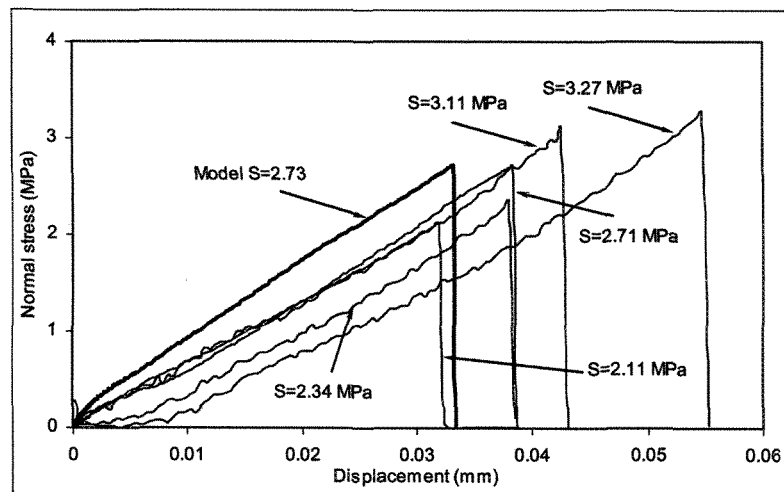
Figure 8.5 shows these four steps. Figure 8.6 shows the contour of stress in four different steps of the fracture of the three-point beam as the crack propagates from the bottom to the top of the beam.

Figure 8.7 shows the comparison between the graph of stress versus displacement in the model and five ice tests. As can be seen in the graph, the value of displacement, or beam

deflection in the model, is less than most corresponding values in the ice tests, possibly because the model does not take into account the plastic behaviour of atmospheric ice.



**Figure 8.6.** The contour of stress in four different steps of fracture of the three-point beam.



**Figure 8.7.** Comparison between the graph of force versus displacement in the model and five ice tests.

The deflection of a simply supported beam can be obtained by using the following equation:

$$v = \frac{FL^3}{48EI} \quad (8.6)$$

where  $F$  is force (N),  $L$  is beam length (m),  $E$  is Young's modulus of beam material, and  $I$  is the moment of inertia with respect to the horizontal axis of the beam cross-section. From this equation, one can conclude that any difference between the value of effective parameters in this equation in model and ice samples can cause a difference in resulting deflection. Therefore, the error in real beam dimensions (length, width and height) can cause a difference in resulting beam deflection. Aside from this error, the difference between the real Young's modulus of the ice samples and the corresponding value in the model (9.31 GPa) can produce a difference between the results.

Young's modulus (GPa)	Fracture energy (N/m)	Force at failure (N)	Beam deflection (mm)	Error of the Force at failure (%)	Error of the Beam deflection (%)
9.31	3.77E-04	414	3.32E-02	2.22	19.30
8.2	4.28E-04	437	3.53E-02	7.90	14.14
8	4.39E-04	440	3.96E-02	8.64	3.89
7.9	4.44E-04	441	4.39E-02	8.89	6.68
7.5	4.66E-04	448	4.62E-02	10.62	12.22
6.5	5.40E-04	465	5.17E-02	14.81	25.63
5.5	6.38E-04	476	5.44E-02	17.53	32.23
5	7.02E-04	504	6.15E-02	24.44	49.34
Ave. of the ice tests		405.04	0.041		

**Table 8.1.** Results of the ABAQUS model for various values of Young's modulus

Figure 8.8 shows a comparison of the model results with different values of Young's modulus and the average value of the ice tests. It is worthwhile to note that changing the Young's modulus changes the value of fracture energy, which causes higher force at failure. Table 8.1 shows the results of the model and the corresponding errors with respect

to the average values of experimental tests. It seems that the Young modulus of 8 GPa yields the best agreement for the force at failure and the beam deflection.

According to the ABAQUS model with the Young's modulus of 8 GPa, the error of calculated force at failure is 8.64% and the calculated beam deflection shows a 3.89% error.

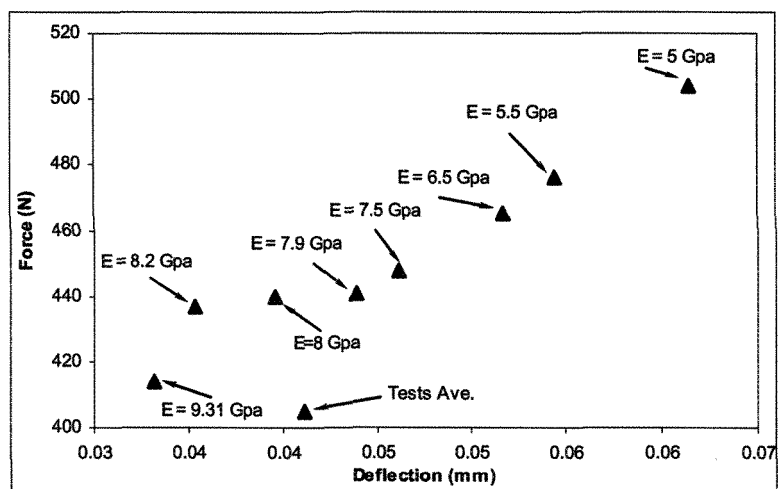


**Figure 8.8.** Comparison between the model result with different values of Young's modulus and the average value of the ice tests.

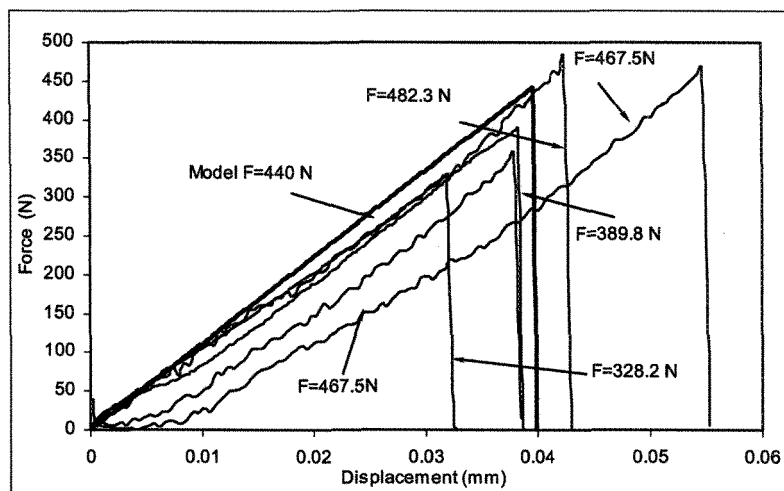


**Figure 8.9.** Comparison between the graph of force versus displacement in the model (Young's modulus of 8 GPa) and five ice tests.

Figure 8.9 shows the comparison between the graph of force versus displacement in the model (with Young's modulus of 8 GPa) and five ice tests.

The average effective modulus of these five tests is 2.65 GPa. When this value is used in the ABAQUS model, the values of force at failure and the beam deflection show errors of 86.67% and 55.58%, respectively. As mentioned before, the reason for these errors is the plasticity of atmospheric ice. The brittle cracking model does not take into account the plasticity of material, while the effective modulus includes both non-elastic and elastic processes.

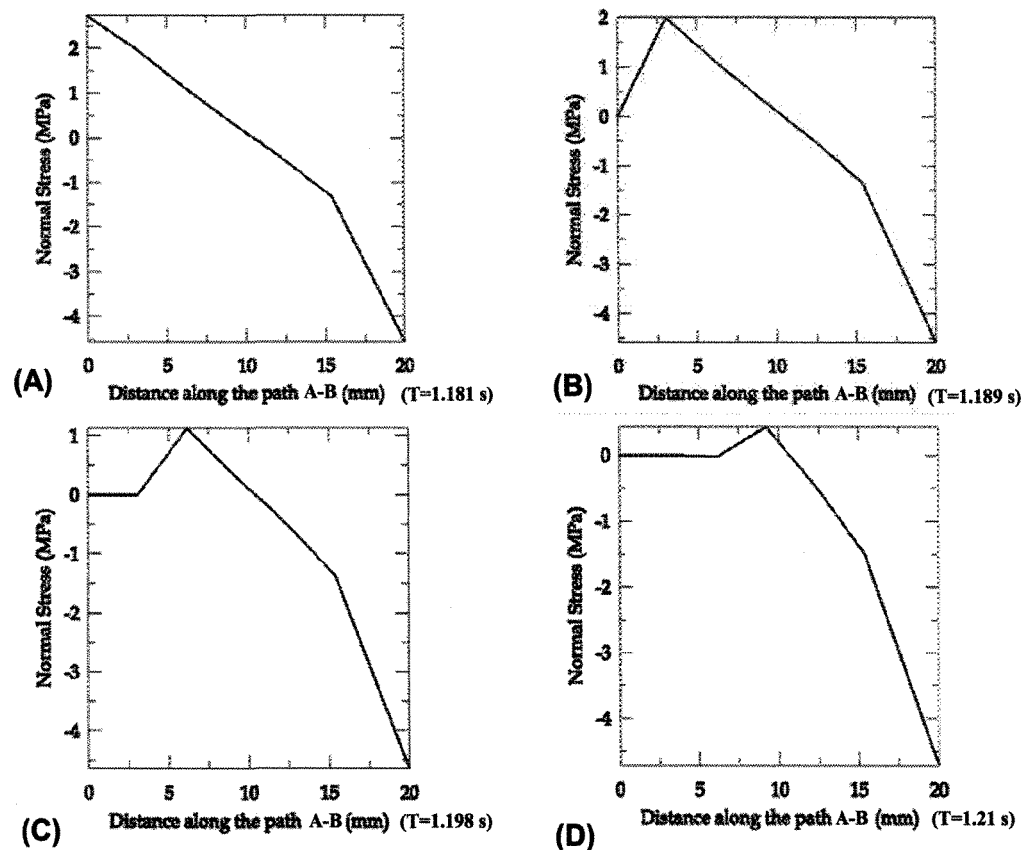


Figure 8.10. The variation of normal stress along the path A-B in Figure 8.11.

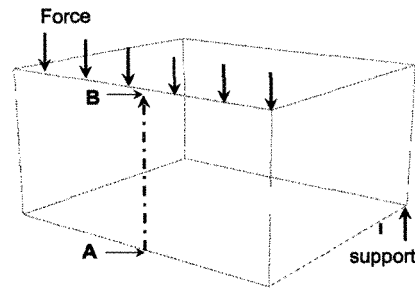


Figure 8.11. The path of crack propagation.

Another reason for the difference between the results of the ABAQUS model and the tests results is the difficulty of measuring beam deflection and its associated errors. Although the nominal uncertainty of measurement of the beam deflection is 0.20%, it seems that its error is actually more than this value.

Figures 8.10-A to 8.10-D show the variation of normal stress along the path A-B in Figure 8.11. A moment before fracture (Figure 8.10-A), the normal stress at the bottom of the beam meets the tensile strength of the ice (2.73 MPa) and a crack starts to propagate along the path A-B. Immediately after this ( $T=1.189$  s), the elements at the bottom of the beam are broken, whereby the normal stress at the zero point of the horizontal axes becomes zero (Figure 8.9-B). The crack then spreads to the next elements and does not match the tensile strength because of the stress concentration at the crack tip. As is seen in Figures 8.10-C and 8.10-D, the level of normal stress at failure is always less than the tensile strength (2.73 MPa). The level of failure stress decreases as the crack propagates from the bottom of the beam to the top, because the average of normal stress on an element close to the natural axis decreases to zero. Furthermore, the only stress that causes element failure is concentrated stress at the crack tip, which is a very small part of the element.

### **8.3 The cracking model of atmospheric ice on the cable**

Although the cracking model of ice explains the behavior of this material and its results are in strong agreement with the experimental works, more aspects of this research area are covered when this model is implemented on the ice accreted on the cable.

#### **8.3.1 General specifications of the model**

In this model, it was again assumed that the behavior of ice is dominated by tensile cracking and linear elasticity in compression. The geometry of the cable with accreted ice is shown in Figure 8.12. Because of symmetry, only one half of the beam is modeled. The ice and the cable were meshed with three-dimensional (C3D8R) elements. As previously mentioned, the elements under compressive stress (the elements on the upper side of the beam) will not break even if their normal stress and Mises stress exceed the predetermined limit, because the brittle fracture model is applied on the elements enduring tensile stress.

As for the model of cracking activity in a three-point beam, the bending force in this model is a nodal load distributed on 11 nodes at the top of the cylinder of ice. This force increases linearly from 0 at the first step of the analysis to 1.7 KN at the final step. The crack initiation starts when the normal stress in the elements at the bottom of the ice meets the failure stress, when the crack propagates to the top of the beam. When the normal stress of an element reaches the failure stress, the element breaks, its stress level is reduced to zero, according to the tension softening model, and the element is eliminated from the calculations.

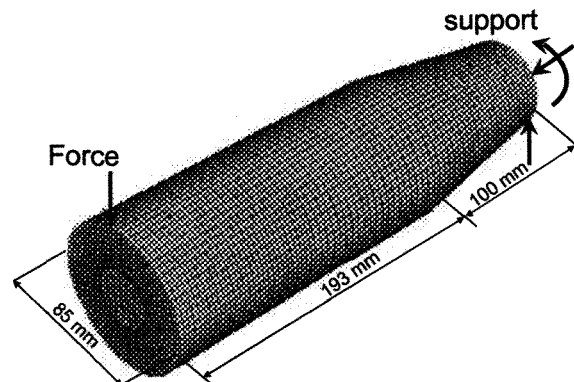


**Figure 8.12.** The model of cracking activity in atmospheric ice on the cable.

### 8.3.2 Mechanical properties of materials in the model

The mechanical properties of atmospheric ice were determined in section 8.1.2. The mechanical properties of the material of the cable are also known. However, modeling the cable with the material property of aluminum alloys and steel does not yield the correct result. This part of the research generated some difficulties, as modeling of the cable with exact geometry is very difficult and needs extremely fine meshes to give acceptable results. The Bersimis cable, which is a typical cable in power transmission lines, was chosen in this study. As Figure 8.13 shows, this cable has 45 strands of aluminum and 7 steel strands. Furthermore, the strands are coiled and the spiral shape of the strands makes the model more complicated. Therefore, the cable is modeled as a solid cylinder (not by modeling the strands). However, when we view the cable as a cylinder, its bending characteristics and flexural rigidity will be different from a real cable. So in the first step, the flexural rigidity of the cable should be extracted.

In order to study the ice fracture on the cable, a fixture was designed and fabricated at the CIGELE (Figure 8.14). The 600 mm cable in this fixture behaves as a fixed-fixed beam, which is the typical condition of a piece of cable in a real situation, provided that we eliminate the movement of the cable.

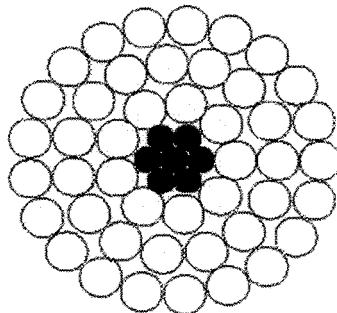


**Figure 8.13.** The Bersimis cable with 7 steel and 45 aluminum strings.

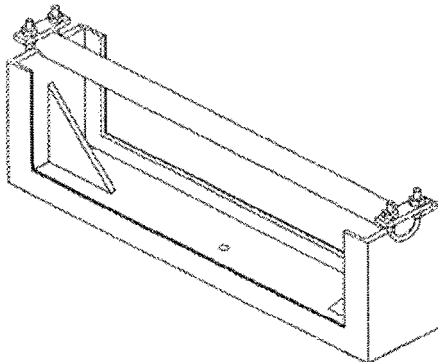


**Figure 8.14.** Schematic of the cable fixture for bending tests.

To extract the flexural rigidity of the bared cable, four tests in the four directions of the cable cross-section were conducted and the average of these four tests was considered as the flexural rigidity of the cable. Owing to the particular geometry and structure of the cable, the flexural rigidity is not a constant number and changes with the increase of the deflection. The deflection of the middle point of a fixed-fixed beam is obtained from the following equation

$$v = \frac{FL^3}{198EI} \quad (8.7)$$

where  $F$  is force (N),  $L$  is the beam length (m),  $E$  is Young's modulus of the beam material, and  $I$  is the moment of inertia with respect to the horizontal axis of the beam cross-section. The product  $EI$  is the flexural rigidity. Figure 8.15 shows the variation of flexural rigidity with respect to the cable deflection.

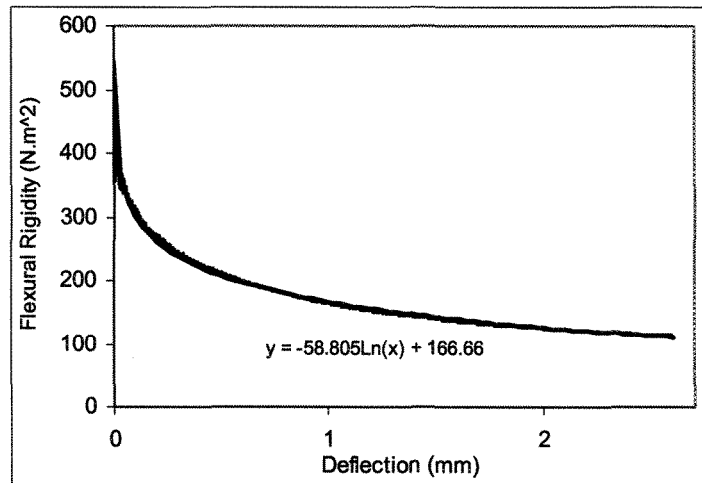


**Figure 8.15.** Variation of flexural rigidity versus cable deflection.

To study the ice fracture on the cable, the atmospheric ice was accumulated on the 600 mm piece of cable in the wind tunnel of the CIGELE. To avoid squashing the ice on the top of the cable by applying the bending force, a steel screw (with very high Young's modulus) was installed in the middle of the cable before ice accumulation and then ice was grown on the cable. It was assumed that the deformation of this screw due to applying force is negligible in comparison with the deflection of the beam. Using this screw, the bending force is always applied to the cable rather than the ice. Since the screw is located at the top of the cable and the ice in this zone normally endures compressive stress, the presence of

the screw cannot affect the results of the ice fracture because the fracture occurs under the cable. Five tests were conducted to study the ice fracture on the cable and in each test the cable deflection at which the first crack appeared was registered and the average of these values was chosen as the deflection of cable at failure.

Table 8.1 shows the force and the beam deflection at failure (when the first crack appears at the bottom of the ice-cable beam). The average of the beam deflections in these five tests is 0.464 mm. Substituting this value in the equation of the curve in Figure 8.15 gives the corresponding flexural rigidity ( $EI$ ) at this deflection. Having flexural rigidity ( $EI$ ) and the moment of inertia with respect to the horizontal axis of the beam cross-section ( $I$ ), the equivalent value of Young's modulus of the cable at this deflection is obtained.

Test No.	Bending force at failure (kN)	Beam deflection at failure (mm)
1	1.53	0.717
2	1.62	0.447
3	1.36	0.595
4	1.45	0.243
5	1.27	0.316
Average	1.45	0.464

**Table 8.2.** The force and the beam deflection at failure.

### 8.3.3 Results and discussion

The accumulated ice on the cable in the wind tunnel was not exactly cylindrical and its shape in each test was different from the others. Therefore, we did not expect uniform results because the experiments for determining the mechanical properties of the ice have shown that even for the ice samples with almost identical dimensions, the values of failure

stress are scattered. So it is not strange if scatter is seen in the results of the fracture of the ice on the cable.

Figure 8.16 shows a plot of force versus time in the model of ABAQUS, which consists of an aluminum cylinder (the cable) and an ice cylinder with a conic shape (as Figure 8.12). The results of the fracture test of five real samples with the shape shown in Figure 8.12 are included in this figure. According to the ABAQUS model, the required force for fracture of the ice on the cable is 1.650 KN. The result of the test shows that the maximum force at failure is in the range between 1.27 KN and 1.62 KN. The average force at failure in these five tests is 1.45 KN. Through comparing the results of the ice tests, the ABAQUS model shows a 14% error in prediction of failure force.

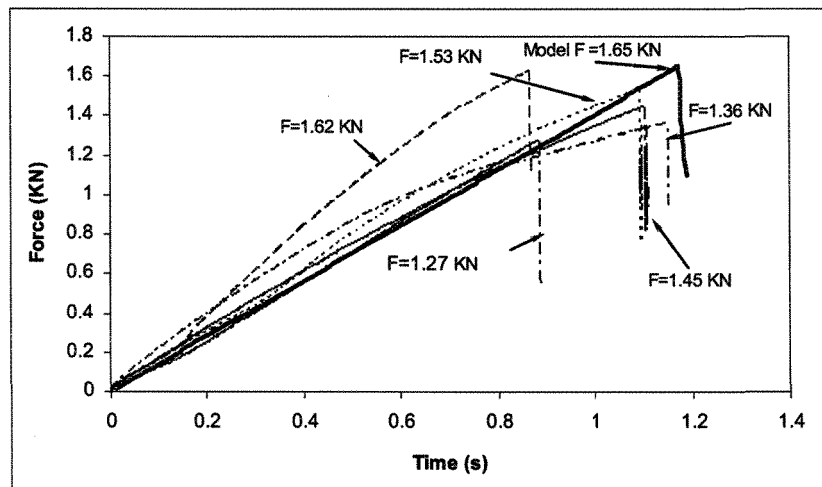


**Figure 8.16.** Variation of force versus time in the ABAQUS model and five tests with cable and accreted ice.

As shown in Figure 8.16, when the ice breaks, the force decreases immediately but never reaches zero, because the cable resists against the bending force. The first crack nucleates under the cross-section of the ice and then propagates up to the neutral axis of the beam.

The force at the failure in all five tests is less than the corresponding value in the ABAQUS model. This can be attributed to the accumulated ice's lack of cylindrical shape at the middle of the beam, and also to the unevenness of the surface of the ice cylinder. Also, in all the tests, the geometrical shape of the ice beam was different from the model geometry, particularly at the conic parts. Figure 8.17 shows one of the ice samples around a BERSIMIS cable. Figure 8.18.a shows the variation of normal stress in the four elements at the middle of the ice-cable beam with the positions as in Figure 8.18-b.

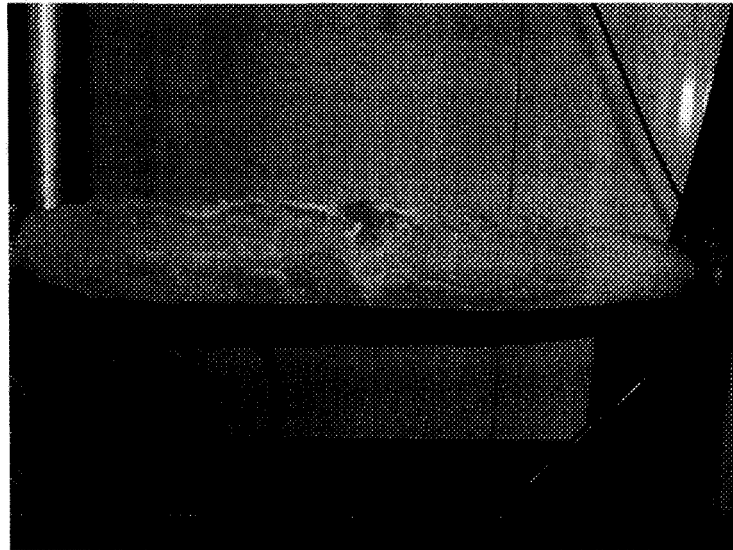


**Figure 8.17.** An ice sample around the BERSIMIS cable.

As is evident, element A endures the maximum normal stress and when the stress in this element matches the tensile strength of the atmospheric ice, the element breaks and the next element endures the normal stress and after its fracture, the next elements play a role. Here again, a little reduction in the stress of elements B, C and D can be seen when the previous element breaks and, therefore, the stress increases until fracture.

Figures 8.19-A to 8.19-D shows the contour of stress at the cross-section of the beam (including ice and cable) starting with the contour of stress a few instances before initiation of the first crack, followed by the spreading of the crack through the cross-section up to the natural axis of the beam.

Figure 8.20 shows the comparison between the graph of force versus displacement in the model and the five ice tests. As seen in the graph of stress versus displacement of a three-point simple supported beam (Figure 8.7), the value of displacement or beam deflection in the model is less than most corresponding values obtained in the ice tests. The ABAQUS model shows a 47% error in calculation of the beam deflection at failure. Once again, the lack of a plasticity analysis of the model could be the cause of this difference.

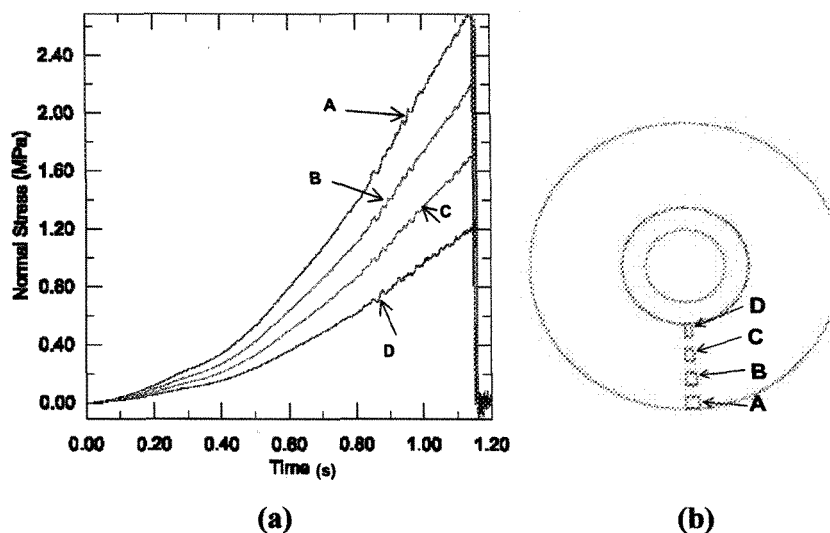


**Figure 8.18.** a) Variation of normal stress versus time for four elements in Figure 8.17-b.  
b) The position of four elements at the middle of the ice-cable beam.

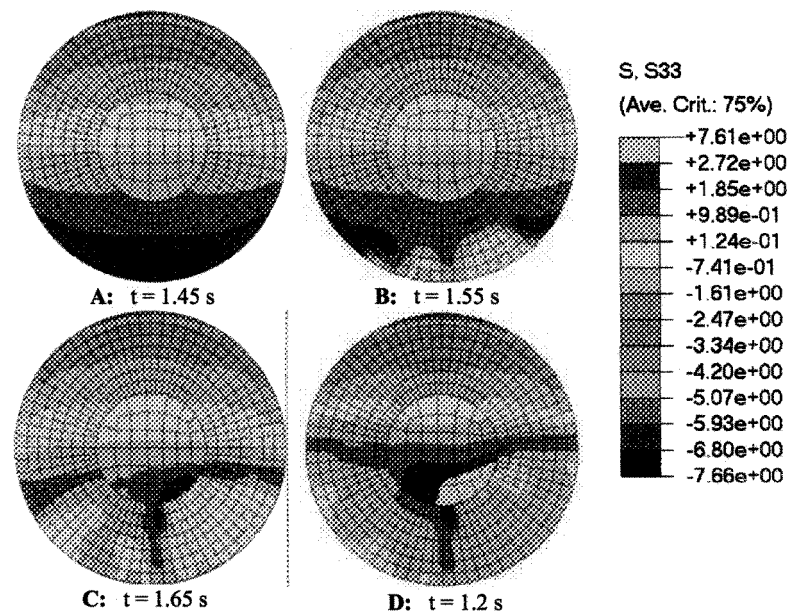


**Figure 8.19.** Contour of normal stress at the cross-section of the ice-cable.

As explained in section 8.2.2, the deflection of the middle point of a fixed-fixed beam is calculated by using Equation 8.7. The reasons for the error described in section 8.1.3 are applicable in this section, as well. The difference between the ice sample's dimensions and the model, the difference between the Young's modulus in the model and the atmospheric ice in the experiments, and the inaccuracy in the deflection measurement can cause some discrepancies in the results of the model in comparison with the experiments. If we assume a Young's modulus of 8 GPa, the error in the beam deflection decreases. The results of the ABAQUS model show a 19% error in calculation of force at failure and a 27% error in the prediction of beam deflection. Figure 8.21 shows the comparison between the graph of force versus deflection in the ABAQUS model with a Young's modulus of 8 GPa and five ice tests.

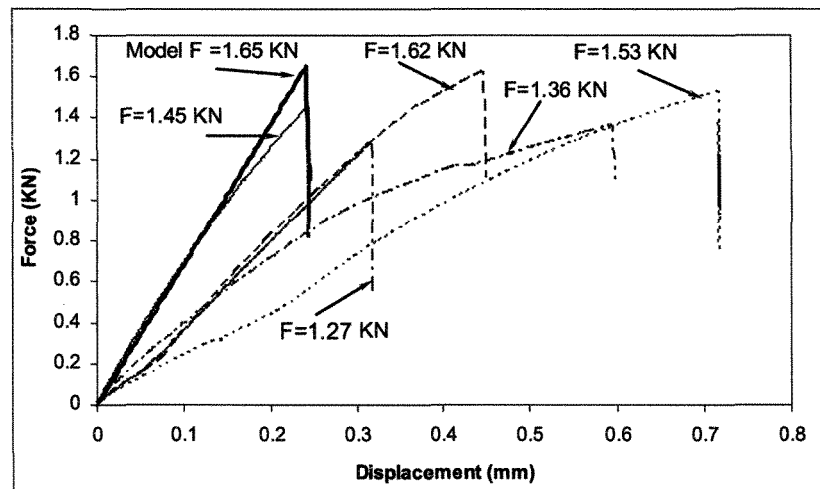


**Figure 8.20.** Variation of force versus displacement in the ABAQUS model and five tests with cable and accreted ice.

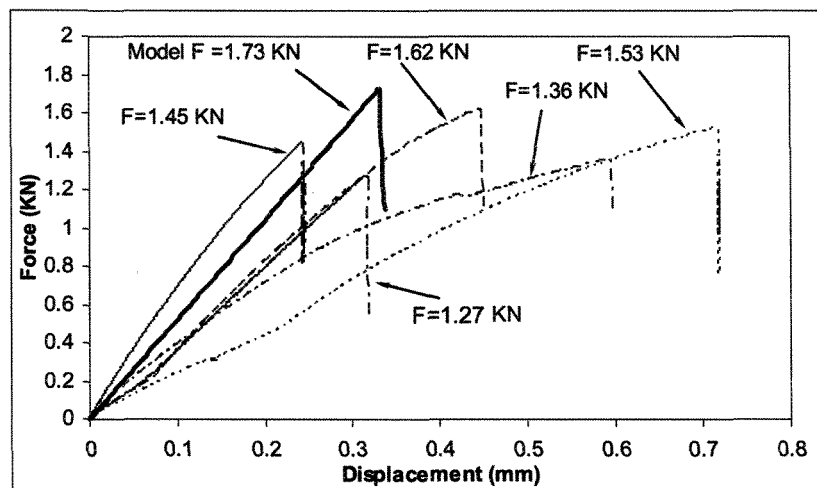


**Figure 8.21.** Variation of force versus beam deflection in the ABAQUS model ( $E= 8$  GPa) and five tests.

Aside from these errors, the difference between the flexural rigidity of the cable and the cylinder, the difference between the ice shape in the model and the experimental tests, where the ice was not cylindrical and conic, as well as the unevenness of the surface of the

ice, are the most important reasons for the difference between the results of the ice tests and the model results.

It is worth repeating that the brittle cracking model in this study does not provide a good estimate for the crack propagation speed in atmospheric ice, because the governing equations in this analysis are not advanced enough to cover all aspects of the material behaviour.

#### **8.4 Conclusion**

In order to study the brittle cracking of atmospheric ice, a three dimensional model was developed, which uses the Rankine criterion for cracking and post-failure behavior of ice for a post-cracking condition. The calculated force for beam fracture by the ABAQUS model shows a 2% error in respect to the average value of the failure force in the experiment, which is a strong agreement. The calculated beam deflection at failure, however, shows a 19% error in comparison with the ice tests. This difference is attributed to the inaccuracy of the measurement of beam deflection and to differences between the beam dimensions and Young's modulus of the ice samples, and the corresponding values in the ABAQUS model. Another source of error was the plasticity in the real samples, which was ignored in the model. The results of the ABAQUS model with the value of 8 GPa for the Young's modulus of atmospheric ice is 8.64% and 3.9% in calculation of force at failure and beam deflection, respectively.

The brittle cracking model was expanded to a model of atmospheric ice on a cable and its results were compared with the experimental tests. Comparing the results of the ice tests,

the ABAQUS model shows a 14% and a 47% error in prediction of failure force and deflection at failure, respectively. If we assume a Young's modulus of 8 GPa, the error in calculated failure force and the beam deflection is 19% and 27%, respectively. Besides the causes of error mentioned for three- point beam model, the difference between the flexural rigidity of the cable and the cylinder, the difference between the ice shape in the model and the experimental tests, the lack of plasticity analysis in the ABAQUS model and the unevenness on the surface of the ice are some sources of error.

## CHAPTER 9

### HIGH-SPEED VIDEO OBSERVATION OF ICE FRACTURE

#### 9.1 Introduction

For a better recognition of the ice shedding phenomenon, an understanding of crack and fracture behavior of atmospheric ice is very important. Many investigators have worked on crack propagation and the fracture of brittle materials. Glenn (1976) studied the fracture of lead glass by applying an impact at 100-300 m/s and imaging by an image converter camera with a speed of 106 frames per second. The measured speed was  $0.464 V_p$  on the impact surface and  $0.322 V_p$  just below the contact point, where  $V_p$  is the longitudinal velocity. Chaudhri and Walley (1978) investigated the impact of a glass and steel sphere on a soda glass and borosilicate at 10-350m/s using a high-speed camera with a speed of 106 frames per second. Many other investigators have studied crack propagation in ice. Arakawa *et al.* (1995) observed the crack growth process in the low and high-velocity impact of water ice with an image-converter camera with  $2 \times 10^5$  and  $5 \times 10^5$ . They reported a maximum growth velocity of 1050 m/s at lower-velocity impacts and a range of 2000 to 3500 m/s at higher-velocity impacts. Gagnon *et al.* (1999) observed the fracture of three-point beams extracted from first year sea ice at 6000 FPS. They reported average crack propagation speeds in the range of 3.6-20.5 m/s and peak velocities in the 30-62 m/s range. They also prepared thin sections of the reconstituted beams and studied the influence of the ice microstructure on the fracture propagation. Gagnon (2003) studied the propagation of

fracture in a 1.7 m thick freshwater ice sheet and stated that the fractures propagate intermittently. In his observation, the average velocity as a fracture progressed through several jump episodes was low (in the 0–50 m/s range), whereas the velocity measured at the brief jumps was in the 0–550 m/s range.

To investigate the initiation, propagation and fracture of atmospheric ice, two series of beam bending experiments were conducted in this research work using high-speed video cameras.

## **9.2 Ice samples**

The tests were conducted on the beams extracted from atmospheric ice accumulated on an aluminum cylinder at  $-10^{\circ}\text{C}$  in the CIGELE wind tunnel. The liquid water content of this type of atmospheric ice was  $2.5 \text{ gr/m}^3$  and the air speed was 10m/s. Atmospheric icing conditions, the CIGELE wind tunnel, sample preparation, the apparatus and test conditions were explained in chapter 4.

Two different types of tests were carried out. In the first series, a simple beam without any notches, as in Figure 9.1-a, was loaded using vertical continuous loading in the middle of the beams and the initiation and propagation of cracks were studied. The dimensions of these beams were 20x40x70 mm. After each experiment, the high-speed video images were output to a standard NTSC video tape recorder, at 1 frame per second when the crack propagation starts. The high-speed video camera (Kodak, Nikon), was capable of providing 1000 full monochrome frames per second and up to 6000 partial frames per second. The beams were illuminated with a 1000 watt projector to get a better image.

The second series of tests was conducted by applying the vertical continuous load to the middle of a notched beam with the same dimensions. After the preparation of the simple beams, they were notched to a depth of 3 mm on the underside, directly under the central loading point (Figure 9.1.b).

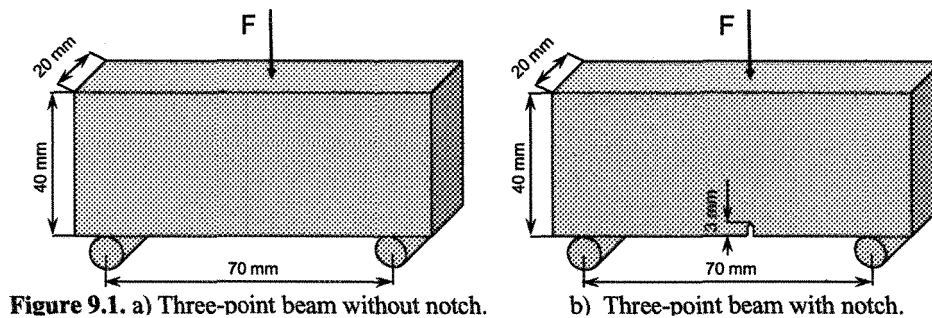


Figure 9.1. a) Three-point beam without notch.

b) Three-point beam with notch.

The high-speed video camera in these tests was an Ultima APX-RS, which provides full mega pixel resolution images at frame rates up to 3000 FPS and at reduced frame size up to 250000 FPS.

### 9.3 Results and discussion

Table 9.1 shows the average crack speed in simple beams of atmospheric ice in the first series. The recording speed (2000 FPS) in these tests was very low. The video was recorded on a VHS tape at the record speed of 1 FPS and, in every test, the crack propagates into the specimen in one frame. So, the conclusion can be drawn that the crack propagation speed is greater than the value that is calculated in these tests. The crack propagation speed was calculated by dividing the beam height by the interval of one frame (1/2000 s or 0.0005 s).

The average velocity of crack propagation in atmospheric ice in these series of tests is 80.8 m/s, which is considerably slower than what was reported for crack propagation in

freshwater ice by Arakawa *et al.* (1995). This discrepancy was expected, because the camera caught just one frame of crack growth and the imaging speed was not rapid enough to capture several steps of crack propagation. Therefore, the value of crack growth speed in this group of tests is a minimum value and does not give an accurate measurement of the speed of crack propagation.

Test	Beam Height (mm)	Crack velocity (m/s)
1	39.55	79.1
2	41.15	82.3
3	40.7	81.4
4	40.85	81.7
5	40.35	80.7
6	40.45	80.9
7	39.8	79.6

**Table 9.1.** Data of 7 ice fracture tests with ice beams without a notch

In the other tests with a notched beam, three tests with three different imaging speeds (test 1 with 20000 FPS, test 2 with 75000 FPS and test 3 with 150000 FPS) were conducted. Table 9.2 shows the values of the crack propagation speed in these three tests. The high-speed video observations show that the crack propagation speed is not constant during the fracture of the beams.

Figure 9.2 shows the variation of crack propagation speed versus time at the three different imaging speeds. Figure 9.3 shows the crack propagation distance from the notch tip versus time. Cracks at times slow down and then speed up. This behavior of cracks has also been reported by other investigators (e.g. Gagnon *et al.*, 1999; DeFranco and Dempsey, 1994; Arakawa *et al.*, 1995). Arakawa *et al.* (1995) attributed these crack velocity fluctuations to heterogeneities in the structure of samples such as grain boundaries. They mentioned that grain boundaries may interact with the crack growth process through

dislocation piled-up in the stress field around the crack tips. Many researchers (e.g. DeFranco and Dempsey, 1994; Gagnon *et al.*, 1999) have also noted the influence of grain boundaries on crack propagation speed.

Test No.	Time (s)	Crack velocity (m/s)	Distance from the notch tip (mm)
1	5.0E-05	360	18
	1.0E-04	240	30
	1.5E-04	160	38
2	1.3E-05	1275.32	17
	2.7E-05	525.13	24
	4.0E-05	300.08	28
	5.3E-05	450.11	34
	6.7E-05	262.57	37.5
	6.7E-06	750.08	5
3	1.3E-05	450.05	8
	2.0E-05	300.03	10
	2.7E-05	600.06	14
	3.3E-05	450.05	17
	4.0E-05	300.03	19
	4.7E-05	450.05	22
	5.3E-05	300.03	24
	6.0E-05	450.05	27
	6.7E-05	450.05	30
	7.3E-05	300.03	32
8.0E-05	450.05	35	
8.7E-05	300.03	37	

**Table 9.2.** Results of high-speed video observations in three tests

It is seen in all three tests that at the first step of crack propagation, the crack speed is higher than in the next steps. This arises from the fact that at the first step, the level of concentrated stress around the notch tip is higher than the next steps when the crack tip is very sharp and needs a lower stress level to propagate. In the two tests with higher imaging speed, multiple episodes of the cracks speeding up and slowing down are seen. In the test

with 20000 FPS, this trend is not seen due to the low imaging speed, which causes loosing of some speeding up and slowing down episodes.

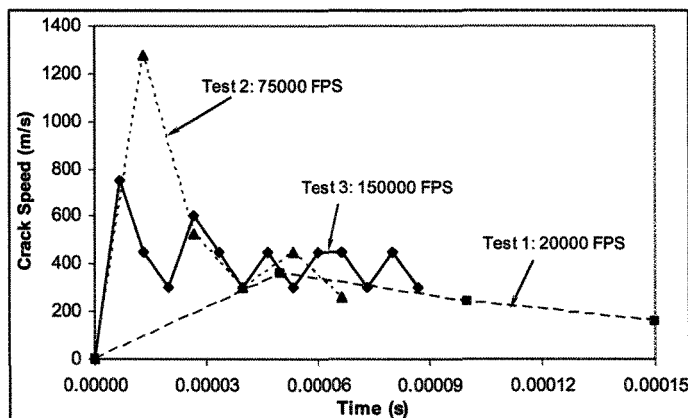


Figure 9.2. The variation of crack propagation speed versus time.

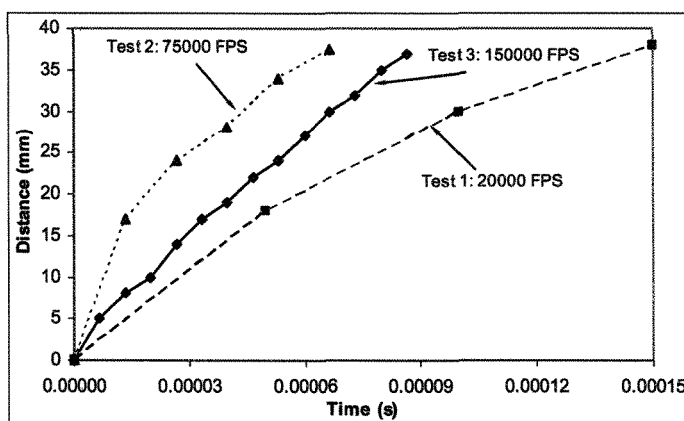
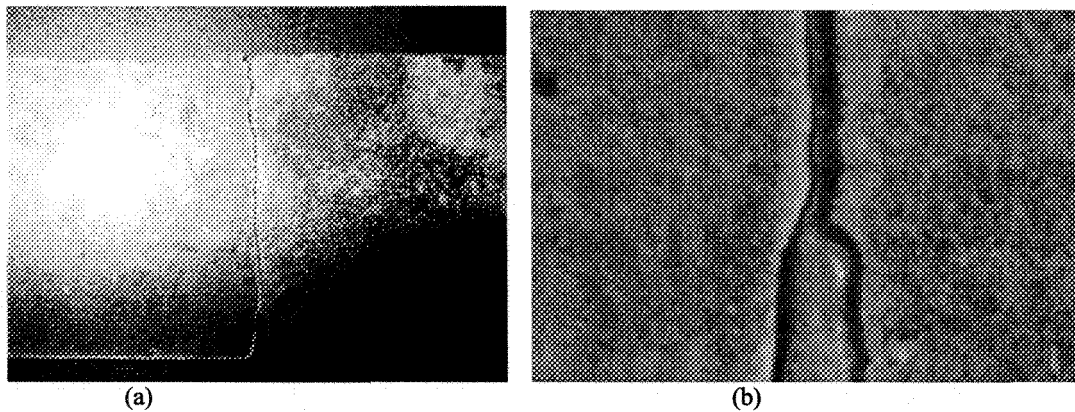


Figure 9.3. The crack propagation distance from the crack tip versus time.

As seen in Figure 9.2, the crack propagation speed in these tests is considerably higher than the corresponding value in the previous tests. In these tests, the peak speeds for the three tests are 360, 750 and 1275 m/s and the average crack speeds are 253.3, 427 and 562.6 m/s for tests 1, 2 and 3, respectively. The results of these tests are in the range of the results of Arakawa *et al.* (1995) and Gagnon (2003). In the test with the imaging speed of 20000 FPS, the crack speed in the first step is slower than in the two other tests because at

this low imaging speed, the peak value of the crack speed cannot be seen, and the crack speed in this step is the average of a peak value (probably more than 800 m/s) and some of the lower speeds in the same interval of the first image.



**Figure 9.4.** Thin section of a reconstituted beam.

Figures 9.4.a and b show the thin section of a reconstituted beam. As seen in the figure, the crack initiated from the notch corner, similar to the findings of Gagnon *et al.* (1999).

Figures 9.5.a and b show the crack propagation through the grains. As can be seen, the crack splits the grains and continues its path to the top of the beam. The grain boundaries show some resistance against crack propagation, which is why the fluctuation in the crack propagation speed is observed. With the increase of stress filed around the crack tip, however, the crack overcomes the resistance of grain boundaries and propagates.

Figure 9.6 shows three photos of crack propagation during the first test with an imaging speed of 20000 FPS. Unfortunately, the quality of the pictures is not good, but some white pixels showing the crack path are visible in the figures. In these photos, the bending force was applied at the top and the crack started to propagate from the end of the notch to the top of the beam.

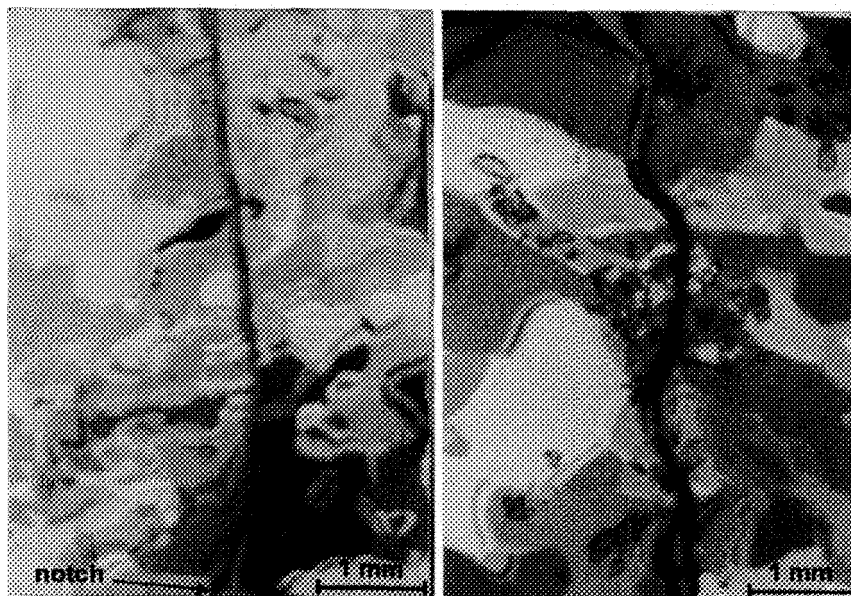


Figure 9.5. Thin sections showing the propagation of the crack through the grains.

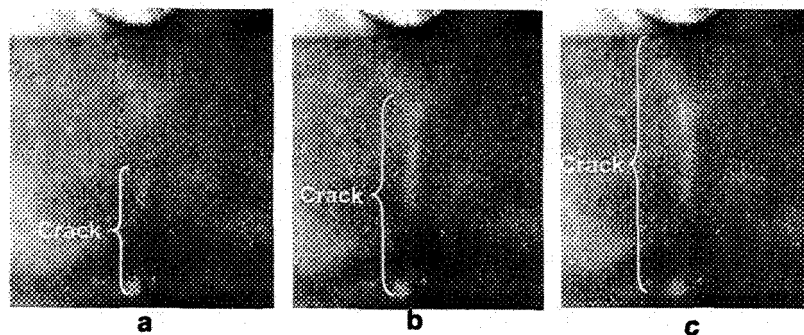


Figure 9.6. The three steps of crack propagation in an atmospheric ice sample.

#### 9.4 Conclusion

The initiation and propagation of a crack in atmospheric ice were studied using high-speed video cameras in two series of beam bending tests. The average velocity of crack propagation in atmospheric ice in 7 tests with a three-point beam (without a notch) was approximately 80 m/s. In the other group of tests with a notched beam, three tests with three different imaging speeds (20000 FPS, 75000 FPS and 150000 FPS) were conducted.

The peak speeds in these tests were 360, 750 and 1275 m/s and the average crack speed was 253.3, 427 and 562.6 m/s. The thin sections of the reconstituted beam show that the crack originates from the notch corner and propagates through the grains, splits them and continues its path to the top of the beam.

The results of these tests will be useful for future models of ice shedding, in cases where the model needs the crack propagation speed in ice along the cable.

## **CHAPTER 10**

### **GENERAL CONCLUSIONS AND RECOMMENDATIONS**

#### **10.1 General conclusions**

Atmospheric icing and its accretion on power transmission lines may cause considerable damage to power networks in cold climate regions. Nowadays, many attempts are being made to reduce the damage caused by atmospheric icing. Uncontrolled ice shedding creates many serious problems in the power transmission line industry. In order to avoid the damage caused by ice shedding, knowledge of ice behavior under loading conditions is indispensable. The general objectives of this research work, as a part of general ice shedding problem, were to estimate the stresses in atmospheric ice on the cables, measure the mechanical properties of atmospheric ice and model the brittle behavior of atmospheric ice. On the basis of the literature review, the experimental work and the analyses of this research work, the following conclusions have been drawn:

- 1) Ice shedding is influenced by some direct and some indirect factors. The direct influence factors act as a source of energy for ice breaking and are the natural loading in ice shedding. Wind force and ice load are the most important ones. The indirect factors provide suitable conditions for ice breaking by reducing ice strength, or eliminating its adhesion to the cable. These factors can be divided into two categories: ice constitutive behaviors and miscellaneous factors. The strength

of atmospheric ice is dependent on temperature, wind velocity, liquid water content of air and mean diameter of supercooled droplets during ice accretion. It also depends on the load rate and temperature during ice shedding. The cable torsional stiffness, tension of the cable and ice shape also have a certain influence on ice shedding.

- 2) Two finite element models were developed to estimate the stresses developed in the ice accreted on an overhead cable during galloping and aeolian vibration. To do this, the equations of cable motion during these vibrations were applied to an iced cable. Then, the other loads (aerodynamic forces, additional horizontal tension acting in the cable during vibration and torque due to spring back) were added to the model. The model of galloping revealed that the highest stresses developed along the vertical diameter of the ice when the mid-point of the cable reached the highest and lowest positions in its trajectory. These stresses exceeded the bending strength of ice in the particular case studied in this research. The other ABAQUS model that was developed to simulate the stress distribution in atmospheric ice during aeolian vibration indicated that under the particular condition analyzed in this study, the maximum Von Mises stresses are 7700 Pa for the elements in the external layer, and 5800 Pa for the elements in the internal layer.
- 3) To study the structure, grain size and air bubbles in various types of atmospheric ice, a rotating cylinder in the CIGELE atmospheric icing wind tunnel was used and ice was accumulated at a LWC of  $2.5 \text{ gr/m}^3$ , a wind speed of 10m/s and various

accumulation temperatures. Thin sections of these three types of atmospheric ice showed that grain size decreases with decreasing accumulation temperatures. The average grain size for accumulated ice is 1.5 mm, 0.5mm and 0.4 mm, for accumulation temperatures of  $-6^{\circ}\text{C}$ ,  $-10^{\circ}\text{C}$  and  $-20^{\circ}\text{C}$ , respectively. In atmospheric ice accumulated at  $-20^{\circ}\text{C}$ , a significant number of cavities, and possibly cracks, were seen.

- 4) In order to measure the mechanical properties of various types of atmospheric ice, more than 350 tests were conducted. The results of these investigations show that the compressive strength, bending strength, and fracture toughness of atmospheric ice are influenced by the accumulation temperature and test temperature. The compressive strength of atmospheric ice increases with decreasing test temperatures. It also increases with increasing strain rates up to  $10^{-3}\text{s}^{-1}$  and then decreases at higher strain rates. At the lower strain rates, the bending strength of the atmospheric ice increases with decreasing temperatures but no temperature effect is seen at the higher strain rates. The effective modulus of atmospheric ice has been found to increase with increasing strain rates. The fracture toughness of atmospheric ice decreases with decreasing accumulation temperatures. The average Young's modulus of atmospheric ice accumulated at  $-6^{\circ}\text{C}$ ,  $-10^{\circ}\text{C}$  and  $-20^{\circ}\text{C}$  is 3.69 GPa, 4.74 GPa and 5.05 GPa, respectively.
- 5) To simulate crack propagation in atmospheric ice, an ABAQUS model was developed, which simulates the quasi-static crack growth in a two dimensional three-point beam. Potential crack surfaces were modeled as slave and master

contact surfaces. The result of the ABAQUS model is in strong agreement with the experimental tests.

- 6) The cracking activity of atmospheric ice can be modeled by the decomposition of the strain rate into two parts: elastic and cracking strain rate. The recoverable elastic strain is related to the corresponding applied stress by Hook's law. To obtain the stress-strain relation in the presence of a crack, a diagonal cracking matrix is defined. The components of the diagonal cracking matrix can be obtained by experimental work and the mechanical properties of material. A Rankine criterion is used to detect crack initiation.
- 7) A three dimensional model was developed that uses the Rankine criterion for cracking and post-failure behavior of ice for post-cracking condition. The Results of the ABAQUS model showed good agreement with the results of the experiments. This brittle cracking model was expanded to a model of atmospheric ice on the cable. Five bending tests were conducted with an ice-cable beam to validate the results of the ABAQUS model. The results of the predicted force in the ABAQUS model showed a 14% error while the results of the predicted beam deflection showed a 49% error. These errors changed when the value of Young's modulus in the model varied.
- 8) Two series of tests were conducted to study crack propagation in ice. High speed video cameras were used for measuring the crack propagation speed. The peak speeds in these tests were 360, 750 and 1275 m/s and the average crack speed was 253.3, 427 and 562.6 m/s.

## **10.2 Recommendations for future studies**

The aspects of this research work can be divided into four subjects. The definition of the problem and its scope, estimation of stresses in atmospheric ice on the cable, measurements of mechanical properties of atmospheric ice and the development of a brittle cracking model of atmospheric ice. These four subjects are therefore recommended for further research.

### **10.2.1 The scope of the ice shedding problem**

The ice shedding problem is still unclear and needs more investigation. In this research, the process of separating atmospheric ice from the cable was not studied. Further investigation is required to study the formation of horizontal cracks, the interaction between the cracks and the influencing factors on ice separation. Some experiments in real conditions will also be useful to gain a better understanding of ice shedding. In this research, the ice shape was assumed to be cylindrical. Using the models developed in this study, various ice shapes (more realistic non-symmetric shapes) can be studied.

### **10.2.2 Estimation of stresses in atmospheric ice on the cable**

The stresses in atmospheric ice during galloping and aeolian vibration were estimated in this study. Estimation of stresses during wake-induced oscillation occurring in bundled conductors should be studied in future works. More vibration modes can be studied during galloping. Using more powerful computers in the future, it will be possible to reproduce the cable with its exact geometry (not as a cylinder). Using the exact geometry, it will be

possible to take a longer piece of the cable in the middle of a span and study the stresses in atmospheric ice. Modeling the ice separation will also be possible in the future by assuming a third material (with zero thickness) located between the ice and the cable and attached to both of them. The failure of this material during vibration will indicate the ice separation from the cable.

Galloping of an ice accreted cable with different shapes and different drag and lift forces is another subject worthwhile of future study.

### **10.2.3 Measurements of mechanical properties of atmospheric ice**

The bending strength, effective modulus, compressive strength, fracture toughness and Young's modulus of atmospheric ice were measured in this study. The measurement of Young's modulus with dynamic loading is more accurate and can be done in future research. The tensile and shear strength of atmospheric ice are some important properties and should be studied in the future. Some other experimental tests are also required with ice accumulated under different icing conditions (various LWC and wind speeds). The value of fracture toughness also can be obtained using other mechanical properties of the material.

More tests for measuring crack propagation speed are required using a proper optical lens and a high speed video camera to obtain more reliable results.

### **10.2.4 The brittle cracking model of atmospheric ice**

The atmospheric ice was considered as an isotropic material, because an analysis of the brittle cracking of a transversely isotropic material is not feasible in ABAQUS. The results

of the model will be more accurate if the ice is considered as a transversely isotropic material. As mentioned in section 10.2.2, by using a more powerful computer in the future, it will be possible to model the exact geometry of the cable. In this way, the flexural rigidity of the cable in the model will be more accurate and closer to the real cable. Consequently, the results of this model will be more precise. The model of brittle cracking of atmospheric ice can be improved by adding the plasticity of the material. This modification gives a higher accuracy in the model results, particularly when we use effective modulus rather than Young's modulus of the material. Modeling of crack propagation in a three-dimensional geometry is not possible in the present model. In the future, however, this will be possible and it will facilitate the modeling of crack propagation in atmospheric ice on cables.

## REFERENCES

- [1] ABAQUS theory manual, 2005. Version 6.5, ABAQUS Incorporation.
- [2] Abdel Rohman, M.A., Spenser, B., 2004. Control of Wind-Induced Nonlinear Oscillations in Suspended Cables, *Nonlinear Dynamics*, Vol. 37, PP 341-355.
- [3] Arakawa, M., Maeno, N. and Higa, M., 1995. Direct observations of growing cracks in ice. *Journal of Geophysical Research*, Vol. 100, No. E4, PP 7539-7547.
- [4] Ashby, M. F., Hallam, S. D., 1986. The failure of brittle solids containing small cracks under compressive stress states, *Acta Metallurgy*, Vol.16, PP 107-144.
- [5] Ayatollahi, M. R., Pavier, M. J., Smith, D. J., 1998. Determination of T-stress from finite element analysis for mode I and mixed mode I/II loading, *Int. J. Fract.*, 91, PP 283–98.
- [6] B. Michel, 1978 . *Ice mechanics*, Les Presses De L'universite Laval.
- [7] Bernardein, S., 1989 . *Etude et analyse du delestage de glase atmospheique sur les cables*, M.Sc.thesis, University of Quebec at Chicoutimi.
- [8] Blevins, R. D., 1990. *Flow induced vibration*, Van Nostrand Reinhold.
- [9] Budd, W.f. and Jacka, T.H., 1989. A Review of ice rheology for ice sheet modeling , *Cold Regions Science and Technology*, Vol. 16, PP 107-144.
- [10] Chaudhri, M. M., and Wallay, S. M., 1978. Damage to glass surface by impact of small glass and steel spheres, *Philos. Mag. A*, 37, PP 153-165.
- [11] CIGRE Working Group 01, 1978. Report on Aeolian Vibration, *ELECTRA*, NO. 124, PP 21-77.
- [12] CIGRE Working Group 11, 1998. Modelling of Aeolian vibration of single conductors: Assessment of the technology, *ELECTRA*, NO.181, PP 53-69.
- [13] Cole, D. M., 1989. Microfracture and the compressive failure of polycrystalline ice, *Proc.IUTAM/IAHR Symposium in Ice-Structure Interaction*, 23.

- [14] Cotterell, B., and Rice, J. R., 1980. Slightly Curved or Kinked Cracks, *International Journal of Fracture*, Vol. 16, PP 155–169.
- [15] Dantl, G., 1969. Elastic moduli of ice, in *Physics of ice*, by Riehl, N., Bullemer, B., and Engelhardt, H., Cambridge University press, Cambridge: PP 223-230.
- [16] Defranco, S. J. and Dempsey, J. P., 1994. Crack propagation and fracture resistance in saline ice. *Journal of Glaciology*, Vol. 40, No. 136, PP 451-462.
- [17] Dempsey, J. P., Adamson, R. M., Mulmule, S.V., 1999. Scale effects on the in-situ tensile strength and fracture of ice. Part II: First-year sea ice at Resolute, N.W.T., *International Journal of Fracture*, Vol. 95, PP 347–366.
- [18] Dempsey, J. P., Wei, Y., DeFranco, S., Ruben, R., Frachetti, R., 1989. Fracture toughness of S2 columnar freshwater ice: Crack length and specimen size effects- Part1, *The Eighth International Conference on Offshore Mechanics and Arctic Engineering*, PP 83-89.
- [19] Doocy, E.S. and Hard, A.R., 1979, Chapter 1 in *Transition Line reference Book Wind-induced conductor motion*, Electric Power Research Institute, Palo Alto, California.
- [20] Dorsey N. E, 1940. *Properties of ordinary water substance*, Rienhold, New York.
- [21] Dowling, N. E., 1998. *Mechanical behavior of materials*, Prentice Hall.
- [22] Druez, J., Laforte, J.L. and Tremblay, C., 1989. Experimental Results on the Tensile Strength of Atmospheric Ice, *The American Society of Mechanical Engineers, 8<sup>th</sup> International Conference on Offshore Mechanics and Arctic Engineering*, Hague, Netherlands, Book No. 10285 D, PP 405-410.
- [23] Druez, J. Nguyeh, D. D. and Lavoie, Y., 1986. Mechanical properties of atmospheric ice, *Cold Regions Science and Technology*, Vol. 13, PP 67-74.
- [24] Eftis, J., Subramonian, N., Liebowitz, H., 1977. Crack border stress and displacement equations revisited, *Eng. Fract. Mech.* 9 (1), PP 189–210.
- [25] Erdogan, F. and Sih, G.C., 1963. On the crack extension in plates under plane loading and transverse shear, *J. Basic. Eng.*, 85, PP 519-527.

- [26] Eskandarian, M., 2005. Ice shedding from overhead electrical lines by mechanical breaking, Ph.D. thesis, University of Quebec at Chicoutimi.
- [27] Farzaneh, M. and Laforte, J. L., 1994. Ice accretion on conductors energized by AC or DC: a laboratory investigation of ice treeing, *Int. J. Offshore Polar Engng* , Vol. 4, PP 40-47.
- [28] Farzaneh, M., 2000. Ice accretions on high-voltage conductors and insulators and related phenomena, *Philosophical Transactions of the Royal society*, Vol. 358, Issue 1776, PP 2971-3005.
- [29] Farzaneh, M., Bouillot, J., Teisseyre, Y., Svensson, E. C. and Dubouchet, P., 1996. Crystallographic structure of ice grown on an energized conductor. In *Proc. 7th Int. Workshop on Atmospheric Icing of Structures*, Chicoutimi, 351-354.
- [30] Fischer, M.P. and Alley, R.B., 1995. Fracture toughness of ice and firm determined from the modified ring test, *Journal of Glaciology*, Vol. 41 , No 138, PP 383- 393.
- [31] Forest, H. J., Colloge, D., 1995. Mechanism of crack nucleation in ice, *Ice Mechanics*, United Engineering Center.
- [32] Frederking, R. M. W. and Svec, O. J., 1985. Stress-Relieving Techniques for Cantilever Beam tests in an Ice Cover, *Cold Regions Science and Technology*, Vol. 11, PP 247-253.
- [33] Fu, P., 2004. Modeling and simulation of the ice accretion process on fixed or rotating cylindrical objects by the boundary element method, Ph.D. thesis, University of Quebec at Chicoutimi.
- [34] Gagnon R. E and Gammon, P.H., 1995. Triaxial experiments on iceberg and glacier ice, *Journal of Glaciology*, 41(139), PP 538-540.
- [35] Gagnon, R. E. and Gammon, P. H., 1995. Characterization and flexural strength of iceberg and glacier ice, *Journal of Glaciology*, Vol. 41, No. 137, PP 103-111.
- [36] Gagnon, R. E., Williams , F. M., Sinha, N. K., 1999. High Speed Video Observations of Fracture from Beam Bending Experiments on Sea Ice, 15th

International Conference on Port and Ocean Engineering Under Arctic Conditions, Espoo, Finland.

- [37] Gagnon, R.E, 2003. High-speed video analysis of fracture propagation in a thick edge-loaded freshwater ice sheet, *Canadian Journal of Physics*, Vol. 81, No. 1/2, PP 261-269.
- [38] Gagnon, R.E., Kieft, K, and Clouter, MJ., 1988. Pressure dependence of the elastic constants of ice Ih to 2.8 kbar by Brillouin Spectroscopy, *Journal of Chem. Phys.*, 89 (8): 4522-4528.
- [39] Gagnon, R.E., 1987. Brillouin Spectroscopic Studies of the Elastic Properties of Ice up to 10 kbar. Ph.D. thesis, Department of Physics, Memorial University of Newfoundland and Labrador.
- [40] Gammon P. H. , Kieft H., Clouter M.J. and Denner W.W., 1983. Elastic constants of artificial and natural ice samples by Brillouin spectroscopy, *Journal of Glaciology*, 29 (103), PP 443-460.
- [41] Glenn, L. A., 1976. The fracture of a glass half-space by projectile impact, *J. Mech. Solids*, 24, PP 93-106.
- [42] Gold L. W, 1963. Crack formation in ice plates by thermal shock, *Canadian Journal of Physics*, 41, PP 1712-1738.
- [43] Gold, L. W., 1972. The process of failure of columnar –grained ice, *Philos. Mag. A*. 26(2), PP 311-328.
- [44] Goodman D.J. and Tabor D., 1978. Fracture toughness of ice: a Preliminary account of some new experiments, *Journal of Glaciology*, 21 (85), PP 651-660.
- [45] Gow, J. A. and Ueda, T. H., 1988. Structure and temperature dependence of the flexural properties of laboratory freshwater ice sheets, *Cold Regions Science and Technology*, Vol. 16, PP 249-269.
- [46] Gratz E. T., and Schulson, E. M., 1994. Preliminary observations of brittle compressive failure of columnar saline ice under uniaxial loading, *Annals of Glaciology*, 19, PP 33-48.

- [47] Griffith, A. A., 1921. The phenomenon of rupture and flow in solids, Ser. A221, Phil. Trans. Roy. Soc, London, PP 55-63.
- [48] Hamza, H. and Muggeridge, D. B., 1984. An analysis of the viscoelastic fracture toughness and crack growth in ice, Cold Regions science and technology, Vol. 9, PP 249-258.
- [49] Hawkes, I., Mellor, M., 1972. Deformation and fracture of ice under uniaxial stress. Journal of Glaciology, 11 (61): 103-31.
- [50] Hayashi, K., and Nemat-Nasser, S., 1981. Energy-Release Rate and Crack Kinking under Combined Loading, Journal of Applied Mechanics, Vol. 48, PP 520–524.
- [51] He, M. Y., Hutchinson, J. W., 1989. Kinking of a Crack out of an Interface: Tabulated Solution Coefficients, Harvard University, Cambridge, Massachusetts, Division of Applied Mechanics.
- [52] Hill R. 1952. The elastic behaviour of a crystalline aggregate, Proc. Phys. Soc. ,65 (a), PP 349-354.
- [53] Holman, J. P., Podlny,W., 1976. Construction and design of cable –stayed bridges, Wiley-interscience publication.
- [54] Hook, R. L. and Moller, M., 1980. Mechanical properties of polycrystalline ice: An assessment of current knowledge and properties for research, Cold Regions science and technology, Vol.3, PP 263-275.
- [55] Hosford, W. F., 2005. Mechanical behavior of materials, Cambridge University Press, New York.
- [56] Hussain, M. A., Pu, S. L., and Underwood, J., 1974. Strain-Energy-Release Rate for a Crack under Combined Mode I and Mode II, ASTM-STP-560, PP 2–28.
- [57] Irvine H. M. and Caughey T.K., 1974. The linear theory of free vibration of a suspended cable, Vol. 341, 299-315.
- [58] Irvine M., 1992. Cable structures, Dover, New York.
- [59] Javan-Mashmool, M., Volat, C., Farzaneh, M., 2005. A Theoretical Model for Measuring Stress Induced by a Vibrating load at Ice/Material Interface.

- Proceedings 11th International Workshop on Atmospheric Icing of Structures, Montreal, PP 141-146.
- [60] Jones, S. J., 1982. The confined compressive strength of polycrystalline ice, *Journal of Glaciology*, 28 (98), PP 171-7.
- [61] Kalifa, P., Jones, S.J. and Slade, T. D., 1991. Microcrack nucleation in granular ice under uniaxial compression: effect of grain size and temperature, *Annals of Glaciology*, 15, PP 222-229.
- [62] Kalman, T., Farzaneh, M., McClure, G., 2007. Numerical analysis of the dynamic effects of shock-load-induced ice shedding on overhead ground wires, *Computers and Structures*, Vol. 85, No. 7-8, PP 375-384.
- [63] Karev, A. R., Farzaneh, M., Kollar, L. E., An Icing Wind Tunnel Study on Characteristics of an Artificial Aerosol Cloud, Part II: Liquid Water Content as a Function of Air Speed, submitted to *J. of Atmospheric and Oceanic Technology*.
- [64] Kazakevitch, M. I., Graftsky, I. Y., 1998. The interaction of wind with ice – covered structural elements, *International Workshop on Atmospheric Icing of Structures*, PP 299-302.
- [65] Kermani, M., Farzaneh, M., Gagnon, R. E., 2007. Compressive strength of atmospheric ice, *Cold Regions science and technology*, Vol. 49, PP 195–205.
- [66] Kim, J., Sunder, S.S., 1997. Statistical effects on the evolution of compliance and compressive fracture stress of ice, *Cold Regions science and technology*, Vol. 26, PP 137-152.
- [67] Kuelln, G. A. and Schulson, E. M., 1994. The mechanical properties of saline ice under uniaxial compressive, *Annals of glaciology*, Vol. 19, PP 39-48.
- [68] Laforte, J. L. and Phan L., 1983. Microstructure of ice accretions grown on aluminum conductors, *Journal of Climate and Applied Meteorology*, 22 (7), PP 1175-1189.
- [69] Laforte, J. L., Allaire, M. A., Laforte, C., 2005. Demonstration of the Feasibility of a New Mechanical Method of Cable De-Icing. *Proceedings 11th International Workshop on Atmospheric Icing of Structures*, Montreal, PP 347-352.

- [70] Lavrov, V.V., 1971. Deformation and strength of ice. Transl. from Russian, Natl. Sci. Found., Israel Program for Scientific Translation, Jerusalem, PP 1-164.
- [71] Liu H. W. and loop L. W., 1972. Fracture toughness of freshwater ice , Journal of glaciology, Vol. 22, PP 135-143.
- [72] Luongo A. and Piccardo G., 1998. Non-linear galloping of saged cables in 1:2 internal resonance, Journal of Sound and Vibration, Vol. 214(5), PP 915-940.
- [73] Maiti, S. K., and Smith, R. A., 1983. Comparison of the Criteria for Mixed Mode Brittle Fracture Based on the Preinstability Stress-Strain Field, Part I: Slit and Elliptical Cracks under Uniaxial Tensile Loading, International Journal of Fracture, Vol. 23, PP 281–295.
- [74] Mellor, M., and Cole, D. M., 1982. Deformation and failure of ice under constant strain rate, 1982, Cold Regions Science and Technology, Vol. 5, PP 201-219.
- [75] Michel B., 1978, Ice mechanics, Press de l'Universite Laval, Quebec.
- [76] Mousavi, M., 2003. Experimental and theoretical verification of two icing codes, M.Sc. thesis, University of Quebec at Chicoutimi.
- [77] Nakamura, T.M., Parks, D.M., 1992. Determination of elastic T-stress along a three-dimensional crack fronts using an interaction integral. Int. J. Solids Struct. 29, PP 1597–611.
- [78] Nanthikesan, S., Sunder, S.S., 1994. Anisotropy elasticity of polycrystalline ice Ih. Cold Regions Science and Technology, Vol. 22, PP 149-169.
- [79] Ohkuma T., Kagami, J., Nakauchi, H. ,Kikuchi, T., Takeda, K., Marukawa, H.,1998. Evaluation of galloping of transmission lines in Gusty winds, International Workshop on Atmospheric Icing of Structures, PP 311-316.
- [80] Orowan, E., 1950. Fatigue and fracture of metals, Proc. Massachusetts institute of technology Symp., PP 139.
- [81] Ozawa, Z. and Col, 1996. Observation of galloping on overhead transmission test line with artificial snow accretion model, International Workshop on Atmospheric Icing of Structures, PP 300-305.

- [82] Palaniswamy, K., Knauss, W. G., 1978. On the Problem of Crack Extension in Brittle Solids under General Loading," *Mechanics Today*, Edited by S. Nemat-Nasser, Vol. 4, Pergamon Press.
- [83] Parsons, B. L., Snellen, J. B. and Hill, B., 1987. Preliminary measurements of terminal crack velocity in ice, *Cold Regions Science and Technology*, Vol. 13, No. 3, PP 233-238.
- [84] Poots, G., 1996. *Ice and snow accretion on structures*, John Willy & Sons Inc.
- [85] Reuss, A., 1929. *Z. Angew. Math. Mech.* 9, 49.
- [86] Richter-Menge, J.A., 1984. Static determination of Young's modulus in sea ice, *Cold Regions Science and Technology*, Vol. 9, PP 283-286.
- [87] Schulson, E. M., 1990. The brittle compressive fracture of ice. *Acta Metal. Mater.*, Vol. 38 (10), PP 1963-76.
- [88] Schulson, E. M., 2001. Brittle failure of ice, *Engineering fracture mechanics*, Vol. 68, PP 1839-1887.
- [89] Schulson, E. M., Canon, N. P., 1984. The effect of grain size on the compressive strength of ice. *IAHR Ice symposium, Hamburg*, PP 109-117.
- [90] Schwarz, J., Frederking, Gavrilov, R., Petrov, I., Hirayama, K., Mellor, M., Tryde, P. and Vaudrey, K., 1981. Standardized testing methods for measuring mechanical properties of ice. *Cold Regions Science and Technology*, Vol. 4, PP 245-253.
- [91] Sherry, A. H., France, C. C., Goldthorpe, M. R., 1995. Compendium of T-stress solutions for two and three dimensional cracked geometries, *Fatigue Fract. Eng. Mater. Struct.*, 18, PP 141-55.
- [92] Sih, G. C., 1974. Strain-energy-density factor applied to mixed mode crack problems. *Int. J. Fract.*, 19(3), PP 305-321.
- [93] Sih, G. C., 1973. Some Basic Problems in Fracture Mechanics and New Concepts, *Engineering Fracture Mechanics*, Vol. 5, PP 365-377.
- [94] Sinha N. K., 1978. Short tem rheology of polycrystalline ice, *Journal of Glaciology*, 21(85), PP 457-473.

- [95] Sinha N. K., 1989. Elasticity of natural types of polycrystalline ice, *Cold Regions science and technology*, Vol. 17, PP 127-135.
- [96] Sinha, N. K., 1984. Intracrystalline cracking, grain-boundary sliding and delayed elasticity at high temperature, *J. mater. Sci.*, 19 (2), PP 359-376.
- [97] Smith, T. R. and Schulson, M.E. and Schulson, 1990. The Fracture Toughness of Porous Ice With and Without Particles, *Proc. 9th Intl. Conf. on Offshore Mech. and Arctic Eng.*, IV, PP 241-246.
- [98] Stallabrass, J. R., 1978. An appraisal of the single rotating cylinder method of liquid water content measurement. National Research Council of Canada, Division of Mechanical Engineering, Rep. LTR-LT-92.
- [99] Structure group of ice storm commission, 2002. Lessons from the ice storm of 1998, *Proceeding of International Workshop of Atmospheric Icing Structures, IWAIS 2002*.
- [100] Sunder, S. S. and Wu, M. S., 1990. Crack nucleation due to elastic anisotropy in polycrystalline ice, *Cold Regions Science and technology*, Vol. 18, PP 29-47.
- [101] Teisseyre, Y. and Farzaneh, M., 1990. On the mechanism of the ice accretion on HV conductors, *Cold Regions Science and technology*, Vol. 18, 1-8.
- [102] Theocaris, P. S. , 1984. A Higher Order Approximation for the T-Criterion of Fracture in Biaxial Fields, *Engineering Fracture Mechanics*, Vol. 19, PP 975–991.
- [103] Timco, G. W. and Frederking, R. M. W , 1982. Comparative strengths of fresh water ice, *Cold Regions Science and Technology*, Vol. 6, PP 21-27.
- [104] Timco, G. W. and Frederking, R. M. W , 1986. The effects of anisotropy and microcracks on the fracture toughness  $K_{IC}$  of freshwater ice, *Proceedings of the 5<sup>th</sup> International OMAE Symposium, Tokyo , Japan*, Vol. IV , PP 341-348.
- [105] Timco, G. W. and O'Brien, S., 1994. Flexural strength equation for sea ice, *Cold Regions Science and Technology*, Vol. 22, PP 285-298.
- [106] Timoshenko, S., 1968. *Elements of Strength of Materials*, 5th Ed. Van Nostrand, Princeton.

- [107] Van Dyke, P. and Havard, D. G., 2005. Effect of ice and snow on the dynamics of transmission line cables, International Workshop on Atmospheric Icing of Structures.
- [108] Voigt, W., 1910. Lehrbuch Der Krystallphysik, Feubner, Berlin.
- [109] Williams, M. L., 1957. On the stress distribution at the base of a stationary crack, J. Appl. Mech., 24, PP 109–14.
- [110] Working group of study committee 22, Report on aeolian vibration, CIGRE, 1989. PP 41-78.
- [111] Wu, M. S., Niu, J., 1994. Micromechanical prediction of the compressive failure of ice: Model development. Mechanics of materials, Vol. 20, PP 9-32.
- [112] Yu, P., Desai, Y. M., Shah, A. H., Popplewell, N., 1993. “Three-degree-of-freedom model for galloping. Part II: Solutions.” Journal of Engineering Mechanics, 119(12), PP 2426-2448.
- [113] Zhao, J., Guo, W., She, C., 2007. The in-plane and out-of-plane stress constraint factors and K-T-Tz description of stress field near the border of a semi-elliptical surface crack , International Journal of Fatigue, Vol. 29, PP 435–443.
- [114] Zsolts Z. , 2006. Modeling and Simulation of the ice melting process on a current-carrying conductor, Ph.D. thesis, University of Quebec at Chicoutimi.

## APPENDIX A

The coefficients  $n_i$ ,  $d_i$  and  $e_i$  in equations (16)-(19) are defined as follows:

$$n_1 = \frac{1.5mgEA}{T_0 f_2} \int_0^l \varphi_2 \varphi_2'^2 ds$$

$$n_2 = \frac{mgEA}{2T_0 f_2} \int_0^l \varphi_2 \varphi_2'^2 ds$$

$$n_3 = \frac{1.5EA}{f_2} \int_0^l \varphi_2 \varphi_2'^2 \varphi_2'' ds$$

$$n_4 = -\left( \frac{EA}{f_2} \int_0^l \varphi_2 \varphi_2' \varphi_1' \varphi_1'' ds + \frac{EA}{2f_2} \int_0^l \varphi_2 \varphi_2'' \varphi_1'^2 ds \right)$$

$$n_5 = \frac{mgEA}{T_0 f_1} \int_0^l \varphi_2' \varphi_1 \varphi_1' ds$$

$$n_6 = -\left( \frac{EA}{f_1} \int_0^l \varphi_1 \varphi_2' \varphi_1' \varphi_2'' ds + \frac{EA}{2f_1} \int_0^l \varphi_1 \varphi_1'' \varphi_2'^2 ds \right)$$

$$n_7 = \frac{1.5EA}{f_1} \int_0^l \varphi_1'' \varphi_1 \varphi_1'^2 ds$$

$$d_0 = \frac{\rho D a_0}{2f_1} \int_0^l \varphi_1 U^2(s,t) ds$$

$$d_1 = -\frac{\rho D a_0}{f_1} \int_0^l \varphi_1^2 U(s,t) ds$$

$$d_2 = \frac{\rho D a_0}{2f_1} \int_0^l \varphi_1^3 ds$$

$$d_3 = \frac{\rho D a_1}{2f_1} \int_0^l \varphi_1 \varphi_2 U(s,t) ds$$

$$d_4 = -\frac{\rho D a_1}{2f_1} \int_0^l \varphi_1^2 \varphi_2 ds$$

$$d_5 = \frac{\rho D a_2}{2f_1} \int_0^l \varphi_2^2 \varphi_1 ds$$

$$d_{(2k)} = \frac{\rho D a_k}{2f_1} \int_0^l \frac{\varphi_2^k \varphi_1}{U^{(k-2)}} ds$$

$$d_{(2k+1)} = \frac{\rho D a_k (k-2)}{2f_1} \int_0^l \frac{\varphi_2^k \varphi_1^2}{U^{(k-1)}} ds \quad k = 3, \dots, 7$$

$$e_0 = \frac{\rho D b_0}{2f_2} \int_0^l \varphi_2 U^2(s,t) ds$$

$$e_1 = -\frac{\rho D b_0}{f_2} \int_0^l \varphi_1 \varphi_2 U(s,t) ds$$

$$e_2 = \frac{\rho D b_0}{2f_2} \int_0^l \varphi_1^2 \varphi_2 ds$$

$$e_3 = \frac{\rho D b_1}{2f_2} \int_0^l \varphi_2^2 U(s,t) ds$$

$$e_4 = -\frac{\rho D b_1}{2 f_2} \int_0^L \varphi_2^2 \varphi_1 ds$$

$$e_5 = \frac{\rho D b_2}{2 f_2} \int_0^L \varphi_2^3 ds$$

$$e_{(2k)} = \frac{\rho D b_k}{2 f_2} \int_0^L \frac{\varphi_2^{k+1}}{U^{(k-2)}} ds$$

$$e_{(2k+1)} = \frac{\rho D b_k (k-2)}{2 f_2} \int_0^L \frac{\varphi_2^{k+2}}{U^{(k-1)}} ds \quad k = 3, \dots, 7$$

where

$$f_1 = m \int_0^L \varphi_1^2 ds$$

$$f_2 = m \int_0^L \varphi_2^2 ds$$

$$T_v = H \sinh\left(\frac{mgl}{2H}\right)$$

$$T_0 = \sqrt{H^2 + T_v^2}$$

$U(s,t)$  is the wind-velocity profile, which was assumed to have a constant value  $U_0$  in this study. The constants  $a_i$  and  $b_i$  are obtained from wind tunnel tests.

$$F_1(t) = \frac{\int_0^L \varphi_1(s) F_1(s,t) ds}{m \int_0^L \varphi_2^2(s) ds}$$

$$F_2(t) = \frac{\int_0^L \varphi_2(s) F_2(s,t) ds}{m \int_0^L \varphi_2^2(s) ds}$$

## APENDIX B

### EXTRACTION OF T-STRESSES

Consider a 3D crack front with a continuously turning tangent as shown in Figure A.1-a (Zhao *et al.*, 2007). Assume a line-load of magnitude  $f_k = f_{u_k}(s)$  to be applied along the crack front as illustrated in Figure A.1-b. In the figure,  $u_k(s)$  defines the direction normal to the crack front and in the plane of the crack at points  $s$ . The solution for this problem is the case of a plane strain semi-infinite crack with a point force  $f$  applied at the crack tip in the direction parallel to the crack. Using the superscript 'L' to designate the stress and displacement fields, the analytical solution gives (Nakamura and Parks, 1992)

$$\sigma_{11}^L = -\frac{f}{\pi r} \cos^3 \theta, \quad \sigma_{22}^L = -\frac{f}{\pi r} \cos \theta \sin^2 \theta, \quad \sigma_{12}^L = -\frac{f}{\pi r} \cos^2 \theta \sin \theta \quad (\text{A-1})$$

$$\sigma_{33}^L = -\frac{f}{\pi r} \nu \cos \theta, \quad \sigma_{13}^L = \sigma_{23}^L = 0 \quad (\text{A-2})$$

The term  $\sigma_{33}^L = 0$  is used for plane stress.

For 3D crack problems, the interaction integral is introduced in the following domain integral form:

$$I(s) = \frac{1}{A_c} \int \left\{ (\sigma_{ij}^L \frac{\partial u_i^L}{\partial x_k} + \sigma_{ij}^L \frac{\partial u_i^L}{\partial x_k}) \frac{\partial q_k}{\partial x_i} - \sigma_{ij}^L \varepsilon_{ij} \frac{\partial q_k}{\partial x_k} \right\} dV \quad (\text{A-3})$$

Here  $V(s)$  is a volume that encloses the crack front segment bounded by  $s - \varepsilon$  and  $s + \varepsilon$  as shown in Figure A.1-c,  $q_k(s)$  defines the virtual extension of the crack front

segment  $s - \varepsilon \leq s \leq s + \varepsilon$  and  $A_c$  is the increase in the crack area generated by the virtual crack advance;  $\sigma_{ij}$ ,  $\varepsilon_{ij}$  and  $u_i$  are the stress, strain and displacement components of the 3D crack problem under consideration;  $\sigma_{ij}^L$ ,  $\varepsilon_{ij}^L$  and  $u_i^L$  are the corresponding components in the line-load auxiliary solution given by (A-1) and (A-2). The T-stress at point  $s$  on the crack front is related to  $I(s)$  by :

$$T(s) = \bar{E} \left\{ -\frac{I(s)}{f} + v\varepsilon_{33}(s) \right\} \quad (\text{A-4})$$

where  $\varepsilon_{33}(s)$  is the extensional strain at point  $s$  in the direction tangential to the crack front.

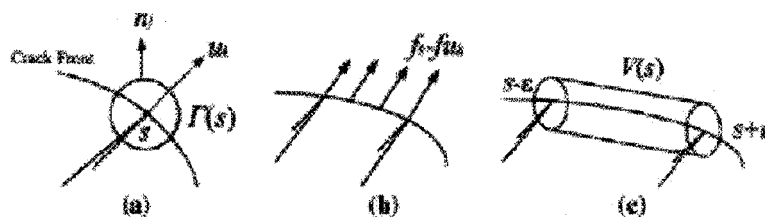


**Fig. A. 1.** A schematic of elements used in the definition of the interaction integral. (a) Crack tip contour  $\Gamma$  on the plane locally perpendicular to the crack front where  $s$  represents the location of the crack tip. (b) Line-load applied in the direction of crack advance along the crack front. (c) Volume  $V$  which encloses the crack front segment  $s - \varepsilon \leq s \leq s + \varepsilon$  (Zhao *et al.*, 2007).